Technological Innovation and Integration of Whole Brain Imaging, Olfactory Stimulation, and Correlative Microscopy in Larval Zebrafish

by

Corban N. Swain
B.S. Biomedical Engineering (2017)
Washington University in St. Louis

Submitted to the Department of Biological Engineering
in partial fulfillment of the requirements for the degree of

Doctor of Philosophy in Biological Engineering

at the

MASSACHUSETTS INSTITUTE OF TECHNOLOGY

September 2024

Authored by: Corban N. Swain
Department of Biological Engineering
August 9, 2024

Certified by: Edward Stuart Boyden
Professor of Brain and Cognitive Sciences
Thesis Supervisor

Accepted by: Douglas A. Lauffenburger
Professor of Biological Engineering
Chair

Technological Innovation and Integration of Whole Brain Imaging, Olfactory Stimulation, and Correlative Microscopy in Larval Zebrafish

by

Corban N. Swain

Submitted to the Department of Biological Engineering on August 9, 2024 in partial fulfillment of the requirements for the degree of Doctor of Philosophy in Biological Engineering

ABSTRACT

Achieving a deep understanding of the brain is a cross-disciplinary endeavor that requires the investigator to consider biomolecular, electrical, and sensory interactions across time and space at many scales. This understanding is important because a deeper understanding of the brain precedes advancements in efficient computing, generalizable frameworks for learning, and, of critical importance, the understanding and treatment of neurological diseases. Towards this end, this thesis presents novel approaches and technologies for whole-brain imaging, olfactory stimulation, and correlative imaging—i.e. the utilization and registration of multiple imaging modalities within a single sample. The overall objective of this thesis research is to not just create technologies, but to integrate them to enabler richer and more contextual understandings of the larval zebrafish's brain.

In this work we show novel light field microscopy algorithms that allow us to reconstruct 3D images from 2D micrographs with improved resolution to enable high-framerate recordings of whole-brain neural activity. We describe the designing and building of the first known system for multi-directional olfactory stimulation of larval zebrafish with up to ten separate odor channels. We demonstrate an optimized expansion microscopy-compatible immunostaining protocol for whole-mount zebrafish which preserves registration epitopes to move towards the neuron-level alignment of structural and functional data. And, finally, we showcase a set of proof-of-concept experiments and analyses which demonstrate our ability to integrate olfactory stimulation, whole-brain calcium imaging, behavioral recording, and structural staining in individual larva.

Thesis Supervisor: Edward Stuart Boyden
Title: Professor of Brain and Cognitive Sciences

Acknowledgements

To God, Abba, thank you for redeeming me out of each and every circumstance that could have swept me away. Knowing and accepting your love through Christ is my greatest treasure.

To my parents Roderick & Denise, thank you for "training me up" in the way that God has blessed me to go. The value of your foundation and support has no comparison.

To my family, thank you for your loyal support and love; your smiles and laughs are etched in my mind.

To my sisters Solome and Ufuoma, thank you for looking out for me in ways that I never knew I needed, you all are irreplaceable gifts in my life.

To my brother Mario, I am so grateful for our brief time together. I look forward to hearing your "Ayeeee!" on the other side of eternity.

To my church families First Missionary Baptist Church, Aletheia Church, and Pentecostal Tabernacle, thank you for "dwelling in unity" with me, the fullness of your presence and care is encouragement for many lifetimes.

To my advisor Ed, thank you for calling me an inventor before I ever acknowledged myself as one, working with you has truly been a dream come true.

To my committee chair Doug, thank you for helping establish the culture of the department that has been such a warm academic home.

To my committee member Florian, thank you for teaching me so much about zebrafish neuroscience. Your ambition, curiosity, and excitement is something I aspire to.

To the Synthetic Neurobiology Group, thank you for creating such an electric and multifaceted environment for doing science. And please don't stop bringing me miscellaneous engineering and debugging tasks from around the lab, helping out in that way is one of my favorite things.

To my trainees Nicole, Alaysia, Andy, Victoria, and Theo, thank you for giving me the opportunity to share with your some of the things that were shared with me. Remember to do the same!

To my roller skates, thank you for making Albany Street my runway and my commute a time in the clouds.

Contents

List of Figures

Chapter 4 *Reading-Out*: Whole-Brain Calcium Imaging, Behavioral Quantification, and Structural Mapping

List of Tables

CHAPTER 1

Introduction

The brain is an incredible, and potentially the quintessential, example of emergent biological complexity. Alongside phenomena like terraformation of the biosphere, tissue differentiation & organization, and immune recognition & response, the activity and organization of the brain represents coordination from the molecular level—e.g. neurotransmitter binding—all the way to the multi-organism scale—e.g. reproduction. Achieving any facet of understanding about this system is important not only for the philosophical reasons, but because a deeper understanding of the brain precedes untapped advancements in efficient and compact computing [1], generalizable frameworks for learning [2, 3], dynamic and modular structures [4], prediction and shaping of behavior [5], and of critical clinical importance: the development of more robust and effective treatments for neurological diseases.

1.1 Paradigms and Perils for Understanding the Brain

Given the depth of complexity and the wealth of potential advancement offered by studying the brain, much work has been done across many scales to observe properties of and develop theories about the brain and its components, i.e. neuroscience. A complete discussion of the existing approaches and frameworks for studying the brain is outside of the scope of this thesis. However, I will highlight a few recent reports that suggest new paradigms for approaching neuroscience questions are needed to develop more fundamental theories regarding how the brain works.

Bargmann & Marder argue that even for simple nervous systems composed of a relatively small number of neurons, it is not enough to know the synaptic connectivity of neurons—the primary goal of "connectomic" approaches—to predict and understand how the system will function [6] (see the commentary by Meinertzhagen for a broader discussion of connectomics [7]). "Parallel and antagonistic pathways" mean that neural circuits can operate differently in different contexts; and the history of activity for a neuron can dramatically affect the parameters of its function. They suggest that **anchoring connectomic**

maps of the brain in cellular identity will be important for taking full advantage of those maps.

Jonas & Kording simulate several common neuroscience experiments and analyses to understand an Atari microprocessor *de novo*. They show that current approaches would fail to make inroads for understanding how a microprocessor works; for example, they show that "lesioning" individual transistors while playing different games on the processor would misleadingly suggest that there are "behavior"-specific "Donkey Kong transistors" [8]. They propose that **building fundamental theories**—e.g. common modules of neural computation—will make it possible have a basis for more holistically understanding neurological phenomena.

Brette argues that that existing experimental frameworks for interrogating sensory systems (like vision) can lead to biased conclusions which suggest brain regions operate by communicating static "codes" [9] (see also the opinion by Tytell *et al.* emphasizing the importance of embodiment and biomechanics to properly understand neural circuits[10]). Instead, Brette submits, **neural activity must be framed and modeled in the context of a dynamic system**...an old but important distinction [11].

Although it will ultimately take several novel approaches to address the issues raised above, we believe **correlative microscopy** is an approach uniquely equipped to tackle at least some of them. With this approach, **we work towards merging cellular identity, connectivity maps, behavioral observation, and dynamical activity across both space and time to develop new theories of brain function and processing through the context of controlled, simulated environments.** Additionally, we see the larval zebrafish as a an ideal model system for applying these approaches with current state-of-the-art imaging techniques (a longer discussion of why we chose larval zebrafish as our model organism is given in §1.3). A long-term goal of this work is to enable the generation of correlated data which is robust enough to both inform the design of and validate the performance of simulatable whole-brain models.

In the following sections we will elaborate on the rationale of our approaches to correlative microscopy, our use of larval zebrafish, and our motivations for using stimulation as a means to give context for our investigations.

1.2 Correlative Microscopy: Reading Out Across Many Modes and Scales

Correlative microscopy approaches use combinations of multiple imaging modalities as a strategy for spanning the temporal and spatial scales required to more holistically study the brain [12], Figure 1. Against the backdrop of the many challenges that still exist to understand how brain function and behavior arise from the interconnected networks of neurons in the brain, we are proposing a technique that builds from existing correlative microscopy approaches. Examples of existing approaches include the following:

- *Correlated light and electron microscopy (2008 – 2015).* Many groups combine fluores-

cence microscopy (FM) with electron microscopy to enable fluorescent molecular labels to be overlaid on high-resolution electron microscopy (EM) images [13–20].

- *Correlative two-photon and light sheet microscopy (2014).* Silvestri et al. combine in vivo two-photon (2P) FM with ex vivo confocal light sheet microscopy (CLSM) such that time-lapse imaging of mouse brain regions can be overlaid with the structure of the imaged neuron and the surrounding network [21].

- *Zebrafish brain atlas (2015).* Randlett et al. and other groups demonstrate registration of immuno-labeled zebrafish brains onto a reference brain and co-registration of in vivo two-photon calcium imaging with ex vivo staining of biochemical correlates of activity [22, Fig. 2d, e][23].

- *Correlative* TPFM *and label-free near-infrared reflectance (2016).* Costantini et al. combine 2P FM with near-infrared reflectance (NIR) to image labeled neurons along with unlabeled neurites in both *ex vivo* and *in vivo* mouse tissue [24].

Despite the development of these and other approaches, there are some gaps in existing correlative microscopy techniques.

- None of the *in vivo* imaging approaches can image at the speeds necessary to take advantage of genetically-encoded fluorescent voltage indicators (GEVIs) [25–28]. These sensors can be used to read out, using light, the primary currency of neuronal activation: membrane voltage. GEVIs stand as higher fidelity neural readout over the more established genetically encoded calcium indicators (GECIs); intracellular calcium is correlated with neuronal activity but at a lower temporal and spatial fidelity compared to membrane voltage [29, 30]. Therefore, we wish to develop technologies that can enable the high volumetric image acquisition speeds required for whole-brain imaging—motivating the work described in Chapter 2.

- Of all the *ex vivo* approaches employed, only EM can resolve the detail needed to pick apart the synaptic connections between neurons. However, EM on its own is not able to take advantage of both high imaging resolution and biomolecular staining in a high-throughput manner. Therefore, we wish to lay the groundwork for developing alternative (i.e. expansion microscopy) mapping techniques compatible with broad biomolecular labeling—leading us to the work in Chapter 4 in immunohistochemistry.

- There is an advantage to performing correlative microscopy in the context of stimulation which we discuss further in §1.4; and this is not highlighted in many existing reports. Therefore, we wish to develop the technology to employ stimulation to an animal while it undergoes live brain imaging—leading us to the work in Chapter 3.

1.2.1 What Modalities Do We Correlate? Our Microscopy and Imaging Toolbox

With each of these gaps in mind it is important for us to discuss the toolbox of modalities which we have chosen to use for this work and why these methods are included our correlative approach.

For live imaging of neural activity we utilize two microscopy techniques: two-photon microscopy and light field microscopy. Two photon microscopy, although it is a relatively slower technique, is utilized because of its sensitivity, image quality, physical compatibility with stimulation (i.e. excitation and light collection occur through a single objective compared to, say, many light-sheet methods) and the ability to image into deep brain tissues. Additionally, through certain technological improvements it is possible to readout volumetric images from the larval zebrafish brain at $\approx 2\,\text{Hz}$. A broader discussion of the motivation for using two-photon microscopy is presented in §4.1.1.1.

The other technique we employed for live imaging of neural activity is a dual-objective light field microscope system. We utilizes this microscope to address gap 2 and overcome the limitations on readout speed associated with volumetric imaging techniques which rely on scanning while still isotropically resolving imaging volumes. Though there are complexities to consider with light-field techniques, discussed in-depth in Chapter 2; the prospective advantage of enabling whole-brain voltage imaging with GEVIs led us to employ and develop this technique.

For behavioral observation, we employ high-speed near-infrared (NIR) imaging with a machine vision camera system. NIR imaging allows us to image zebrafish motion with minimal optical stimulation, the high-speed acquisition allow for accurate tracking of rapid tail movements over time. Furthermore machine vision analysis tools allow us to transform the videos into quantitative metrics. See §4.5.6.

For structural imaging, we utilize spinning-disk confocal microscopy with contrast provided by immunohistochemical (IHC) staining. These are well tried techniques, with spinning-disk confocal microscopy enabling rapid acquisition of volumetric images with diffraction-limited resolution along the optical axis. While immunohistochemical staining enables us to readout a host of different epitopes with a wide array of commercially available primary antibodies. However a key limitation of IHC-based imaging is that only 4–6 different epitopes can be simultaneously stained in a sample without cross-talk between excitation-emission channels. See §4.1.3 for more discussion of IHC for structural imaging.

To address gap 1, expansion microscopy (ExM) is a technique that is well-suited to push to the maximum resolution of light-microscopy approaches to the point of enabling connectomic mapping. In short, ExM enables super-resolution of biological specimens by physical expansion [31–33] of the sample by embedding the sample in a hydrogel, destabilizing the structure of the tissue, then physically swelling the tissue-hydrogel matrix by thermodynamic driving forces. ExM remains underutilized as a tool in correlative techniques even though it overcomes many of the limitations of electron microscopy and optical super-resolution [34], Figure 1. In this work we only minimally employed ExM (in a few trial experiments); however, utilizing ExM frames the context for how we designed our

molecularly-annotated structural imaging protocols. We aimed for all steps of the structure imaging methods to be compatible with ExM-based connectomic and *in situ* sequencing approaches being developed by our research group.

1.3 Larval Zebrafish as Our Model System

Zebrafish (*Danio rerio*) are a well-established model vertebrate system for performing neuroscience experiments [35]. The benefits of zebrafish as a model system include physiological and genetic homology to humans, accessibility to manipulation by genetic tools, transparent tissue which allows in vivo imaging of larvae, rapid development to maturity ($\approx$ 90 days), and a many stereotyped (e.g. the optomotor reflex) and complex behaviors [36–39]. Another important feature of zebrafish, specifically larvae aged 5 – 7 days post fertilization, is that their entire brain fits within a $\approx 600 \times 400 \times 400\,\mu m^3$ volume, a size which is amenable to imaging within a single microscope field of view (with a 16×–20× objective). Each of these qualities mean that zebrafish, in the context of this proposed work, are well posed to enable us to develop and apply a novel correlative microscopy technique in a way that is relevant to asking and answering important neuroscience questions.

1.4 Stimulation as a Context for Building Hypothesis-driven Understanding

In building an understanding of how a network of neurons, glia, and other cells go on to create the complexity of coordination and behavior. We can imagine that each cell, and each sub-network of cells can occupy a certain locations in high-dimensional activation space, the range of locations that are traversed in this high dimensional space are potentially limited when we consider only the baseline "stream of conciousness" activity. To move into different domains of activation and traverse into otherwise unreachable regions of that high-dimensional space we see perturbation as a powerful mechanism to enable that motion. Perturbation can come in many types of forms including "natural" stimulants like visual stimuli, presentation with prey, presentation with different water-borne odorants, heat, or physical touch. Perturbation can also come in forms that do not have an ethological analog including optogenetic activation of neurons and physical neuron ablation.

Perturbation is well understood to be critical to build holistic understanding of the brain and is a requirement to test hypotheses. Furthermore, we see the development of stimulation methods which can not only perturb an animal, but can simulate virtual environments as particularly useful because of the possibility of providing closed-loop stimulation. In this type of environment the larvae is able to interact, in real time, with the stimulus in a manner similar to "real" free behavior in natural contexts. Such type of stimulation further expands our exploration of cellular activation space and allows gleaned results to inform neuroscience theories which can generalize across a broader set of context. Because of this, we chose to focus on the development of an olfactory stimulation system which is

capable of providing a virtual environment for the larvae, a broader discussion of why we choose olfaction over other stimulation methods is presented in §3.1.

When we acquire correlated datasets in the context of stimulation, it allows us to test hypotheses on multiple levels. For example, we could test if a particular stimulus presentation is responded to at a certain probability level based on the relative presence of a particular population of cells. We could also test if the the time it takes for a larva to stop performing escape motions in response to a given stimulus are correlated to the initial activity state of a particular subset of neurons. It's these types of hypotheses that, particular when tested a large scale with machine learning methods, can enable the design of new generalizable theroies which we aim to work toward. This work focuses on the development of the technologies needed to enable these types of experiments; however, these examples highlight the rationale behind the specific technologies developed and demonstrated here. In Chapter 5 we provide an exploration of how we leverage our technologies, showing the types of experiments we can perform and the analysis they yield in the context of olfactory stimulation with correlated functional activity, behavioral, and structure data.

1.5 The Evolution of This Work

While we have setup an introduction to the content of this thesis thematically, it is also useful to understand how the scope and aims of this work evolved over time to lead to the "final" product presented here.

I initially came to the lab with a desire to design and create truly "neuromorphic" computing "wetware" in which synthetic biological materials, structures, paradigms, and interconnects were utilized to create objects capable of computation in radical different and biomolecularly-mediated ways—the biological analogs of quantum computers. However, in presenting these ideas to my advisor, Ed Boyden, he made it clear that we had yet to develop the fundamental understating of how the brain works to even begin designing such systems. Thus began my pivot into the development Synthetic Neurobiology group as one straddled between the wet-lab's bench and the dry-lab's workstation. Over the coming years, the focus of my work became the development of the technologies and approaches needed to build those fundamental understanding. This is what I present here.

1.6 The Structure of Thesis Chapters

Each of the following four chapters of this thesis contain their own *introduction*s which provides some background on the necessity of that subset of development and study, the rational behind the approaches used, and connects the work to that of the broader community as well as our specific goals. Each chapter then goes on to present: important the "Results" from experiments performed in figures and exposition; a "Discussion" which explains and contextualizes the results, their implications, and future directions; an exposition on the "Methods" used to acquire the results; and, finally, a "Conclusion" to summarize all of what was presented.

In each of Chapters 2 to 4 we include an additional section (§2.2, §3.2, §4.2) which discusses the development and/or design of some of the technologies developed, engineered and implemented towards the goals of the study. These sections outline the design of algorithms, technologies, and systems which were a major portion of the intellectual labor for this thesis work. These design sections outline the key design requirements for the relevant system or subsystem, then walk through, in detail, the components of that design and why relevant choices were made. For brevity we do not include a discussion of previous design iterations, but focus on the current, utilized versions.

This work was a joy to undertake and I sincerely hope that the following presentation is a joy to read and meaningfully contributes to the scientific endeavors of future readers.

1.7 References

1. Burgt, Y. V. D., Melianas, A., Keene, S. T., Malliaras, G. & Salleo, A. Organic electronics for neuromorphic computing. *Nature Electronics* **1,** 386–397. ISSN: 25201131 (7 July 2018).
2. Zarr, N. & Brown, J. Foundations of human problem solving. *bioRxiv,* 779322. https://www.biorxiv.org/content/10.1101/779322v1 (2019).
3. Zarr, N. & Brown, J. W. Foundations of human spatial problem solving. *Scientific Reports 2023 13:1* **13,** 1–18. ISSN: 2045-2322. https://www.nature.com/articles/s41598-023-28834-3 (1 Jan. 2023).
4. Canales, A. *et al.* Multifunctional fibers for simultaneous optical, electrical and chemical interrogation of neural circuits in vivo. *Nature Biotechnology* **33,** 277–284. ISSN: 15461696 (3 2015).
5. Rosenberg, M. D., Casey, B. J. & Holmes, A. J. Prediction complements explanation in understanding the developing brain. *Nature Communications* **9.** ISSN: 20411723 (1 Dec. 2018).
6. Bargmann, C. I. & Marder, E. From the connectome to brain function. *Nature Methods* **10,** 483–490. ISSN: 15487091 (6 Apr. 2013).
7. Meinertzhagen, I. A. Of what use is connectomics? A personal perspective on the Drosophila connectome. *Journal of Experimental Biology* **221.** ISSN: 00220949. https://dx.doi.org/10.1242/jeb.164954 (10 May 2018).
8. Jonas, E. & Kording, K. P. Could a Neuroscientist Understand a Microprocessor? *PLOS Computational Biology* **13** (ed Diedrichsen, J.) e1005268. ISSN: 1553-7358. http://dx.plos.org/10.1371/journal.pcbi.1005268 (1 Jan. 2017).
9. Brette, R. Is coding a relevant metaphor for the brain? *Behavioral and Brain Sciences,* 1–44. ISSN: 0140-525X. https://www.cambridge.org/core/product/identifier/S0140525X19000049/type/journal_article (Feb. 2019).
10. Tytell, E. D., Holmes, P. & Cohen, A. H. Spikes alone do not behavior make: Why neuroscience needs biomechanics. *Current Opinion in Neurobiology* **21,** 816–822. ISSN: 09594388 (5 Oct. 2011).
11. Van Gelder, T. What Might Cognition Be, If Not Computation? *Journal of Philosophy* **91** (ed Smylie, J.) 345–381. ISSN: 0022-362X. https://www.jstor.org/stable/pdf/2941061.pdf (7 1995).
12. Mascaro, A. L. A., Silvestri, L., Sacconi, L. & Pavone, F. S. Towards a comprehensive understanding of brain machinery by correlative microscopy. *Journal of Biomedical Optics* **20,** 061105. ISSN: 1083-3668 (6 Mar. 2015).
13. Boer, P. D., Hoogenboom, J. P. & Giepmans, B. N. Correlated light and electron microscopy: Ultrastructure lights up! *Nature Methods* **12,** 503–513. ISSN: 15487105 (6 May 2015).

14. Giepmans, B. N. Bridging fluorescence microscopy and electron microscopy. *Histochemistry and Cell Biology* **130,** 211–217. ISSN: 09486143 (2 Aug. 2008).

15. Verkade, P. Moving EM: The Rapid Transfer System as a new tool for correlative light and electron microscopy and high throughput for high-pressure freezing. *Journal of Microscopy* **230,** 317–328. ISSN: 00222720 (2 May 2008).

16. Liss, V., Barlag, B., Nietschke, M. & Hensel, M. Self-labelling enzymes as universal tags for fluorescence microscopy, super-resolution microscopy and electron microscopy. *Scientific Reports* **5.** ISSN: 20452322 (Dec. 2015).

17. Brown, E. & Verkade, P. The use of markers for correlative light electron microscopy. *Protoplasma* **244,** 91–97. ISSN: 0033183X (1 2010).

18. Ellisman, M. H., Deerinck, T. J., Shu, X. & Sosinsky, G. E. in, 139–155 (Academic Press Inc., 2012).

19. Watanabe, S. *et al.* Protein localization in electron micrographs using fluorescence nanoscopy. *Nature Methods* **8,** 80–84. ISSN: 15487091 (1 Jan. 2011).

20. Betzig, E. *et al.* Imaging intracellular fluorescent proteins at nanometer resolution. *Science* **313,** 1642–1645. ISSN: 00368075 (5793 Sept. 2006).

21. Silvestri, L., Mascaro, A. L. A., Costantini, I., Sacconi, L. & Pavone, F. S. Correlative two-photon and light sheet microscopy. *Methods* **66,** 268–272. ISSN: 10462023. https://linkinghub.elsevier.com/retrieve/pii/S1046202313002144 (2 Mar. 2014).

22. Randlett, O. *et al.* Whole-brain activity mapping onto a zebrafish brain atlas. *Nature Methods* **12,** 1039–1046. ISSN: 1548-7091. http://www.nature.com/articles/nmeth.3581 (11 Nov. 2015).

23. Kunst, M. *et al.* A Cellular-Resolution Atlas of the Larval Zebrafish Brain. *Neuron* **103,** 21–38.e5. ISSN: 10974199 (1 July 2019).

24. Costantini, I. *et al. Combination of two-photon fluorescence microscopy and label-free near-infrared reflectance: a new complementary approach for brain imaging* in *Biomedical Optics 2016* (OSA, 2016), JW3A.23. ISBN: 978-1-943580-10-1. https://www.osapublishing.org/abstract.cfm?URI=Cancer-2016-JW3A.23.

25. Abdelfattah, A. *et al.* Bright and photostable chemigenetic indicators for extended in vivo voltage imaging. *bioRxiv,* 436840. https://www.biorxiv.org/content/10.1101/436840v1 (Oct. 2018).

26. Piatkevich, K. D. *et al.* A robotic multidimensional directed evolution approach applied to fluorescent voltage reporters. *Nature Chemical Biology,* 1. ISSN: 1552-4450. http://www.nature.com/articles/s41589-018-0004-9 (Feb. 2018).

27. Abdelfattah, A. S. *et al.* A general approach to engineer positive-going eFRET voltage indicators. *bioRxiv,* 690925. http://dx.doi.org/10.1101/690925 (2019).

28. Yang, H. H. & St-Pierre, F. Genetically encoded voltage indicators: Opportunities and challenges. *Journal of Neuroscience* **36,** 9977–9989. ISSN: 15292401 (39 Sept. 2016).

29. Grienberger, C. & Konnerth, A. Imaging Calcium in Neurons. *Neuron* **73,** 862–885. ISSN: 08966273 (5 Mar. 2012).

30. Bando, Y., Sakamoto, M., Kim, S., Ayzenshtat, I. & Yuste, R. Comparative Evaluation of Genetically Encoded Voltage Indicators. *Cell Reports* **26,** 802–813.e4. ISSN: 2211-1247. https://www.sciencedirect.com/science/article/pii/S2211124718320485 (2019).

31. Chen, F., Tillberg, P. W. & Boyden, E. S. Optical imaging. Expansion microscopy. *Science (New York, N.Y.)* **347,** 543–8. ISSN: 1095-9203. http://www.ncbi.nlm.nih.gov/pubmed/25592419 (6221 Jan. 2015).

32. Tillberg, P. W. *et al.* Protein-retention expansion microscopy of cells and tissues labeled using standard fluorescent proteins and antibodies. *Nature Biotechnology* **34,** 987–992. ISSN: 1087-0156. http://www.nature.com/articles/nbt.3625 (9 Sept. 2016).

33. Freifeld, L. *et al.* Expansion microscopy of zebrafish for neuroscience and developmental biology studies. *Proceedings of the National Academy of Sciences of the United States of America* **114,** E10799–E10808. ISSN: 1091-6490. http://www.ncbi.nlm.nih.gov/pubmed/29162696 (50 Dec. 2017).

34. Gallagher, B. R. & Zhao, Y. Expansion microscopy: A powerful nanoscale imaging tool for neuroscientists. *Neurobiology of Disease* **154,** 105362. ISSN: 0969-9961 (July 2021).

35. Fetcho, J. R. & Liu, K. S. Zebrafish as a Model System for Studying Neuronal Circuits and Behavior. *Annals of the New York Academy of Sciences* **860,** 333–345. https://nyaspubs.onlinelibrary.wiley.com/doi/abs/10.1111/j.1749-6632.1998.tb09060.x (1998).

36. Fishman, M. C. Zebrafish - The canonical vertebrate. *Science* **294,** 1290–1291. ISSN: 00368075 (5545 Nov. 2001).

37. Stewart, A. M., Braubach, O., Spitsbergen, J., Gerlai, R. & Kalueff, A. V. Zebrafish models for translational neuroscience research: From tank to bedside. *Trends in Neurosciences* **37,** 264–278. ISSN: 1878108X (5 2014).

38. Driever, W., Stemple, D., Schier, A. & Solnica-Krezel, L. Zebrafish: genetic tools for studying vertebrate development. *Trends in Genetics* **10,** 152–159. ISSN: 01689525 (5 1994).

39. Naumann, E. A. *et al.* From Whole-Brain Data to Functional Circuit Models: The Zebrafish Optomotor Response. *Cell* **167,** 947–960.e20. ISSN: 0092-8674. https://www.sciencedirect.com/science/article/pii/S0092867416314027 (4 Nov. 2016).

CHAPTER 2

Unified Methods for 3D Reconstruction in Multiview Light Field Microscopy

2.1 Introduction

Optical imaging of *in vivo* biological processes such as neuronal activity [2–7] is a popular recording method due to its low invasiveness, high spatial resolution, and ability to record from a population of neurons (see §4.1.1 for a more in-depth discussion of calcium imaging and how it is enabled). However, since most microscopy techniques rely on sequential scanning of a point, line, or plane in 3-D space [5–7], it can often be difficult to optically record activity across an entire brain volume or organism at sampling rates that are faster than the activity itself (particularly as it relates to voltage imaging), leading to a loss of information Figure 2.1.

Light field microscopy (LFM) is a technique that allows for three-dimensional (3D) imaging at speeds as fast as the camera frame rate [8–10]. This is achieved by a two step process of **1)** light field capture followed by **2)** computational reconstruction. The first step is to capture two-dimensional (2D) "light fields" which contain information regarding both the location and the angle of the incident light. This multiplexing of spatial and angular information is achieved by placing a lenslet (or *micro-lens*) array at the the conjugate image plane of an epifluorescence microscope system and placing the camera sensor at the focal plane of the lenslets Figure 2.2. In the second step, these 2D light fields can be utilized via computational algorithms to "reconstruct" a 3D image volume of the sample Figure 2.3B. Prevedel *et al.* have previously shown that LFM can be used to record neural activity throughout the entire *C. elegans* and larval zebrafish brains [10], but there are several problems that prevent LFM from being broadly applied and utilized.

In this chapter we will discuss the approaches taken to address two general problems with light field imaging and two problems specific to the reconstruction process: 1) poor

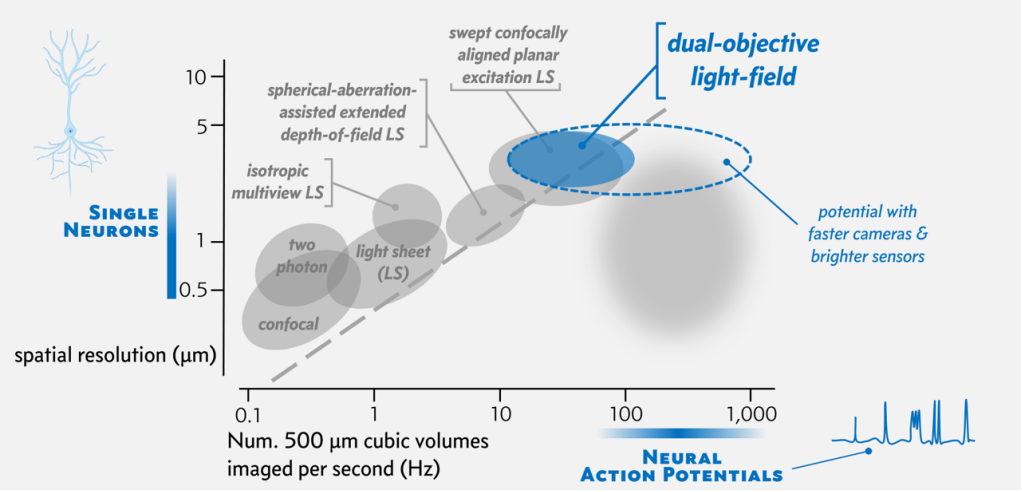

Figure 2.1: Microscopy technologies for whole-brain functional imaging negotiate a trade-off between maximum volumetric imaging speed and the minimum resolvable spatial resolution. Chart depicts a number of different microscopy techniques and places their approximate range of volumetric imaging acquisition rates (for a $500 \times 500 \times 500\,\mu m^3$ imaging volume) along the x-axis and their achievable spatial resolutions under the same conditions along the y-axis. For whole-brain volumetric imaging, the desired volumetric rate would be ≈ 500 Hz while the ideal spatial resolution would be $< 1\,\mu m$ for larval zebrafish (blue gradients along axes). Most technologies must trade off between having higher resolution and higher imaging speed. Our dual-objective LFM technique and associated computational microscopy algorithms are capable of imaging at high-speed, but relatively poor with imaging at the single-neuron resolution (dark blue circle). With improvements to camera technologies and development of brighter sensors* dual-objective LFM and related techniques may be able to move (blue dashed ellipse) into the imaging regime required for whole-brain voltage imaging (dark grey gradient).
Note: Abbreviation LS: light sheet. Figure adapted from Wang [1, Figure 4].

axial resolution, 2) artifacts and aliasing at the native object plane in the reconstructed volume, 3) speed of volumetric reconstruction, 4) optimization of multi-view reconstruction hyper-parameters.

2.1.1 Poor Axial Resolution

A significant loss of resolution in LFM comes from the fact that the axial resolution (that is, the resolution along the reconstructed axis) is significantly worse than the lateral resolution (≈ 4 times), see Figure 2.7A. This is because the microscope objective only images a limited number of views of the sample. The amount of light an individual objective lens can obtain is limited by its numerical aperture. A conceptually simple way of increasing the rays of light that we capture would be to have multiple objectives image the same sample and combine the information into a single volume. Both this work and Wagner *et al.* present the design of an LFM having two arms [11] that view the sample from orthogonal directions to address this problem, Figure 2.3A.

However, existing methods to date utilize the light fields *independently* in their 3D image reconstruction algorithms Figure 2.3B. Such methods potentially fail to efficiently computationally extract all the information contained in a series of light fields obtained from multiple views and limit the maximum resolution attainable when imaging a dense sample. Here, we pioneer and explore the space of what we coin as "multimerge" algorithms

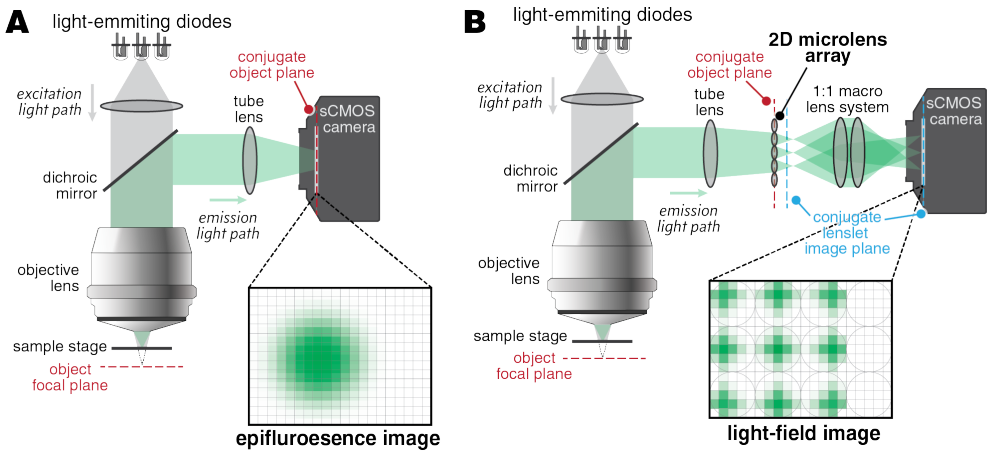

Figure 2.2: Light-field microscope (LFM) systems simultaneously capture both spatial and angular information from a sample in a single image. **A**: In a simple epifluorescence system, an out-of-focus point emitter (object) will focus into blurred "blob" onto the conjugate focal plane (i.e. where the camera is located, red dashed line). The center of the "blob" gives information about the spatial *xy*-location of the object; however, no information regarding axial *z*-location of the object relative to the system's focal plane is encoded in the image. Only by mechanically scanning either the objective or the illumination light along the optical axis, and acquiring multiple images at different *z*-locations over time can this axial *z*-information be read-out. Whereas, **B**: an LFM system will capture angular information at the conjugate object plane through the use of a 2D lenslet array and a relay lens will image a "light field" from the lenslet image plane (blue dashed line) onto the camera sensor. This light field contains both spatial information about the *xy*-location of the object and angular information about the axial *z*-location. Therefore, from a single image we can computationally reconstruct image volumes (see Figure 2.3) and perform volumetric imaging at the frame rate of the camera.
Note: The terms "microlens" and "lenslet" are interchangeable.

that perform 3D image reconstruction from a series of light fields in a *dependent* manner incorporating all light field observations in concert in an iterative scheme, Figure 2.3C.

2.1.2 Artifacts and Aliasing

Another source of loss of resolution in LFM is due to the strong artifacts at the native object plane due to "depth-dependent sampling patterns and induced aliasing in light field imaging" as Stefanoiu *et al.* [12] describe in citing Bishop & Favaro [13], see white arrows in Figure 2.4. Various methods have been introduced by Stefanoiu *et al.* and other authors ([14–16]) to address such artifacts in image volumes reconstructed from light fields; however, these methods are framed and demonstrated in the single-view context. Here, we will also demonstrate the adaptation anti-aliasing and artifact removal methods to the multiview light field context.

2.1.3 Volumetric Reconstruction Speed

Reconstructing 3D image volumes from light field images can be a time intensive process. Attention must be paid to the design of algorithms, the optimization and parallelization of those algorithms for GPU's, multithreaded CPU's and other hardware. And the establishment of criteria that determine when a volumetric reconstruction has reached a point of convergence. In this chapter we will discuss methods employed for speeding up the re-

construction process and adaptations of methods to the multi-view context. We will also discuss considerations given to the process of reconstructing a temporal series of light fields and methods where the result of prior frames can allow for the speedup of reconstructing subsequent frames.

2.1.4 Hyper-parameter Optimization

We discuss a number of algorithmic innovations in the following text of this chapter, §2.2.2. However, while the adaptation of existing algorithms to the multiview context has the potential to provide benefits in reconstruction quality as well as convergence speedup there is an expansion of possibilities in many reconstruction steps afforded due to the presence of multiple views. For example there are many schemes which can be taken to combine multiple image volumes, there are different algorithmic process steps where volumetric transformations can be applied to project to/from individual views from/to the mutual view, there are various ways to weight an update to the output volumetric image, etc.

These schemes and decisions can be classified as values for various algorithmic "hyper-parameters" and the choice made for each of them can have a major effect on reconstruction quality. Furthermore, different combinations of hyper-parameter values may be optimal for micrographs of different sparsity or 3D structure. Because of these factors, it is important to also have a process for selecting and fine-tuning hyper-parameters for a particular image reconstruction scheme. In this chapter we will discuss the methods developed

Figure 2.3 *(following page)*: The invention of the dual-objective light field microscope (LFM) required innovating image-to-volume reconstruction algorithms. **A**: Schematic of our dual-objective LFM (dLFM) system. The dLFM system consists of two mechanically aligned, optically identical, and independent epifluorescence LFMs (see Figure 2.2B) designed to allow for isotropic resolution across all axes (see §2.1.1). The objectives for each microscope are oriented at $\approx 90°$ to one another in the *xz*-plane. Each "arm" of the system reads out its own 2D light field image $\mathbf{I}_n$ aligned to it's own coordinate system. As such the *y*-axis of one arm corresponds to the *z*-axis (roughly speaking) of the other arm. The coordinate system of each arm and the reconstructed 3D space that it captures we describe as a "view" V_n. To align reconstructed volumes $\mathbf{V}_n$ from view V_2 onto view $V_{\text{ref}} \equiv V_1$ we must define a registration transformation $\mathscr{T}_2$ (and $\mathscr{T}_2^{-1}$ is the inverse transform of V_{ref} onto V_2). When this registration function is applied to a view or an image volume, we call it a "warp" as is depicted. **B**: Algorithmic block diagram of dLFM reconstructions via independent reconstructions followed by registration and fusion; discussed in §2.2.2.2. A simple approach to utilizing the dLFM system would be to computationally reconstruct volumes for each arm separately—achieved by utilizing the light field point-spread function $\mathbf{H}$ and its transpose $\mathbf{H}^{\mathbf{T}}$ to perform a modified multi-plane deconvolution of $\mathbf{I}_n$, see Equation (2.20). After these parallel reconstructions, we warp $\mathbf{V}_2$ onto $\mathbf{V}_1$, then fuse the two volumes (e.g. by taking their mean). We call this result $\mathbf{V}_{\text{independent}}$ since the reconstructions are performed independent of one another. **C**: Algorithmic block diagram of dLFM reconstruction via the multimerge reconstruction algorithm we developed; discussed in §2.2.2.4. A more nuanced approach to utilizing our system is to incorporate images from each view into the reconstruction scheme iteratively generate and update a output reconstruction $\mathbf{V}_{\text{multimerge}}$. In this way, information from each view is be utilized during the reconstruction process and potentially make the computation more efficient, faster to converge, and producing better results.
Note: Additional dLFM reconstruction algorithms were developed, although not depicted here, and are discussed in-depth in §2.2. Abbreviations: RL: light field-modified Richardson-Lucy deconvolution, FP: forward projection (Equation (2.8)), BP: back projection (Equation (2.9)), "compound": compound PSF computation (§2.2.3). For the block diagram arrow heads indicate inputs into the block while line stems from a block or variable indicate outputs; bold lines represent recursive steps potentially repeated multiple times.

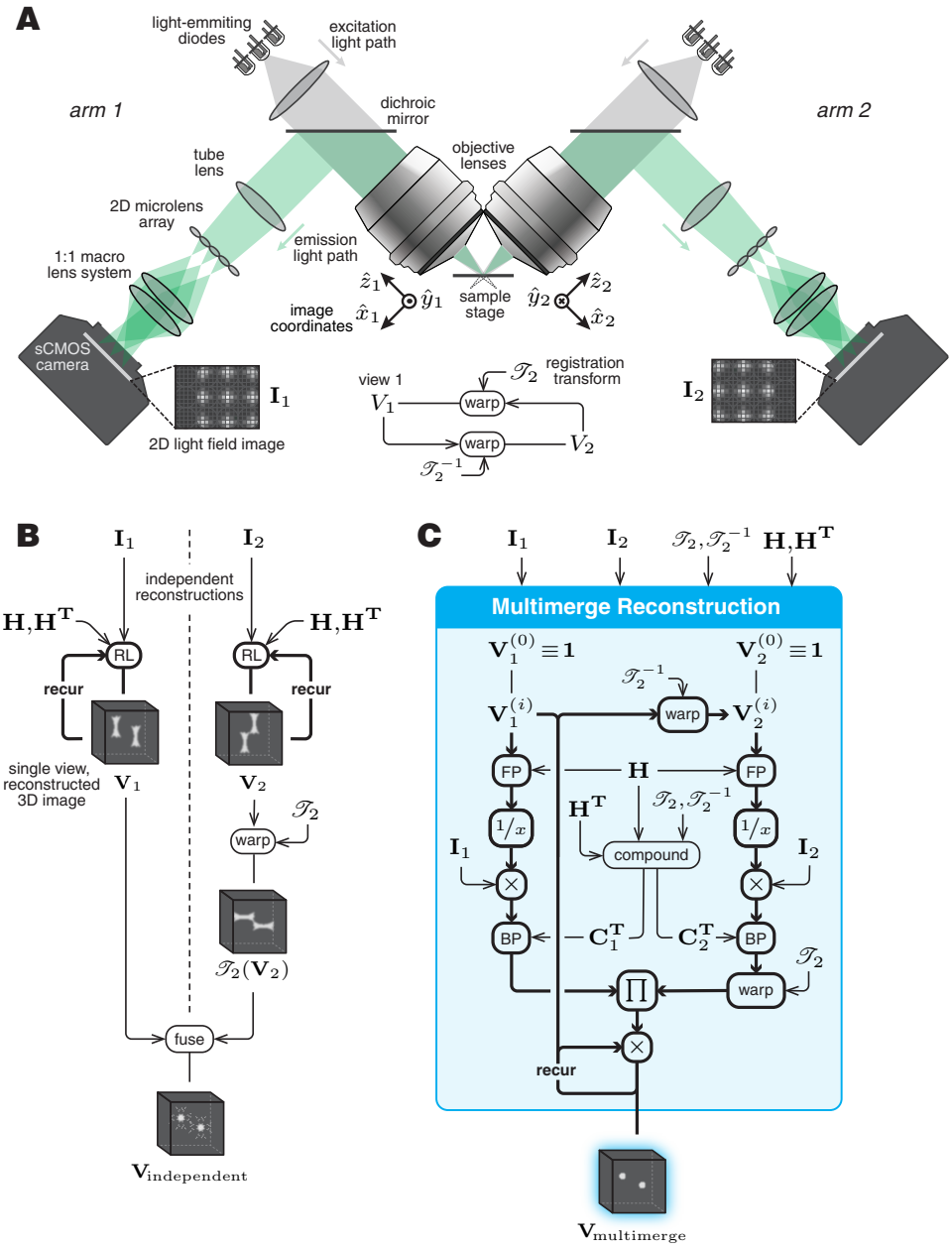
A
light-emmiting diodes
excitation light path
arm 1
dichroic mirror
arm 2
tube lens
objective lenses
2D microlens array
emission light path
1:1 macro lens system
image coordinates
sample stage
sCMOS camera
2D light field image
view 1
registration transform
warp
warp
B
independent reconstructions
RL
RL
recur
recur
single view, reconstructed 3D image
warp
fuse
C
Multimerge Reconstruction
warp
FP
FP
compound
BP
BP
warp
recur

for hyper-parameter optimization for performing multi-view reconstruction using various algorithms.

2.2 Algorithmic Development

A description of the algorithms we have developed for multiview light-field 3D image reconstruction.

2.2.1 Symbols and Definitions

First the we will outline the meaning of the symbols to be used in these algorithmic descriptions:

N_v The total number of views.

V_n The spatial view into 3D space provided by the nth arm of the imaging system. $n \in \{1, \ldots, N_v\}$.

$\mathbf{I}_n$ The rectified two-dimensional (2D) light field image obtained from view V_n having size N_{x,I_n}-by-N_{y,I_n}. As a rectified image, there are constraints on the valid values for N_{x,I_n} and N_{y,I_n} discussed in the description of $\mathbf{H}$.

$\mathbf{V}_n^{(i)}$ The reconstructed three-dimensional (3D) image corresponding to view V_n at the the ith iteration.

$\mathbf{H}$ A five-dimensional (5D) array representing the computationally simulated point spread function (PSF) for the light field microscope. An implementation of the optical simulation to compute light field microscope PSFs is discussed by Prevedel *et al.* in the Methods and Supplementary Software sections of [10].
The first and second dimensions have size N_x-by-N_y and represent represent "image space." The third and fourth dimensions represent "object space" (or "phase space"), these dimensions have size N_α-by-N_β which must correspond to the rectification of $\mathbf{I}_n$. That is, the number of pixels behind each lenslet in the light field image must be N_α-by-N_β. Note that N_{x,I_n} must be an integer multiple of N_α and N_{y,I_n} must be an integer multiple of N_β (i.e. $\mathbf{I}_n$ must be able to be perfectly covered by a grid of whole tiles of size N_α-by-N_β). The fifth dimension represents axial position in object space having size N_z.

$\mathbf{X}_{[i_1,\ldots,i_N]}$ A shorthand notation to describe indexing into the N-D array $\mathbf{X}$ to retrieve the element at location i_1 along dimension 1, i_2 along dimension 2, and so on until i_N along dimension N. If

$$i_n = \hat{i}_n \,,$$

where $\hat{i}_n$ is an indexing vector with scalar elements $[\, j_1, \ldots, j_M \,]$, then $\mathbf{X}_{[\ldots, i_n, \ldots]}$ describes retrieving each of the elements j_m for $m \in \{1, \ldots, M\}$ along the nth dimension of $\mathbf{X}$ yielding a non-scalar "slice" of $\mathbf{X}$. $i_n =$ `":"` describes retrieving all elements along the nth dimension similar to the MATLAB colon indexing syntax.

$\lceil \cdot \rceil$ Shorthand for the ceil$(\cdot)$ rounding function.

$\lfloor \cdot \rfloor$ Shorthand for the floor$(\cdot)$ rounding function.

$\mathbf{H^T}$ A 5D array. The transpose of the PSF $\mathbf{H}$. The computation of a light field PSF transpose is not as trivial as a symmetric reflection of $\mathbf{H}$; the underlying theory, relevance, and derivation of the implemented computation is discussed and illustrated in detail by Eberhart in "Efficient computation of backprojection arrays for 3D light field deconvolution" [17]. Summarizing Eberhart here, the computation we define as

$$\mathbf{H^T} \coloneqq \mathrm{T}_{\mathrm{lf}}(\mathbf{H}) \tag{2.1}$$

can be understood as the reindexing operation

$$\mathbf{H}^{\mathbf{T}}_{[x',y',\alpha',\beta',z]} = \mathbf{H}_{[x,y,A,B,z]}\,, \tag{2.2}$$

where
$$\begin{aligned}
x' &= N_x - x + (N_x \bmod 2) \\
y' &= N_y - y + \big(N_y \bmod 2\big) \\
\alpha' &= x - N_\alpha + a + \left\lfloor \frac{N_\alpha - 1}{2} \right\rfloor - \left\lfloor \frac{N_x - N_\alpha}{2} \right\rfloor \\
\beta' &= y - N_\beta + b + \left\lfloor \frac{N_\beta - 1}{2} \right\rfloor - \left\lfloor \frac{N_y - N_\beta}{2} \right\rfloor
\end{aligned}$$

$$A = \begin{cases} a + \left\lceil \frac{1-a}{N_\alpha} \right\rceil N_\alpha & a \le 0 \\ a & 0 < a \le N_\alpha \\ a - \left\lfloor \frac{a-1}{N_\alpha} \right\rfloor N_\alpha & a > N_\alpha \end{cases}$$

$$B = \begin{cases} b + \left\lceil \frac{1-b}{N_\beta} \right\rceil N_\beta & a \le 0 \\ b & 0 < b \le N_\beta \\ b - \left\lfloor \frac{b-1}{N_\beta} \right\rfloor N_\beta & a > N_\beta \end{cases},$$

$$\text{and where} \quad a = \alpha - \left\lfloor \frac{N_x - N_\alpha}{2} \right\rfloor$$
$$b = \beta - \left\lfloor \frac{N_y - N_\beta}{2} \right\rfloor$$
$$\text{for} \quad x \in \{1, \ldots, N_x\}$$
$$\text{for} \quad y \in \{1, \ldots, N_y\}$$
$$\text{for} \quad \alpha \in \{1, \ldots, N_\alpha\}$$
$$\text{for} \quad \beta \in \{1, \ldots, N_\beta\}$$
$$\text{for} \quad z \in \{1, \ldots, N_z\} .$$

Similar to a simple transpose

$$\mathbf{H} \approx \mathrm{T}_{\mathrm{lf}}(\mathrm{T}_{\mathrm{lf}}(\mathbf{H})) , \tag{2.3}$$

with equality satisfied at most PSF locations withholding some edge cases.

$\hat{m}_{I_n,k}$ Indexing vectors (for indexing into $\mathbf{I}_n$) defined as follows for $k \in \{\alpha, \beta\}$

$$\hat{m}_{I_n,\alpha} = \left[\alpha,\ \alpha + 1N_\alpha,\ \alpha + 2N_\alpha,\ \ldots,\ \alpha + \left(\left\lfloor \frac{N_{x,I_n}}{N_\alpha} \right\rfloor - 1\right) N_\alpha\right] , \tag{2.4}$$
$$\hat{m}_{I_n,\beta} = \left[\beta,\ \beta + 1N_\beta,\ \beta + 2N_\beta,\ \ldots,\ \beta + \left(\left\lfloor \frac{N_{y,I_n}}{N_\beta} \right\rfloor - 1\right) N_\beta\right] . \tag{2.5}$$

$\mathbf{m}_{I_n,\alpha,\beta}$ A sparse, binary, 2D image mask the same size as $\mathbf{I}_n$ with value 1 at pixel location $\langle \alpha,\ \beta \rangle$ repeated every N_α pixels along dimension 1, every N_β pixels along dimension 2, and has value 0 everywhere else (i.e. a bounded, discrete 2D comb$(\cdot)$ function). Expressed with indexing vectors

$$\mathbf{m}_{I_n,\alpha,\beta,[x,y]} = \begin{cases} 1 & \text{if} \quad x \in \hat{m}_{I_n,\alpha} \wedge y \in \hat{m}_{I_n,\beta} \\ 0 & \text{otherwise} \end{cases} \tag{2.6}$$
$$\text{for} \quad x \in \{1, \ldots, N_{x,I_n}\}$$
$$\text{for} \quad y \in \{1, \ldots, N_{y,I_n}\} ,$$

such that

$$\mathbf{m}_{I_n,\alpha,\beta,[\hat{m}_\alpha,\hat{m}_\beta]} \equiv \mathbf{1} . \tag{2.7}$$
$$\mathbf{I}_n\, \mathbf{m}_{I_n,\alpha,\beta}$$

can be understood to be a 2D image where the single $\langle \alpha, \beta \rangle$ pixel behind each lenslet has been kept and all other image values discarded (set to zero). This represents a single "angular view" into the observed volume, and is used in the projection operations discussed next.

$\circledast$ An arrayed convolutional operation performed between either a 3D image and $\mathbf{H}$ resulting in the 2D image or between a rectified 2D image and $\mathbf{H}^{\mathbf{T}}$ resulting in a 3D image. The former could be characterized as a "forward projection" and the latter a "backward projection." For the two cases, the operation can be defined as follows.

$$\begin{aligned}\mathbf{I} &= \mathbf{V} \circledast \mathbf{H} \\ &= \sum_{z=1}^{N_z} \sum_{\beta=1}^{N_\beta} \sum_{\alpha=1}^{N_\alpha} \left(\mathbf{V}_{[:,:,z]}\, \mathbf{m}_{I,\alpha,\beta}\right) * \mathbf{H}_{[:,:,\alpha,\beta,z]}\end{aligned} \tag{2.8}$$

$$\begin{aligned}\mathbf{V} &= \mathbf{I} \circledast \mathbf{H}^{\mathbf{T}} \\ \mathbf{V}_{[:,:,z]} &= \sum_{\beta=1}^{N_\beta} \sum_{\alpha=1}^{N_\alpha} \left(\mathbf{I}\, \mathbf{m}_{I,\alpha,\beta}\right) * \mathbf{H}^{\mathbf{T}}_{[:,:,\alpha,\beta,z]} \\ &\text{for } z \in \{1, \ldots, N_z\}\end{aligned} \tag{2.9}$$

where $*$ is the discrete 2D convolution operation.

$\mathbf{B}_{I_n}$ A 2D image which serves to "background correct" the result of a forward projection; it is defined as

$$\mathbf{B}_I = \mathbf{1}_{V_n} \circledast \mathbf{H}\,, \tag{2.10}$$

where $\mathbf{1}_{V_n}$ is a 3D image of ones the same size as $\mathbf{V}_n$.

$\mathbf{B}_{V_n}$ Similarly, a 3D image which serves to background correct the result of a backward projection; it is defined as

$$\mathbf{B}_{V_n} = \mathbf{B}_{I_n} \circledast \mathbf{H}^{\mathbf{T}}\,. \tag{2.11}$$

$\mathscr{T}_n(\cdot)$ A registration transformation function which takes in a 3D image corresponding to view V_n and warps it onto a mutual reference view V_{mutual}.

$$\mathscr{T}_n(\cdot) = \text{“ } \mathscr{T}_{V_n \to V_{\text{mutual}}}(\cdot) \text{ ”}$$

If a given view V_{n^*} is chosen to be V_{mutual}, then $\mathscr{T}_{n^*}(\mathbf{V}_{n^*}) \equiv \mathbf{V}_{n^*}$, and all other transformation operators will register their correspondeing 3D images onto view V_{n^*}.

$\mathscr{T}_n^{-1}(\cdot)$ A transformation function which inverts $\mathscr{T}_n(\cdot)$, taking 3D image corresponding to view V_{mutual} warping it onto view V_n.

$$\mathscr{T}_n(\cdot) = \text{“ } \mathscr{T}_{V_{\text{mutual}} \to V_n}(\cdot) \text{ ”}$$

$\mathscr{A}_n(\cdot)$ An anti-aliasing (AA) filter which can be applied to $\mathbf{V}_n$; see §2.2.2.5 and ref. [12] for more information.

$F_{\mathrm{LP}}(x)$ A 2D low-pass filter having a cutoff frequency of $\frac{1}{x}$ defined as a circ$(\cdot)$ function in the spatial-frequency domain.

$$F_{\mathrm{LP}}(x) = \mathscr{F}^{-1}\left(\mathrm{circ}\left(\frac{1}{x}\right)\right)_{u,v} \tag{2.12}$$

$$\mathrm{circ}(r) = \mathrm{rect}\left(\frac{1}{2}\sqrt{\left(\frac{u}{r}\right)^2 + \left(\frac{v}{r}\right)^2}\right) \tag{2.13}$$

$$\mathrm{rect}(x) \coloneqq \begin{cases} 1 & |x| < \frac{1}{2} \\ \frac{1}{2} & |x| = \frac{1}{2} \\ 0 & |x| > \frac{1}{2} \end{cases} \tag{2.14}$$

where $\mathscr{F}^{-1}(\cdot)_{u,v}$ is the 2D inverse Fourier transform operator with respect to spatial frequencies u and v.

$\mathbf{H}_{\mathbf{P}}^{\mathbf{T}}$ The transpose of the phase space light field PSF. It is simpler to define $\mathbf{H}_{\mathbf{P}}^{\mathbf{T}}$ before defining $\mathbf{H}_{\mathbf{P}}$. See [18] for a full theoretical discussion of the phase space PSF; however, the computation is a rather straight forward reindexing

$$\mathbf{H}^{\mathbf{T}}_{\mathbf{P}[x',y',\alpha,\beta,z]} = \mathbf{H}^{\mathbf{T}}_{[x,y,\alpha,\beta,z]} \tag{2.15}$$

$$\begin{aligned} \text{where} \quad x' &= x - \left(\alpha - \frac{N_\alpha + 1}{2}\right) \\ y' &= y - \left(\beta - \frac{N_\beta + 1}{2}\right) \\ \text{for} \quad x &\in \{1, \ldots, N_x\} \\ \text{for} \quad y &\in \{1, \ldots, N_y\} \\ \text{for} \quad \alpha &\in \{1, \ldots, N_\alpha\} \\ \text{for} \quad \beta &\in \{1, \ldots, N_\beta\} \\ \text{for} \quad z &\in \{1, \ldots, N_z\} \\ \text{if} \quad 1 \le x' \le N_x \quad &\wedge \quad 1 \le y' \le N_y\,. \end{aligned}$$

$\mathbf{H}_{\mathbf{P}}$ The phase space light field PSF,

$$\mathbf{H}_{\mathbf{P}} = \mathrm{T}_{\mathrm{lf}}\left(\mathbf{H}_{\mathbf{P}}^{\mathbf{T}}\right)\,. \tag{2.16}$$

$w_{\alpha,\beta}$ Weight number for the phase-space PSF $\mathbf{H}_{\mathbf{P}}$ at each phase space location α, β based on the energy distribution of the PSF.

$$w_{\alpha,\beta} = \frac{\sum_{z=1}^{N_z}\sum_{y=1}^{N_y}\sum_{x=1}^{N_x}|\mathbf{H}_{\mathbf{P},[x,y,\alpha,\beta,z]}|}{\sum_{z=1}^{N_z}\sum_{\beta'=1}^{N_\beta}\sum_{\alpha'=1}^{N_\alpha}\sum_{y=1}^{N_y}\sum_{x=1}^{N_x}|\mathbf{H}_{\mathbf{P},[x,y,\alpha',\beta',z]}|} \tag{2.17}$$

$\overline{(\mathbf{X})}$ A shorthand notation for the mean value of $\mathbf{X}$ across all values of $\mathbf{X}$.

Also note that all operations are element-wise unless explicitly mentioned or defined otherwise. All uses of "… " are used to represent incriminating by 1 between two values unless otherwise implied. All boldface symbols (e.g. $\mathbf{H}$) represent multi-dimensional data arrays (i.e. N-D images).

2.2.1.1 z-Subsampling and z-Interpolation During Reconstruction and Transformations

For computational efficiency, it can be advantageous during the volumetric reconstruction process to perform arrayed convolution at a z-spacing which is at a lower resolution (i.e. larger spatial sampling period) than the xy image space resolution. When this is done the size of the $\mathbf{H}$ array can be significantly smaller since the PSF does not need to be computed for as many z-locations. When this lower resolution z reconstruction is utilized, there is a required step the reconstruction and image warping process where image volumes must be either sub-sampled to match the z-pitch of $\mathbf{H}$ or interpolated along the z-dimension to be isotropically rendered in preparation for transformation and merging.

Subsampling can be performed by simply extracting slices from the 3D image array; however, this method will discard information in intermediate planes. Another approach is to take a weighted average across multiple z-planes centered on a subset of z-locations (i.e. convolution with a symmetric kernel and a stride > 1). Interpolation or "up-sampling" of a subsampled 3D image can be performed with different interpolation methods including linear, cubic, etc.[1] In this work we allow for the subsampling and interpolation methods to be set as hyperparameters.

2.2.2 Reconstruction Algorithms

2.2.2.1 Single-View Reconstruction

This algorithm is very similar to that used by Prevedel *et al.* — utilizing an iterative Richardson-Lucy deconvolution scheme modified to use arrayed convolutions $\circledast$, described in Equations (2.8) and (2.9), for forward- and back-projection [10]. The number of iterations performed is determined heuristically to maximize the signal-to-noise ratio (usually between 2 and 10 iterations).

$$\mathbf{V}^{(i+1)} \leftarrow \mathbf{V}^{(i)} \left(\frac{\mathbf{I}}{\mathbf{V}^{(i)} \circledast \mathbf{H}} \circledast \mathbf{H}^{\mathbf{T}} \right) , \tag{2.18}$$

where the initial "guess" volume $\mathbf{V}^{(0)}$ in the iterative reconstruction is set to one of the following values:

$$\mathbf{V}^{(0)} \in \left\{ \mathbf{1},\ \mathbf{1}\,\overline{(\mathbf{I})},\ \mathbf{I} \circledast \mathbf{H}^{\mathbf{T}},\ \mathbf{1}\,\overline{(\mathbf{I} \circledast \mathbf{H}^{\mathbf{T}})} \right\} . \tag{2.19}$$

[1] see the SciPy documentation for an extended outline of interpolation methods, https://docs.scipy.org/doc/scipy/tutorial/interpolate.html

2.2.2.2 Merged Single-View Reconstruction

A 3D image corresponding to each view n is independently reconstructed according to the single view algorithm discussed in §2.2.2.1. Modifying Equation (2.18) to the multi-view context gives (recall we assume each imaging arm is identical and can thus share the PSF $\mathbf{H}$):

$$\mathbf{V}_n^{(i+1)} \leftarrow \mathbf{V}_n^{(i)} \left(\frac{\mathbf{I}_n}{\mathbf{V}_n^{(i)} \circledast \mathbf{H}} \circledast \mathbf{H}^{\mathbf{T}} \right), \tag{2.20}$$

where the initial "guess" volume for each view $\mathbf{V}_n^{(0)}$ can similarly be one of:

$$\mathbf{V}_n^{(0)} \in \left\{ \mathbf{1},\ \mathbf{1}\,\overline{(\mathbf{I}_n)},\ \mathbf{I}_n \circledast \mathbf{H}^{\mathbf{T}},\ \mathbf{1}\,\overline{(\mathbf{I}_n \circledast \mathbf{H}^{\mathbf{T}})} \right\}. \tag{2.21}$$

The independently reconstructed 3D images are merged by warping them to be aligned and taking their geometric mean to produce a final reconstructed 3D image $\mathbf{V}^{(i)}$ incorporating all views.

$$\mathbf{V}^{(i)} = \left(\prod_{n=1}^{N_v} \mathscr{T}_n\left(\mathbf{V}_n^{(i)}\right) \right)^{\frac{1}{N_v}} \tag{2.22}$$

This algorithm is illustrated in Figure 2.3B.

2.2.2.3 Single-View Reconstruction & Multiview Fusion

As with the Merged Single-View Reconstruction, this algorithm begins with independently reconstructing a 3D image corresponding to each view by the RL scheme outlined in Equation (2.20). The independently reconstructed volumes are then combined using the "Multiview-Reconstruction" Fiji plugin. This is the method utilized by Wagner *et al.* for their multi-view light field imaging system [11].

2.2.2.4 Multimerge Reconstruction

In this algorithm the iterative updates are not performed independently to produce multiple 3D images as in the prior methods; rather, the error estimations $\mathbf{E}_n$ obtained from each view are aligned, multiplied together, and then applied (by another multiplication) to update a combined 3D image $\mathbf{V}^{(i)}$ at each iteration.

$$\mathbf{V}^{(i+1)} \leftarrow \mathbf{V}^{(i)} \prod_{n=1}^{N_v} \mathscr{T}_n\left(\mathbf{E}_n^{(i)}\right), \tag{2.23}$$

$$\mathbf{E}_n^{(i)} = \frac{\mathbf{I}_n}{\mathscr{T}_n^{-1}(\mathbf{V}^{(i)}) \circledast \mathbf{H}} \circledast \mathbf{H}^{\mathbf{T}}, \tag{2.24}$$

where the initial "guess" volume $\mathbf{V}^{(0)}$ can be one of the following: (1) homogeneous volume of ones, (2) homogeneous volume containing the mean value across all starting light field images from each view, or (3) the geometric mean of all back projected and registered

light field images from each view.

$$\mathbf{V}^{(0)} \in \left\{ \mathbf{1},\ \frac{\mathbf{1}}{N_v} \sum_{n=1}^{N_v} \overline{(\mathbf{I}_n)},\ \left(\prod_{n=1}^{N_v} \mathscr{T}_n(\mathbf{I}_n \circledast \mathbf{H}^{\mathbf{T}}) \right)^{\frac{1}{N_v}} \right\}$$

This method, applied with the compound PSF (see §2.2.3.2), is illustrated in Figure 2.3C. This method takes the multiview deconvolution algorithm described by Preibisch *et al.* [19] and extends it to work with multiview light-field reconstructions. Our Equations (2.23) and (2.24) correspond to [19] Equations (2) and (1), respectively.

2.2.2.5 Artifact-free Multimerge Reconstruction

This reconstruction algorithm follows a similar scheme to that of the Multimerge Reconstruction; however, an anti-aliasing (AA) filter $\mathscr{A}_n(\cdot)$ is used to remove reconstruction artifacts. The filter must be applied to the 3D image while it corresponds to view V_n (i.e. before warping onto V_{mutual}), therefore there are multiple methods by which the AA filter can be utilized in the multiview context.

2.2.2.5.1 Scheme 1. AA filter is applied to each temporary guess image $\mathbf{U}_n^{(i)}$ (for $n \in \{1, ..., N_v\}$) derived from a combined multiview update, then the filtered images are recombined to update $\mathbf{V}^{(i)}$:

$$\begin{aligned} \mathbf{V}^{(i+1)} &= \left(\prod_{n=1}^{N_v} \mathscr{T}_n\left(\mathscr{A}_n\left(\mathbf{U}_n^{(i+1)}\right)\right) \right)^{\frac{1}{N_v}}, \\ \mathbf{U}_n^{(i+1)} &= \mathscr{T}_n^{-1}\left(\mathbf{U}^{(i+1)}\right) \quad \text{for} \quad n \in \{1, \ldots, N_v\}, \\ \mathbf{U}^{(i+1)} &\leftarrow \mathbf{V}^{(i)} \prod_{n=1}^{N_v} \mathscr{T}_n\left(\frac{\mathbf{I}_n}{\mathscr{T}_n^{-1}(\mathbf{V}^{(i)}) \circledast \mathbf{H}} \circledast \mathbf{H}^{\mathbf{T}} \right) \end{aligned} \tag{2.25}$$

2.2.2.5.2 Scheme 2. AA filter is applied to each 3D image after an independent update, then the geometric mean of the updated 3D images is taken to yield the combined 3D image:

$$\begin{aligned} \mathbf{V}^{(i+1)} &= \left(\prod_{n=1}^{N_v} \mathscr{T}_n\left(\mathscr{A}_n\left(\mathbf{V}_n^{(i+1)}\right)\right) \right)^{\frac{1}{N_v}}, \\ \mathbf{V}_n^{(i+1)} &\leftarrow \mathscr{T}_n^{-1}\left(\mathbf{V}^{(i)}\right) \left(\frac{\mathbf{I}_n}{\mathscr{T}_n^{-1}(\mathbf{V}^{(i)}) \circledast \mathbf{H}} \circledast \mathbf{H}^{\mathbf{T}} \right) \\ &\text{for} \quad n \in \{1, \ldots, N_v\} \end{aligned} \tag{2.26}$$

2.2.2.5.3 Scheme 3. Same as §2.2.2.5.2, however no combination is performed until the final iteration i^*:

$$\begin{aligned}\mathbf{V}^{(i^*)} &= \left(\prod_{n=1}^{N_v} \mathscr{T}_n\Big(\mathscr{A}_n\Big(\mathbf{V}_n^{(i^*)}\Big)\Big)\right)^{\frac{1}{N_v}}, \\ \mathbf{V}_n^{(i+1)} &\leftarrow \mathbf{V}_n^{(i)}\left(\frac{\mathbf{I}_n}{\mathbf{V}_n^{(i)} \circledast \mathbf{H}} \circledast \mathbf{H}^{\mathbf{T}}\right) \\ &\text{for} \quad n \in \{1, \dots, N_v\} \\ &\text{while} \quad i < i^*.\end{aligned} \tag{2.27}$$

2.2.2.5.4 Scheme 4. Here, we only utilize one view per update in a rotating/alternating fashion. See §2.2.2.4 for the implementation details.

2.2.2.5.5 Scheme 5. AA filter is applied to the error image at each iteration:

$$\begin{aligned}\mathbf{V}^{(i+1)} &\leftarrow \mathbf{V}^{(i)} \times \prod_{n=1}^{N_v} \mathscr{T}_n\Big(\mathscr{A}_n\Big(\mathbf{E}_n^{(i)}\Big)\Big), \\ \text{where} \quad \mathbf{E}_n^{(i)} &= \frac{\mathbf{I}_n}{\mathscr{T}_n^{-1}(\mathbf{V}^{(i)}) \circledast \mathbf{H}} \circledast \mathbf{H}^{\mathbf{T}}\end{aligned} \tag{2.28}$$

2.2.2.5.6 Scheme 6. AA filter is applied to each 3D image, then the normalized product is taken in combined space.

$$\begin{aligned}\mathbf{V}^{(i+1)} \leftarrow &\left(\frac{1}{\mathbf{V}^{(i)}}\right)^{(N_v-1)} \\ &\times \prod_{n=1}^{N_v} \mathscr{T}_n\left(\mathscr{A}_n\left(\mathscr{T}_n^{-1}(\mathbf{V}^{(i)})\left(\frac{\mathbf{I}_n}{\mathscr{T}_n^{-1}(\mathbf{V}^{(i)}) \circledast \mathbf{H}} \circledast \mathbf{H}^{\mathbf{T}}\right)\right)\right)\end{aligned} \tag{2.29}$$

2.2.2.5.7 Initial Volume For all of the above schemes the initial guess volume $\mathbf{V}^{(0)}$ can be any of the following:

$$\mathbf{V}^{(0)} \in \left\{\mathbf{1}, \frac{\mathbf{1}}{N_v}\sum_{n=1}^{N_v} \overline{(\mathbf{I}_n)}, \left(\prod_{n=1}^{N_v} \mathscr{T}_n(\mathscr{A}_n(\mathbf{I}_n \circledast \mathbf{H}^{\mathbf{T}}))\right)^{\frac{1}{N_v}}, \frac{\mathbf{1}}{\left(\left(\prod_{n=1}^{N_v} \mathscr{T}_n(\mathscr{A}_n(\mathbf{I}_n \circledast \mathbf{H}^{\mathbf{T}}))\right)^{\frac{1}{N_v}}\right)}\right\}. \tag{2.30}$$

The description, derivations, and applications of the light-field AA filter are discussed at length by Stefanoiu *et al.* [12], who developed the algorithms for single-view artifact-free reconstruction.

2.2.2.6 Phase-space Multi-merge Reconstruction

In this algorithm the input 2D light field image is first converted into a N_α-by-N_β series of 2D images, each sampled and upscaled (by 2D cubic interpolation, cubic$(\cdot)$) from the original image and each giving a different angular view into the sample. This series of images P_n can itself be considered a 4D image where the first two dimensions represent image space $\approx N_{x,I_n}$-by-N_{y,I_n} and the second two dimensions represent phase space N_α-by-N_β.

$$\begin{aligned} P_{n,[:,:,\alpha,\beta]} &= \text{cubic}\Big(\mathbf{I}_{n,[\hat{m}_\alpha,\hat{m}_\beta]}\Big) * F_{\text{LP}}(\Delta x_{\text{lenslet}}) \\ &\text{for} \quad \alpha \in \{1,\, \dots,\, N_\alpha\} \\ &\text{for} \quad \beta \in \{1,\, \dots,\, N_\beta\} \end{aligned} \tag{2.31}$$

where $\Delta x_{\text{lenslet}}$ is the pitch between lenslets (e.g. $= N_\alpha$ pixels).

Following this processing on the input light-field image, each pair of phase images is used to update the the 3D guess image, in a manner similar to the Multimerge Reconstruction. However, in this case rather than using an arrayed convolution (i.e. $\circledast$, which sums and convolves at all phase space locations in one step), the RL updates are performed at each phase space location sequentially. The order of this sequence is not done as

$$\langle \alpha, \beta \rangle \text{ for } \alpha \in \{1,\, \dots,\, N_\alpha\} \text{ for } \beta \in \{1,\, \dots,\, N_\beta\}\,;$$

rather the phase space indices α, β are iterated over following an inward spiraling (ptychographic) index beginning at $\langle \alpha = 1,\, \beta = 1 \rangle$ and ending at $\left\langle \alpha = \frac{N_\alpha+1}{2},\, \beta = \frac{N_\beta+1}{2} \right\rangle$ (recall that N_α and N_β must be odd valued). Note that this corresponds to iterating from high-spatial-frequency components at the margins of the phase space array to low-spatial-frequency components at the center of the phase-space array. This new indexing order will be indicated by $q \in \{1,\, \dots,\, N_\alpha N_\beta\}$, where when

$$\begin{array}{lll} q = 1\,, & \hat{q} \equiv \langle \alpha = 1\,, & \beta = 1 \rangle \\ \quad\vdots & \quad\vdots & \quad\vdots \\ = (N_\alpha - 1) + 1\,, & = N_\alpha & = 1 \\ \quad\vdots & \quad\vdots & \quad\vdots \\ = (N_\alpha - 1) + \big(N_\beta - 1\big) + 1\,, & = N_\alpha & = N_\beta \\ \quad\vdots & \quad\vdots & \quad\vdots \\ = 2\,(N_\alpha - 1) + \big(N_\beta - 1\big) + 1\,, & = 1 & = N_\beta \\ \quad\vdots & \quad\vdots & \quad\vdots \\ = 2\,(N_\alpha - 1) + 2\big(N_\beta - 1\big)\,, & = 1 & = 2 \\ = 2\,(N_\alpha - 1) + 2\big(N_\beta - 1\big) + 1\,, & = 2 & = 2 \\ \quad\vdots & \quad\vdots & \quad\vdots \\ = N_\alpha N_\beta\,, & = \dfrac{N_\alpha + 1}{2} & = \dfrac{N_\beta + 1}{2} \end{array}$$

The weight of each phase component $w_{\alpha,\beta}\,\big(\equiv w_{\hat{q}}\big)$ is used to scale each update. The

full Phase space Multimerge Reconstruction algorithm is as follows:

$$\mathbf{V}^{(q+1,i)}_{[:,:,z]} \leftarrow cw_{\hat{q}}\mathbf{V}^{(q,i)}_{[:,:,z]}$$

$$\times \prod_{n=1}^{N_v} \mathscr{T}_n\left(\frac{P_{n,[:,:,\hat{q}]}}{\sum_{z'=1}^{N_z} \mathscr{T}_n^{-1}\left(\mathbf{V}^{(q,i)}_{[:,:,z']}\right) * \mathbf{H}_{\mathbf{P},[:,:,\hat{q},z']}} * \mathbf{H}^{\mathbf{T}}_{\mathbf{P},[:,:,\hat{q},z]}\right)$$

$$+ \left(1 - cw_{\hat{q}}\right) \times \mathbf{V}^{(q,i)}_{[:,:,z]} \quad \text{for} \quad z \in \{1, \ldots, N_z\} ,$$

$$\text{when} \quad q > N_\alpha N_\beta \quad \text{then} \quad i \leftarrow i+1,\ q \leftarrow 1 \tag{2.32}$$

$$\mathbf{V}^{(0,0)}_n = \mathbf{1}(\overline{\mathbf{I}_n}) \tag{2.33}$$

where c is an arbitrary constant for the convergence speed; c must be chosen such that $cw_{\hat{q}} < 1$ for all q. Note that with this algorithm one large iteration i consists of $N_\alpha N_\beta$ separate updates to $\mathbf{V}$, therefore many fewer i iterations are needed for convergence.

For a full derivation and explanation of the phase space reconstruction algorithm in the single-view context, see [18].

2.2.3 Reconstruction Optimizations

A number of further algorithmic optimizations and enhancements were implemented to improve the quality of the reconstructed 3D images and stability of convergence over multiple iterations.

2.2.3.1 Background Correction

This optimization adds an additional normalization operation to the result of each forward projection and back projection using $\mathbf{B}_{I_n}$ and $\mathbf{B}_{V_n}$ whose definitions are described in Equations (2.10) and (2.11), respectively. When applied to the forward projection, the background corrected 2D image $\mathbf{I}'_n$ for view V_n is defined as:

$$\mathbf{I}'_n = \frac{\mathbf{I}_n}{\mathbf{B}_{I_n}} = \frac{\mathbf{V} \circledast \mathbf{H}}{\mathbf{1}_{V_n} \circledast \mathbf{H}} . \tag{2.34}$$

And when applied to the back projection, the background corrected 3D image $\mathbf{V}'_n$ is defined as:

$$\mathbf{V}'_n = \frac{\mathbf{V}_n}{\mathbf{B}_{V_n}} = \frac{\mathbf{I} \circledast \mathbf{H}^{\mathbf{T}}}{\left(\mathbf{1}_{V_n} \circledast \mathbf{H}\right) \circledast \mathbf{H}^{\mathbf{T}}} . \tag{2.35}$$

Note that $\mathbf{B}_{I_n}$ and $\mathbf{B}_{V_n}$ need only be computed once for a given PSF and image size.

As an example, rewriting Equation (2.18) with both forward and background background correction gives:

$$\mathbf{V}^{(i+1)} \leftarrow \frac{\mathbf{V}^{(i)}}{\mathbf{B}_V}\left(\frac{\mathbf{I}\,\mathbf{B}_I}{\mathbf{V}^{(i)} \circledast \mathbf{H}} \circledast \mathbf{H}^{\mathbf{T}}\right) . \tag{2.36}$$

2.2.3.2 Compound Point Spread Function

This optimization replaces $\mathbf{H}^{\mathbf{T}}$ or $\mathbf{H}_{\mathbf{P}}^{\mathbf{T}}$ with a "compound PSF" $\mathbf{C}_{V_n}^{\mathbf{T}}$ or $\mathbf{C}_{\mathbf{P},V_n}^{\mathbf{T}}$ unique to each view V_n. See the supplemental information of Preibisch *et al.* for a full theoretical discussion of why this substitution is made [19]. In short, using the compound PSF allows us to speed up convergence by incorporating the fact that images produced by each view are not independent, but are related by transformation and a re-propagation through the image forming system.

The following methods address the challenge of computing compound PSFs for the 5D light-field PSFs when the original method was designed for computations on 2D or 3D PSFs.

Consider each 3D view into a volume $\left\{V_1, \ldots, V_{N_v}\right\}$. At each target view V_n we can build a estimates for that view based on each of the remaining source views $V_{n'}$ (i.e. $V_{n'}$ while $n' \neq n$); by this scheme we can list $N_v(N_v - 1)$ "virtual" views using the notation $W_n^{V_{n'}}$:

$$\left\{W_1^{V_2}, \ldots, W_1^{V_{N_v}}, W_2^{V_1}, W_2^{V_3} \ldots, W_2^{V_{N_v}}, \ldots, W_{N_v}^{V_1}, \ldots, W_{N_v}^{V_{N_v-1}}\right\}.$$

The virtual views can be divided into subsets W_n for each target view V_n:

$$W_1 = \left\{W_1^{V_2}, \ldots, W_1^{V_{N_v}}\right\} \tag{2.37}$$

$$W_2 = \left\{W_2^{V_1}, W_2^{V_3} \ldots, W_2^{V_{N_v}}\right\} \tag{2.38}$$

$$\ldots$$

$$W_{N_v} = \left\{W_{N_v}^{V_1}, \ldots, W_{N_v}^{V_{N_v-1}}\right\}. \tag{2.39}$$

Throughout the following schemes we will use the notation w to stand in for the general virtual view $W_n^{V_{n'}}$.

It will also be useful to define a series of transformation functions for each virtual view $\mathscr{T}_w(\cdot)$ and $\mathscr{T}_w^{-1}(\cdot)$ to warp a volume corresponding to view $V_{n'}$ onto view V_n and back, respectively.

$$\mathscr{T}_{w=W_n^{V_{n'}}}(\cdot) \coloneqq \mathscr{T}_n^{-1}(\mathscr{T}_{n'}(\cdot)) \qquad = \text{"}\ \mathscr{T}_{n'\to n}(\cdot)\text{"} \tag{2.40}$$

$$\mathscr{T}^{-1}_{w=W_n^{V_{n'}}}(\cdot) \coloneqq \mathscr{T}_{n'}^{-1}(\mathscr{T}_n(\cdot)) \qquad = \text{"}\ \mathscr{T}_{n\to n'}(\cdot)\text{"} \tag{2.41}$$

2.2.3.2.1 Scheme 1 For each of these virtual views, an associated PSF $\mathbf{H}_w^{\mathbf{T}}$ can be computed

$$\begin{aligned}\mathbf{H}^{\mathbf{T}}_{w,[:,:,\alpha,\beta,:]} = \mathscr{T}_w^{-1}\left(\mathbf{H}^{\mathbf{T}}_{V_n,[:,:,\alpha,\beta,:]}\right)\\ \text{for} \quad \alpha \in \left\{1, \ldots, N_\alpha|_{\mathbf{H}_{V_n}}\right\}\\ \text{for} \quad \beta \in \left\{1, \ldots, N_\beta|_{\mathbf{H}_{V_n}}\right\},\end{aligned} \tag{2.42}$$

where

$$\mathbf{H}_{V_n}^{\mathbf{T}} \equiv \mathbf{H}^{\mathbf{T}} \quad \forall \quad n \tag{2.43}$$

in our case because all views use optically identical light-field setups, recall Figure 2.3A (however, we specify the view for each PSF so that this work can be applied to microscopes with different optical setups for each view).

Note: We must treat the 5D slice $\mathbf{H}^{\mathbf{T}}_{V_n,[:,:,\alpha,\beta,:]}$ as a 3D image (e.g. with the `squeeze` function in MATLAB) and conversely treat a 3D image as a 5D slice (e.g. with the `reshape` function) where appropriate in these and following equations.

We can then compute a compound PSF for each view as follows

$$\mathbf{C}^{\mathbf{T}}_{V_n,[:,:,\alpha,\beta,:]} = \mathbf{H}^{\mathbf{T}}_{V_n,[:,:,\alpha,\beta,:]} \prod_{w \in W_n} \mathscr{T}_w\left(\left(\mathbf{H}^{\mathbf{T}}_{w,[:,:,\alpha,\beta,:]} \circledast \mathbf{H}_{V_{n'}}\right) \circledast \mathbf{H}^{\mathbf{T}}_{V_{n'}}\right) \quad \text{for} \quad \alpha \in \left\{1, \ldots, N_\alpha|_{\mathbf{H}_{V_n}}\right\} \quad \text{for} \quad \beta \in \left\{1, \ldots, N_\beta|_{\mathbf{H}_{V_n}}\right\}. \tag{2.44}$$

2.2.3.2.2 Scheme 2 In this scheme we begin by generating a 3D image $\mathbf{\Gamma}^{\alpha,\beta,z}_w$ by forward- and back-projecting a transformed 3D unit-sample function $\boldsymbol{\delta}_{V_n}[\alpha^*, \beta^*, z]$ for each virtual view for each object space location $\langle \alpha, \beta, z \rangle$

$$\mathbf{\Gamma}^{\alpha,\beta,z}_w = \left(\mathscr{T}_w^{-1}(\boldsymbol{\delta}_{V_n}[\alpha^*, \beta^*, z]) \circledast \mathbf{H}_{V_{n'}}\right) \circledast \mathbf{H}^{\mathbf{T}}_{V_{n'}} \tag{2.45}$$

where $\boldsymbol{\delta}_{V_n}[\alpha^*, \beta^*, z]$ is a 3D image of size $[S_x, S_y, S_z]$ corresponding to view V_n with value 1 at voxel location $\langle \alpha^*, \beta^*, z \rangle$ and value 0 at all other locations where

$$\alpha^* = \frac{S_x + 1}{2} + \left(\alpha - \frac{N_\alpha|_{\mathbf{H}_{V_n}} + 1}{2}\right) \tag{2.46}$$

$$\beta^* = \frac{S_y + 1}{2} + \left(\beta + \frac{N_\beta|_{\mathbf{H}_{V_n}} + 1}{2}\right) \tag{2.47}$$

$$S_x = N_\alpha|_{\mathbf{H}_{V_n}} \left(1 + 2 \left\lceil \frac{N_x|_{\mathbf{H}_{V_n}}}{2\, N_\alpha|_{\mathbf{H}_{V_n}}} \right\rceil\right) \tag{2.48}$$

$$S_y = N_\beta|_{\mathbf{H}_{V_n}} \left(1 + 2 \left\lceil \frac{N_y|_{\mathbf{H}_{V_n}}}{2\, N_\beta|_{\mathbf{H}_{V_n}}} \right\rceil\right) \tag{2.49}$$

$$S_z = N_z|_{\mathbf{H}_{V_n}}\,. \tag{2.50}$$

$\mathbf{\Gamma}^{\alpha,\beta,z}_w$ can be understood to represent the probability distribution across the source 3D image space $V_{n'}$ that a voxel contributed to the observation of the light-field image that would be obtained from a centered, single-voxel point emitter corresponding to a specific object space location in the target 3D image space V_n.

A PSF $\mathbf{H}_w$ for each virtual view is then computed by warping $\mathbf{\Gamma}^{\alpha,\beta,z}_w$ and forward-projecting

the result at each $\langle \alpha, \beta, z \rangle$ location

$$\begin{aligned} \mathbf{H}_{w,[:,:,\alpha,\beta,z]} &= \mathscr{T}_w\left(\mathbf{\Gamma}_w^{\alpha,\beta,z}\right) \circledast \mathbf{H}_{V_n} \\ &\text{for} \quad \alpha \in \{1, \ldots, N_\alpha\} \\ &\text{for} \quad \beta \in \{1, \ldots, N_\beta\} \\ &\text{for} \quad z \in \{1, \ldots, N_z\} \,. \end{aligned} \tag{2.51}$$

These PSFs $\mathbf{H}_w$ for each virtual view are transposed (recall Equations (2.1) and (2.2)) then multiplied together to obtain the compound PSF $\mathbf{C}_{V_n}^{\mathbf{T}}$ at each view

$$\mathbf{C}_{V_n}^{\mathbf{T}} = \mathbf{H}_{V_n}^{\mathbf{T}} \prod_{w \in W_n} \mathrm{T}_{\mathrm{lf}}(\mathbf{H}_w) \,. \tag{2.52}$$

2.2.3.3 Moving Average for Iterative Updates.

This optimization is designed to stabilize reconstruction convergence over multiple iterations by averaging the current update with previous updates. Essentially the guess image at a given iteration $\mathbf{V}^{(i)}$ is replaced by an average $\mathbf{V}^{(i)'}$ for $i \geq 1$ computed as

$$\mathbf{V}^{(i)'} = c_0 \mathbf{V}^{(i)} + \sum_{k=1}^{N_k - 1} c_k \mathbf{V}^{(i-k)} \,, \tag{2.53}$$

where N_k is a parameter setting the length of the moving average and c_k for $k \in \{0, \ldots, N_k - 1\}$ is the weight coefficient applied each term. The summation is only taken over values of k while $(i - k) \geq 0$. Note that if $N_k = 1$ and $c_0 = 1$, then $\mathbf{V}^{(i)'} \equiv \mathbf{V}^{(i)}$.

2.2.3.4 Alternating View at each Iterative Update

This optimization is designed to speed up reconstruction while still incorporating all views in the reconstruction scheme. Using Equations (2.23) and (2.24) as an example, their reformulation into the alternating view scheme would be as follows

$$\begin{aligned} \mathbf{V}^{(1)} &\leftarrow \mathbf{V}^{(0)} \mathscr{T}_1\left(\frac{\mathbf{I}_1}{\mathscr{T}_1^{-1}(\mathbf{V}^{(0)}) \circledast \mathbf{H}} \circledast \mathbf{H}^{\mathbf{T}}\right) , \\ \mathbf{V}^{(2)} &\leftarrow \mathbf{V}^{(1)} \mathscr{T}_2\left(\frac{\mathbf{I}_2}{\mathscr{T}_2^{-1}(\mathbf{V}^{(1)}) \circledast \mathbf{H}} \circledast \mathbf{H}^{\mathbf{T}}\right) , \\ &\ldots \\ \mathbf{V}^{(i+1)} &\leftarrow \mathbf{V}^{(i)} \mathscr{T}_m\left(\frac{\mathbf{I}_m}{\mathscr{T}_m^{-1}(\mathbf{V}^{(i)}) \circledast \mathbf{H}} \circledast \mathbf{H}^{\mathbf{T}}\right) \\ &\text{where} \quad m = 1 + (i \bmod N_v) \,. \end{aligned} \tag{2.54}$$

Essentially, this method sequentially uses the single view version of each reconstruction method and applies it to update a mutual guess image $\mathbf{V}^{(i)}$ through an error estimation from each view. This method can be combined with the optimization discussed in §2.2.3.2 to still incorporate multi-view interdependence into each update.

2.2.3.5 Tikhonov Regularization

This optimization is designed to improve convergence stability by suppressing ballooning values and of mitigate the effects of noise on the 3D image reconstruction. The following is applied to each guess image $\mathbf{V}$ to yield the regularized guess image $\mathbf{V}'$

$$\mathbf{V}' = \frac{1}{\lambda}\left(\sqrt{1 + 2\lambda\mathbf{V}} - 1\right) \tag{2.55}$$

where λ is a parameter that affects how aggressively the regularization is applied. A $\lambda = 0$ represents the case of no regularization (i.e. $\mathbf{V}' \equiv \mathbf{V}$), typical values for λ fall between 10^{-3} and 10^{-1}. See examples of this term's effects in [19] Supplementary Figures 6 and 7.

2.2.4 Hyper-parameter Search and Optimization

To determine the effect that the many approaches and schemes outlined above have on various aspects of the reconstruction run and output we developed a process for evaluating hyper-parameter selection. First, a reference image is chosen for the reconstruction this reference image can either be an actual light field or a simulated light field of a real (i.e. high resolution confocal z-stack of a zebrafish) or modeled image volume (e.g. a volume of randomly positioned spheres). In the case of an actual light field image evaluation metrics can include the change in the reconstructed volume from iteration to the next, the difference between the obtained light field image and simulated imaging of the reconstructed volume. In the case of a simulated light field we can additionally evaluate the signal-to-noise ratio between the reconstructed volume and the actual volume, compare the x, y, and z resolution or profile of features (e.g. beads) to the actual image, signal to noise ratio between the modeled volume and the reconstruction, magnitude of intensity in the background (e.g. zero-valued areas of the modeled volume) of the reconstructed image.

2.3 Results

2.3.1 *In silico* Reconstruction Evaluations and Experiments

We performed a number of imaging simulations to both qualitatively and quantitatively evaluate the different algorithms which we developed. Simulated light-field imaging of a larval zebrafish brain with sparse 1 µm beads followed by reconstruction using various single-view and multi-view reconstruction algorithms gives us a qualitative understanding of how various reconstruction techniques perform, Figure 2.4. We see that the single view methods are unable to effectively resolve the anatomical outline of the brain along the reconstructed z-axis Figure 2.4B–D. We also notice the strong striping artifacts cause by aliasing at the central z-planes of the reconstruction, white arrow in Figure 2.4B. Both the artifact-free OLAF and phase-space methods produce output volumes without these artifacts Figure 2.4C–D. The single-view phase-space reconstruction seems to introduce some ring-artifacts at the locations of beads Figure 2.4D.

The introduction of the second view into the reconstruction pipeline significantly improved the ability to resolve the brain shape along the z-axis Figure 2.4E–H. Measurements

of a simulated volume of fluorescent beads shows that most of the multiview methods markedly improve (reduce) the z-resolution Figure 2.5. Both the merged single-view and multi-merge algorithms continue to show the native plane aliasing for both reconstructed axes—z and x—white arrows in Figure 2.4E–F. We also observe relatively higher background intensity in for the merged single-view compared to the multi-merge result Figure 2.4F. The OLAF and phase-space multi-view reconstructions yeild outputs which most closely resemble the ground truth volume; however, they still appear significantly blurry compared to the ground truth Figure 2.4G–H.

Measuring resolution from a simulated volume of fluorescent beads we see that for the single view reconstruction, x and y dimensions can be resolved at a median value of ≈ 4 µm FWHM Figure 2.5. While the reconstructed z dimension is resolved at ≈ 14 µm with some observations as high as 50 µm. The OLAF single-view method shows $\approx 60\%$ worse (higher) resolution and the phase-space single- view method shows $\approx 120\%$ worse resolution in x and y compared to the single view method.

For each of the multi-view algorithms one of the most notable distinctions we see is a significantly lower z-resolution compared to that for the corresponding single view reconstruction. Additionally the z-resolution is on the same order of magnitude as the x and y resolutions. We also notice that for the multi-view algorithms, the resolution in y shows a much tighter distribution and a lower value than x and z. We can understand this observation by recognizing that the reconstructed axis for view 1 is the z-axis and the reconstructed axis for view 2 is the x-axis, i.e. the x- and z-axes are sampled with (relatively) high resolution from on view and low (limited by reconstruction) from the other view. While the y-axis is sampled with high resolution from both views, thus when the views are combined y-resolution improves to a greater degree than x or y.

Using the compound PSF seems to offer a slight improvement in the resolution when compared to the same algorithm performed without the compound PSF. For example, the median y resolution for the multi-merge algorithm is ≈ 3.3 µm, while the median y resolution for the multi-merge algorithm with utilization of the compound PSF is ≈ 3.2 µm. We see a similar marginal improvement with the compound PSF for the other algorithms and dimensions.

The phase-space reconstruction algorithm shows the smallest improvement with the additional of the second view, and some points even show poorer resolution compared to the single view method. The merged single-view and multi-merge reconstructions show the lowest median resolutions compared to any other methods.

A survey of different hyper-parameter configurations and the values of different metrics for the OLAF multi-view reconstruction process (see §2.2.2.5) and output 3D image shows that the effects of many hyper-parameter choices are not unambiguously better or worse. Rather, many hyper-parameter choices improve reconstruction in some ways and make the results worse in others Figure 2.6. For example, we see that using the alternating PSF generally worsens resolution, but significantly decreases reconstruction time. The selection of the start volume (see Equation (2.30)) and the background selection method (see §2.2.3.1) does not appear to noticeably affect the reconstruction results. Increasing the maximum

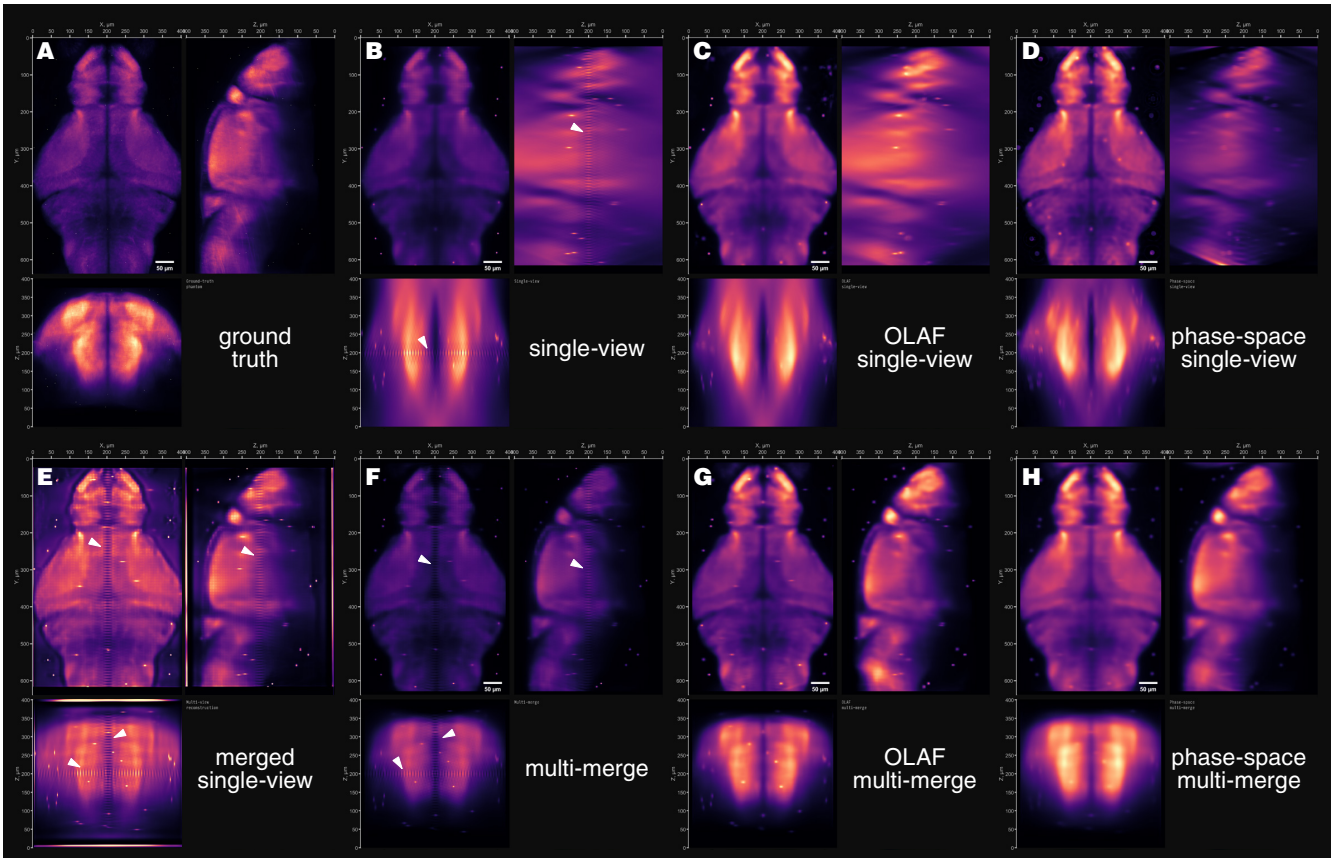

Figure 2.4: Reconstructing simulated light field micrographs of a larval zebrafish brain qualitatively shows the stark improvement offered by the dual-objective system and the benefits offered by our novel artifact-free, multi-merge algorithms. Each sub-panel shows orthogonal mean intensity projections of a volumetric image in *xy* (upper left), *yz* (upper right), and *xz* (lower left). The images shown are as follows **A**: A 6 dpf larval zebrafish brain expressing a pan-neuronal fluorescent reporter (taken from the Z-Brain Atlas [20, 21]). We also added 1 µm "fluorescent beads" around the brain *in silico* for quantitative and qualitative resolution evaluation. This image volume serves as the "ground truth" for the subsequent reconstructions. We simulated imaging of this brain *in silico* with a model of our dual-objective light field LF microscope Figure 2.3 to produce a pair of 2D LFs. **B**: Single-view SV Reconstruction produced (from a single light field) using the single-view algorithm, Equation (2.18). White arrows point out artifacts at the native (central) image plane; also in **E** and **F**. **C**: SV reconstruction using the anti-aliased, artifact free (OLAF) algorithm described by Stefanoiu *et al.* [12]. **D**: SV reconstruction using the phase space algorithm described by Lu *et al.* [18]. **E**: Multi-view (MV) reconstruction (from the pair of simulated LF images) using the merged single view algorithm, Equations (2.20) and (2.22). **F**: MV reconstruction using the multi-merge algorithm, Equations (2.23) and (2.24). **G**: MV reconstruction using the OLAF algorithm adapted to the MV context, Equation (2.25). **H**: MV reconstruction using the phase space algorithm adapted to the MV context, Equation (2.32). *Note: Scale bar is 50 µm. Image projections are 16-bit/voxel grey-scale data rendered with the "magma" colormap and scaled arbitrarily to maximize view-ability.*

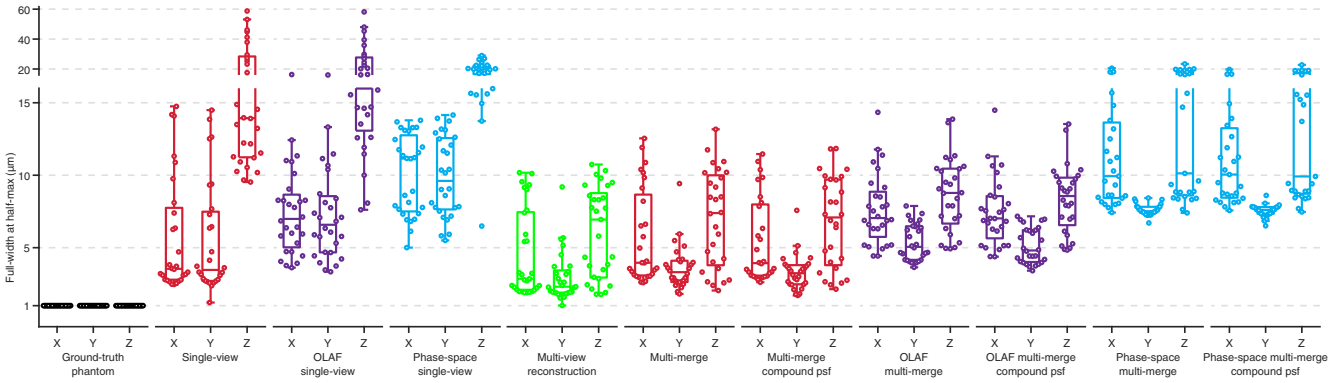

Figure 2.5: 3D images reconstructed with multiview approaches render beads with higher resolution and with more isotropy across dimensions compared to single-view approaches based on *in silico* experiments. Box-and-whisker plots of the full-width at half-max (FWHM) resolution in *x*, *y*, and *z* of simulated volumetric images containing 1 µm fluorescent beads. The "ground-truth phantom" plots (black) represent the resolution of the original computationally generated image volume representing what we simulated to be under the microscope objective. The reaming plots (colors) represent evaluating the resolution a 3D image reconstructed by the labeled method from 1 (single) or 2 (multi-view) simulated light field micrographs. Since the ground truth locations of the beads are known, we use their locations to evaluate the resolution at which the beads are rendered after simulated imaging and reconstruction pipelines.
Note: Color Key: red – Richardson-Lucy-based single-view and multi-merge algorithms; purple – artifact-free (OLAF) [12] single-view and multi-merge algorithms; blue – phase-space [18] single-view and multi-merge algorithms; green – merged single-view reconstruction algorithm. See §2.2.2 for descriptions of each of the algorithms. Plots labeled with "compound PSF" represent utilizing the described algorithm with the compound PSF **C** *replacing the standard PSF* **H***; see §2.2.3.2.*

number of iterations appears to improve resolution, improve signal-to-noise, improve the magnitude of background voxels, and worsen reconstruction time.

2.3.2 Resolution Evaluation and Live Brain Imaging

The simulated resolution results were recapitulated with imaging of a sample of sparse 1 µm beads with our dual-objective LFM system. We see that the z resolution improves from ≈ 20 µm with single view reconstruction to ≈ 4 µm with dual-objective reconstruction.

We used the dual-objective microscope to record baseline calcium activity in the brain of a zebrafish larva sparsely expressing *Tg*(somaGCaMP6s) [22]. We imaged at 30 Hz and successfully reconstructed 3D images for 1 min (1800 frames) of activity using the phase-space multimerge algorithm §2.2.2.6. Segmentation of fluorescent puncta in the 3D volume revealed calcium activity time-courses.

2.4 Discussion

We have shown the development, implementation, and application of a suite of novel algorithms for reconstructing light field imaging data. Based on the *in silico* resolution and simulated brain imaging experiments, we see the OLAF multimerge algorithm with use of the compound PSF to be the best candidate algorithm for use with multi-objective imaging systems and further development of these methods. The compound PSF OLAF multi-

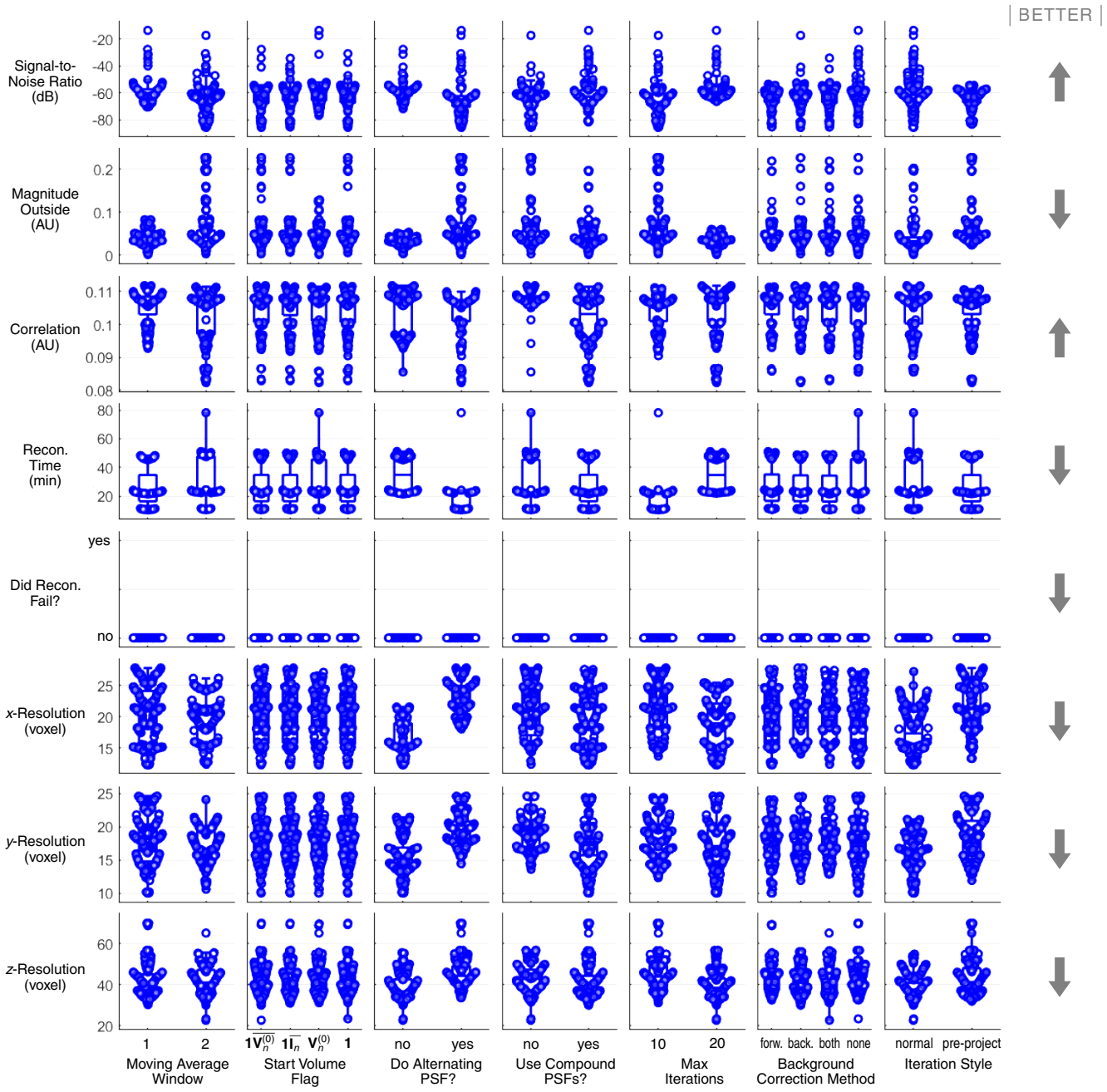

Figure 2.6: There are many possible combinations of multi-view light field reconstruction hyperparameters; we evaluated some of them using a range of metrics to determine optimal configurations. Summary of the results from 512 artifact-free multi-view light field reconstruction runs across a grid search of 6 different hyperparameters (columns) produced from a simulated light field micrographs of a zebrafish brain with 1 µm beads (see Figure 2.4A); each run was evaluated using 7 metrics (rows) as well as flagged if the reconstruction run failed in some way (5th row). Each cell shows box-and-whisker plots with points of the given evaluation metric (*y*-axis) for each run aggregated for each the given hyperparameter's possible values (*x*-axis). Each evaluation metric can be considered to indicate better results if the value is a smaller value (i.e. resolution) or better results if the metric is a larger value (i.e. correlation), the direction of "better" is indicated by the arrows along the right side. *Note: Abbreviations: "magnitude outside"–average intensity of voxels in the reconstruction volume that were zero or near-zero in the ground-truth volume; "recon. time"–the time it took for the reconstruction process to run; "do alternating psf"–if yes, update the reconstructed volume with a different single view at each reconstruction iteration (see §2.2.3.4).*

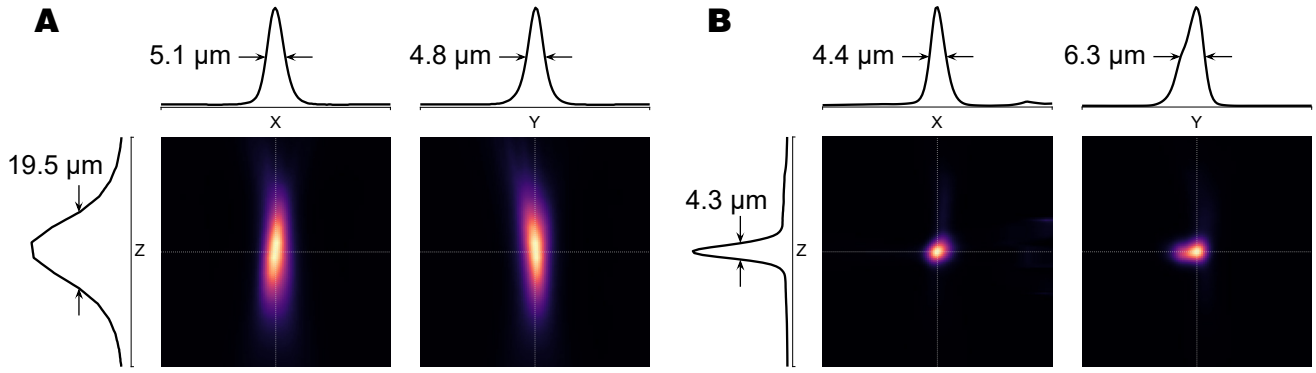

Figure 2.7: With single-view light field imaging and reconstruction, the reconstructed axis suffers ≈ 4× lower resolution; however, bead imaging experiments show our dual-objective system enables similar resolution across all dimensions. Both sub-panels show *xz* and *yz* maximum intensity projections taken from a region of interest within a reconstructed 3D image produced from light field (LF) micrographs taken with our dual-objective LF microscope (see Figure 2.3A) in a sample containing sparse 1 µm beads. Intensity line profiles along the image, intersecting with the bead's brightest point, are shown for the *x*, *y*, and *z* axes. The full-width at half-max for each of the intensity line profiles is also annotated. **A:** Only one of the LF micrographs was used to reconstruct the 3D image using the single-view reconstruction algorithm, Equation (2.18). **B:** Both LF micrographs were used to reconstruct the 3D image using the single-view merge algorithm, Equations (2.20) and (2.22), *Note: All images represent 16-bit/voxel grey-scale data rendered with the "magma" colormap.*

merge algorithm is able to incorporate multiple light fields for reconstruction in both the deconvolution and PSF definition, deals with the native-plane artifacts seen in other methods, and does not reduce the output resolution to the extent of the phase space methods.

Our development and implementation of a method to produce compound light field PSFs is the first known report of such a procedure and may prove useful in other light field and multi-view deconvolution applications. Since our work on this project (2017–2021), additional LFM reconstruction methods have been reported which might benefit from adaptation to the multiview context, including the dictionary LFM method by Zhang *et al.* [15].

2.4.1 Challenges for Practical Use of LFM for Neuroscience

Although we were able to successfully use our dual-objective LFM system and reconstruction algorithms to perform brain imaging in zebrafish larvae, a number of attributes of the LFM workflow made it difficult for us to employ for neuroscience experiments.

First, the reconstruction process takes orders of magnitude longer than the time for image acquisition. We can acquire light field images on the order of 100 Hz, which equates to 10 ms per frame acquisition; however, a single reconstruction can take more than 20 min. This reconstruction time is more than 5 orders of magnitude longer and even with parallel computing and other optimizations it is difficult to practically reconstruct volumetric datasets acquired at the scale of experimental work. For example a 5 min recording taken at 50 Hz could take upwards of 3 continuous days of compute time to be reconstructed.

Second, for neuroscience experiments, its important that we are able to readout from different neurons and brain regions independently to draw conclusions about signal pro-

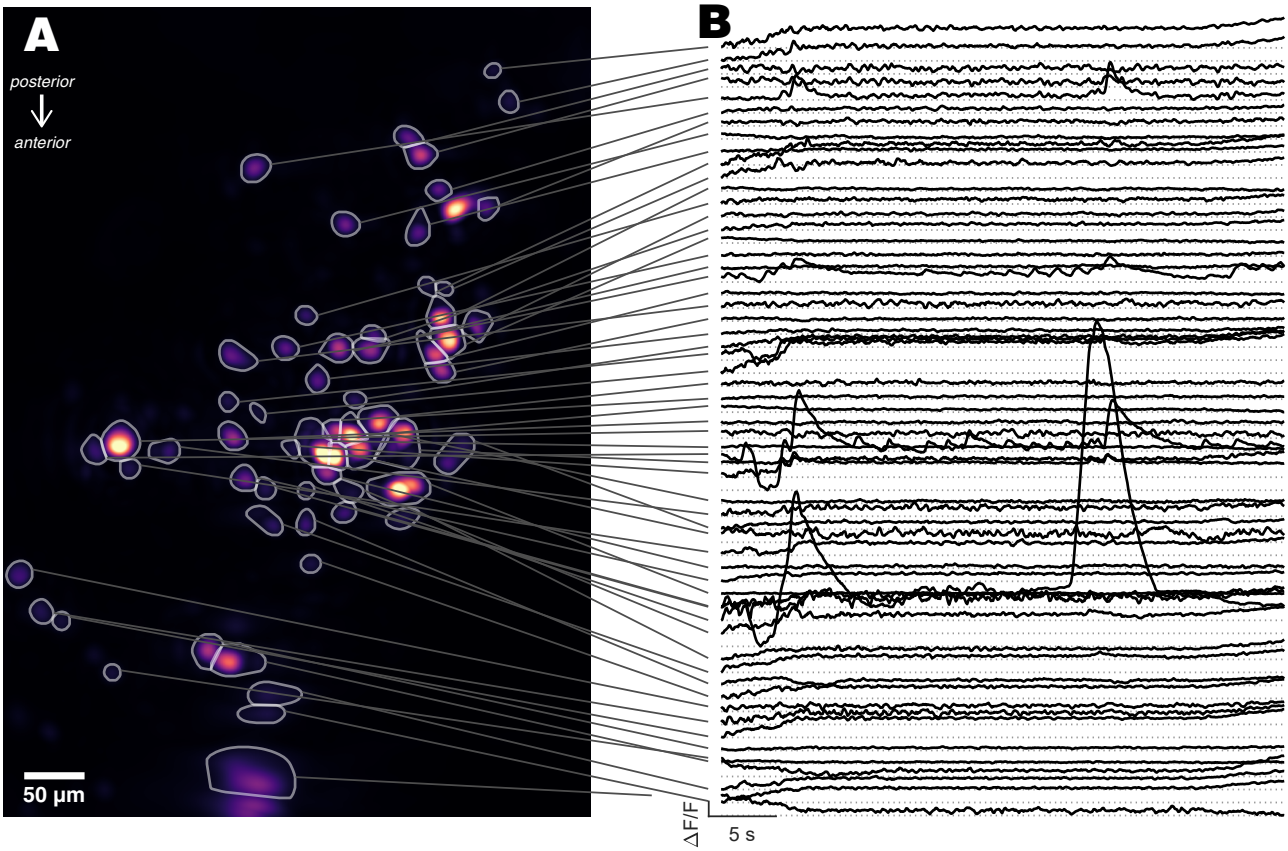

Figure 2.8: Our dual-objective light field microscope enables whole-brain calcium imaging in a sparsely expressing larval zebrafish. **A**: Maximum intensity *t*- and *z*-projection of a reconstructed image volume obtained from a baseline (i.e. unstimulated) recording the brain of an agarose-immobilized zebrafish larva sparsely expressing *Tg*(somaGCaMP6s). Image was reconstructed from light field images using the phase-space multimerge algorithm (see §2.2.2.6). Regions showing fluorescence were segmented into voxel selections each outlined in white. Scale bar = 50 µm. **B**: Relative fluorescence time-courses ΔF/F from each segmented region shown in **A**. A few regions showed strong calcium events.
Note: Recording was performed at 10 Hz.

cessing and the propagation patterns of activity through the brain. However, due to the way that light fields overlay angular and spatial information there is potential for it to be difficult to be fully confident that observed activity patters are real and not artifacts of the acquisition and reconstruction process. We can perform a series of *in silico* studies to assess the extent that spatial artifacts affect our ability to extract independent signals.

Third, light field imaging negotiates a trade-off between spatial resolution along the reconstructed axis and resolution in the imaging plane. Additionally, due to the nature of the reconstruction process, it is difficult to reconstruct dense samples with the same resolution as sparse samples. The larval zebrafish brain is very densely packed with neurons (relative to a sample of sparse beads) and we have found it difficult to achieve acceptable resolutions when performing whole-brain light field imaging in transgenic GCaMP expressing larvae compared to light sheet and two photon techniques. This issue was partially addressed with the development of the "sparse decomposition" reconstruction method by Yoon *et al.* [23]; however, the resolution is still reduced compared to other methods and many of

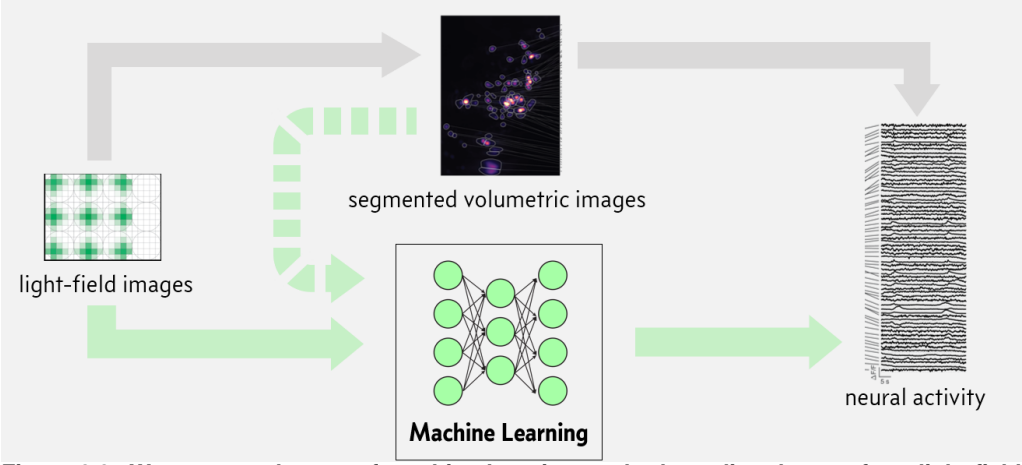

Figure 2.9: We propose the use of machine learning methods to directly transform light field micrographs to neural activity traces in a "reconstruction-free" method. Light field images have on the order of 10^6 parameters (pixels), 3D (volumetric) images contain on the order of 10^9 parameters (voxels) and take significant computational resources to reconstruct. Neural activity traces for the whole zebrafish brain would have on the order of 10^3–10^5 parameters (regions or neurons). The current approach (grey arrows) relies on reconstructing each light field micrograph into a volumetric image, followed by segmentation and extraction of traces. However by these parameter counts, we might assume that there is degenerate information latent within the 3D images. To improve the time to extract neural activity from light fields, we propose a machine learning method in which a model is trained on subset of light field micrographs, 3D images, and extracted traces to extract the activity traces directly from all recorded light fields (green arrows).

the other challenges still remain.

For these reasons, we chose not to utilize our light field system for performing whole-brain imaging experiments and opted instead for galvo/resonant two-photon microscopy, which is discussed in §4.1.1.1. However, with improvement to cameras, computing hardware, and light field microscopy techniques we may be able to return to utilize light field for neuroscience work.

2.4.2 Machine Learning Approaches for "Reconstruction-Free" Activity Segmentation

One such innovation we have considered is the development of machine learning model which can transform light field micrographs directly into neural activity traces, Figure 2.9. Theoretically, all of the information in a reconstructed 3D image should be contained in the original micrographs so we can design and experiment with methods to build and train models capable of this transformation. Such a model would be able to markedly speed-up the process of reading out neural activity from light field-imaged sample.

2.5 Methods

2.5.1 Reconstruction Implementation and Imaging Simulations

All code for light field reconstruction and optical simulation was written in MATLAB. Refer to Appendix A for a link to the code repository.

2.5.2 Dual-objective Light Field Microscope

The design, assembly, and operation of the dual objective light field system is discussed in detail in the doctoral dissertation of Pak [24, Chapter 3].

2.5.3 Bead Sample Preparation

Sparse beads samples were prepared by suspending fluorescent microspheres in agarose. A stock suspension of 1 µm green fluorescent polystyrene microspheres (Bangs Labs, FSDG005) were diluted in DI water $10^5\times$ (by serial dilution). An aliquot of agarose (1%) was then heated to liquefaction and vortexed to homogenize. To a microcentrifuge tube we added the dilute microsphere suspension (2.5 µL) and molten agarose (200 µL). The mixture was vortexed for 30 s then quickly pipetted onto a glass slide. Due to the geometry of the dual-objective LFM we wanted the sample to protrude significantly from the slide, so we would allow a mound of agarose (held by surface tension) to harden on the slide. To prepare a dense bead sample we would use $10^3\times$ diluted microspheres added to agarose at a ratio of 1:9 (e.g. 20 µL diluted microspheres in 180 µL of agarose).

2.5.4 Zebrafish Mounting and Imaging

Live larval zebrafish virally injected with a HuC:somaGCaMP6s construct [22] were mounted on a mound of agarose for imaging under the dual objective LFM (see §4.5.2 for more details on zebrafish care). The protocol is very near identical to that described in §4.5.3 with a small modification to raise the larva higher from the dish. Before adding the larva to the dish, we first pipetted a few drops of low gelling temperature agarose (≈ 1 mL, same type and concentration used for mounting) onto the center of the dish to create a mound $\approx 2-4$ mm in height. We allowed the mound to harden for 5 min at room temperature. Then the fish was transferred to the top of this mound and mounting proceeded as described in §4.5.3.

Mounted fish were placed underneath the two objectives on a three axis translation stage. The dish holding the larva was manually rotated such that the rostral-caudal axis of the larva pointed along the y-axis of each camera. Fish facility water (see §4.5.2) was pipetted between both objectives and the dish and held in place by surface tension. Using a live feed from the cameras, the larva was translated along all axes until the fluorescent brain was centered in the field of view for both cameras. See [24, Chapter 3] for the camera synchronization and image acquisition protocol.

2.6 Conclusion

Here we present the first known development and implementation of a suite of algorithms for multi-view light field reconstruction which incorporate information from all views into each reconstruction iteration. This includes the adaptation of an anti-aliasing reconstruction method, a phase space reconstruction method, and the computation of the compound PSF to the multi-view context. We show *in silico* experiments which allowed us to compare

the different methods and concluded that the multimerge, anti-aliasing, reconstruction with use of the compound PSF is the best candidate algorithm for further development and testing. We use one of our reconstruction methods along with our dual-objective light field system to image and read out calcium activity from ≈ 50 neurons at an acquisition rate of 30 Hz. We also believe that these new approaches may find utility in other branches of the light field imaging community.

Ultimately, we also conclude that light field microscopy, though promising, is not yet a mature enough technology for us to use in neuroscience experiments. Particularly developments to significantly speed up the reconstruction and/or activity extraction process by 3–5 orders of magnitude are needed to allow for light field microscopy to be practically applicable for neuroscientists. Moving forward to the following chapters we will present our how we use two photon microscopy along with extensive development of stimulation and behavioral imaging technologies to move towards the very experiments that were otherwise intractable with light field microscopy.

2.7 References

1. Wang, Z. *Whole-brain Voltage Imaging in Larval Zebrafish using Light-field Microscopy* (Massachusetts Institute of Technology, May 2020). https://dspace.mit.edu/handle/1721.1/127486.
2. Chen, T.-W. *et al.* Ultrasensitive fluorescent proteins for imaging neuronal activity. *Nature* **499,** 295–300 (2013).
3. Tian, L. *et al.* Imaging neural activity in worms, flies and mice with improved GCaMP calcium indicators. *Nature Methods* **6,** 875–881 (2009).
4. Chen, Q. *et al.* Imaging neural activity using Thy1-GCaMP transgenic mice. *Neuron* **76,** 297–308 (2012).
5. Ahrens, M. B., Orger, M. B., Robson, D. N., Li, J. M. & Keller, P. J. Whole-brain functional imaging at cellular resolution using light-sheet microscopy. *Nature Methods* **10,** 413–420 (2013).
6. Portugues, R., Feierstein, C. E., Engert, F. & Orger, M. B. Whole-brain activity maps reveal stereotyped, distributed networks for visuomotor behavior. *Neuron* **81,** 1328–1343 (2014).
7. Bouchard, M. B. *et al.* Swept confocally-aligned planar excitation (SCAPE) microscopy for high-speed volumetric imaging of behaving organisms. *Nature Photonics* **9,** 113–119 (2015).
8. Levoy, M., Ng, R., Adams, A., Footer, M. & Horowitz, M. Light field microscopy. *ACM Trans. Graph.* **25,** 924–934. ISSN: 0730-0301. https://doi.org/10.1145/1141911.1141976 (July 2006).
9. Broxton, M. *et al.* Wave optics theory and 3-D deconvolution for the light field microscope. *Optics Express* **21,** 25418–25439 (2013).
10. Prevedel, R. *et al.* Simultaneous whole-animal 3D imaging of neuronal activity using light-field microscopy. *Nature Methods* **11,** 727–730. https://www.nature.com/articles/nmeth.2964 (May 2014).
11. Wagner, N. *et al.* Instantaneous isotropic volumetric imaging of fast biological processes. *Nature Methods* **16,** 497–500. https://www.nature.com/articles/s41592-019-0393-z (Apr. 2019).
12. Stefanoiu, A., Page, J., Symvoulidis, P., Westmeyer, G. G. & Lasser, T. Artifact-free deconvolution in light field microscopy. *Optics Express* **27,** 31644–31666. http://www.opticsexpress.org/abstract.cfm?URI=oe-27-22-31644 (Oct. 2019).
13. Bishop, T. E. & Favaro, P. The light field camera: Extended depth of field, aliasing, and superresolution. *IEEE Transactions on Pattern Analysis and Machine Intelligence* **34,** 972–986. ISSN: 01628828 (5 2012).

14. Liu, F. L. *et al.* Fourier DiffuserScope: single-shot 3D Fourier light field microscopy with a diffuser. *Optics Express, Vol. 28, Issue 20, pp. 28969-28986* **28,** 28969–28986. ISSN: 1094-4087. https://opg.optica.org/viewmedia.cfm?uri=oe-28-20-28969 (20 Sept. 2020).

15. Zhang, Y. *et al.* DiLFM: an artifact-suppressed and noise-robust light-field microscopy through dictionary learning. *Light: Science & Applications 2021 10:1* **10,** 1–12. ISSN: 2047-7538. https://www.nature.com/articles/s41377-021-00587-6 (1 July 2021).

16. Wang, Z. *et al.* Real-time volumetric reconstruction of biological dynamics with light-field microscopy and deep learning. *Nature Methods 2021 18:5* **18,** 551–556. ISSN: 1548-7105. https://www.nature.com/articles/s41592-021-01058-x (5 Feb. 2021).

17. Eberhart, M. Efficient computation of backprojection arrays for 3D light field deconvolution. *Optics Express* **29,** 24129–24143. http://www.osapublishing.org/oe/abstract.cfm?URI=oe-29-15-24129 (July 2021).

18. Lu, Z. *et al.* Phase-space deconvolution for light field microscopy. *Optics Express* **27,** 18131–18145. http://www.opticsexpress.org/abstract.cfm?URI=oe-27-13-18131 (June 2019).

19. Preibisch, S. *et al.* Efficient Bayesian-based multiview deconvolution. *Nature Methods* **11,** 645–648. https://www.nature.com/articles/nmeth.2929 (Apr. 2014).

20. *Frequently Asked Questions, Z Brain Atlas, Engert Lab* https://zebrafishexplorer.zib.de/faq.

21. Randlett, O. *et al.* Whole-brain activity mapping onto a zebrafish brain atlas. *Nature Methods* **12,** 1039–1046. ISSN: 1548-7091. http://www.nature.com/articles/nmeth.3581 (11 Nov. 2015).

22. Shemesh, O. A. *et al.* Precision Calcium Imaging of Dense Neural Populations via a Cell-Body-Targeted Calcium Indicator. *Neuron* **107,** 470–486.e11. ISSN: 0896-6273 (3 Aug. 2020).

23. Yoon, Y.-G. *et al.* Sparse decomposition light-field microscopy for high speed imaging of neuronal activity. *Optica, Vol. 7, Issue 10, pp. 1457-1468* **7,** 1457–1468. ISSN: 2334-2536. https://opg.optica.org/viewmedia.cfm?uri=optica-7-10-1457 (10 Oct. 2020).

24. Pak, N. *Automation and scalability of in vivo neuroscience* (Massachusetts Institute of Technology, June 2018). https://dspace.mit.edu/handle/1721.1/119094.

CHAPTER 3

Stimulation Input: Zebrafish Olfactory Stimulation Platform

3.1 Introduction

Zebrafish exhibit many interesting behaviors beginning very early in their development as larvae [1]. Such behaviors include the opto-motor response [2], prey tracking and capture [3], phototaxis [4], kin recognition [5–9], and chemo-sensation and gradient navigation[10, 11], Figure 3.1. Each of these different behaviors present different aspects of neural processing to explore. For this work we chose to focus on the exploration of behaviors connected to the olfactory detection of waterborne chemical cues.

We chose to focus on olfaction because of the different valences of odors which can be utilized to stimulate the zebrafish. For example, attractive odors like amino acid cocktails

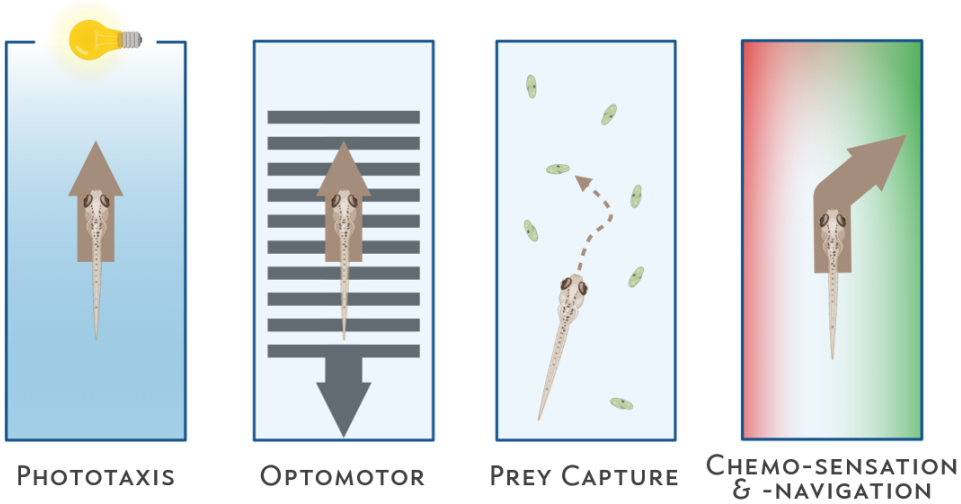

Figure 3.1: Zebrafish larvae exhibit many well-known behaviors that we can leverage to understand brain function [1]. In this work we investigate chemo-sensation and navigation through the olfactory system.

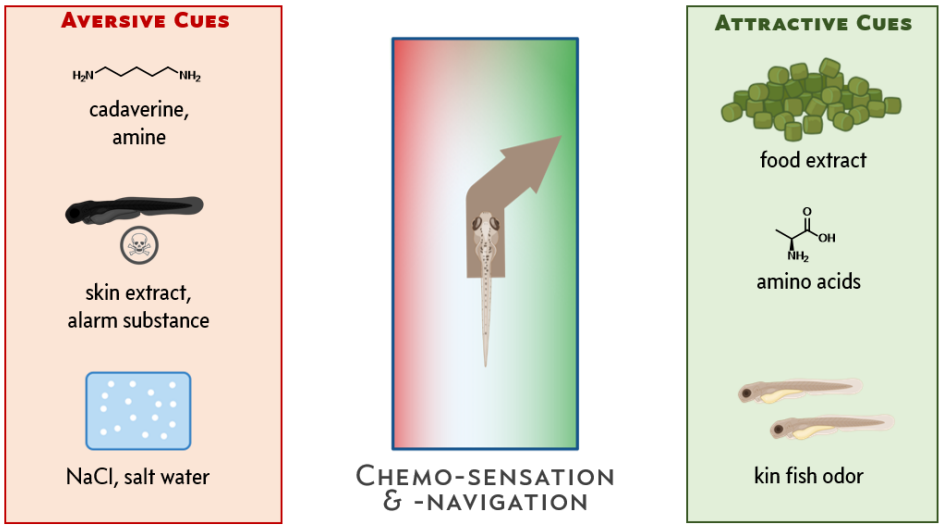

Figure 3.2: Sensing of waterborne olfactory cues by larval zebrafish serves many functions and can produce a range of responses.

as well as aversive odors like alarm substance are all experienced and processed through the olfactory system, Figure 3.2. We also chose to explore olfaction because of the timescales over which olfactory changes happen, the diffusing and sampling of chemical cues through the water happens on the time-scale of seconds (rather than milliseconds) which makes the elucidation of olfactory cue processing in the context of 1–5 Hz volumetric brain imaging more approachable and matched as compared to other behaviors. (Consider the speed with which some visual cues are processed.) We also chose to focus on olfaction because of the bilaterality of the olfactory system; zebrafish posses a left and a right olfactory epithelium (analogous to left and right nostrils), therefore there are a broad array of questions we are able to explore regarding the ability of the zebrafish to utilized bilateral differences to compute odor source locations and inform the navigational movements of the larvae. Given that one of the goals of this work was to incorporate live behavioral observations—that is, tail movements—into our studies, probing the olfactory system, a sensory paradigm utilized for navigation (potentially in a bilateral way), was a decision that supported the broader context of the work we wish to accomplish.

With these considerations in mind, we set out to design and build an olfactory stimulation system. The requirements for this system were:

- The system must allow for spatial control of odor delivery to the fish's nose. It must be possible to stimulate the left and right olfactory epithelia separately (located approximately 80 µm apart).
- The system must allow for temporal control of odor delivery to the fish's nose. It must be possible to stimulate with well defined odor pulses on the order of seconds.
- The system must be designed such that other modalities including live brain imaging and behavioral recording can be simultaneously synchronized to and recorded along side the olfactory stimulation.

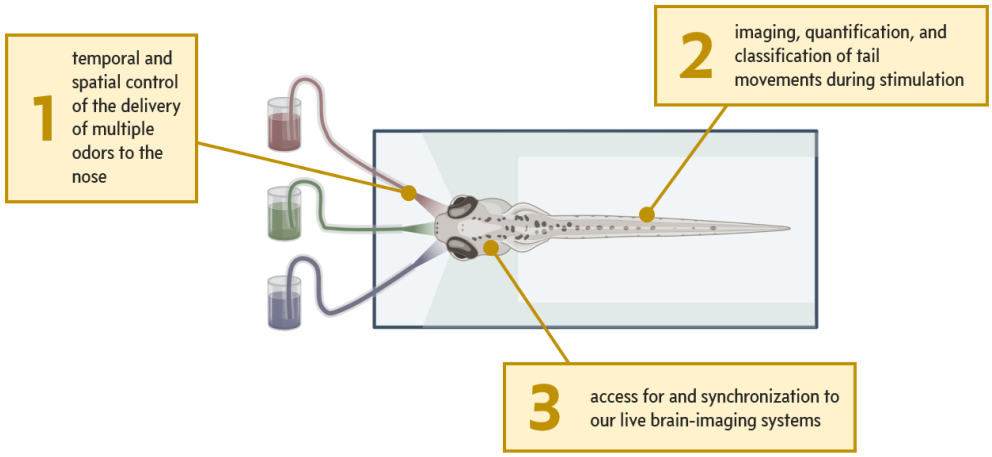

Figure 3.3: There are three primary design requirement for our olfactory stimulation platform.

Table 3.1: Our olfactory stimulation system fills a gap in existing stimulation technologies by enabling multi-directional, real-time stimulation with many odors simultaneous with whole brain imaging. Table of various reported zebrafish olfactory stimulation technologies/methods along with the attributes of the fish and correlated modalities. Green boxes correspond to those attributes which are the "best" for a given column compared across all rows.
Note: Column header abbreviations: "Num. Odor Channels:" The number of odors the system is capable of delivering to the fish over the course of a stimulation experiment?; "Num. Stim. Dirs.:" The number of simultaneous stimulation directions which can be applied to the fish; "Age:" The fish's age post-fertilization; "Realtime?:" Is the olfactory stimulation done dynamically over the course of monitoring/imaging?; "Behav. Image?:" Is behavioral imaging performed simultaneous with stimulation?; "Brain Image?:" Is brain activity imaging (i.e. calcium imaging) performed simultaneous with stimulation?; "Bilateral?:" Can the left and right olfactory epithelia be stimulated independently?; "Platform:" The type of setup the fish is contained in for the stimulation experiment; "Addnl. Modalities:" The additional modalities, if any, that the fish is stimulated with.

Author & Reference	Year	Number of Odor Channels	Num. Stim. Dirs.	Age	Fish State	Real-time?	Behav. Image?	Brain Image?	Bilateral?	Platform	Addnl. Modalities
Maaswinkel & Li[12]	2003	1	1	4–12 month	free swimming	YES	YES	NO	NO	ring-shaped tank with rotating drum	visual stimulation
Bhinder & Tierney[13]	2012	1	1	> 2 week	free swimming	YES	YES	NO	NO	4 quadrant ring-shaped tank	food application
Braubach *et al.*[10]	2009	1	0	3–7 day	free swimming	NO	YES	NO	NO	96-well plate wells	—
Biechl *et al.*[14]	2016	2	2	9 day	free swimming	YES	YES	NO	NO	2 channel choice flume	—
Jeong *et al.*[15]	2021	1	1	5 day	free swimming	YES	YES	NO	NO	cross shaped maze	optogenetic activation
Herrera *et al.*[16]	2021	8	1	5–7 day	head-fixed, tail-free	YES	YES	YES	NO	agarose-embedding in dish	—
Sy *et al.*[17]	2023	2	2	5–7 day	head-fixed, tail-free	YES	YES	YES	YES	microfluidic chip	—
this work	2024	10	3	6–7 day	head-fixed, tail-free	YES	YES	YES	YES	agarose-embedding in dish	—

These requirements Figure 3.3 guided the design and refinement process of our zebrafish olfactory stimulation system (ZOSS).

3.1.1 Existing Olfactory Stimulation Methods

A number of groups have developed means to stimulate larvae with different odors. A summary of prior art in the context of zebrafish olfactory stimulation is provided in Table 3.1 along with the placement of this current work. Here we will give a brief overview of two key prior olfactory stimulation technologies which integrated whole-brain imaging. Sy *et al.*

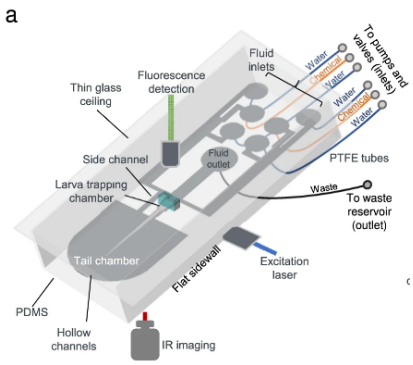

Figure 3.4: Sy *et al.* present an optofluidic chip for performing olfactory stimulation and brain imaging; however, it is capable of only delivering one odor per lateral side.
Note: Taken from [17, Figure 2a]

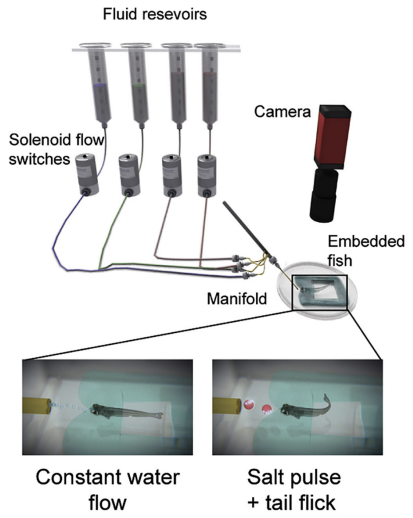

Figure 3.5: Herrera *et al.* present a stimulation manifold capable of delivering multiple odors; however, their system does not incorporate the ability for lateral stimulation, or stimulation with multiple odors streams simultaneously.
Note: Taken from [16, Figure 2a]

utilize a custom optofluidic chip capable of flowing separate, controlled streams of odors over the left and right olfactory placodes, Figure 3.4. Their use of an optofluidic chip produced by microfabrication methods allows for highly controlled and repeatable stimulation [17]. Drawbacks of this design include the requirement of a highly specialized and potentially fragile chip to be utilized for any fish to be imaged, limitations around the number of possible different odors which can be delivered.

Herrera *et al.* [16] head-immobilize larvae in agarose for two-photon brain imaging and utilize a 360 µm-diameter perfusion pencil tip (AutoMate Scientific 04-360) attached to an 8-channel manifold along with solenoids to direct odors to the rostral end of the immobilized larvae, Figure 3.5. This system allows for the exchange of up to 7 odor solutions (+ 1 water/control stream) to the larvae with temporal control. However, due to the large size of the stimulation tip, and the fact that only one stimulation source is employed, there cannot be independent stimulation of the left and right olfactory placodes.

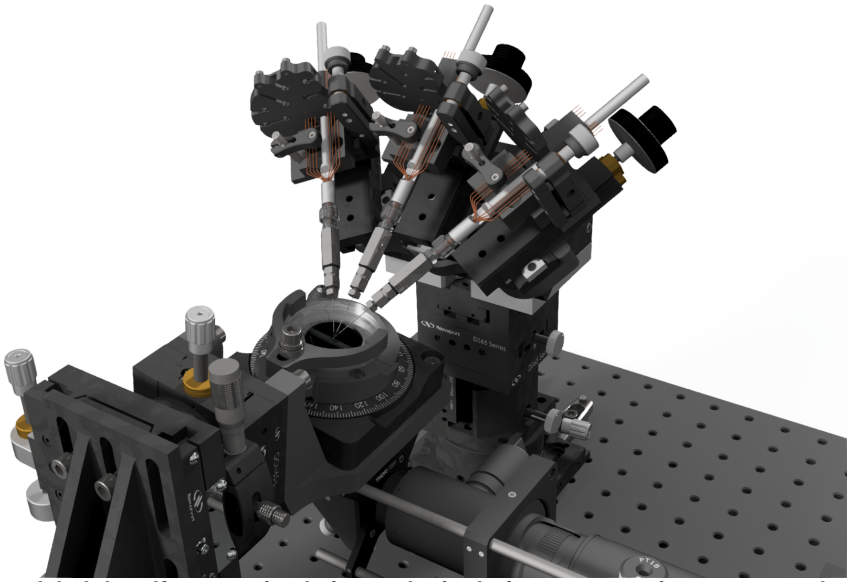

Figure 3.6: We modeled the olfactory stimulation endpoint before construction to ensure the system could be physically integrated and aligned. 3D rendering of the olfactory stimulation endpoint design; created prior to assembly and deployment.

As demonstrated by Table 3.1, the system we outline in this chapter is the first system of it's kind to enable 3-directional olfactory stimulation of zebrafish capable of bilateral separation and the use of up to 10 different odorants synchronous with brain imaging and behavioral imaging.

3.2 Design of Olfactory Stimulation System

Here, we present a olfactory stimulator and control system capable of delivering odors from 3 different positions (left, center, and right) to the olfactory epithelium of a head-immobilized larvae. The design of this stimulator is shown in Figure 3.6. The stimulator serves as the endpoint, hardware for delivering odor streams to the olfactory epithelium; in addition to the stimulator we have a stimulation control platform Figure 3.7 of fluid plumbing, air handling, and electronic controls which regulate and actuate the outputs of the stimulation endpoint.

Together the stimulation endpoint, the stimulation control platform, and the the umbilical connecting them comprise the Zebrafish Olfactory Stimulation System (ZOSS).

We will discuss each of these subsystems in detail working from backward from the components that directly deliver odor solutions to the olfactory epithelium back to the platform's power and pressure sources. As an overview these are the relevant subsystems:

- Stimulation Endpoint
- System Umbilical
- Flow Sensing

Figure 3.7: We designed the olfactory stimulation control cart to be portable and house all of the components for electronic control, air handling, and fluid handling. 3D rendering of the olfactory stimulation cart design; created prior to assembly and deployment.

- Flow Routing and Control
- Fluid Reservoir and Collection
- Air Handling
- Power Distribution
- Stimulation Cart Framing
- Stimulation Software

3.2.1 Stimulation Endpoint

3.2.1.1 Delivery Needles

We utilized custom mounted 35 gauge, blunt-tipped NanoFil needles to deliver odors to the larvae through the free water. These needles have an tip outer diameter of 135 µm and a inner diameter of 55 µm. These needles were chosen as they are some of the smallest available needles which are commercially available and can produce an odor stream small enough to be directed to a single olfactory rosette.

The 35G NanoFil needles on its own is formed as a 35 mm long stainless steel cylinder with a small tip end and a larger shank end (460 µm in diameter). The shank end is smooth along its length and is not easily coupled to a larger fluidic system via any standard connections. Therefore we mounted the barrel of the shank coaxial within a standard 22G blunt tip needle fitted with a female leur connection, Figure 3.8. The 35G NanoFil needle was

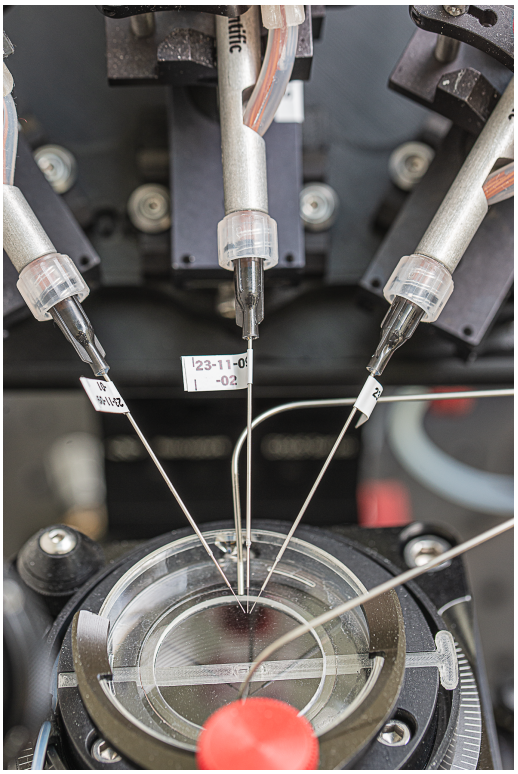

Figure 3.8: We utilized three custom mounted NanoFil needles each within a 22 gauge blunt-tip needle to provide micron-precise delivery of odor streams. Detail photograph of stimulation system focusing on the stimulation needles and the tips of the stimulation manifolds above dish where a zebrafish larvae would typically be mounted.

sealed to the standard 23G using high-purity instant-bond adhesive gel. This combination forms the delivery needle assembly.

3.2.1.2 Stimulation Manifolds

We utilized an 8-channel manifold (Perfusion Pencil by AutoMate Scientific) to combine different odor streams and couple them into the delivery needle assembly Figure 3.9. The outlet of the manifold has a standard male leur connection on which the delivery needle assembly is mounted, while there are 8 female leur inlets to the manifold to which the odor lines are attached. The body of the manifold is an approx 15 cm aluminum rod which allows for holding the manifold-needle assembly in position. We utilized three of these manifolds in the stimulation system for control of odor delivery to the left, center, and right of the larvae.

Polyimide micro-bore tubing is utilized (by the manufacturer) to connect each of the manifolds inputs to the combined output. We found this tubing to be delicate and prone to kinking and clogging, so we shrouded the bundle of micro-bore tubes with a flexible sheath tube and utilized a custom designed strain relief to hold each of the input ports in a reliable position which cannot be twisted or pulled .

Each of the female leur input ports on the manifold was converted to a female 1/4″-28 compression fitting port with a female 1/4″-28 to male leur-lock adapter to allow for

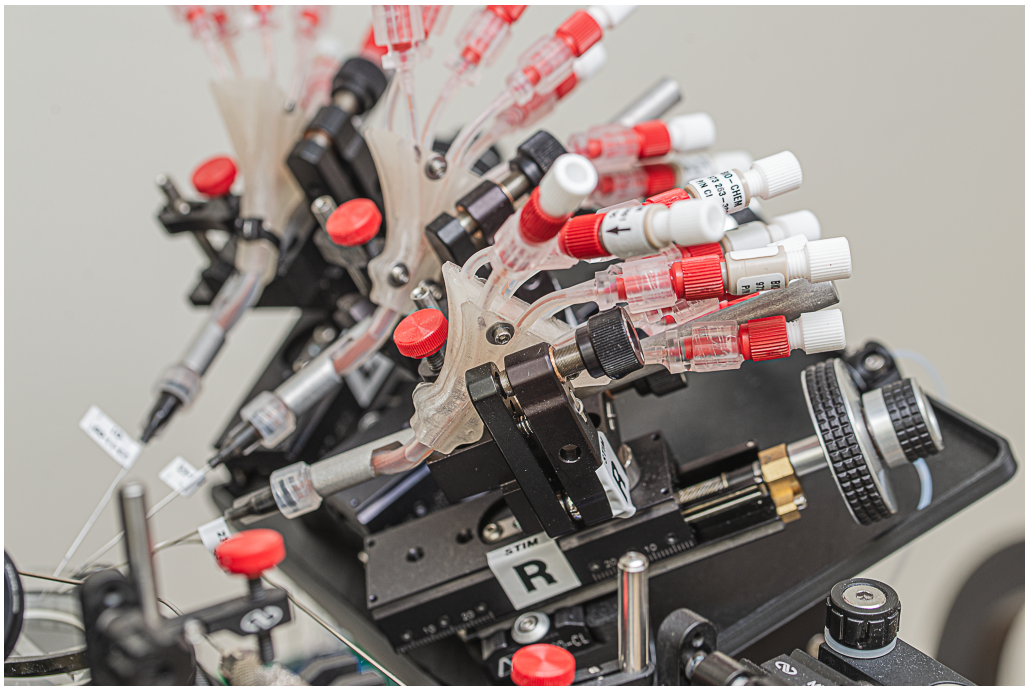

Figure 3.9: Each stimulation manifold could combine as many as 8 odor streams into a single stimulation needle for switching between different odors in real time. Additionaly, each stimulation manifold could be independently adjusted for alignment. Detail photograph of the stimulation endpoint focusing on the right stimulation manifold and positioner.

integration with the rest of the fluidic system. Ports which were utilized for odor delivery were attached to the upstream 1/32″ ID tubing with a 1/4″-28 male compression tube fitting. Ports which were not utilized were sealed off using a male 1/4-20 plug.

3.2.1.3 Stimulation Positioner

The stimulation micropositioner is an assembly of mechanical hardware utilized to position the each of the delivery needle- manifold assemblies with micron precision around the larva's olfactory epithelia. The stimulator positioner is made up of four subassemblies: one 5- DOF bulk positioner which moves all stimulation manifold together and three identical 3-DOF individual positioners which allows for each stimulation manifolds (left, center, and right) to be positioned independently.

3.2.1.3.1 Bulk Positioner The bulk positioner attaches directly to the entire platform's mechanical breadboard, Figure 3.10. It is made up of (from base to top):

3.2.1.3.1.1 DOF 1 z-rotation A rotation stage (Newport 481-A-S) which allows for angular positioning around the yaw (z) axis with 360° of coarse control and 5° of fine control (via an fine-pitched adjustment screw).

3.2.1.3.1.2 DOF 2 z-translation A vertical positioner (Newport DS65-Z) which allows for 14 mm of z-axis travel.

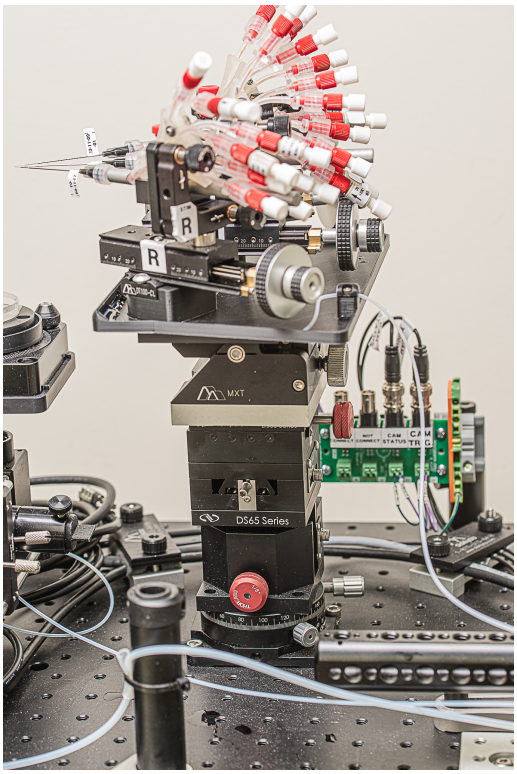

Figure 3.10: The stimulation positioner subassembly enabled the alignment of the olfactory stimulator needles to a zebrafish larvae and the alignment of each of the needles to one another.

3.2.1.3.1.3 DOF 3–4 xy-translation A pair of linear stages (Newport DS65-X) which allows for 25.4 mm of x-axis and y-axis travel.

3.2.1.3.1.4 DOF 5 y-rotation A locking tilt platform (Siskiyou MXT Series Platform) which allows for 45° of coarse rotation about the y-axis. Essentially, this motions tilts the stimulation manifolds from a horizontal orientation ($\theta_y = 0°$) to a position at which the stimualtion manifolds point down toward the fish and the dish containing the fish ($\theta_y \approx -40°$). These positioning components were fastened together with standard imperial hardware and mounted to the base mechanical breadboard.

3.2.1.3.2 Individual Positioners The three individual positioner assemblies (one for each stimulation manifold) are mounted to the Siskiyou tilt platform, Figure 3.11. These positioner assemblies are mounted through a riser post and roughly aligned using a custom jig such that each stimulation manifold pointed approximately to a single point with the left and right stimulation manifolds angled in to a common point at ≈ 30°. The positioner assemblies are constructed of two main components:

3.2.1.3.2.1 DOF 1 y'-translation A linear translation stage (Siskiyou DT-130-X) which provides 42 mm of coarse adjustment and 3 mm of fine adjustment along the axis of each delivery needle (which we will refer to as the y'-axis). Essentially, this motion moves

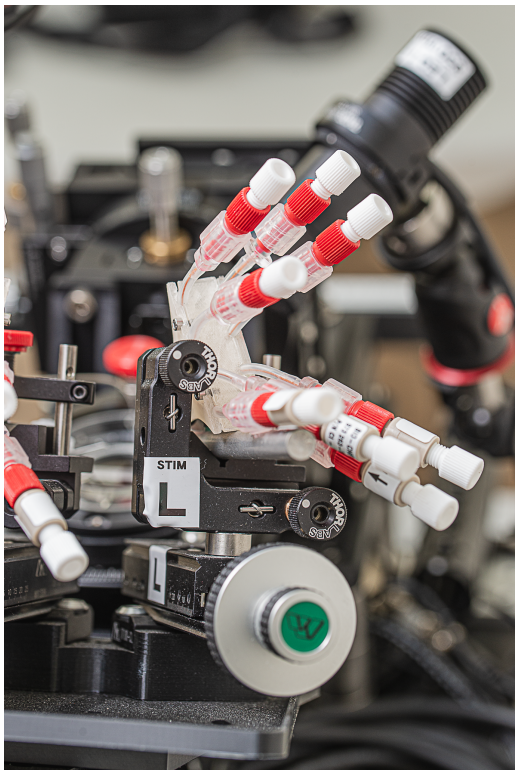

Figure 3.11: Each stimulation manifold could be independently position along it's axis as well as in "tip" and "tilt" directions. Photograph of the left individual stimulator positioner and translation stage.

each of the stimulator manifold-delivery needle assemblies directly toward and directly away from the larvae.

3.2.1.3.2.2 DOF 2–3 $x'z'$-rotation A pitch-yaw kinematic V-mount (Thorlabs KM100V) provides 8° of fine tip and tilt adjustment. Essentially, this motion adjusts the pointing direction of each of the simulator manifold-delivery needle assemblies. The V-clamp portion of the mount is where the cylindrical body of the stimulator manifold is clamped to securely connect it to the kinematic V-mount and the entire stimulator positioning assembly.

3.2.1.4 Wash and Vacuum Delivery Assemblies

To facilitate the exchange of fluid into and out of the larva-containing dish, we utilized two segments of needle tubing: one for flowing fish water *into* the dish (wash) and one withdrawing the dish/odor liquid *out of* the dish (vacuum). The end of the wash tubing was directed toward the center of the dish and located ≈1.5 cm from the center of the dish with flow directed in the same direction as the middle stimulation needle. The end of the vacuum tubing located on the opposite (tail) side of the dish with suction direction vertically (i.e. the face of the needle is parallel to the water surface); the vertical position. Each of these segments of needle tubing were mounted in a compression fitting to $1/4''$-28 female adapter, then each adapter was connected to the wash and vacuum ports on the

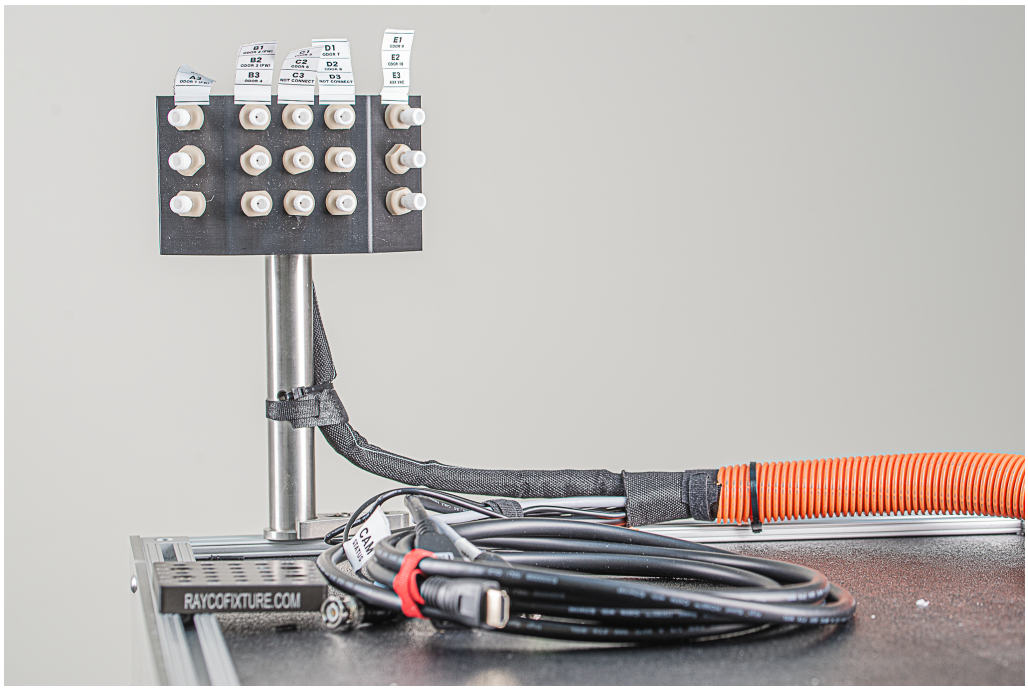

Figure 3.12: The endpoint bulkhead panel contained 15 1/4″-28 connections and lines for delivering fluid between the stimulator cart and stimulation endpoint. Photograph of endpoint bulkhead panel attached to the system umbilical

distal bulkhead panel with a 1/8 inner diameter needle tubing fitted on both ends with 1/4″-28 male compression fittings.

3.2.1.5 Endpoint Plumbing Lines

The next upstream components are the fluid lines and bulkhead panel which connect from the stimulator manifold to the system umbilical.

3.2.1.5.1 Microfluidic Routing Lines For each line utilized on each manifold a 1/32″ ID tubing was used to connect from the stimulation manifold to the appropriate position on the bulkhead panel (discussed in the following section). Each line was fitted with male 1/4″-28 compression fitting-ferrule assemblies on both ends for connection to other components. Each of these lines was labeled to indicate the stimulator it connected to ("L", "M", "R"), the bulkhead panel position it connected from ("[A–E][1–3]"), and the fluid line that it carried ("Odor [1–10]").

3.2.1.5.2 Bulkhead Panel (15-position) The next downstream component (and the final upstream component prior to the system umbilical) is a 15-position bulkhead panel. This panel contains an array of 3 rows × 5 columns of flat-bottomed 1/4″-28 female to 1/4″-28 female adapters mounted within a custom bulkhead mount with through holes for each adapter, Figure 3.12. The panel was mounted to a 1″ metal pedestal post for securely mounting to the platform's mechanical breadboard with the use of a clamping fork. The downstream side of each adapter connected either one of the microfluidic routing lines, a

Figure 3.13: The system umbilical contained a bundle of fluid lines as well as electrical connections, it was sheathed and shielded to protect and isolate the contained interconnections. Photograph system umbilical as is breaks out into different lines at the distal end

1/4″-28 plug (i.e. not connected), or to the vacuum and wash lines. The upstream side of each adapter is connected directly to a fluid line of the system umbilical (discussed further in §3.2.2). The entire bulkhead panel is designed to stay attached to the system umbilical and can be stored with the stimulator control cart when the stimulation endpoint and control cart need to be separated, in this way each of the fluid lines stays separated.

The bulkhead is labeled at each adapter position by its column with letters "A"–"E"; and by its row with numbers 1–3. Additionally each position is labeled with the contents of that line.

3.2.2 System Umbilical

The system umbilical bridges between the stimulation endpoint subsystem and the collections of subsystems on the simulator cart (flow sensors, flow routing, reservoirs, etc.). The umbilical enables the stimulation endpoint, imaging, monitoring, and other processes that must be located near the zebrafish to be controlled remotely (within about 20 ft) from the stimulator cart and its operation subsystems. This satisfies an important design requirement to make the stimulation system compatible with zebrafish larva whole-brain imaging.

The system umbilical is a sheathed, 15′ bundle of fluid lines, power lines, and data communication lines, Figure 3.13. We will focus on the fluid lines here. The bundle of fluid lines consists of 12 1/32″ ID tubes and 3 1/16″ ID tubes each tube is terminated on both ends with male 1/4″-28 compression fittings. On both ends of the umbilical, each of the tubes is fitted into corresponding 15-position bulkhead panels. The bundle of fluid lines is sheathed in a spiral plastic cable wrap to prevent any kinking of the individual lines. The fluid line

Figure 3.14: Each of the 15 fluid lines in the system umbilical is connected, on the cart side, to another bulkhead panel. Photograph 1/4″-28 bulkhead panel at the proximal end of the umbilical where the fluid lines are bundled at the stimulator cart.

bundle, along with the other power and signal cables, are wrapped in a fabric cable wrap further covered by an orange corrugated plastic sheath.

On the stimulation cart end of the umbilical, similar to the simulation endpoint end, there is an identical bulkhead panel to the one described in §3.2.1.5.2. Each of the 15 fluid lines is connected into this bulkhead panel in a similar fashion, Figure 3.14. This stimulator cart panel is mounted directly to the cart near the bottom shelf directly connected, on the upstream side, to the flow sensors (see §3.2.3). The umbilical was assembled to have 3 excess fluid lines in the case of an issue or for future addition of features; these fluid lines are plugged on the downstream end of the stimulation endpoint bulkhead panel and on the upstream end of the cart bulkhead panel with 1/4″-28 male plugs.

3.2.3 Flow Sensing

The next upstream subsystem is the collection of components responsible for sensing and communicating the flow rates through each of the fluid lines. This subsystem is made up of flow sensors, multiplexing I_2C breakout board, and a readout microcontroller.

3.2.3.1 Flow Sensors

The stimulation system utilized 12 flow sensors, Figure 3.15, for monitoring flow through each of the main fluid lines, 10 of the sensors are designed to monitor flow rates within the range 0.001 – 2 mL min^{-1} (Sensirion SLF3S-0600F), and 2 of the sensors are designed to monitor flow rates within the range 0.1 – 40 mL min^{-1} (Sensirion SLF3S-1300F). Up-

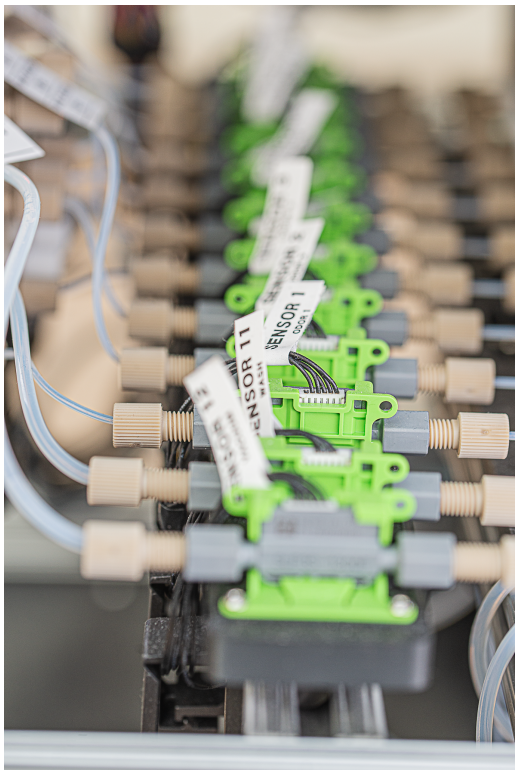

Figure 3.15: We utilized 12 flow sensors to continuously monitor flow through each of the stimulation, wash, and vacuum lines. Photograph of the array of flow sensors on the stimulator cart with electronic and fluidic connections.

stream of the cart bulkhead panel, each of the twelve main fluid lines (Odors 1–10, vacuum, wash) is routed with a short run of microfluidic tubing to the outlet of each flow sensor (with the exception of the vacuum line which is routed to the sensors input side). Each flow sensor has two female flat-bottomed 1/4″-28 ports for making fluidic connections.

The flow sensors are also equipped with a 6-pin connector (Molex 53261-0671 1.25 mm PicoBlade) for data and power signals. The data and power lines, Figure 3.16, from each of the sensors is connected to the I_2C breakout board (discussed more in the §3.2.3.2) with female 1.25 mm PicoBlade to female JST-XH cables (custom fabricated in-house).

The 12 flow sensors are mounted in brackets (Sensirion SLF3x mounting clamp) and each of the brackets are arranged at equal spacing with two 6-sensor bracket mounts (custom fabricated in-house). In this way each of the flow sensors is securely held in identical positions to minimize any inter-sensor variation and reduce readout noise.

3.2.3.2 Multiplexing I_2C Breakout Board

As mentioned in §3.2.3.1 each of the sensors is connected to a multiplexing I_2C breakout board for data and power connections, Figure 3.17. Each sensor connection consists of four wires:

1. Power (+3.3 V)
2. I_2C Clock (SCL)

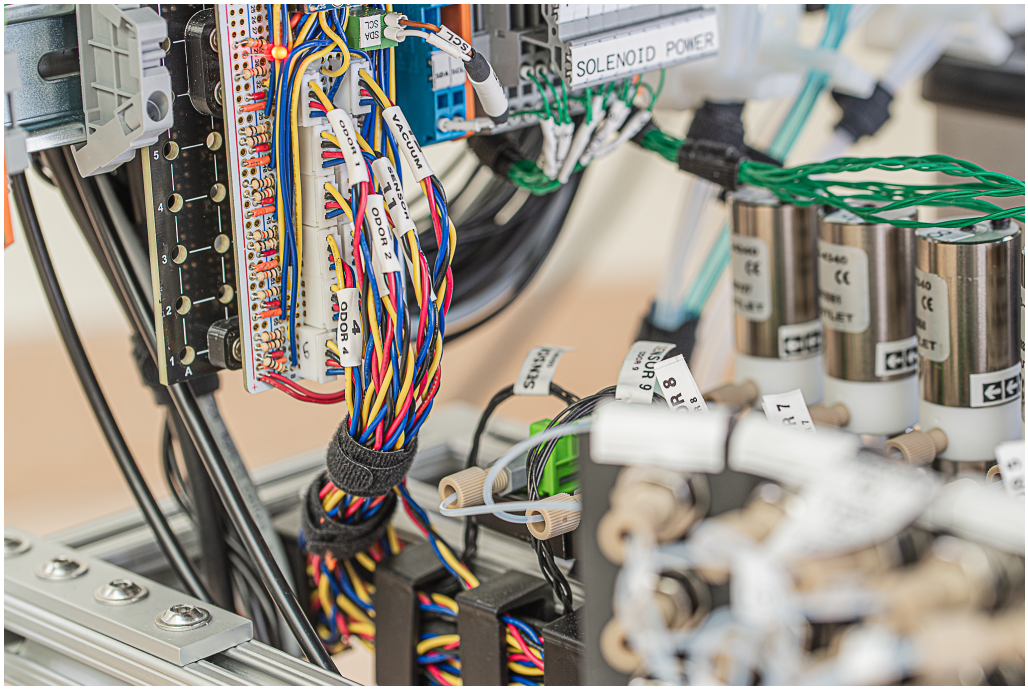

Figure 3.16: We utilized a custom breakout board for powering and communicating, via I_2C, to the flow sensors. Photograph bundle of custom flow sensor connection cables coming out of the I_2C multiplexer breakout board.

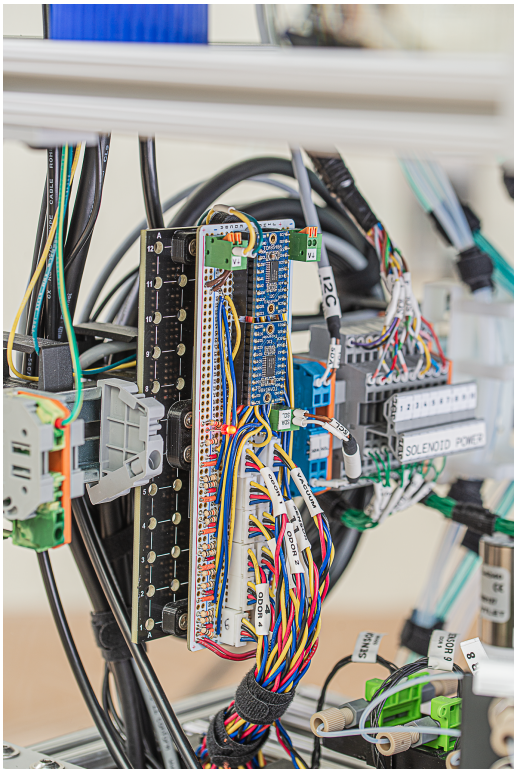

Figure 3.17: DIN rails were used to mount the flow sensor breakout board as well as many other electronic components. Multiplexing I_2C breakout board for flow sensor communication.

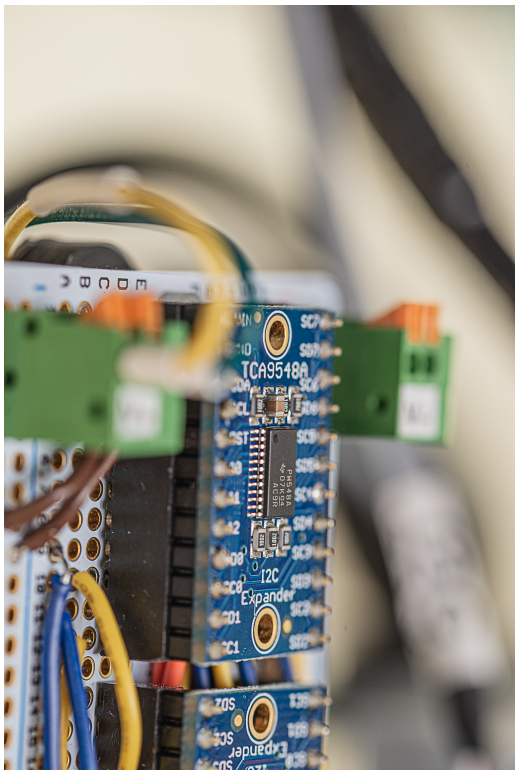

Figure 3.18: A pair of integrated circuits were utilized for multiplexing communication to all twelve sensors over a single I_2C line-pair. Photograph TCA9458A I_2Cmultiplexing daughter board.

3. I_2C Data (SDA)
4. Ground ($\perp$)

The breakout board supplies power and routes signal for each of these lines for each sensor.

The breakout board is powered with 3.3 V power and ground connections which are supplied by the stimulator cart's power distribution system (see §3.2.8). The breakout board also has a pair of I_2C (SDA, SCL) data lines which run I/O to the microcontroller for sensor readout (see §3.2.3.4).

The primary functional components of the I_2C breakout board are a pair of TCA9458A 1-to-8 I_2C multiplexer (Adafruit 2717) daughter boards, Figure 3.18. These boards enable all of the sensors to communicate through a single I_2C line pair. This is otherwise problematic because each of the sensors are internally encoded with the same device address and commands addressed to the sensor could not be directed to an individual device leading to crosstalk and an inability to unambiguously send and receive signals from each sensor. The multiplexer daughter boards are each able to take on 1 of 8 possible I_2C device addresses and a command can be sent to each daughter board to select a given child device (i.e. flow sensor) as "active". The flow sensors are wired such that sensors 1–8 are SDA and SCL lines are wired to multiplexer daughter board 0 and the remaining 4 flow sensors 9–12 SDA and SCL lines are wired to multiplexer daughter board 1.

The multiplexing breakout board was fabricated from a through-hole breadboard and wired by soldering jumper cables according to the diagram shown in Figure 3.19. The

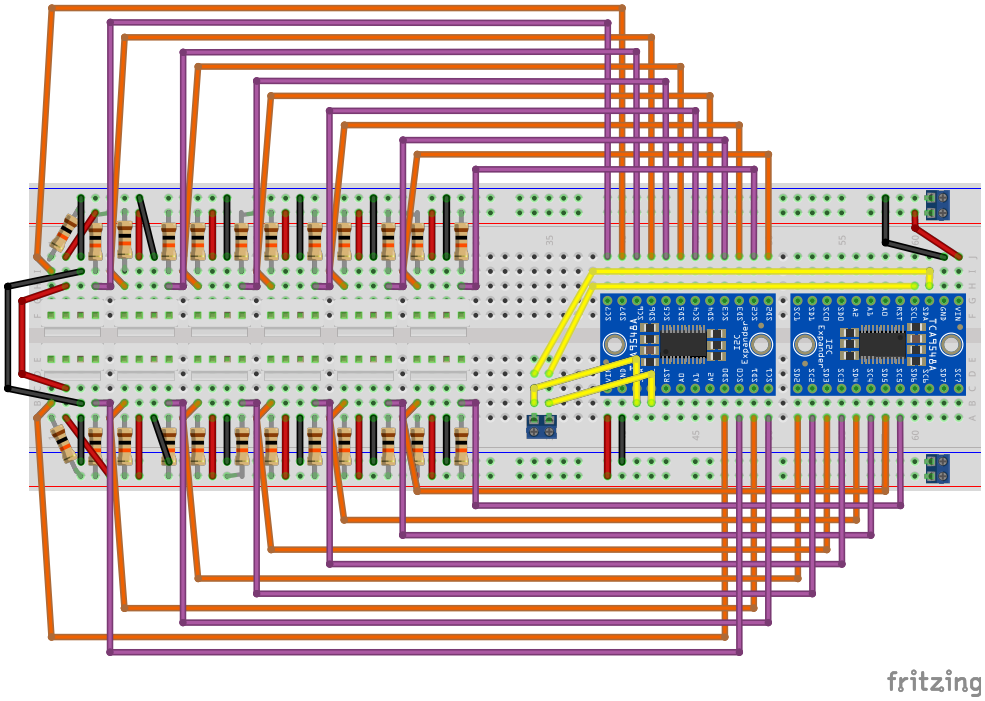

Figure 3.19: The wiring diagram and component layout for the 12-flow meter I_2C-multiplexing breakout board.

daughter multiplexer boards were soldered to headers, keyed to prevent placing the component in an inverted orientation.

3.2.3.3 I_2C Bidirectional Level Shifter

The I_2C communication lines coming out of the multiplexing breakout board are at a 3.3 V logic level; however, the microcontroller interfacing with the sensors operates at a 5 V logic level. Therefore we needed to employ a bidirectional logic level shifting device to allow for communication between the flow sensors and the microcontroller. We utilized a 4-Channel I_2C-safe Bidirectional Logic Level Converter (Adafruit 757) to accomplish this conversion, Figure 3.20. The low-voltage side of the converter was wired to the 3.3 V power supply, digital ground (D ⏚), and I_2C data and clock lines coming out of the multiplexing board. The high-voltage side of the converter was wired to the 5 V power supply, digital ground (D ⏚), and I_2C data and clock line going into the micro controller.

The level-shifter board was mounted in a DIN rail-compatible breakout board (Winford Engineering DTA3514) with the use of soldered male headers and matching female headers soldered to the breakout board. The breakout board made it possible to easily and securely interconnect wires to the level-shifter between other system components.

3.2.3.4 Readout Microcontroller (Arduino)

In order to readout data from the flow sensors an I_2C-compatible microcontroller, Figure 3.21, was needed to send commands to each of the sensors, receive data from them, and

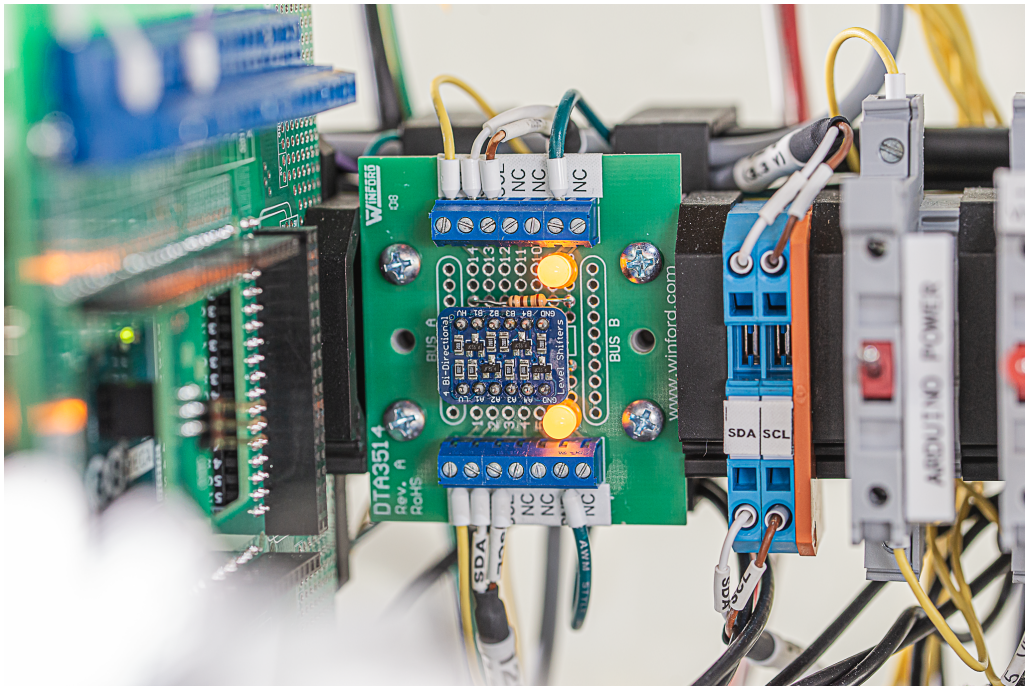

Figure 3.20: The I_2C communication signal level was modulated from 3.3 V sensor-side to 5 V Arduino-side. Photograph of the mounted bidirectional level shifting board for I_2C communication.

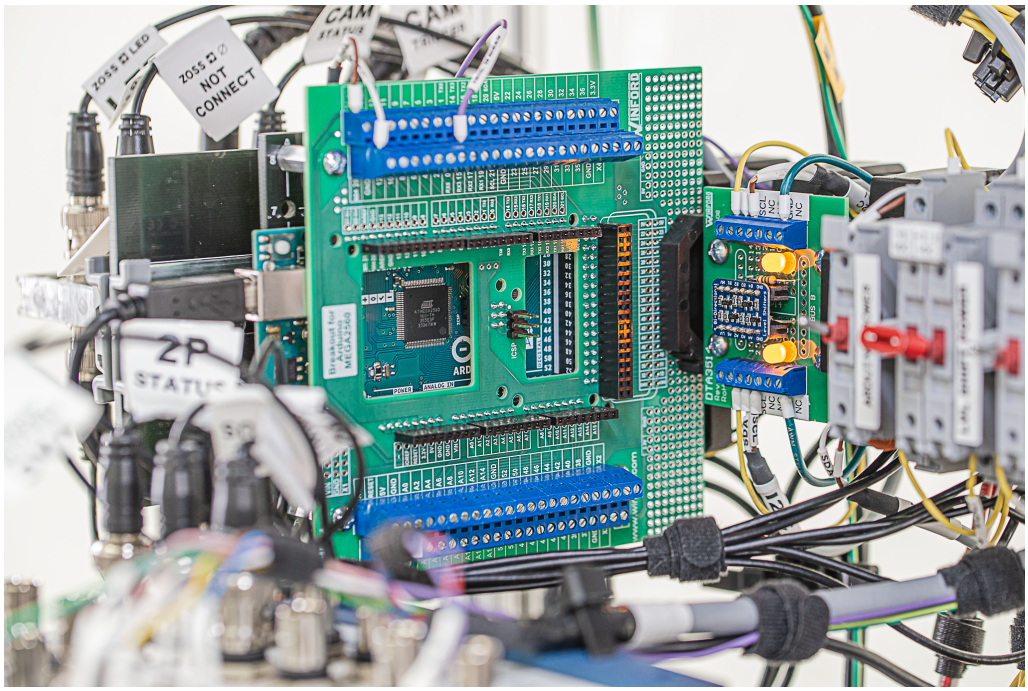

Figure 3.21: We used an Arduino microcontroller to handle low-level communication, initial data processing, and serial data transmission of the flow sensor readings. Photograph of Arduino readout microcontroller mounted in DIN rail-mount bracket.

Figure 3.22: We utilized ten solenoid valves to control flow through each of the odor stimulation lines. Photograph solenoids mounted in the stimulation cart for fluid line control.

the format that data. We utilized an Arduino (Arduino Mega 2650) for this purpose. We connected the 5 V logic level I_2C data and clock lines into the Arduino Mega's corresponding SDA and SCL inputs. The Arduino was powered with 12 V power rails and ground connections from the stimulator cart's power distribution system. A detailed breakdown of the sensor readout and flow data communication scheme is described in the Sensirion datasheets.[1]

3.2.4 Flow Routing and Control

Upstream from the flow sensors are an array of 10 solenoids and 2 needle valves for flow control. The fluid connection between the flow sensors and flow control devices are made with short runs of microfluidic tubing terminated with male 1/4″-28 compression fittings and ferrules. The needle valves are controlled manually, while the solenoids are controlled electronically by the stimulation system control computer via an intermediate solenoid control board.

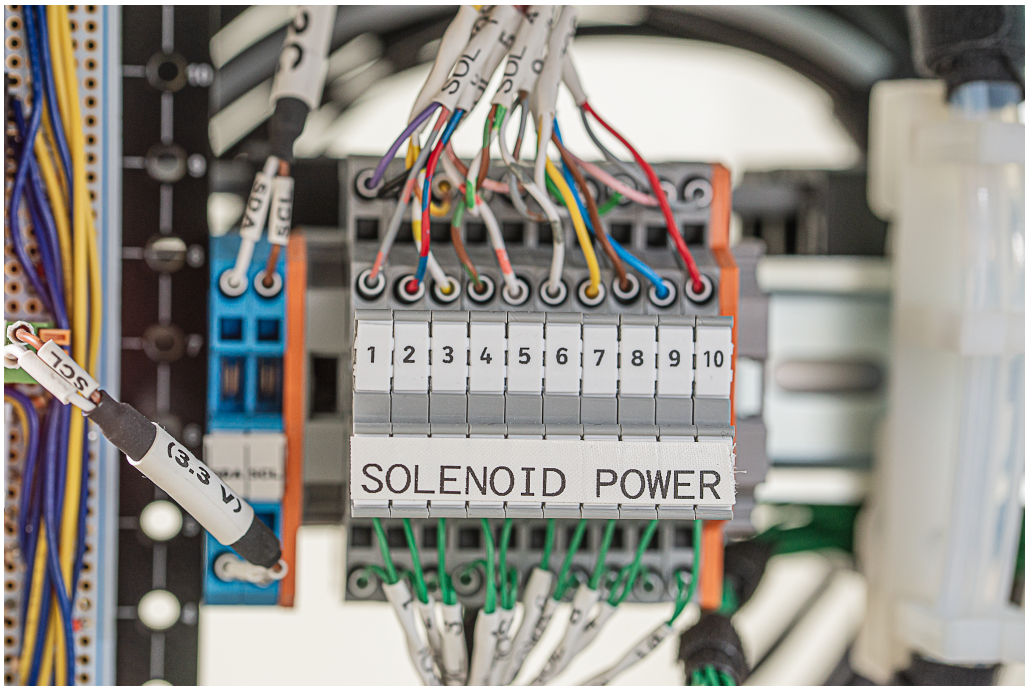

Figure 3.23: DIN-rail mounted terminal blocks were used throughout the system for making secure, testable, and re-configurable electrical connections. Photograph of solenoid terminal block for distribution of power signals.

3.2.4.1 Solenoids

The 10 solenoids (Masterflex 01540-01) are used to control flow along each of the 10 odor lines, Figure 3.22. The solenoids are "normally clossed" and require a 12 V signal across the two input leads to open the valves. The input leads for each solenoid are wired into two-terminal, two-circuit terminal blocks (one terminal block for each solenoid) for securely routing power connections, Figure 3.23. The solenoids' wetted surfaces are entirely PTFE. The array of 10 solenoids were mounted in a bracket (custom in-house) on threaded steel standoffs at equal spacing to the flow sensor array. The standoffs and brackets were sized such that the input port into each flow sensor was co-linear with the output port of each solenoid.

3.2.4.2 Solenoid Control Board

The solenoid control board is a printed circuit board (custom in-house) along with electronic components for converting between logic-level 5 V TTLcontrol signals and 12 V solenoid power signals for 10 solenoids. This board enables logic-level TTL pulses to actuate each of the solenoids. The control board is powered by 12 V rails connected to the stimulator cart's power distribution system. The logic-level inputs are wired to the board through a 10-wire cable from the NIDAQ's digital output port. The solenoid power

[1] Datasheets for the Sensirion SLF3S-1300F can be found at https://sensirion.com/media/documents/6971528D/63625D22/Sensirion_Datasheet_SLF3S-1300F.pdf in § 4 Digital Interface Description.

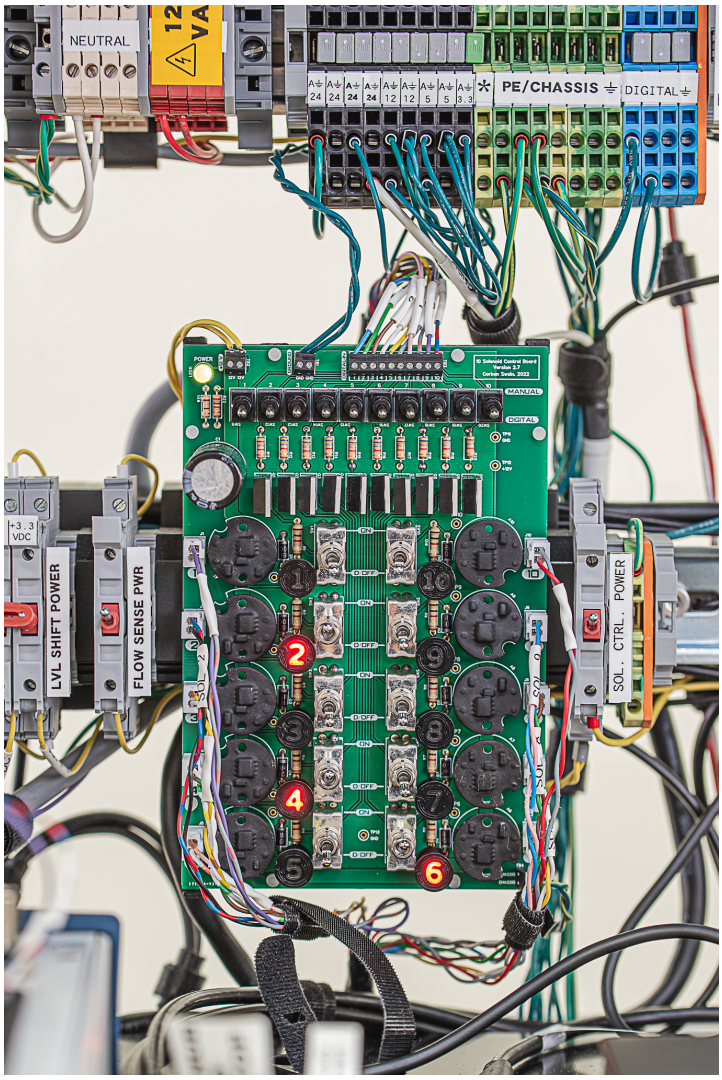

Figure 3.24: A custom fabricated solenoid control board allowed for manual and digital control of solenoid state as well as solenoid monitoring. Photograph of custom fabricated solenoid control printed circuit board with components and connections.

outputs are wired through 10 2-position JST-XH connections, a 20-wire cable carries the power-ground wire pairs to be distributed to each solenoid through the two-position, two-circuit terminal blocks.

The basic circuit for each signal converter consists of an NPN Darlington bipolar transistor (TIP20G) which is gated by the logic-level TTL signal (connected to the base) and gates the negative end of each solenoid's power input (connected to the collector) to a ground connection (connected to the emitter). There is also an indicator LED for each circuit which is powered in parallel to the corresponding solenoid. Each LED is shrouded with a filter which allows each LED light to illuminate translucent numeral corresponding to the odor line number that is active. Each circuit also has two switches, one switch enables and disables the digital control input while the other switch allows for manual powering of each solenoid.

3.2.4.3 Needle Valves

A pair of needle "micro-metering" valves (Idex P-445) controls the flow rate through the wash and vacuum lines. The needle valves have female 1/4″-28 inlet and outlet ports for making fluidic connections. The valves enable control from 0 – 50 mL min^{-1} at the typical operating pressures used for our system. The valve is controlled manually with a small knob. Each valve is mounted on to the stimulator cart's framing structure with a bracket (custom in-house). Fluidic connections are made downstream of each valve to the corresponding flow sensor and upstream of each valve to the pressurized fluid reservoir/collection vessels (see §3.2.5).

3.2.5 Fluid Reservoir and Collection

Upstream from each of the solenoids and valves are vessels which hold (or collect) the liquid solutions delivered through each of the lines. We utilized 10 120 mL bottles (Corning 1399-125) for each of the odor lines, 1 1 L bottle (Corning 1399-1L) for the wash line, and 1 3.5 L bottle (Corning 1395-3X) for vacuum collection, Figure 3.25. The bottles were all glass bottles with standard GL45 threaded tops.

To facilitate pressurization and fluid connections each of the bottles was fitted with adapter lids capable of sealing each bottle and connecting and making plumbing connections. The150 mL odor line bottles were fitted with tops having 4 female 1/4″-28 ports (Cole-Parmer EW-12018-05), while the wash water and vacuum collection bottle were fitted with tops having 3 tube adapter ports. The connections on the wash and vacuum tops were made with direct-to-tube compression fittings (Duran 1129814, GL45 connection system).

For each of the odor lines the bottle top was connected to a 1/32″ ID outlet tube arranged with the ferrule ≈ 4″ above the end of the tube, such that when the fitting was tightened the end of the outlet tube reached the bottom of the bottle (i.e. below the liquid level when the bottle is filled). The bottle for each odor line bottle was also connected to and air pressure manifold (see §3.2.6) with a 1/16″ ID tube. The remaining two ports the bottle top for each odor were sealed with male 1/4″-28 plugs.

For the wash line, the 1 L bottle was connected with a 1/16″ ID outlet tube to the downstream needle valve, an air pressure inlet was also connected with a 1/8″ ID tube, the third opening was sealed. For the vacuum line, the 3.5 L bottle was connected to the vacuum needle valve with 1/16″ ID tube, to the vacuum manifold (see §3.2.6) with 1/8″ ID tube, and to an downstream auxiliary vacuum line with 1/8″ ID tube.

The reservoir bottles for the odor and wash lines were held in a metal bead bath at ≈ 37 °C at this temperature the fluid was ≈ 28 °C by the time it reached the stimulation endpoint. The vacuum collection bottle was mounted directly to the cart framing using a pair of cradle brackets (custom in-house) and a hook-and-loop cinch strap.

Figure 3.25: Water was continually cycled through the larva's dish to reduce the build of of odors in solution, a vacuum line and collection vessel served to withdraw water from the dish. Photograph of vacuum collection assembly.

3.2.6 Air Handling

The next upstream subsystem of components is the air handling subsystem. This subsystem can be divided into three independently regulated partitions, the odor pressure partition, the wash pressure partition, and the vacuum partition. All downstream components connected within on of these partitions is regulated to have the same pressure.

3.2.6.1 Odor Pressure Partition

The odor pressure partition begins with an input air line (common to both the odor and wash pressure partition) which is routed into a high precision regulator (McMaster-Carr 6162K1). This regulator allows for fine pressure control over the range 2 – 120 psi. The output of this regulator is then routed via pipe fittings to both an electronic (McMaster-Carr 3160T183) and an analog pressure gauge (McMaster-Carr 4003K81, 0 – 30 psi) as well as to a 3-position control valve. The 3-position control valve can either turn the pressure (1: OFF) off sealing the downstream system, (2: VENT) vent the downstream system to the atmosphere through a muffler, or (3: ON) turn on the pressure connecting the regulator's output to downstream components (ON). From the control valve the odor air line is routed through tubes to a 16-port distribution manifold with a pair of 8-port manifolds (McMaster-Carr 5779K389) connected by a $1/8''$-NPT pipe nipple (McMaster-Carr 5779K389). Each of the 10 $1/16''$ ID air lines which form each odor bottle are connected into

this manifold which supplies the same air pressure into each bottle to power flow whenever a line's solenoid is opened. The remaining 4-ports on the manifold are sealed with 1/8″ OD push-to-connect plugs.

3.2.6.2 Wash Pressure Partition

The wash pressure partition is nearly identical to the odor pressure partition taking the input air line and regulating it, albeit with a lower pressure regulator (2 – 25 psi, McMaster-Carr 6162K13). Since the resistance in the wash line is lower the required pressures are much lower to maintain the necessary flow rates. There is also a similar 3-position control valve to control the downstream pressurization state. However, the output of the valve is routed to a much smaller 4-position distribution manifold with 1/4″ OD push-to-connect output ports (McMaster-Carr 5203K943). These output ports connect to the wash reservoir bottle and other auxiliary systems requiring pressure.

3.2.6.3 Vacuum Partition

The vacuum partition follows a similar architecture to the odor and wash pressure partitions. The vacuum partition begins with an input vacuum supply line which is routed through a vacuum regulator (Cole-Parmer EW-00910-10) which controls the pressure over the range 0 – 29 mmHg. The regulated vacuum partition is monitored with both digital and analog vacuum gauges. The regulated output is passed through a 5 µm-particle filter (McMaster-Carr 4274K92) to catch any moisture or particles which make their way into the line from the downstream suction. From the particle filter, the output is pass through a 3-position output control valve, which can route the downstream vacuum partition to either (1: ON) the vacuum source, (2: OFF) sealing the downstream partition (OFF), or (3: VENT) venting to the atmosphere through a muffler. The control valve's output leads to the 3.5 L collection bottle through a 1/4″-OD tube.

3.2.6.4 Supply Line Control

Each of the previously discussed partitions initially is supplied with pressure source from a supply line. Both the pressure and vacuum supply lines are passed through identical control structures to allow for turning on and off as well as venting the entire system (particularly used at system shutdown and startup). The input line is first connected into to an on-off valve. Then that valves output is routed into a diverting valve with shut-off which can either connect the downstream system to the supply, seal the downstream system, or vent the downstream system to atmosphere through a muffler.

3.2.6.5 Digital Pressure Sensors

There are three digital pressure transmitters employed for each pressure partition. These transmitters have a digital display and can be connected for power and data signals through a 4-pin micro M12 connection, Figure 3.26. Two pins of this connection supply +12 V

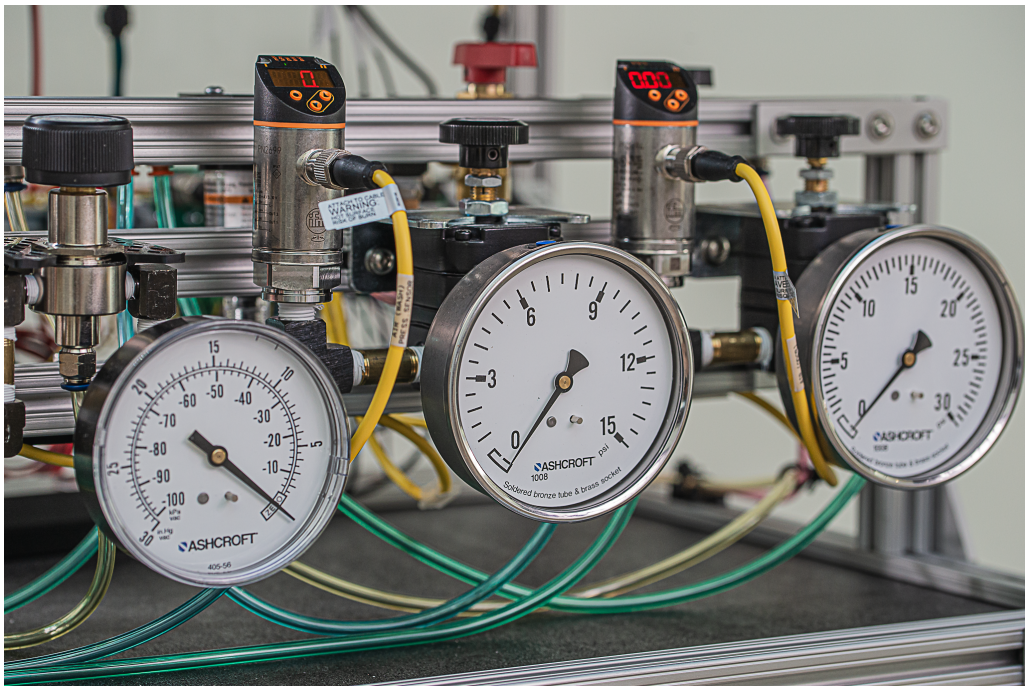

Figure 3.26: We used air pressure/vacuum to drive the fluidics of the stimulation system; analog pressure gauges as well as digital pressure transmitters allowed us to consistently set the pressures for each manifold and to log the system pressures over time. Gauges are for the vacuum manifold, wash manifold, and odor manifold from left to right.

and ground power connections, while one of the other pins is configured to transmit the measured pressure level via a voltage signal between 0 – 10 V (the transmitter can be programmed to map a particular pressure range to the 10 V output voltage range). The transmitters micro M12 connector is wired into a DIN-rail mount breakout board (Winford Engineering BRKGM12A-4FS-DIN) to which wires are connected for supplying power from the stimulator cart's power distribution system (see §3.2.8) and the voltage signal is coupled into a BNC-terminated coaxial cable for transmission to the NIDAQ for readout into the stimulation control computer.

Mounting note: All of the air handling components are mounted to the stimulator cart's framing with a combinations of brackets and metal pipe fittings (those fittings serving both a structural and functional purpose).

3.2.7 System Integration

The different subsystems, data streams, and control boards needed to be integrated into a centralized place to orchestrate control and monitoring. The main integrating components we use are a multi-functional acquisition and control input/output device, a control computer, and a software "virtual instrument."

3.2.7.1 Hardware Integration Device

The main piece of hardware we employed for integration is a USB multi-functional analog and digital input/output device (National Instruments NI USB-6229), Figure 3.27. Inputs

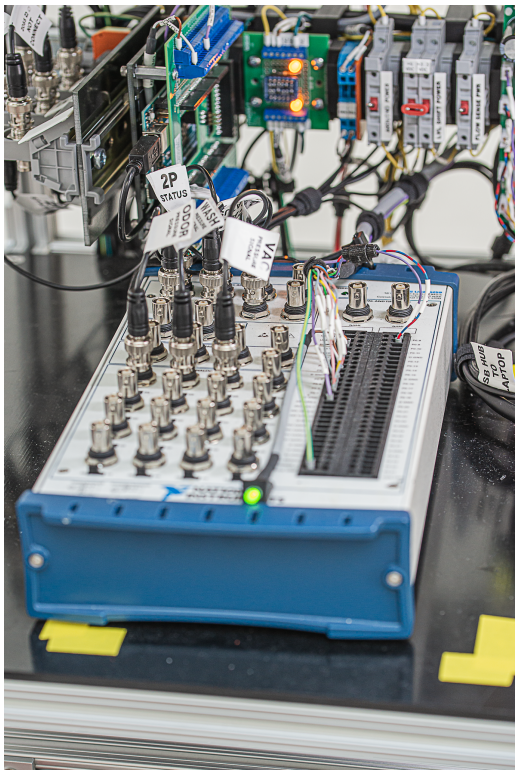

Figure 3.27: Digital and analog control inputs and outputs were handled with a National Instruments USB-6229 device. Photograph of the multi-functional acquisition and control input/output device with system connections.

from and outputs to the different subsystems are as follows:

- 10× Digital Outputs (wire leads) – Control signal to solenoid control board (§3.2.4.2). 5 V TTL digital level raised high sends 12 V to the hit-and-hold circuit and/or solenoid on that corresponding line.
- Digital Output (BNC) – Synchronization signal, which gets distributed to the infrared imaging camera and to the two-photon imaging system. 5 V TTL signal raised high triggers acquisition for downstream devices.
- 3× Analog Inputs (BNC) – Analog voltage pressure readings (0 – 10 V from the odor, wash and vacuum manifold pressure transmitters (§3.2.6.5)
- Digital I/O (USB) – Connection to the control computer (§3.2.7.2) and thereby the virtual instrument (§3.2.7.3)which enables the virtual instrument to interface with the hardware inputs and outputs.
- Digital Input (BNC) – Acquisition signal from two photon imaging system. 5 V TTL digital level raised high at the beginning of each scan acquisition.
- Digital Input (BNC) – Acquisition signal from the infrared imaging camera. Similarly, 5 V TTL digital level raised high at the beginning of each frame acquisition.

- Digital Input (BNC) – Manual 5 V TTL signal from momentary switch mounted to control cart for miscellaneous use and system testing.

The I/O Device also takes a 24 V power input via a DC barrel connector supplied from the cart's power distribution system. The device's chassis ground is connected to the cart's chassis ground, the device's AI ground is connected to the cart analog ground, and the device's digital ground is connected to the cart's digital ground.

3.2.7.2 Control Computer

The control computer, as additional hardware for integration the stimulation system, runs the virtual instrument(see §3.2.7.3); stores, reads, and writes, system configuration files; logs instrument data; communicated with the Arduino microcomputer (see §3.2.3.4) and facilitates acquisition, monitoring, and video storage from the infrared imaging camera. We use a 6-core, Intel, workstation-grade laptop (Lenovo P1 Gen3) with 3 TB of storage and 32 GB of memory. The laptop connects to the multifunctional I/O device (via USB) the infrared camera (via USB), the Arduino microcomputer (via USB), and a secondary monitor (via HDMI) used for visual feedback during the alignment procedure.

3.2.7.3 Stimulation Control and Monitoring Virtual Instrument

To orchestrate the monitoring and operation of all the different stimulation system components we developed a custom "virtual instrument" (VI, e.g. a LabView program which allows for performing arbitrary interconnected operations programmed visually in a "block diagram" and provides user interface "front panel" for interacting with and controlling those operations when the program runs). Our VI provided functionality needed to

- Define and visualize the solutions in each odor reservoir. The VI also enabled us to be able to save the odor configuration in a machine readable format.
- Define, visualize, and save the way each odor line is connected to the left, middle and right stimulator manifolds.
- Define, visualize, and save the sequence of stimulation (i.e. delivered odors) to be performed over time through the three-manifold stimulation system.
- Trigger two-photon imaging, and behavioral imaging synchronous with stimulation.
- Log and summarize the metadata about each experiment such that multiple imaging runs can be identified and correlated in post processing.
- Monitor stimulation progress over time.

We summarize our VI with these bullets (the VI code is contained in the dissertation repository Appendix A).

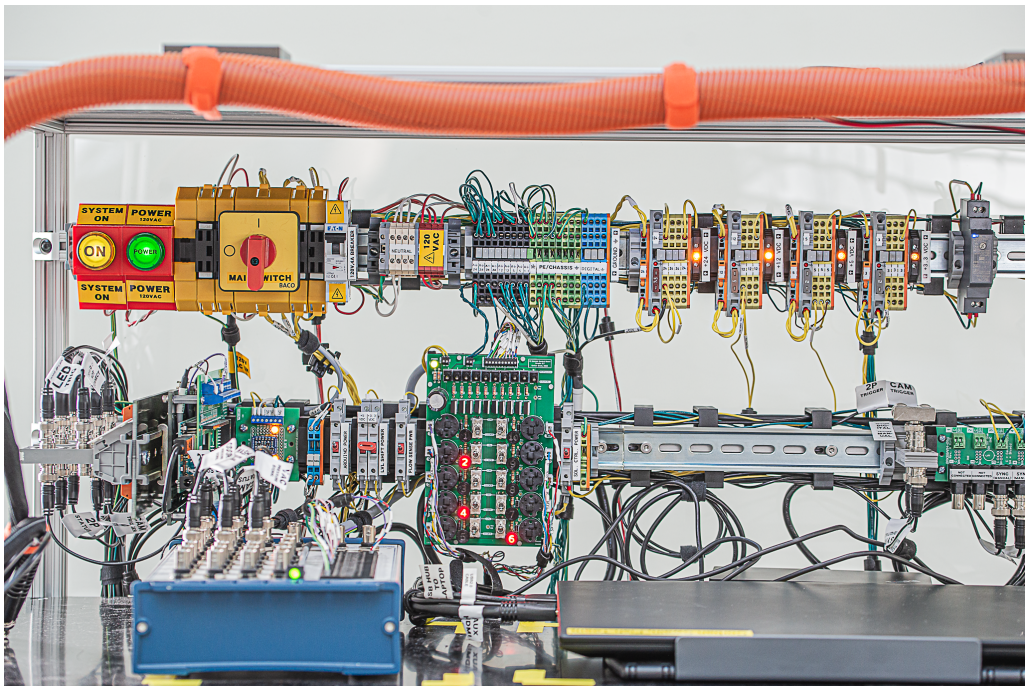

Figure 3.28: The top-level of the stimulation cart housed the power distribution subsystem as well as the control computer and many other electronic components.. Photograph power distribution terminal blocks, wiring and related components.

3.2.8 Power Distribution

Many of the components described above require DC power at various levels to function as previously mentioned throughout. The stimulation system has 4 primary DC power rails: 24 V, 12 V, 5 V, and 3.3 V as well as an 120 V AC power rail, Figure 3.28. The flow for power distribution is described over the following subsections:

3.2.8.1 120 V AC Distribution

120 V AC power is routed from the mains in parallel into a "POWER" indicator light and a multi-pole disconnect switch (Baco 0172002 with various auxiliary contact blocks) with the ground connection routed to be permanently maintained. the output of the disconnect switch is routed into terminal blocks for the "hot", "neutral", and "ground" connections distribution. The hot line is routed into a 4 A circuit breaker (McMaster-Carr 7026K6/4A) before distribution. The ground line is connected to the "*" ground which is the central connection where the digital and analog grounds converge.

3.2.8.2 DC Conversion and Distribution

The 120 V power is then distributed out of the corresponding terminal block connections to three AC-to-DC power supplies: 24 V (McMaster-Carr 7009K82), 12 V (McMaster-Carr 3670N19), and 5 V (McMaster-Carr 3670N14). The positive output of each of these AC-to-DC power supplies is routed in series through a fuse, an LED indicator light, and a knife disconnect terminal block before passing into a set of commoned terminal blocks for

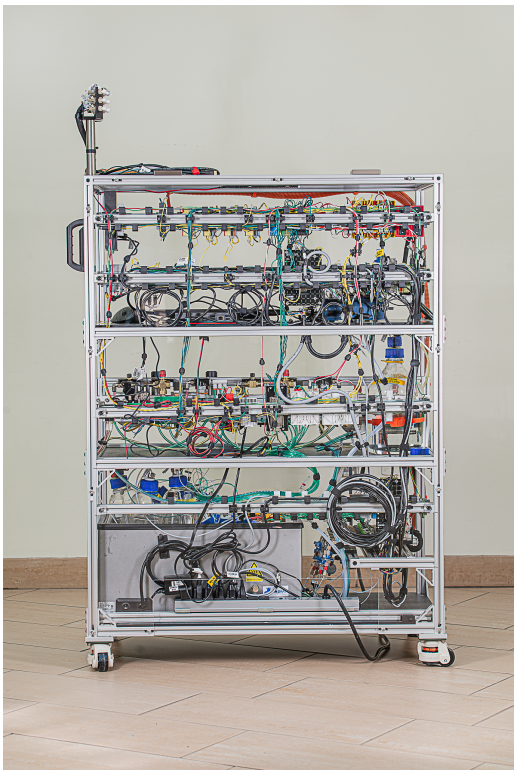

Figure 3.29: Extensive wiring was required to connect power and data between all of the different subsystems; it was organized and bundled along the rear of the stimulator cart. Photograph of wiring runs at on the back of the cart.

distribution at the given DC level. The negative output of each of these AC-to-DC power supplies is routed directly to analog ground. The 3.3 V power level is produced through a DC-to-DC power supply (Mean Well DDR-15G-3.3), the input to this power supply comes from the +12 V distribution and analog ground. The output of this power supply is routed identically to the AC-to-DC power supplies into a set of commoned 3.3 V terminal blocks.

3.2.8.3 Wiring

Most electrical connections were made with ferrule-terminated stranded copper wire according to the following convention:

- **Gauge and Multiplicity.** Generally, digital lines utilized a single 22 gauge wire. Analog or DC power supply lines expected to carry < 0.5 A utilizes a single 22 gauge wire. Analog or DC power supply lines expected to carry < 2.5 A utilized a single 18 gauge wire. Analog or DC power supply lines expected to carry < 10 A utilized a pair of 18 gauge wire. 120 VAC power supply distribution lines utilized a single 18 gauge wire. Current return paths and device ground connections utilized a wire configuration of matching gauge. Chassis ground connections for the cart utilized 18 or 14 gauge wire.
  Generally these guidelines applied to the system wiring; some terminal blocks would not accept ferrule-terminated 18 gauge wire, so a pair of 22 gauge wires might be

used (e.g. the solenoid control board power rails and chassis ground connection). Additionally some connections utilized cables rather than individual wires to make wiring runs more compact.

- **Color.** Red: 120 VAC, white: neutral (from AC mains), green: AC or DC ground, black: digital ground, green and yellow: chassis ground, yellow: DC power (+), purple: analog signal, blue: digital signal.

Some connections were made using cables with multiple conductors; at the cable ends the sheathing was stripped and each conductor was ferrule terminated for durability.

3.2.8.4 Mounting

All of the electrical power distribution components (along with most other electronics) were mounted along multiple rows of standard top hat DIN rails mounted to the rear of the stimulator cart.

3.2.9 Stimulation Cart Framing

All of the components outlined upstream of the umbilical are mounted and housed within the stimulator cart, Figure 3.30. The stimulator cart is 5′ tall, 3.5′ wide and 22″ deep and has three internal shelves. The cart's framing structure is made from 1″-square t-slotted aluminum extrusions (80/20 10-series products) and brackets to hold the framing members together. Each of the shelves and the top of the cart are covered with plastic boards to create the shelf surface. The cart is fitted with 4 leveling casters which allow for rolling the cart easily as well as lifting the cart onto leveling pads that lift the cart off of its wheels.

The lower shelf holds the heat bath (filled with dry beads) which contains all of the odor bottles and the wash bottle. The lower shelf is fitted with a bracket to hold the solenoids, flow sensors, and the upstream bulkhead panel (see §3.2.2). There is also a DIN rail at the back of the lower shelf which holds the I_2Cmultiplexer breakout board, solenoid power terminal blocks, and the brackets for routing tubes. The lower shelf also houses a flush system for clearing all of the fluid lines.

The middle shelf holds all of the air handling components mounted on a series of parallel brackets as well as the 3.5 L collection bottle. The DIN rail at the back of the middle shelf holds all of the AC-to-DC converters and a separate power distribution system for powering the cart's lights.

The upper shelf holds many of the electronics of the system including the stimulation control computer, the computer's docking station, and the NIDAQ. The upper shelf has two rows of DIN rails which holds system pilot lights the primary power disconnect switch, most of the power distribution and grounding terminal blocks, the solenoid control board, Arduino Mega and its break out board, and I/O BNC connections.

The top of the cart can hold miscellaneous items and can also be adapted to mount the stimulation endpoint platform when needed.

Figure 3.30: The olfactory stimulation cart fully assembled is allows for use of the stimulation system at different locations and microscopes. Photograph of the stimulator cart and framing.

3.3 Results

We demonstrate the first known invention, construction, and application of a three-direction, ten-channel waterborne chemical delivery system utilized to stimulate the olfactory epithelia of larval zebrafish with lateral independence Figures 3.31 and 3.33. We performed a number of validation experiments to determine the quality of operation and control which we were able to achieve and to identify any areas for further optimization and improvement.

As designed, the air pressure of the odor manifold could be adjusted to set the nominal flow rate achieved through the stimulator needle when the solenoid was open. For example, using the pressure regulator we could adjust to a flow rate of $\approx 0.2\,{}^{\mathrm{mL}}/_{\mathrm{min}}$ out of the needle with a pressure of 135 kPa in the odor manifold, to $\approx 0.1\,{}^{\mathrm{mL}}/_{\mathrm{min}}$ with 92 kPa, and to $\approx 0.045\,{}^{\mathrm{mL}}/_{\mathrm{min}}$ with 41 kPa.

By utilizing the flow sensors in-line with each odor channel, we observed the kinetics

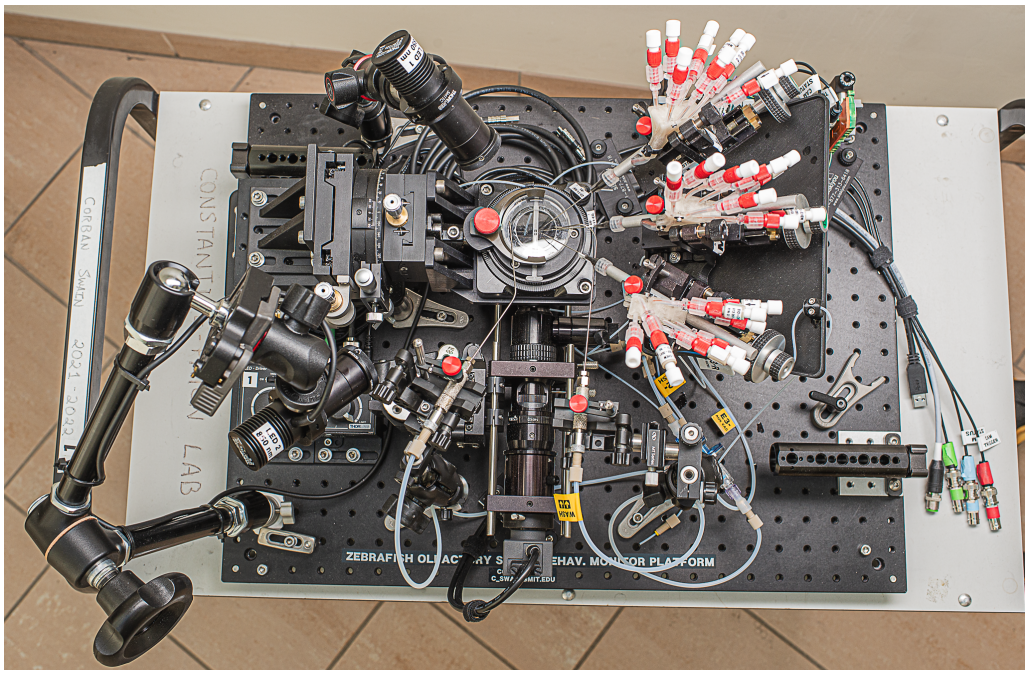

Figure 3.31: The olfactory stimulation platform enabled multi-directional olfactory stimulation and imaging of a zebrafish larva through the integration of many hardware components.

of flow upon solenoid opening and closing Figure 3.32A, D. Upon solenoid opening, we observed an almost immediate transient response within 100 ms followed by a sigmoidal rise to the target flow rate within ≈1 s. Upon solenoid closing, we similarly observed an immediate transient spike in flow rate within 200 ms which then settled to 0 mL min^{-1} within 400 ms. We also observed some transitions where the flow rate either started or ended at an intermediate flow rate—that is, neither ≈ 0 nor ≈ 0.1 mL min^{-1}—which we classified as "incomplete transitions." For the experiment shown in Figure 3.32 these incomplete transitions represent 26% of the ON and OFF transitions. For complete transition, the median transition time to 90% of the target flow rate was 650 ms for ON transition and was 440 ms for OFF transitions, Figure 3.32E.

We also analysed flow sensor data to estimate the net flow rate through each stimulation manifold/needle over the course of a simultaneously triggered ON transition on one input line and OFF transition on another input line, Figure 3.32C. We see the transient associated with solenoid closing leading to a spike in flow rate followed by a depression in flow rate due to the later rise of the odor line which was turned on (see in Figure 3.32B the ON and OFF average curves cross when both are relatively quite low). The system settles back to the target flow rate within ≈ 800 ms, Figure 3.32C, F.

We stimulated a fixed larva sample (mounted in agarose identically to a live larva) with a rhodamine B dye solution to quantify and localize the chemical delivery over time by imaging. A bright-field image of the field of view and the quantified regions shown in Figure 3.33C; temporal color projection of the two-photon fluorescence dye imaging shown in Figure 3.33D. The stimulation sequence is depicted in Figure 3.35A. Fluorescence traces at the needle output and the olfactory epithelia show dye concentration follows a low-passed

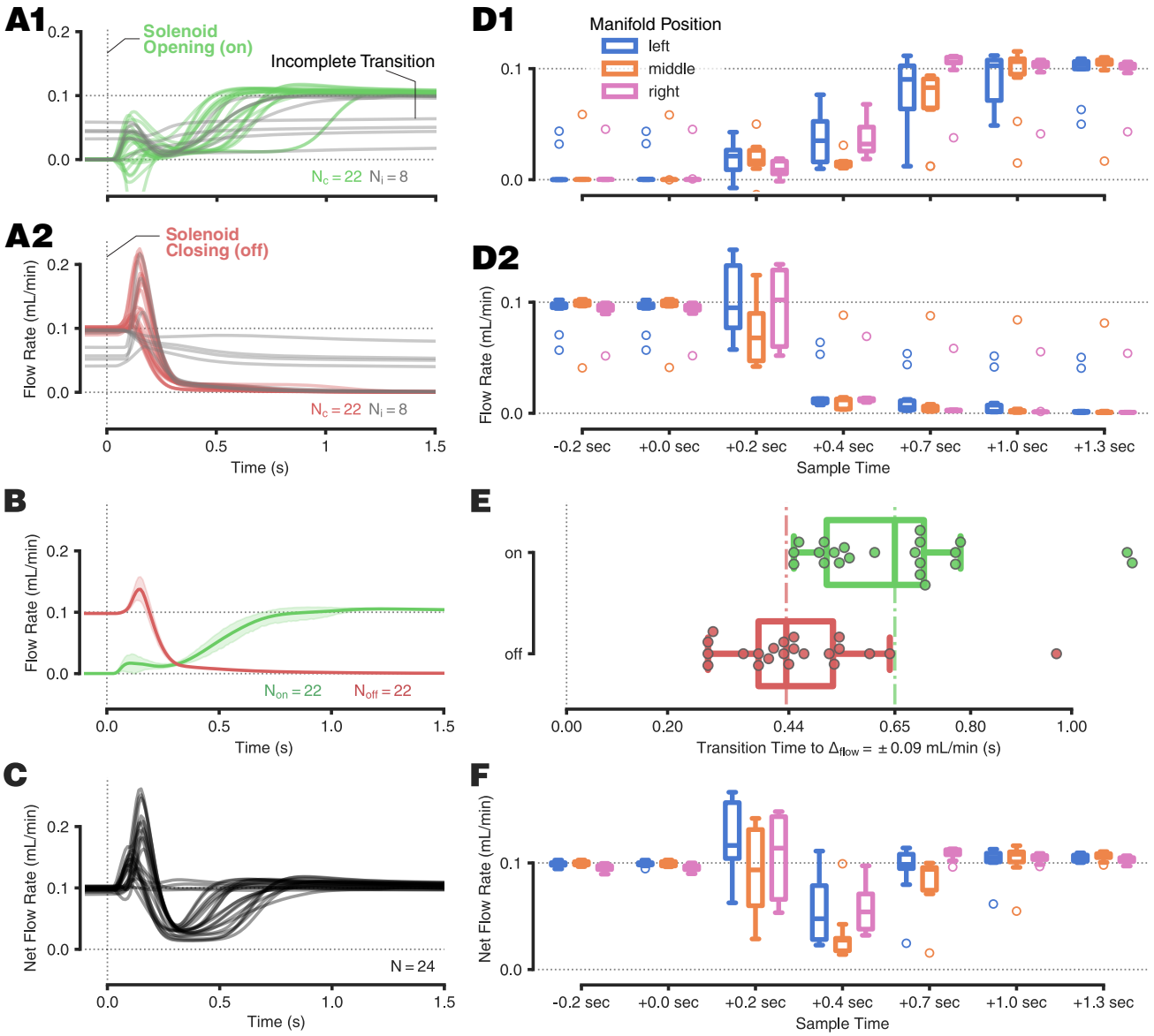

Figure 3.32: Flow rates at the solenoid output show transitions from off to on (and vice versa) occur within 1 s for most trials with some transient irregularities. **A**: Line plots of flow rate vs. time across 30 trials as the solenoid was sent a signal to open—**A1**, *on* transition, green—or close—**A2**, *off* transition, red—at $t = 0$ s (vertical dotted line). Odor manifold air pressure was adjusted* so that nominal *on* flow rates were 0.1 mL min^{-1} (horizontal dotted line). Trials plotted in color show transitions where the flow rate successfully completed a change between states within 1 s (N_c), while trials plotted in gray show incomplete transitions (N_i). **B**: Flow rate vs. time averaged across the 22 successful switching trials for the on transition (green) and the off transition (red). Shaded regions represent 95% confidence intervals on the mean. **C**: Flow rate vs. time across 24 trails of the *net* flow rate through a stimulation manifold (see §3.2.1.2) at the time of a transition signal at $t = 0$ s as estimated by summing all flow rates into the manifold at each time point. **D**: Box-and-whisker plots showing the distribution of flow rates at different time-points relative to the time of solenoid opening (**D1**) or closing (**D2**). At each sampled time point (x-axis), the average flow rate over a window of 70 ms was taken for each transition at each manifold position (left: blue, middle: orange, right: pink). **E**: Box-and-whisker plots comparing the time for the flow rate to rise to 0.09 mL min^{-1} (on, green) from 0 or to fall to 0.01 mL min^{-1} (off, red) from 0.1 (i.e. a 90% change) across the 22 successful switching trials (incomplete transitions were excluded). The median times for these transition are shown with the corresponding vertical dash-dot lines and tick labels. **F**: Same as **B**, however boxplots show the net flow at each of the sampled time-points.

*Note: Data for this figure were extracted from flow sensor readings during 5 trials of the dye pulse system evaluation experiment (see Figure 3.35A). For all box-and-whisker plots, center line: median, box: 25%–75% interquartile range (IQR), whisker: 1.5 × IQR, points: values outside whiskers (all points shown in **E**). *Nominal air pressure in the odor manifold was 10.6 psi.*

response to stimulation initiation and cessation, Figure 3.33E. For most trials, signal at one stimulation position did not significantly correlate to stimulation at other stimulation positions or to the background. This serves as one indication that stimulation of the left and right olfactory epethelia can be performed independently, Figure 3.33F. We did observe some correlation between the background signal and the left stimulator for these trials.

Looking more closely at the ON and OFF transitions as measured by flow rate at the solenoid and by fluorescence intensity at the needle output and olfactory epithelium, we can make a number of observations, Figure 3.34. We see a ≈ 2 s delay between solenoid opening and the beginning of any observable change at the needle output, Figure 3.34B. We also see that the transient spikes or depressions in flow rate at the solenoid are not observed in at the needle output and olfactory epithelia. The median time from solenoid opening/closing to transition to 50% at the needle outlet is ≈ 4 s (2 s if you subtract the onset delay); median 50% transition times at the solenoid are < 1 s. The median time to 50% transition at the olfactory epithelium is ≈ 4.6 s for the ON transition and ≈ 6.4 s for the OFF transition, Figure 3.34A. The broadest range of transition times accross is seen at the olfactory epithelium spanning about 2.5 s between quartiles, Figure 3.34A.

3.4 Discussion

3.4.1 Stimulation Experiment Designs

We utilized the olfactory stimulation system to perform evaluation experiments and to perform two first-of-their-kind bilateral olfactory stimulation experiments; the timecourses of these experiments are outlined in Figure 3.35 with detailed descriptions of each of the stimulation timecourses provided in the Figure 3.35's caption.

Figure 3.33 ***(following page)*****: Dye quantification shows our stimulation system can deliver dissolved stimulants to individual olfactory epithelia with little cross-talk.** **A:** Photograph of the stimulation endpoint with a mounted larvae under the two photon microscope objective, with each of the three stimulation manifolds and respective stimulation needles directed to the larva's olfactory epithelia. **B:** Infrared images of an agarose-embedded, head-fixed larvae with the three delivery needles directed toward the larvae. This image was take prior to final alignment and movement of the needles to their final position closer to the larvae. Scale bar = 2 mm. **C:** Bright-field micrograph of a head-fixed larvae with delivery needles directed at the olfactory epithelia. Overlaid patches depict the image pixels selected for quantifying the fluorescence at the needle outlet for each manifold position (left/top: blue, middle: orange, right: pink) and at the olfactory epithelia for each lateral side. The dashed white line encloses the non-background region, pixels values outside of this region were aggregated to produce the time-courses of background intensity (see **E** and **F**). Scale bar = 200 µm. **D:** Temporal color projection of Rhodamine B fluorescent signal over the course of a dye pulse system evaluation trial (see Figure 3.35.) Color bar depicts the temporal color code ranging from green at $t = 0$ s to red at $t = 300$ s Same fish as shown in **C**. Scale bar = 200 µm. **E:** Line plots of relative fluorescent intensity over time across four trials for each quantified image region as shown in **C**. Each region and trial was linearly normalized such that the maximum values of the trial was 100% and the minimum was 0%. **F:** Correlation heatmap showing the average correlation coefficient R across four trials between the control signal "C", the normalized flow rate "F", the image-quantified needle output "N", the image-quantified intensity at each olfactory epithelia "OE", and the image-quantified background intensity "B" for each lateral side and/or manifold position "L", "M", "R". Heatmap squares that are darker/more red correspond to pairs that are more positively correlated. Margin color bars highlight the position groups along the top and left.
Note: For the heatmap, control signal and flow rate time-courses were resampled to the time-base of the dye recordings to compute the correlations. Imaging was performed at 7.6 Hz.

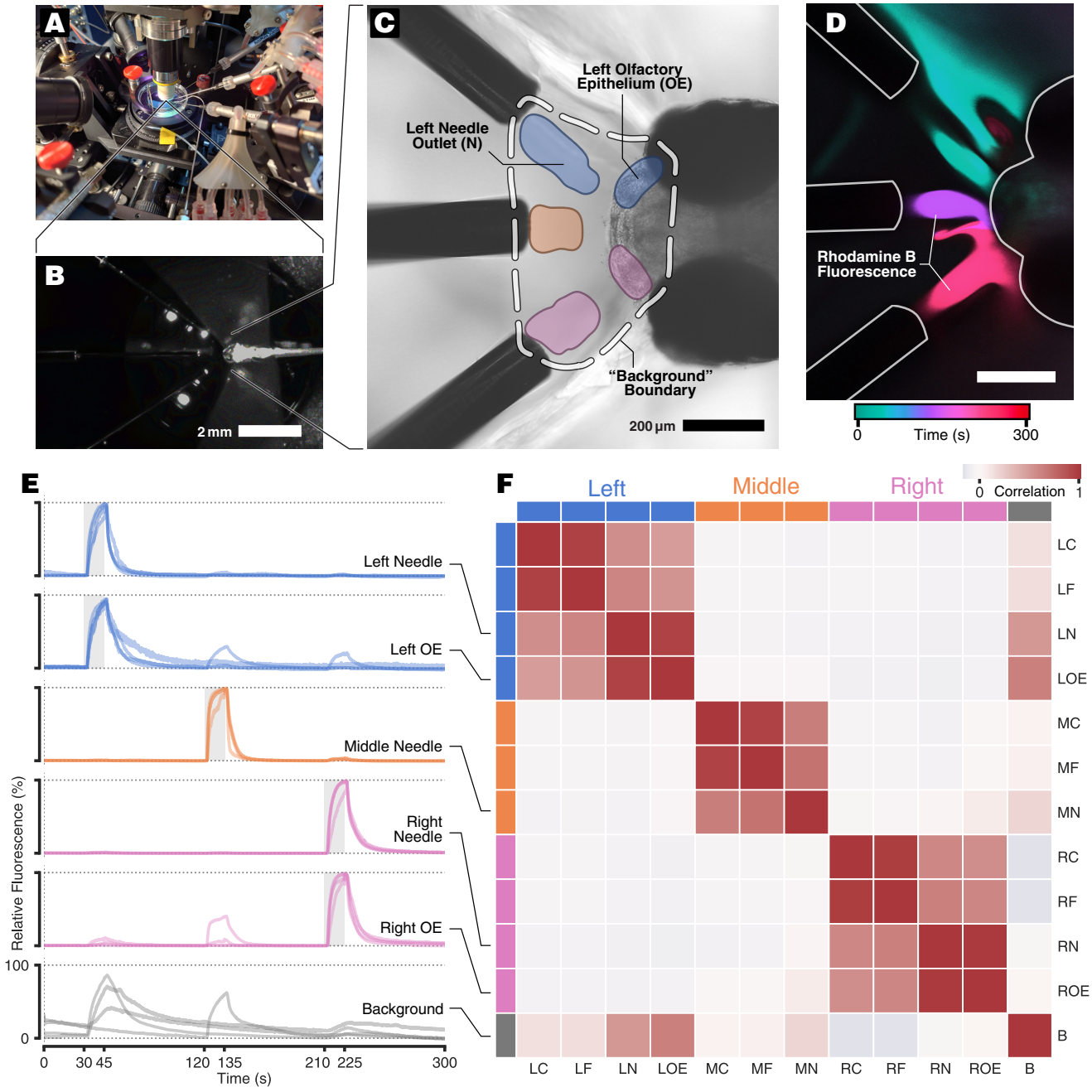
A
B
2 mm
C
Left Olfactory Epithelium (OE)
Left Needle Outlet (N)
"Background" Boundary
200 µm
D
Rhodamine B Fluorescence
0
Time (s)
300
E
Left Needle
Left OE
Middle Needle
Right Needle
Right OE
Background
Relative Fluorescence (%)
100
0
0 30 45 120 135 210 225 300
Time (s)
F
Left
Middle
Right
0 Correlation 1
LC
LF
LN
LOE
MC
MF
MN
RC
RF
RN
ROE
B

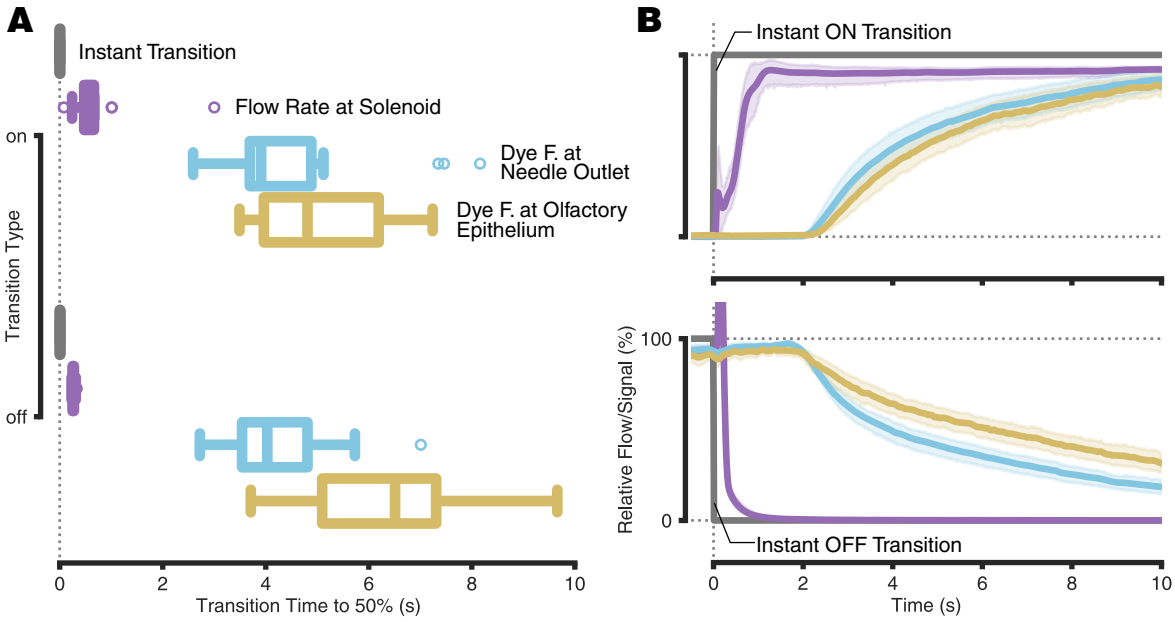

Figure 3.34: Dye quantification reveals 2 s delay between control signal and stimulus onset at the needle output and a graded increase in stimulant concentration over ≈ 5 s. A: Box-and-whisker plots showing the distribution of transition times to 50% across multiple trials for grey: a perfect transition, purple: the flow rate at the solenoid, blue: the dye intensity at the needle outlet, and yellow: dye intensity at the corresponding olfactory epithelium (i.e. left stimulation manifold to left olfactory epithelium). Transition time distribution are shown for both the *on* transition where $t = 0$ s is the time of the signal to begin dye stimulation and for the *off*. **B:** Line plots of relative flow or relative fluorescent signal over time for the same conditions as **A** and averaged across all trials. Shaded regions show 95% confidence intervals.
*Note: For all sub-figures flow rates were normalized to the scale 0–100%; dye fluorescence was normalized to the maximum value across time for each recording (see Figure 3.33 for how dye fluorescence over time was obtained) such that value range went from 0–100%; data was obtained from dye pule system evaluation experiment as described in Figure 3.35A For all box-and-whisker plots, center line: median, box: 25%–75% interquartile range (IQR), whisker: 1.5 × IQR, points: values outside whiskers (all points shown in **E**).*

The dye pulse system evaluation experiment, Figure 3.35A, was performed to evaluate and quantify the systems performance is discussed in this section and shown in Figures 3.33 and 3.34. This experiment where dye is delivered to the larva from three different directions in succession is the first reported of its kind, only possible with our stimulation system.

The tactile pulse stimulation experiment, Figure 3.35B, was performed as a validation experiment for the behavioral imaging, brain imaging, and image analysis pipelines which is discussed in §4.3 and shown in Figures 5.1 and 5.2. Since the water pulses turn on and off completely (no switching) this stimulation sequence yielded a relatively strong tactile stimulation to the larva and served as a positive control for neural and behavioral readouts.

The single-odor bilateral stimulation experiment, Figure 3.35C, was performed to compare behavioral and neural responses of an odor delivered to the left olfactory epithelium only, to the right OE only, and to both OEs simultaneously. This experiment is discussed in §5.2 and shown in Figures 5.5 and 5.6. An experiment of this kind has been reported once before by Sy *et al.* so we replicated it here to compare the results. However, it is im-

portant to note that our system 1) utilized a continuous flow of fish water from the middle stimulator to isolate the stimulation streams and 2) uses positionable stimulator needles in free-water to deliver the odors, so our experiment is unique in those respects.

The dual-odor bilateral stimulation experiment, Figure 3.35D, was performed to assess the larva's response to mixtures of odors delivered at the same time, but to different OEs. This experiment is discussed in §5.2 and partly shown in Figures 5.5 and 5.6; we were unable to perform a full analysis of these experiments due to technical issues outlined in §5.3. An experiment of this kind has not been previously reported and demonstrates the type of new experiments that we will continue to explore with this stimulation system.

3.4.2 Investigating Incomplete Transitions

We described in Figure 3.32A that some actuations of the solenoid did not lead to a complete transition of the flow between the expected on and off flow rates. We will further investigate the cause of this transition issue to determine if it is caused by an issue with the flow sensors, solenoids or some other component. Two potential causes that we might predict are the following:

1. Incomplete transitions are due to a malfunctioning of the hit-and-hold circuit that we use. These circuits to between the switched 12 V power supply lines sent to each solenoid and the circuits essentially send a full 12 V pulse or "hit" of voltage to the solenoid to open it when the input 12 V signal is received, then "hold"s the solenoid open with a lower ≈ 4 V constant voltage until the input 12 V signal is turned off which prevents excess heating of the solenoid. However, it is possible that this lower "hold" voltage allows for the solenoid to partially re-close and prevents the flow rate from reaching it's maximum target value.

2. Incomplete transitions are due to the solenoids being operated a too high of a pressure. The solenoids that we are using do not have detailed datasheets, so it is possible that they are rated to only be used within a certain range of pressures which we exceed in our stimulation manifold. We will test the solenoids for reliability and frequency of incomplete transition at a range of pressures to determine if this is the cause of the issues we see and determine if we should use solenoids explicitly rated for the pressures and flow rates of our application.

3.4.3 Accounting for Fluid-Line Transmission Time

As highlighted in Figure 3.34 there is a significant ≈ 2 s delay between the signal to change odors and the onset of that transition near the larva. We will further probe the dependence of this delay on the flow rates through the line (i.e. odor manifold pressure) and develop a formula to account for this delay in either the stimulation definition, or in the post processing. In this way, we can ensure the the assumed time of stimulus onset lines up, with minimal error, to the time of onset experienced by the larva.

3.4.4 Standardization of Larva and Needle Positioning

One of the benefits of our stimulation system is that we are able to manipulate the position of each stimulation needle with micron-level precision; however, this freedom has can lead to the issue of inconsistent stimulation position, direction, and effective odor application across different larvae and experiments. As we can observe in Figure 3.33D, the flow coming out of each of the stimulation needles can have different shapes and is affected by the position of the larva and the way the agarose is cut around the larva (§4.5.3). To ensure reproducibility from experiment to experiment, particularly with respect to selective stimulation of each olfactory epithelium, we will develop a process for templating and ensuring quality at key steps in the mounting and alignment process.

For the process of larvae mounting, we will design and print a physical template which outlines the location of the fish and where to cut and remove the agarose relative to the fish. This template will be printed on translucent paper and will be placed under the dish for direct referencing when mounting the fish on the dissection microscope. For the process of aligning the stimulators, we will produce a template which can be overlaid on our behavioral camera feed to allow us to position each of the simulation needles consistently relative to the fish in x and y. To help with standardizing the z alignment we will test two different methods. 1) We reference the z-location of the zebrafish's olfactory epithelium using two photon images of the GCaMP reporter. Then we will use live imaging of a dye (with a different two photon fluorescence profile from the GCaMP) being dispensed from each stimulator in pulses to visualize and align the tip of the stimulator to a templated location relative to the larvae's OE. 2) We can utilize a camera and lens positioned in the xy-plane of the dish to image the relative z-position of the stimulation needles and utilize a template and live feed from the camera to align the stimulator needles along the z-axis.

Figure 3.35 *(following page)*: We utilized our stimulation system to perform an array of tactile and bilateral olfactory stimulation experiments. All sub-figures depict the manifold control signal time-courses for stimulation experiments. For each experiment a time-course of each active line is shown for each manifold position/stimulus direction. Grey line and shaded region represents fish water control. The colored lines and shaded regions represent dye or odorant control signal. In the context of these experiments, no more than one line is ever active at a given time. **A**: Dye pulse system evaluation (5 min long) begins with an equilibration period followed by 10 s dye (Rhodamine B, 100 µM) pulse followed by an 80 s break delivered from the left, middle, and right simulators in sequence. **B**: Tactile pulse stimulation experiment (14 min long) only utilizes the middle manifold and the fish water line begins off. After a 5 min equilibration period the fish water line is turned on for 60 s then off for 120 s. The pulse is repeated three total times per experiment run. **C**: Single-odor bilateral stimulation experiment (12.5 min long) begins with a 3 min equilibration followed by short 10 s odor pulses followed by a 60 s fish water break; pulses are delivered to left only, right only and both sides. This sequence is repeated with longer 30 s odor pulses and 90 s breaks. The middle stimulator had continuously active fish water. For these experiments the odor was one of: Cadaverine (1.3 µM), 12-amino-acid cocktail (2 µM), or a fish water negative control (but still delivered along separate lines and from separate reservoirs). We also performed a variation of this experiment where the different odor pulses were shuffled. **D**: Two-odor bilateral stimulation experiment (22 min long) begins with a 5 minequilibration followed by short pulses of odor A, then short pulses of odor B with each having a 5 s stimulation followed by a 30 s break. Then short mixed pulses with corresponding breaks are applied with odor A on the right and odor B on the left and vice versa. Then a mix-switch pulse is applied where the lateral side of the stimulant is changed with no break in between. The stimulation sequence ends with 30 s pulses with 120 s breaks repeated for each odor twice. For this experiment odor A was Cadaverine (1.3 µM) while odor B was the 12-amino-acid cocktail (2 µM).

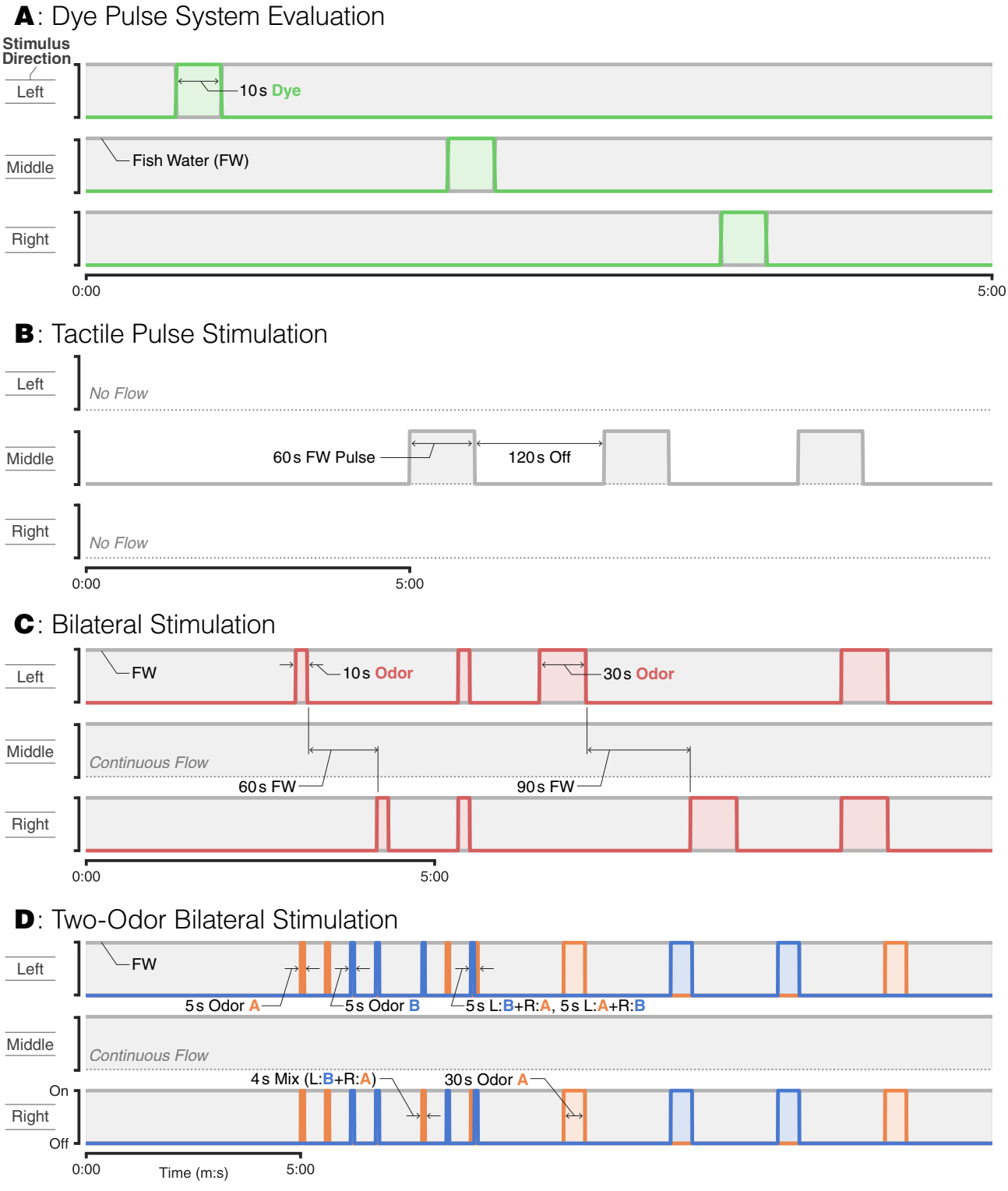
A: Dye Pulse System Evaluation
Stimulus Direction
Left
Middle
Right
10 s Dye
Fish Water (FW)
0:00
5:00
B: Tactile Pulse Stimulation
Left
Middle
Right
No Flow
60 s FW Pulse
120 s Off
No Flow
0:00
5:00
C: Bilateral Stimulation
Left
Middle
Right
FW
10 s Odor
30 s Odor
Continuous Flow
60 s FW
90 s FW
0:00
5:00
D: Two-Odor Bilateral Stimulation
Left
Middle
On
Right
Off
FW
5 s Odor A
5 s Odor B
5 s L:B+R:A, 5 s L:A+R:B
Continuous Flow
4 s Mix (L:B+R:A)
30 s Odor A
0:00
Time (m:s)
5:00

3.5 Methods

3.5.1 Defining Stimulation in Software

Before performing stimulation, we must encode the odor manifold layout and the stimulation time-course within the stimulation control software (Appendix A). We first decided on the type of stimulation experiment we want to perform, determined the odor lines and corresponding reservoirs needed to accomplish that experiment, chose an number between 1 and 10 for each reservoir, and decide on the route mapping between each reservoir and each manifold. Then, the odor reservoirs and manifold mapping are digitally recorded in the control software as an "Odor-Manifold Configuration." With this configuration setup, we then would digitally assign the stimulation sequence steps where each step is defined by the stimulation step's duration, and the odor—or lack thereof—assigned to be delivered out of each manifold (left, middle, and right). This is saved in the software as an "Stimulation Sequence Configuration."

3.5.2 Reservoir Preparation

Based on the desired stimulation experiment, we would prepare the solutions which would be used for stimulation. Once the solution were prepared we would aliquot ≈ 100 mL of each solution into the appropriate odor solution reservoir(s) (§3.2.5) as defined by the odor line configuration. We would prepare 1 – 2 L of fish water in the wash reservoir for running the wash line. And we would also ensure the 3.5 L vacuum reservoir was emptied.

We would ensure each of the fluid reservoirs are sealed by tightening the connection caps securely. We would then test the seal by pressurizing the wash and odor manifolds and listening for any leakage of air from each of the caps; if we observed leakage, we would further torque down the cap to ensure a proper seal.

3.5.3 Fluid-Line Priming

Another preparation step prior to stimulation is to prepare all of the stimulation, wash, and vacuum fluid lines by filling them with fluid and, to the extent possible, expelling air from all parts of the fluid distribution and control system. We perform separate priming of the cart with it's umbilical fluid lines and the individual stimulation manifolds before joining them together as described in §3.5.4.

3.5.3.1 Cart and Umbilical Priming

Once each of the reservoirs are prepared as described in §3.5.2 we would pressurize the odor manifold to ≈ 0 psi. Then we would attach a short fluidic line terminated with 1/4″-28 male compression fittings to each port on the distal end of the fluidic bulkhead manifold which would be utilized in the upcoming experiment. We would direct the outlets of each of these lines into a large beaker. Then, in sequence we would open each of the solenoids for each line and allow flow to pass through the line until a consistent stream (with no

bubbles) was observed at the distal end. We also used the flow sensor and control software to monitor the line for air and consistent flow rate value during the priming. This procedure was repeated for the wash fluidic line as well.

We would not prime the vacuum line since during the experimental setup, significant air is drawn into the vacuum line and a steady state is not reached until the dish is filled with fish water from the wash line and the inflow and outflow rates are matched. See §3.5.5.

3.5.3.2 Stimulation Manifold Priming

To prime each of the stimulation manifold assemblies (left, middle, and right; §3.2.1.2) we first submerged the entire assembly in a bath of water (deionized). Similar to the manifold construction process, we kept the entire assembly underwater during the priming process. We removed the protective cap sealing the male leur output end of the manifold to allow for flow to exit the manifold. Using a custom priming pump (assembled from a syringe and a valve assembly) fitted with a 1/4″-28 male compression fitting as its output, we flushed each of the 8 lines on the manifold with ≈ 5 mL of fluid. For each flush run, we would be sure the 7 other manifold inputs were tightly capped with 1/4″-28-male plugs. Continuing to keep the entire assembly underwater, we finally would recap the output of the manifold with a female leur-lock plug. We would then store the primed manifolds underwater until just before mounting them do the stimulation platform when beginning an experiment.

Note: We found it very important to keep the dead volume of the manifold free from any air. This is because trapped air in the manifold will compress when pressurized and lead to slower switching between the odor streams. Additionally, trapped air can allow for fluid from a given odor stream to back flow into another manifold input line and lead to contamination when a different odor stream is switched on . Therefore, when connecting fluidic components to the manifold (specifically, when attaching the delivery needle to the output and when attaching the female 1/4″-28 to male leur-lock adapters to the inputs) we would perform the assembly under water immersion. Further we will regularly flush each of the fluid lines and delivery needles with water to minimize the volume of trapped air in the system.

3.5.4 Joining the Stimulation Cart and Platform

After priming all of the stimulation lines, we then mounted the stimulation platform and connected the fluidic and electrical components between the stimulation platform and the stimulation cart. These two partitions of the stimulation system can be placed independently and then linked through the system umbilical. Typically we will first mount the stimulation platform under our two photon microscope objective by fastening it to the optical table; however, stimulation experiments did not necessarily have to performed under the microscope. After fixing down the stimulation platform we would position the stimulator cart within a few feet of the platform, then mount the distal 1/4″-28 bulkhead panel (§3.2.1.5.2) to the platform using a clamping fork (Thorlabs CF125).

We would then connect the electrical components between the platform and the umbilical including the LED power (M12), Camera TTL (BNC), Camera Sync Signal (BNC), LED TTL (BNC), behavioral camera digital I/O (USB-A).

Before we made the fluidic connections, we mounted each of the primed stimulation manifolds into each of the kinematic V-mounts (§3.2.1.3.2.2). Then, we used a set of pre-labeled, pre-primed 1/4″-28 male compression fitting-terminated tubing lines to connect the female 1/4″-28 ports on the bulkhead panel to each of the manifold inputs. The lines would be labeled with the connection name on the bulkhead panel and the connection on the platform; for example, the label "A3–M" would indicate a connection between bulkhead position A3 and the middle stimulation manifold. The connections were determined based on the defined stimulation (§3.5.1) and the layout of the bulkhead panel (§3.2.1.5.2).

3.5.5 Wash and Vacuum Flow Setup

As described in §3.2.1.4 we designed the stimulation system to run with the ability to have continuous inflow of fish water and outflow of dish water. To setup this continuous flow, we needed to position the wash and vacuum needles within the dish then adjust the flow through each line until the flow rates are matched. First we used the grip arm's of the wash and vacuum positioning assemblies to move the tips of each needle into position. The wash Needle was positions to direct it's flow directly toward the nose of the larva from a distance of approximately 1 cm in x and the tip of the needle was put at approx the same z-position as the larva. The vacuum needle was positioned at the opposite side of the dish within 5 mm of the dish's wall. The tip of the needle was positioned $\approx 1-2$ mm below the z-plane formed by the rim of the dish.

With the needles in position we would begin with turning on the vacuum manifold. Typically the starting volume in the dish was relatively low, so the positioned vacuum needle would not initially withdraw any water. Then we would close the wash line needle valve, pressurize the wash manifold to ≈ 5 psi. We then slowly opened the wash line needle valve until the flow rate approached the dish turnover set-point (typically 10 mL min^{-1}). As the dish filled with water, and the vacuum needle would begin to withdraw fluid, we adjusted the vacuum needle valve until it's steady-state flow rate reached the same dish turnover set-point. This process would often take some time as all the air was removed from the vacuum line.

Throughout the experiment we would closely monitor the in and out flow rates as well as the estimated dish volume in the flow rate monitoring panel of the stimulation system virtual instrument. As needed we would adjust the needle valves to restore volume balance to the dish.

3.5.6 Larva-Stimulator Alignment

To effectively deliver odors to a larva's olfactory epithelium we must align each of the stimulator needles to the larva. The procedure for preparing the larva for stimulation by mounting it in agarose and freeing the nose is described in §4.5.3. Additionally, before

performing the stimulator alignment we must orient the larva to a standard position in 3D space and align each of the imaging systems to the larva; these orientation and alignment procedures are described in §4.5.4. Throughout the alignment process we utilize a combination of line of sight, the behavioral camera feed, and the wide-field microscope camera feed (ordered from lowest magnification to highest) as feedback for our positioning.

The stimulator needle alignment procedure begins with aligning the center stimulator to the most caudal point of the fish. We utilize the coarse z-rotation platform (§3.2.1.3.1.1) to point the center stimulation needle toward the larva. We then adjust the tilt platform (§3.2.1.3.1.4) to the desired stimulation angle (typically 40°) using the platform's degree scale. We then carefully use the middle y' translation stage (§3.2.1.3.2.1) to extend the stimulation needle within a few mm of the larvae. Then we utilize the x and y translation stages (§3.2.1.3.1.3) to position the tip of the stimulation needle directly toward the larva. If there is any misalignment between the needle axis and the rostral-caudal axis of the larva, we use a combination of x-translation and z-rotation (§3.2.1.3.1.1) to align the needle axis to the larva. To align the stimulation needle along the z-axis toward the larva's olfactory epithelium, we use the vertical positioner (§3.2.1.3.1.2) referencing the position with a line-of-sight side-view of the dish and stimulators. We can also identify the z position of the stimulation needs by identifying the point on the needle barrel of highest sharpness (this identifies the microscope focal plane) and referencing how the shift of that sharpest position during z-adjustments.

After alignment of the center stimulation needle, we align the left and right stimulation needles by similar procedures. We extend the y' translation stage (§3.2.1.3.2.1) for the side stimulator to move the needle within a few mm of both the larva and the middle stimulation needle tip. We then adjust tip and tilt (§3.2.1.3.2.2) of each side stimulator point its stimulation needle to nearly the same position on the larva as the middle needle and the opposite side stimulator. Finally we use the fine adjustment knob on each of the side y' translation stages to get each of the needles equally distant from the larva's nose.

With this procedure, all of the stimulation needles have been aligned to the larva, and the larva is ready to be stimulated.

3.5.7 Olfactory Stimulation

With all setup of the system complete, we can proceed to utilize the system for live stimulation. Control of each of the odor lines is controlled by the software and the stimulation configuration (described in §3.5.1). If performing synchronous imaging, we would update the "run number" in the stimulation virtual instrument to match the other modalities, the click "run" to begin the stimulation. During the stimulation run, we would check the flow rates coming through each of the odor lines to ensure the expected flow rates were achieved and the expected line numbers were being activated.

If we encountered any issue with a drop in flow, it often indicated a clogged stimulation needle. To resolve this we would wait for the completion of a stimulation run, then change out the stimulation needle for a functioning one. We would then check the flow coming out of that needle to determine if the issue was resolved.

The procedure for integrating the stimulation system with two photon and behavioral imaging to perform correlated acquisition is discussed in §5.4.1.

3.6 Conclusion

In this chapter we detail the invention and implementation of a mobile, three-direction, ten-odor, olfactory stimulation system capable of performing experiments not otherwise possible. We also quantify the kinetics of flow and odor delivery through the system and out to a larva's olfactory epithelia. We show, via imaging experiments, the ability for independent stimulation of the left and right olfactory epithelia and temporal control on the order of 1 – 4 s. Finally, we outline the types of bilateral stimulation experiments that we are able to perform using our system. Looking forward to Chapter 5, we will show how we integrate stimulation into brain imaging, behavioral, and structural readouts to enable investigation into the neuroscience of sensory processing in the brain.

3.7 References

1. Kalueff, A. V. *et al.* Towards a comprehensive catalog of zebrafish behavior 1.0 and beyond. *Zebrafish* **10,** 70–86. ISSN: 15458547. eprint: https://doi.org/10.1089/zeb.2012.0861. https://doi.org/10.1089/zeb.2012.0861 (1 Mar. 2013).
2. Naumann, E. A. *et al.* From Whole-Brain Data to Functional Circuit Models: The Zebrafish Optomotor Response. *Cell* **167,** 947–960.e20. ISSN: 10974172. http://www.cell.com/article/S0092867416314027/fulltext (4 Nov. 2016).
3. Bianco, I. H., Kampff, A. R. & Engert, F. Prey capture behavior evoked by simple visual stimuli in larval zebrafish. *Frontiers in Systems Neuroscience* **5,** 18496. ISSN: 16625137 (DECEMBER 2011 Dec. 2011).
4. Guggiana-Nilo, D. A. & Engert, F. Properties of the visible light phototaxis and UV avoidance behaviors in the Larval Zebrafish. *Frontiers in Behavioral Neuroscience* **10,** 195249. ISSN: 16625153 (AUG Aug. 2016).
5. Gerlach, G. & Lysiak, N. Kin recognition and inbreeding avoidance in zebrafish, Danio rerio, is based on phenotype matching. *Animal Behaviour.* ISSN: 00033472 (2006).
6. Gerlach, G. *et al.* Behavioural and neuronal basis of olfactory imprinting and kin recognition in larval fish. *Journal of Experimental Biology* **222.** ISSN: 00220949 (Feb. 2019).
7. Hinz, C. *et al.* Kin recognition in zebrafish, Danio rerio, is based on imprinting on olfactory and visual stimuli. *Animal Behaviour* **85,** 925–930. ISSN: 00033472 (5 May 2013).
8. Hinz, C. *et al.* Olfactory imprinting is triggered by MHC peptide ligands. *Scientific Reports* **3,** 2800. ISSN: 2045-2322. http://www.nature.com/articles/srep02800 (1 Dec. 2013).
9. Wee, C. L. *et al.* Zebrafish oxytocin neurons drive nocifensive behavior via brainstem premotor targets. *Nature Neuroscience* **22,** 1477–1492. ISSN: 1097-6256. http://www.nature.com/articles/s41593-019-0452-x (9 July 2019).
10. Braubach, O. R., Wood, H. D., Gadbois, S., Fine, A. & Croll, R. P. Olfactory conditioning in the zebrafish (Danio rerio). *Behavioural Brain Research* **198,** 190–198. ISSN: 0166-4328 (1 Mar. 2009).
11. Valentincic, T., Miklavc, P., Dolenšek, J. & Pliberšek, K. Correlations between Olfactory Discrimination, Olfactory Receptor Neuron Responses and Chemotopy of Amino Acids in Fishes. *Chemical Senses* **30,** 312–314. https://academic.oup.com/chemse/article/30/suppl_1/i312/270534 (1 2005).
12. Maaswinkel, H. & Li, L. Olfactory input increases visual sensitivity in zebrafish: a possible function for the terminal nerve and dopaminergic interplexiform cells. *Journal of Experimental Biology* **206,** 2201–2209. ISSN: 0022-0949. https://dx.doi.org/10.1242/jeb.00397 (13 July 2003).

13. Bhinder, G. & Tierney, K. B. Olfactory-Evoked Activity Assay for Larval Zebrafish. *Springer Protocols* **66,** 71–84. ISSN: 1940-6045. https://link.springer.com/protocol/10.1007/978-1-61779-597-8_5 (2012).

14. Biechl, D., Tietje, K., Gerlach, G. & Wullimann, M. F. Crypt cells are involved in kin recognition in larval zebrafish. *Scientific Reports* **6,** 1–13. ISSN: 2045-2322. https://www.nature.com/articles/srep24590 (1 Apr. 2016).

15. Jeong, Y. M. *et al.* Optogenetic manipulation of olfactory responses in transgenic zebrafish: A neurobiological and behavioral study. *International Journal of Molecular Sciences* **22,** 7191. ISSN: 14220067. https://www.mdpi.com/1422-0067/22/13/7191/htm (13 July 2021).

16. Herrera, K. J., Panier, T., Guggiana-Nilo, D., Correspondence, F. E. & Engert, F. Larval Zebrafish Use Olfactory Detection of Sodium and Chloride to Avoid Salt Water In Brief Larval Zebrafish Use Olfactory Detection of Sodium and Chloride to Avoid Salt Water. *Current Biology* **31,** 782–793.e3. https://doi.org/10.1016/j.cub.2020.11.051 (2021).

17. Sy, S. K. H. *et al.* An optofluidic platform for interrogating chemosensory behavior and brainwide neural representation in larval zebrafish. *Nature Communications* **14.** https://doi.org/10.1038/s41467-023-35836-2 (227 2023).

CHAPTER 4

Reading-Out: Whole-Brain Calcium Imaging, Behavioral Quantification, and Structural Mapping

4.1 Introduction

In Chapter 3 we discuss the motivation for, as well as the design and implementation of the zebrafish olfactory virtual reality platform. This system can be conceptually categorized as stimulating the larvae—and there by it's brain—by way of an "input." In this chapter we will discuss the different ways that, given this form of input, we "read out" from the larvae across time, space and modalities and thereby ask questions about how the stimulation inputs influence the activity of the brain and create differential possibilities of behavioral outputs. The three primary types of data that we read out from the larvae are: live whole-brain calcium imaging, live tail recording, and *ex-vivo* structural and epitope maps. Each of these data gives insight into different aspects of the larvae's "state" from both functional and structural perspectives. The development of methods for acquiring these data within a single organism undergoing stimulation primes us for the final integration of the insights as we will see in Chapter 5. However, for now we will focus the following exposition on the development utilization of each of these three methods separately.

4.1.1 *In vivo* Whole-Brain Calcium Imaging

In the context of this work, the live readout of brain activity across a majority of the neurons in the brain at near single-cell resolution in the context of stimulation and behavior is *the* primary type of data that we collect.

As briefly discussed in §2.1 utilizing light to readout activity from the brain is particularly useful because it enables non-invasive inspection of neurons both superficial and deep in the brain. This light-based readout is made possible through the use of zebrafish

lines expressing genetically encoded calcium sensors (GECIs) formed from the fusion of green fluorescent protein (GFP) and calmodulin (CaM) know as GCaMPs [1, 2]. Since the first generation of these proteins, they have been evolved and engineered to be brighter, more sensitive, and better expressing to various degrees. In this work we primarily utilize a nuclearly-localized, 8th generation sensor optimized for sensitivity Huc:GCaMP8s [3].

The intracellular concentration of calcium in neurons can be understood to be an indirect measure of the activity of a neuron and it is a well established practice to image calcium using GECIs-expressing cells to readout brain activity in organisms [4].

4.1.1.1 Two-photon Microscopy

There are many optical systems which can be utilized for performing calcium imaging—including the light-field microscope as described in depth in Chapter 2—however, I will leave an in-depth comparison of different calcium imaging methods for the reader to explore in the following reviews [4–6].

For this work, we utilize two-photon (2P) microscopy to perform whole-brain imaging. In short, a 2P microscope creates images of fluorescent molecules through a physical phenomena known as the 2P absorption to excite fluorophores. In 2P absorption, two photons having a wavelength near double the fluorophores excitation wavelength (and near half the energy) are simultaneously absorbed by the fluorophore which excites an electron and leads to fluorescent emission from the molecule. The requirement of two photons to arrive at a given fluorophore at the same time means that the absorption process is nonlinear, and the intensity required to appreciably lead to a high probability of emission is limited only to a very small spot at the focal point of the imaging objective. Because a flophouse must simultaneously absorb two photons to lead to an emission event, two photon imaging systems can leverage the nonlinearity of absorption in both space and time to readout images with resolution comparable to a confocal system (which utilizes excitation light at the single-photon excitation wavelength) without the use of pinhole apertures.

The physics of 2P microscopy lead to a number of benefits (and some drawbacks) for whole-brain imaging. One benefit is that imaging deeper layers of the is improved brain because of the longer near infrared (NIR) wavelength and the observation that biological tissues (including the larvae's brain and surrounding structures) exhibit less scattering of light in the NIR range compared to visible light [7, 8]. Another benefit is that the NIR light is not as stimulating to the zebrafish's eyes as compared to visible light which ameliorates a potential confound to activity readouts and the effects of intentional stimulation [9]. A third benefit is that the readout of fluorescent light from a 2P microscope is performed with a photomultipler tube (PMT) or similar photodetector device. These classes of devices are often much more sensitive and less prone to noise as compared to camera imaging sensors.

One drawback of the use of two-photon imaging systems is that every pixel/voxel location in the image must be read out in sequence as the focal spot is scanned across the sample (in x, y, and z). In traditional galvo-galvo 2P imaging systems this can mean very slow imaging speeds (on the order of seconds) to read out a single plane at a resolution of $x = 512 \times y = 512$ pixel. However, by utilizing a resonant galvo-galvo 2P imaging system, as

we do, scan speeds can be significantly faster at the same resolutions such that a single plane can be imaged at a rate of 30 Hz. Additionally we can utilize a fast objective piezo scanning unit which can be synchronized with the resonant galvo unit to allow for volumetric scanning at a resolution of $x = 512 \times y = 400 \times z = 40$ voxel at an acquisition rate of 0.5 – 2 Hz, reference imaging data shown in Figure 4.10. . These different technical abilities allow the relatively "slow" point-scanning 2P imaging modality to acquire images quickly enough for whole-brain calcium imaging.

4.1.2 *In vivo* Behavioral Tail Imaging

In the perfect platform for live monitoring of zebrafish towards understanding the larval brain's processing of the environment to yeild behavioral outcomes, we would be able to read out whole-brain neural activity, track the larva's location and body position, and monitor physiologic conditions like heart rate, all while the larva freely swims in a controlled environment. However, with the current state-of-the-art technology, this is not possible; we must navigate a landscape of trade-offs by prioritizing the types of data that it is most important for us to acquire given the types of questions and explorations we wish to take one. For this work, our priority is performing whole-brain calcium imaging; since we are performing this imaging with 2P microscopy, we must immobilize the larva such that their brain remains directly beneath the imaging objective. While this immobilization limits the types of behavioral readouts we can obtain, we are able to mount the fish in a "head-fixed, tail-free" configuration such that the anterior head region is held in position in agarose of brain imaging, while the posterior tail region is released from the agarose such that the the larva can move its tail relatively freely ($\pm 90°$) relative to its body without completely moving [10, 11].

Our goal for capturing tail movement as a behavioral readout is to enable our experiments to answer questions about how the fish respond to different odors. The responses are captured though the metric of tail angle and tail curvature versus time; however, this readout can be analysed to classify movements such as forward swims, escape maneuvers, and left and right turning maneuvers. These quantitative measures and their qualitative classifications can allow us to ground our hypotheses in observable behavioral decisions and changes rather than relying on activity alone. The behavioral readouts also allow us to make predictions about how the fish will move given inputs and brain imaging and validate those predictions based on the observations.

4.1.3 *Ex vivo* Immunohistochemical Structural Mapping

While the readouts that we capture during live imaging can be classified as "functional" imaging, the readout which we focused on for larva after live imaging (sacrificed) are "structural" images. We can also refer to these images as structural "maps" which highlights the fact that these images are mapping the location of different epitpoe-mediated markers in the brain. These epitpoes include targets for relative neural activity (ERK, phospho-ERK), specific neuromodulation receptors, and synapse markers. Although these maps are static,

they provide the ability to capture information which cannot otherwise be obtained in the live context and contributes to the more holistic understanding of the brain.

We utilize standard immunohistochemical (IHC) methods to detect and image the different proteins and molecules of interest. However, while there is a precedent [12], there are many difficulties that exist to perform IHC on undissected whole-mount (i.e. unsectioned) larval zebrafish tissue, including getting full penetration of antibodies throughout the tissue, optical clearing of the tissue for deep imaging, ensuring compatibility of antibodies raised against analogous protein targets from other species.

In addition to providing additional context for our understanding, the acquisition of structural images allows us to validate our ability to register *in vivo* data onto *ex vivo* data. This capacity is critical as we look forward to the correlated acquisition of connectomic, *in situ* sequencing, and other rich structural datasets.

Furthermore, with the ability to register between functional and structural images, the acquisition of epitope markers makes it possible for us to segment the functional imaging data based on the structural maps. This correlated acquition, its motivation, and its enabling capabilities are discussed in Chapter 5.

4.2 Behavioral Imaging System Design

Concurrent with the design of the olfactory stimulation system (§3.2), we also designed a system for tail imaging of head-fixed, tail-free zebrafish larvae. This system consisted of three subsystems: an infrared camera along with it's associated optics, 6-DOF stage for holding the mounted larva with accessibility for imaging from both above and below, and infrared lighting to illuminate the larvae.

The primary design requirements for the behavioral imaging system are as follows:

1. $>$ 200 fps recording speed. Larval tail flicks can be very fast (on the order of 11 000 ° s^{-1} or 300 mm s^{-1}).

2. Imaging light only within 750 – 900 nm. The lower wavelength bound aims to minimize stimulation of the larvae with visible light, therefore we require that the camera images light at wavelengths no shorter than 750 nm. The upper wavelength bound aims to avoid 2P laser light ($\approx$ 950 nm) from overexposing the behavioral imaging camera; therefore we also require image light no longer than 900 nm.

3. Ability to synchronize acquisition and/or image timecode with live imaging and stimulation.

4. The imaging system design must physically allow for full compatibility with olfactory stimulation and whole-brain imaging.

5. Must be able to have an imaging field of view that captures the full tail range of motion of a 7 dpf larval zebrafish. This area is an approximately 5 mm $\times$ 5 mm square area.

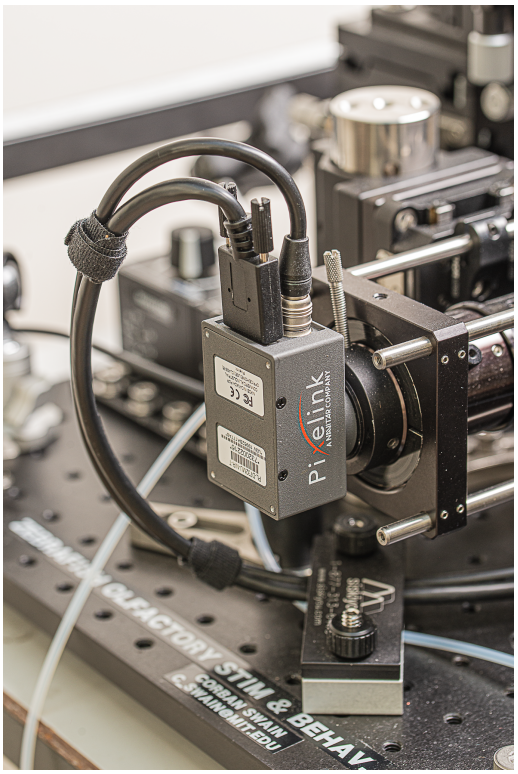

Figure 4.1: A high-speed near-infrared USB camera was used to create behavioral recordings.

4.2.1 Behavioral Infrared Camera and Optics

The core data-generating component of the behavioral imaging system is the the camera. We utilized a monochrome near-infrared USB CMOS camera (Pixelink PL-D732MU-NIR-T) which is capable of imaging at ≈ 200 fps with 2×2 pixel binning, Figure 4.1. This camera selection satisfies the recording speed requirement. The camera also is responsive to visible wavelengths up to 950 nm wavelength light (at ≥ 10% quantum efficiency), making it compatible with our wavelength requirements. The camera is mounted to a machine vision lens for image formation. We utilized a 6X zoom lens (Navitar Zoom 6000) fitted with a 2×lens adapter (Navitar 1-6233)and a 0.5×front-element attachment (Navitar 1-60110). This lens setup provides for a field of view zoomable between 10 – 2.5 mm across—given the camera's 2/3″ sensor size—as well as a working distance of 143 – 187 mm. These attributes meet our field of view requirements as well. To ensure laser light and visible light are prevented from reaching the image sensor, we designed a custom filter set, Figure 4.2. The filter set consisted of—starting closest to the camera—a 900 nm shortpass filter (Thorlabs FESH0900), a 900 nm longpass dichroic mirror (Thorlabs DMLP900R, camera receives reflected light), and a 800 nm longpass filter (Thorlabs FELH0800). This filter set satisfies the received wavelength requirements.

The camera and lens are oriented horizontally and the dichroic mirror turns the imaging direction up vertically to allow the camera to look up through the observation stage into the larva. The camera, lens, and filter assembly are mounted in a lens cage system mounted to a 1.5″ optical post for coarse focus adjustment and mounting to the platform breadboard.

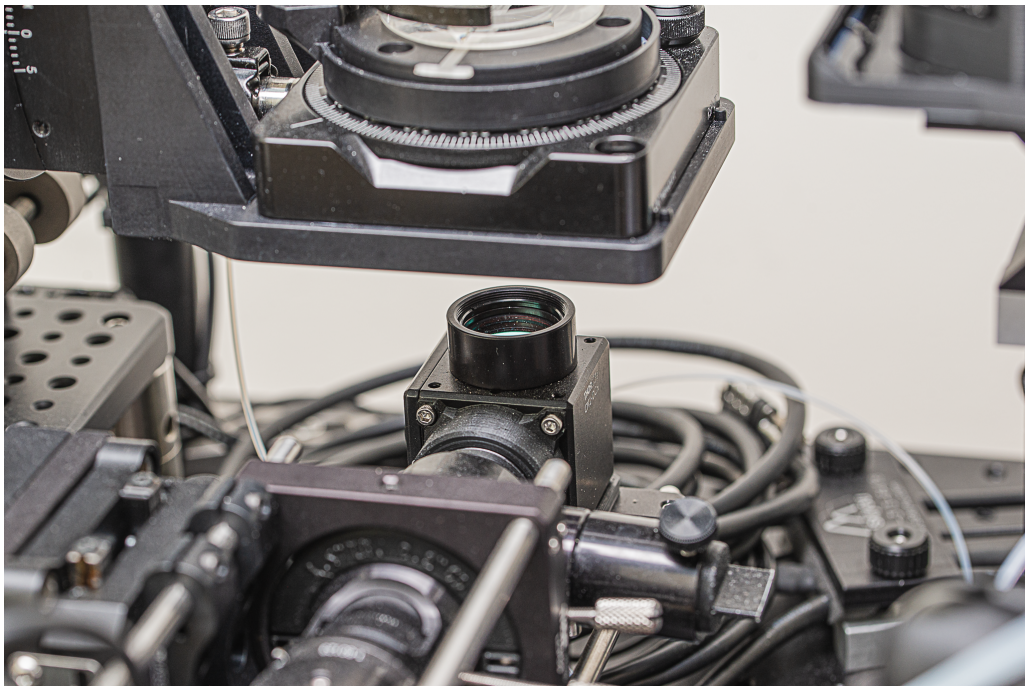

Figure 4.2: A machine vision lens coupled to a 850 nm bandpass mirror and filter assembly enables imaging through the bottom of the larva-holding dish.

The camera assembly is mounted to the post through a vertical translation stage (Thorlabs LX10) which allows for medium to fine focus adjustment. Fine focus adjustment can be performed with a control ring on the lens barrel.

4.2.2 6-DOF Observation Stage for Mounted Larvae

As previously described the zebrafish larvae are mounted in a head-fixed, tail-free arrangement. To do this mounting the fish and agarose are held within a 50 mm-diameter low-profile, glass-bottomed dish. To allow for simultaneous imaging of the mounted larva from above for two-photon imaging and from below for behavioral imaging, we designed an integrated dish-holder and stage with an $\approx 1.5''$-diameter clear aperture below the dish. The components of the stage, Figure 4.3, are as follows, beginning with components closest to the fish and ending with those farthest.

4.2.2.1 Dish Platform and Holding Fork

The dish platform and holding fork are a custom components machined from aluminum, Figure 4.4. The holding fork fits over the rim of the dish and allows for the dish to be held with minimal intrusion on all sides of the dish to give maximum space for the stimulation system odor delivery needles, illumination light, and the 2P objective to fit above the dish. Using a clamping which brings together the clamping fork and dish platform, the dish can be freely oriented then locked into position stably. The dish platform has a through hole below the dish for imaging. The dish platform also has a dovetail alignment slot which can

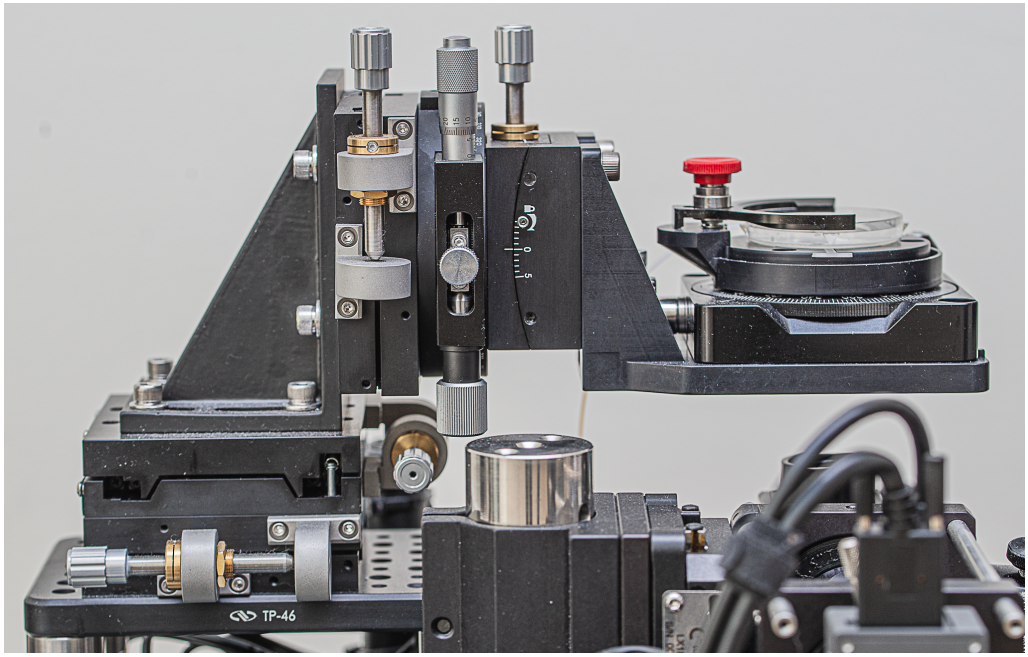

Figure 4.3: A custom 6-DOF positioner was used to align head-fixed larve to imaging and stimulation systems consistently across experiments.

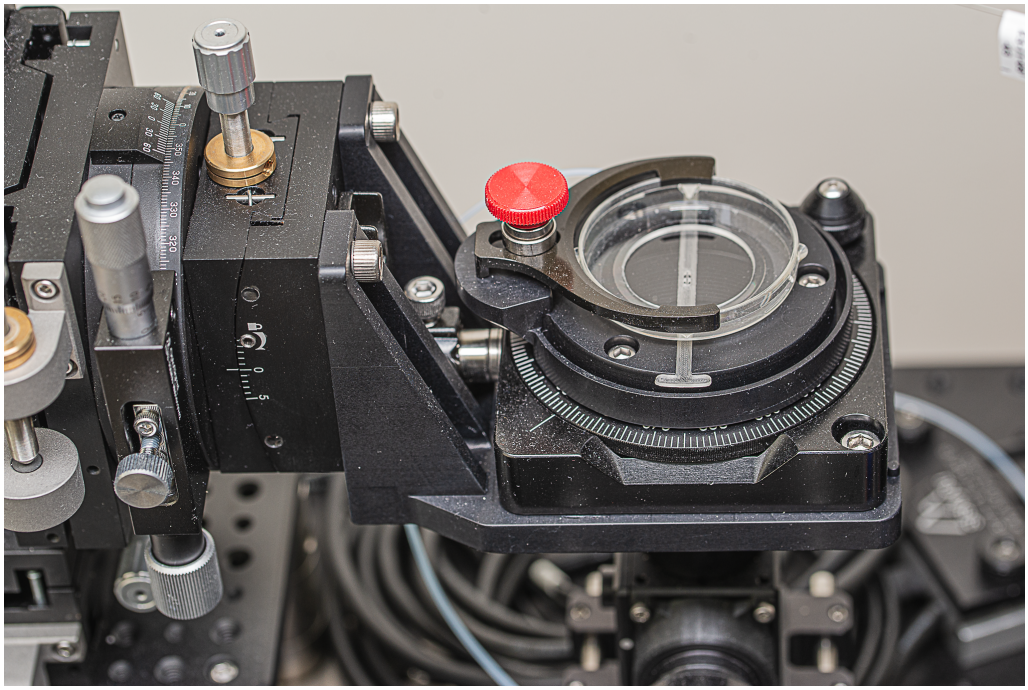

Figure 4.4: A custom machined dish holding platform and clamping fork provided quick mounting and removal of larva within a 50 mm dish, as well as a clear aperture both above and below the dish.

accept a dovetail-mounted cross hair reticle (custom in-house) for centering the fish at the observation stage's common point of rotation.

The dish platform also features an overflow channel to catch any liquid that might spill from the dish. Using a small tube clamp (custom part number , we are able to hold a $1/16''$ outer diameter auxiliary vacuum in the to continuously suction away any collected liquid.

The dish platform mounts directly to the z-rotation (yaw) adjuster with machine screws.

4.2.2.2 DOF 1 z-rotation

We adapted a $2''$ clear aperture optic rotation mount (Newport RSP-2T) to support the dish platform and allow for $\approx 160°$ of z-rotation for the the dish. The center point of the rotation is consistent for each of the rotational degrees of freedom, located approx 10 mm above the top of the dish mount, centered which is the approximate location of the larvae when mounted in the dish. This degree of freedom allows us to align the antero-posterior axis of the larvae with the x-axis of the stage and other imaging systems.

The z-rotation mount was held using an aluminum right-angle bracket (custom) which connected to the y-rotation (pitch) adjuster. The also had a $2''$ clear aperture in it's base to maintain the ability to image from below.

4.2.2.3 DOF 2 y-rotation

We utilized a goinometric stage (Newport GON65-L) to allow for rotation of the larvae and dish about the y-axis with 10° of adjustment range. The construction of the goinometer allows for the axis of rotation to fall outside of the dimensions of the part, 80 mm in front of the platform. As previously mentioned, the geometry of the right angle bracket mounting locations of the other components were chosen such that this rotation axis intersects with the location of the mounted zebrafish larvae. This degree of freedom allows us to ensure the antero-posterior axis is horizontally oriented and allows us to correct for small inconsistencies in the larvae mounting.

The y goinometer was mounted directly to the x-rotation (roll) stage with machine screws.

4.2.2.4 DOF 3 x-rotation

We utilized a high-load rotation stage (OptoSigma KSPB-906MUU) to allow for rotation of the larvae about the x-axis with 360° of coarse adjustment range (although adjustments past $\pm 30°$ would likely empty the dish of water and lead to physical collision with other components) and 10° of fine adjustment. This rotation stage is subjected to a substantial rotational moment—due to gravity—about the y-axis since all of the previously discussed components are to the stage while it is vertically mounted, therefore we utilized this component which capable of handling rotational moments up to 5 N m while still allowing for smoothe rotations.This degree of freedom allows us to align the dorso-ventral axis of the larvae with the z-axis of the imaging cameras.

The x rotation stage was mounted directly to the xyz-translation sub-assembly.

Figure 4.5: Collimated infrared illumination assemblies mounted on positiong arms enable our behavioral camera to capture tail motion.

4.2.2.5 DOF 4–6 *xyz*-translation

We utilized three translation stages (Newport 426, each with adjustment screw AJS100-1) to control the position of the larvae about the x, y, and z axes with 1″ of travel range. The xy controls allowed us to center the larvae above the behavioral camera. The z control allowed us to choose the height of the fish above the platform breadboard, this affected the relative height of all the other imaging and stimulation components, which we sometimes needed to modify to keep other adjusters near the center of their travel range (e.g. the stimulation endpoint's vertical positioner §3.2.1.3.1.2).

The z translation stage was mounted to the y-stage with a right angle bracket (Newport 360-90). The y translation stage was mounted directly to the x-stage with machine screws, and the x-stage was mounted to a riser platform.

4.2.2.6 Stage Riser Platform

The entire positioning sub-assembly was mounted on a 3.5″ riser platform. This platform positioned the zebrafish larvae near the center of travel range for the stimulator endpoint, the behavioral camera's plane of focus, and the 2P imaging plane of focus. The riser also securely held the positioning sub-assembly to the platform breadboard through a small aluminum breadboard (Newport TP-46), 4 3″ tall, optical pedestal posts (Newport PS-3) and 4 clamping forks (Newport PSF-1.0).

Figure 4.6: An LED driver supplies power and switching control of our infrared imaging light sources.

4.2.3 Infrared Lighting and Collimation Optics

In order to perform infrared imaging of tail movements, we needed to employ an illumination source. We utilized a pair of identical illumination assemblies which consisted of an light emitting diode (LED), collimation optics, and a positioning arm, Figure 4.5.

4.2.3.1 LED and LED Controller

We utilized a 850 nm center wavelength, 1 W mounted LED (Thorlabs M850L3) for our illumination source. The typical illumination bandwidth for this LED was 30 nm which falls directly in the 700 – 800 nm range passed by the camera's filter set. The mounted LED was attached to the light collimation optics with SM1 lens tube threads.

The LED was powered by an LED controller (Thorlabs LED1B) which allowed us to turn on and off the LED, control of the LED's output level, and trigger and modulate and output electronically, Figure 4.6. Power for the LED controller was supplied by a 14 V AC-to-DC adapter with the DC power line extended through the stimulation system umbilical to the LED Controller boxes.

4.2.3.2 Light Collimation Optics

The mounted LED's light output was diffused with a ground glass diffuser (Thorlabs DG10-1500-B) and collimated using an aspheric condenser lens (Thorlabs ACL25416U-B). The output from the condenser was passed through an adjustable iris which allowed for control over the projected spot size. Collimation of the LED light allowed for significantly more powerful illumination intensity and makes for more efficient use of the LED's output.

4.2.3.3 LED Positioning Arm

The LED-collimation assembly was mounted to an small ball head (Manfrotto MH492-BHUS) which allows for quick tip, tilt and rotational adjustment of the assembly's pointing direction (similar to a tripod head). This ball head was mounted to a 20″ variable-friction "magic arm" (Manfrotto 244N) which allows for lockable positioning of the LED nearly anywhere above the stimulation platform. We utilize this magic arm to make positioning of the LEDs at the ideal position for illuminating the tail among all of the other hardware around the larvae simple and stable. The magic arm was attached to the platform breadboard with a 5/8″ stud adapter and a 1/4″-20 set screw.

4.3 Results

Many of the results from whole-brain imaging and behavioral imaging are discussed at length in §5.2 where we combine the data from these modalities to quantify how larvae respond to various stimulation trials. Here we will focus on proof-of-concept data from each live modality as well as from the structural mapping in isolation. Most of the data presented here represent datasets typical of the state of the art and is not the focus of this thesis work; however, this data does frame the work performed for a broad audience and lays the foundation for downstream analyses and results presentations.

We successfully demonstrated volumetric whole-brain calcium imaging of head-fixed larval zebrafish using two-photon microscopy, Figure 4.10. We performed imaging at a spatial resolution of ≈ 2 µm in xy and ≈ 5 µm in z and at a temporal rate of ≈ 1 Hz. We were able to perform continuous imaging for up to ≈ 30 min. Further we developed a method for aligning the live imaging datasets to an anatomical reference Figure 4.7.

We used this alignment to extract mean calcium traces from each of the annotated brain regions contained in our data, Figure 4.10B. This scheme allowed us to extract data from ≈ 575 brain regions (considering each lateral side as a separate region). This regional analysis allows us to qualitatively identify regions of interest and to observe general trends and patterns in the data Figure 5.1.

Our behavioral imaging platform performed as designed and allowed us to capture 250 fps infrared recordings of zebrafish tail motion over the course of a 30 min experiment Figure 4.9. Using computational analysis of these videos we were able to track the tail angle and curvature over time and flag bouts of movement Figure 4.9C–D with accuracy on the order of tens of milliseconds.

We also demonstrated the ability to stain and image the localization of GCaMP in transgenic fish via immunofluorescence Figure 4.8B. We also show successful staining of ERK and phospho-ERK Figure 4.8F–H. Attempts at staining other targets including Oxytocin receptor and serotonin show some success, but require further optimization due to poor signal and non-specific staining against these epitopes Figure 4.8C–E.

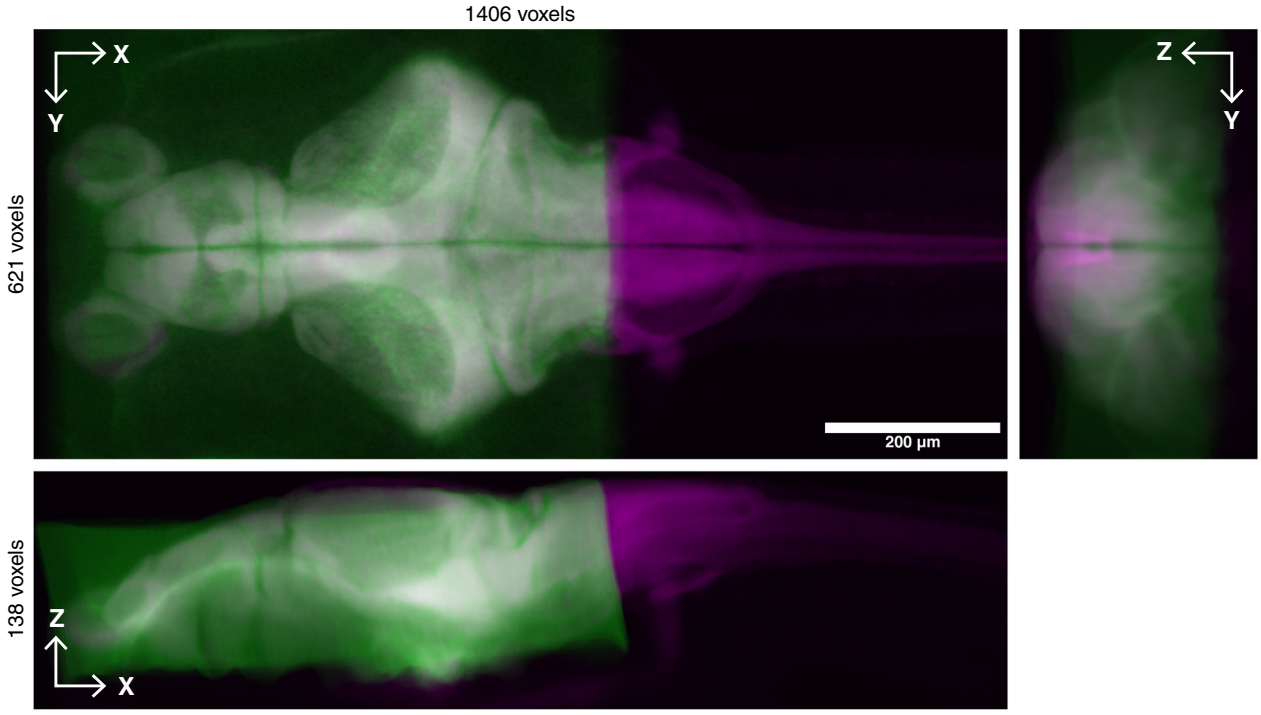

Figure 4.7: We successfully registered live whole brain calcium imaging datasets onto the Z-Brain Atlas for subsequent regional activity segmentation.. Orthogonal mean intensity projections of the 3D image of live brain images (max-projection across time, green) acquired on out two photon system non-rigidly registered onto the Z-Brain Atlas's reference *Tg*(HuC:H2B-RFP) (panneuronal, nuclear-localized red fluorescent protein) dataset (magenta). Overlap and correspondence between the images appears as shades of grey in the overlaid volume. This figure illustrates the step prior to activity extraction shown in Figure 4.10.
Note: Scale bar is 200 µm. When performing the analysis, the inverse registration is actually perform; warping the atlas regions onto the live-brain imaging data.

4.4 Discussion

4.4.1 Optimizing 2P Imaging Parameters

Some of the issues we encountered with two-photon calcium imaging include difficulty in the refinement of many of the imaging parameters which control various aspects of volumetric two-photon imaging. Particularly, keeping laser powers below the damage threshold of the tissue for long term scans proved to be difficult to properly assess. Performing an experiment in which we test the biocompatibility of various laser powers combined with different objectives, scan rates, and other parameters would likely yield a helpful collection of heuristics for better deciding on imaging powers.

4.4.2 Quantifying the Effect of 2P Calcium Imaging

An assumption that we make in our live 2P imaging experiments is that behavior and activity read out during imaging has correspondence to the the larva's behavior and activity in the unobserved state. While this assumption does not have to be completely upheld for our data to be useful and insightful, it would be good to have a quantifiable measure of the ex-

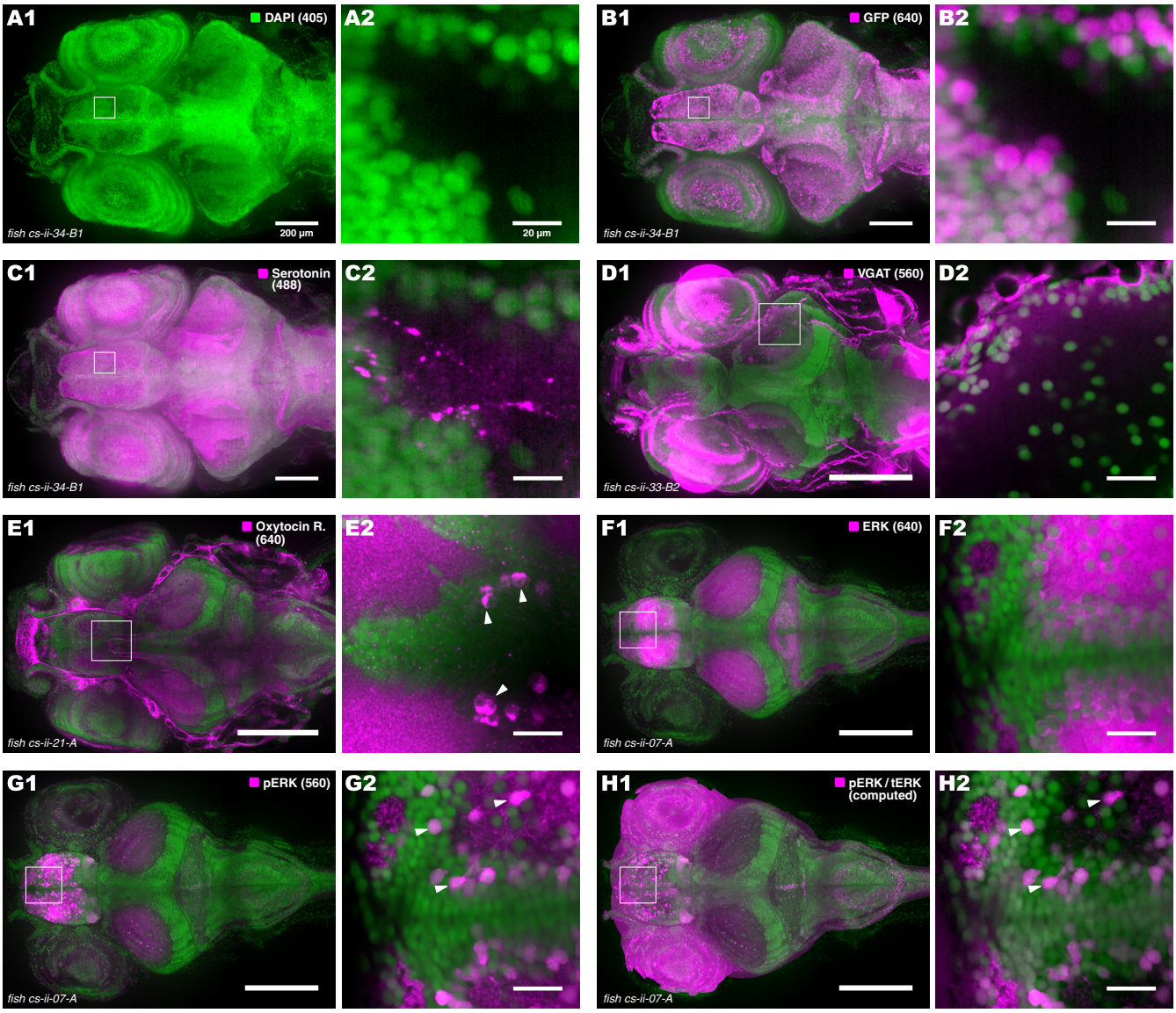

Figure 4.8: We demonstrate immunohistochemical (IHC) structural staining against a range of neurobiologically relevant targets. All images are spinning disk confocal micrographs stitched across 6–15 fields of view; in green is shown the fluorescent signal of DAPI (nuclear) stain imaged with the 405 nm laser line. While overlaid in magenta for **B–H** are shown fluorescent or computed signal against different immunostained targets. Left **_1**-panels are maximum intensity projections (MIPS) across 6–20 *z*-planes ranging from the dorsal end of the brain to 250 µm ventral. Right **_2**-panels are magnified regions-of-interest (ROI) from a single *z*-plane. The location of the ROI is shown in a white outlined box on the left **_1**-panel. **A:** DAPI only. Nuclei staining was of good quality and a reference for the other channels. **B:** GFP staining on 640 nm laser line. (anti-GFP IHC staining of GCaMP is shown more thoroughly in Figure 4.11.) **C:** Serotonin staining on 488 nm laser line. Staining signal seems to be mostly non-specific. **D:** Vesicular GABA transporter (VGAT) staining on 560 nm laser line. Signal appears to saturate in the eyes and skin. **E:** Oxytocin receptor (OXTR) staining 640 nm laser line. **E2** ROI highlights (white arrows) some cells showing OXTR signal also appears to have non specific staining of skin. **F:** ERK staining on 488 nm laser line. Staining quality is very good with little non-specific signal; bright region in telencephalon corresponds with expected expression pattern. **G:** phosphorylated ERK (pERK) staining on 560 nm laser line. Staining quality is good and single neurons expressing pERK can be observed (white arrows). **H:** Computed pERK/tERK (tERK: total ERK, i.e. ERK staining) signal. Image volumes of pERK and ERK were acquired in the same fish, normalized, masked then divided to produce this image. Computation refines the pERK signal in some cells (see top right white arrow in **G2** and **H2**) pERK/tERK can be used a correlate to neural activation just prior to the time of euthanasia [13–15]. *Note: All images/channels were normalized to to clip 15% of pixels to black/0 and 0.5% of pixels to white/1 for MIPs while for the ROIs were normalized to clip 5% of pixels to black and 0.5% of pixels to white. Green/DAPI channel was attenuated to 75% intensity in all two color images.*

tent to which the fish behaves differently when the brain undergoes 2P exposure. Aspects of the 2P imaging which we would like to consider are:

- the environment of the 2P imaging stage including the room, dimmed lighting, the shrouded scope enclosure, the sounds of imaging (e.g. shutter opening and glavo scanning), and the proximity of the objective overhead of the larvae.
- the pulsed laser exposure as the galvo mirrors scan light in x and y across the brain.
- the objective motion as it moves in z directly closer and further from the larvae in either a triangle (bi-directional scan) or sawtooth (mono-directional scan) fashion.

We can perform an experiment of monitoring tail movements with different combination of these imaging aspects and then compare the statistics of tail movement between the conditions. Furthermore, we can also utilize the stimulation system to assess if the larva's responses to stimulation are significantly different when various aspects of the imaging are ongoing or not. This experiment would help us to determine if any aspects of our imaging setup and protocol modulate the larva's internal state to a degree significantly different from the head-fixed preparation alone. For example, this experiment might reveal that objective movement has a significant effect on tail movement behaviors and therefore next generations of our experiments should consider implementing a remote z-scanning system to ameliorate this issue.

4.4.2.1 Aberrations in Registration of Functional and Atlas Datasets

The whole-brain imaging data was aligned to the Z-Brain atlas using a Python registration library (described in §4.5.5.3.2). In order to deform the atlas onto our data, we utilized

Figure 4.9 *(following page)*: We utilized infrared behavioral imaging to record larvae, quantify tail motion, and detect swim bouts. A: Infrared image taken as a single frame of a larva at rest. Frame extracted from a 20 min recording. Agarose fixing the head in place is shown in the outlined, bar-shaded region; agarose was cut away from the nose to allow for olfactory stimulation (delivery needles outlined in white) and cut away from the tail to allow for motion. **B:** Single frame from same recording with larva's tail in motion at $t = t^*$ (during swim bout # 50, see **D2**). Tail base selected as the origin and the fish coordinate system shown in white lines. The 9 tail positions $\{\langle x_0, y_0\rangle, \ldots, \langle x_9, y_9\rangle\}(t)$—tracked by the ZebraZoom machine vision software over time—are shown in green circles with the position of the tail tip in a red circle. The tail angle is defined as the angular position (relative to the $+x$-direction) of the tail tip in the larva's coordinate system. **C:** Plot of the tail angle over time (black line) for an entire experiment recording. Detected times periods of tail movement or "swim bouts" are indicated with the shaded red bars and the bout number is shown in red text above the x-axis. Bouts were detected by thresholding of the difference between tail angle and a sliding median of the tail angle (see §4.5.6.2.2 for the detailed scheme). **D:** Tail angle (upper) and tail curvature (lower) timecourses are shown for two swim bouts, # 10: **D1** and #50: **D2**. **D1** shows a rhythmic, low magnitude swim bout while **D2** shows a more erratic, high-magnitude swim bout. Note that the moment $t = t^*$ is indicated in **D2** with the vertical black line. The magnitude of the swim bout is quantified as the difference between the maximum and minimum of the tail angle over the duration of the bout. The tail curvature heatmaps derived from tail positions show time along the x-axis and caudal to rostral tail position along the y-axis; green regions show positive, "right-handed" curvature while red show negative curvature (see §4.5.6.2.3 for the computation scheme.)
*Note: Infrared imaging was performed at a frame rate of 250 Hz with 850 nm illumination. Both scale bars = 1 mm. y-axis scales are different between **D1** and **D2**.*

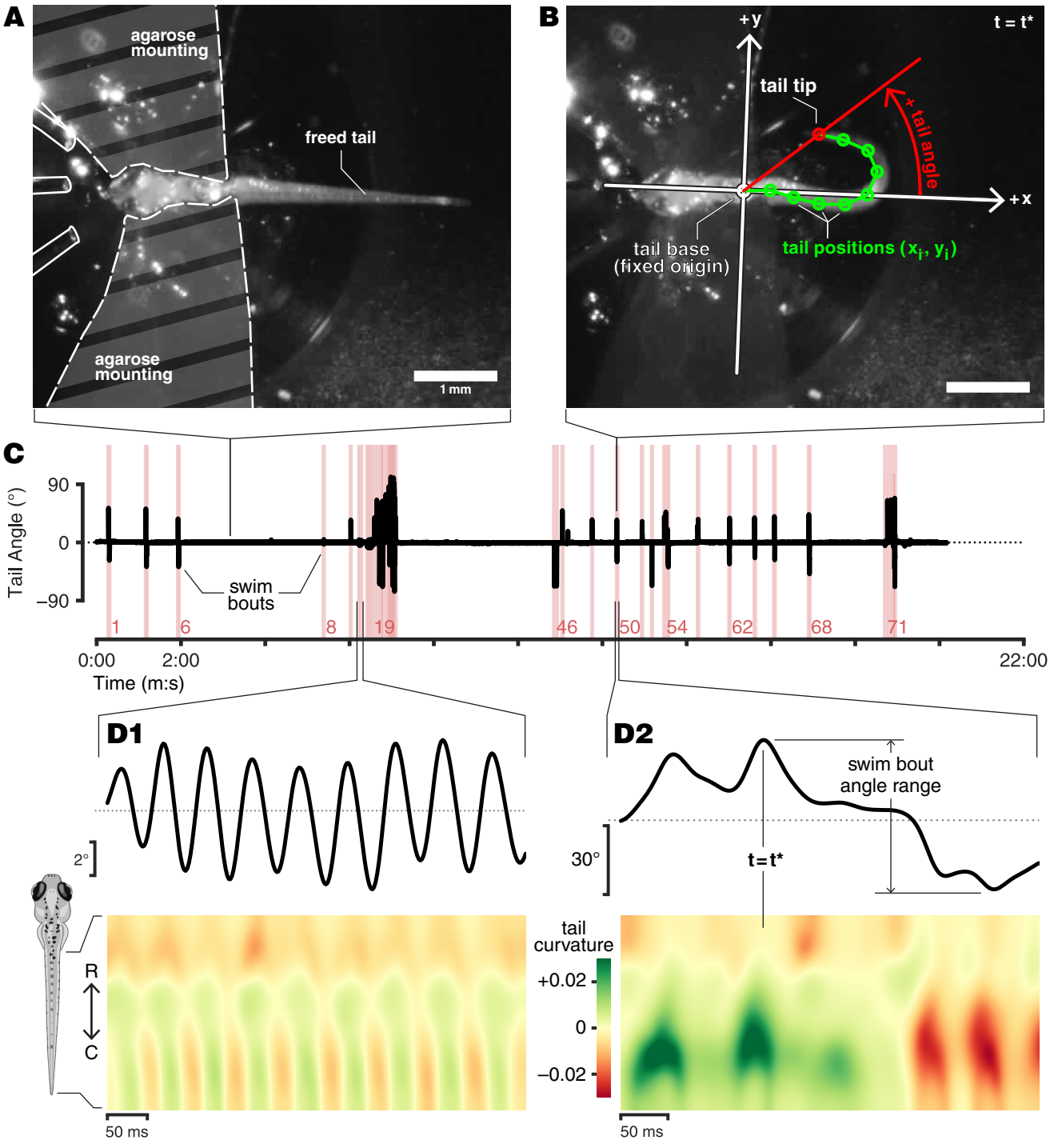
A
agarose mounting
freed tail
agarose mounting
1 mm
B
+y
t = t*
tail tip
+ tail angle
+x
tail base (fixed origin)
tail positions (x_i, y_i)
C
Tail Angle (°)
90
0
–90
swim bouts
1
6
8
19
46
50
54
62
68
71
0:00
2:00
22:00
Time (m:s)
D1
2°
D2
swim bout angle range
30°
t=t*
R
C
tail curvature
+0.02
0
–0.02
50 ms
50 ms

a non-rigid registration; however, the non-rigid registration scheme utilized would sometimes lead to distorted warping of the image volume, particularly evident when inspecting the hull of brain regions after being transformed into the live-image space. Moving forward we can improve the quality of the registration to minimize the extent of distortions in the volume by developing a set of registration metrics which quantify these aberrations and then using those metrics to tune the registration parameters for improved results.

4.4.2.2 Acquisition of Registration "Bridge" Datasets

In order to aid in the registration of live and fixed imaging datasets, we acquired a "bridge" dataset of the larvae immediately after live imaging on the 2P scope at a higher imaging magnification and slower scan rates under treatment with a muscle relaxant to produce a high-resolution, motion artifact-free image. Since the live imaging data is acquired at a significantly relatively lower resolution ($\approx 2 \times 2 \times 5\,\mu$m/pixel in *xyz*) compared to the structural maps ($\approx 0.1 \times 0.1 \times 1\,\mu$m/pixel in *xyz*), we postulated that utilizing an intermediate reference image of the endogenous GCaMP expression could serve as a template for registering the live imaging onto as well as registering structural maps and reference atlas data onto. Moving forward we can compare registration and cell-segmentation pipelines which utilize the bridge data to those that do not to determine if the bridge data collection is a worthwhile procedure.

4.4.3 Issues with Infrared Illumination of the Larva

We struggled to get even illumination of the larva—without flare or reflections—and this led to issues when performing tail imaging and subsequent video analysis. These issues were not so drastic as to prevent successful tail tracking and analysis; however we had to carefully tune the tail tracking parameters in the ZebraZoom software[1] to prevent the software from occasionally tracking reflections instead of the tail itself (this is why we perform

[1] Thank you to Olivier Mirat and the ZebraZoom team for bringing their experience to help in performing this parameter optimization.

Figure 4.10 *(following page)*: We perform whole-brain calcium imaging and utilize it to readout functional activity time-courses across multiple brain regions. A: Maximum intensity projection (MIP) across time and space for a whole brain imaging session. Recording of a larval zebrafish's brain acquired images across 38 *z*-planes over the course of 14 min. Images show *xy*-, *xz*-, and *yz*- projections of the temporal MIP volume. The gray-scale values represent magnitude of detected photons < 575 nm (i.e. green light) emitted by two-photon excitation with 950 nm pulsed laser. In the *xz*-projection, the projection, the the projected outline of three brain regions is shown—blue, **B1**: tectum stratum pereventriculare, green, **B2**: pallium, orange, **B3**: intermediate hypothalamus. These regions were obtained from the Z-brain atlas and registered onto our dataset as described in §4.5.5.3.2 [13]. **B:** For each brain region is shown (upper) an *xy*-slice through the temporal MIP at the indicated *z*-location with the region boundary shaded in the corresponding color. The mean fluorescent signal $F_{\text{raw}}(t)$ over time from all voxels in the region is shown in the line plot (lower). The dashed line represents the baseline value $F_{\text{baseline}}(t)$ computed by a 2 min moving 1% quantile. The shaded region between the baseline and the raw trace represents $\Delta F(t)$. **C:** Line plots show ΔF/Ftime-courses for each region. Dotted line represents the "0%" baseline for each time-course.
Note: Volumetric image acquisition rate was ≈ 1 Hz. Fish shown is cs-ii-29-B, Tg(HuC:H2B-GCaMP8s) undergoing a tactile stimulation trial.

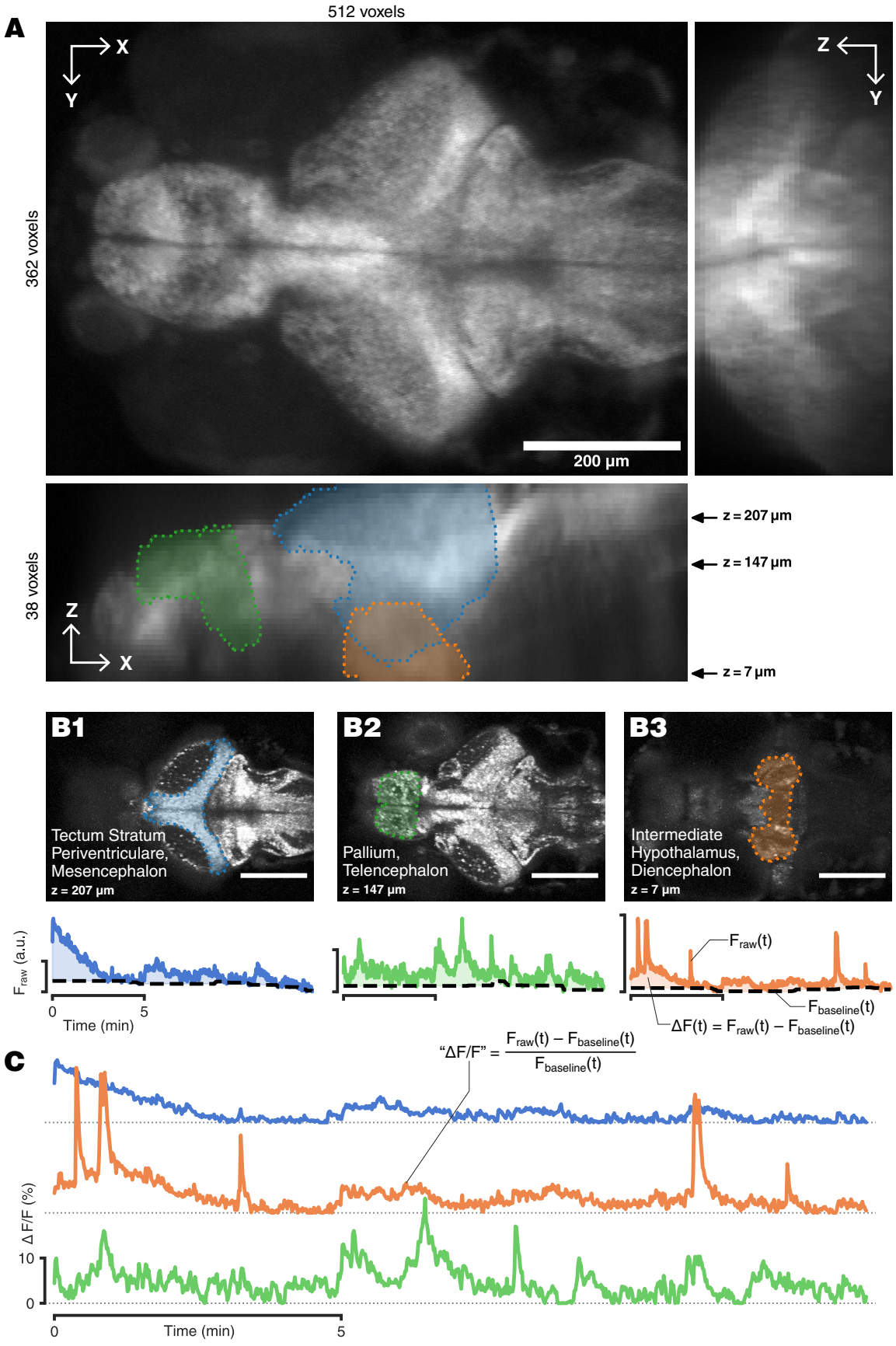
A
512 voxels
362 voxels
X
Y
Z
Y
200 µm
38 voxels
Z
X
z = 207 µm
z = 147 µm
z = 7 µm
B1
Tectum Stratum Periventriculare, Mesencephalon
z = 207 µm
B2
Pallium, Telencephalon
z = 147 µm
B3
Intermediate Hypothalamus, Diencephalon
z = 7 µm
F_raw (a.u.)
0
5
Time (min)
F_raw(t)
F_baseline(t)
ΔF(t) = F_raw(t) – F_baseline(t)
C
"ΔF/F" = (F_raw(t) – F_baseline(t)) / F_baseline(t)
ΔF/F (%)
10
0
0
Time (min)
5

the "glitch" filter described in §4.5.6.2.1). Essentially, because of the objective motion and the angle of the incident infrared light, there would be reflections that would move in the behavioral camera's field of view as the objective moved up and down (another reason to consider remote focusing for the next generation of experiments as mentioned in §4.4.2). To address this issue we can test different illumination sources (e.g. an LED ring light) and illumination directions to see if there is a configuration which reduces or eliminates the flare and reflections.

4.4.4 Immunohistochemistry Protocol Refinement

When we initially started this work, we utilized a combination of protocols developed by Freifeld *et al.* and Randlett *et al.* [13, 16]. However, in our hands the staining results against GCaMP were not of sufficient quality to enable registration of the structural confocal volumetric micrographs onto functional, two-photon volumes. Therefore, over the last years, we have refined a protocol that preserves the structure of the olfactory bulb, and effectively stains against GCaMP in deep ventral brain regions. Briefly we can outline the adjustments made to arrive at the protocol described in §4.5.7, these adjustments are summarized as well in Figure 4.11, Table.

4.11F–G The first modification we made to the protocols was to cut off the tails of the fish immediately following fixation, we believed this might help with creating an opening in the skin for antibody diffusion; however this did not significantly affect staining quality and it had the negative effect of leading to over digestion of the tissue. We also attempted to utilize Proteinase K as a permeabilization agent; however, it's activity was too strong and also led to over digestion.

4.11E We attempted to improve staining by performing a methanol dehydration-freezing-rehydration protocol as utilized by others for improving morphological resolution

Figure 4.11 *(following page)*: We developed a robust method for immunohistochemical staining against GCaMP from superficial to deep brain regions through many protocol adjustments and modifications. All images are spinning-disk confocal micrographs of the GFP antigen*. The first image in each row, sub-panel **1**, is a maximum intensity projection of 6–15 *z*-planes taken over a range from the dorsal top of the brain to ≈ 250 µm ventral down into the brain. Scale bar = 200 µm. The second image in each row, sub-panel **2**, is a single plane at ≈ 200 µm ventral from the top of the brain to give a comparison of staining in deep brain regions. Scale bar = 200 µm. The third image in each row, sub-panel **3**, shows a magnified single plane of the right olfactory bulb and olfactory epithelium, exact region magnified is shown by the white box of sub-panel **1**. Scale bar = 20 µm. The adjacent **Table** outlines the distinct protocol steps† performed (see §4.4.4). The rows, in reverse chronological, are as follows: **A**: *Tg*(HuC:H2B-CGaMP8s). Arrow in **A2** identifies successful staining in center of the ventral brain. **B**: *Tg*(HuC:H2B-GCaMP8s). Arrow in **B2** identifies relatively poor staining in the center of the ventral brain. **C**: *Tg*(HuC:H2B-GCaMP6s). Arrow in **C1** identifies region of over-digestion and damage to structure. **D**: *Tg*(Huc:H2B-GCaMP6s). Arrow in **D2** identifies lack of staining and contrast in the ventral brain region. **E**: *Tg*(Huc:H2B-GCaMP6s). Arrow in **E1** identifies non-specific staining of the larvae's skin tissue. **F**: *Tg*(Huc:GCaMP6s). Arrow in **F1** identifies complete digestion and loss of the tissue and brain structure. **G**: *Tg*(Huc:GCaMP6s). Arrow in **G2** identifies strong non-specific staining of the larvae's skin and lack of antibody penetration.
*Note: *anti-GFP primary antibodies are utilized for staining GCaMP because of the homology of the proteins. †Included **Table** is not a comprehensive list of all protocol steps, rather the table highlights the steps modified or added during the process of protocol refinement; see §§ 4.4.4 and 4.5.7 for a full discussion.*

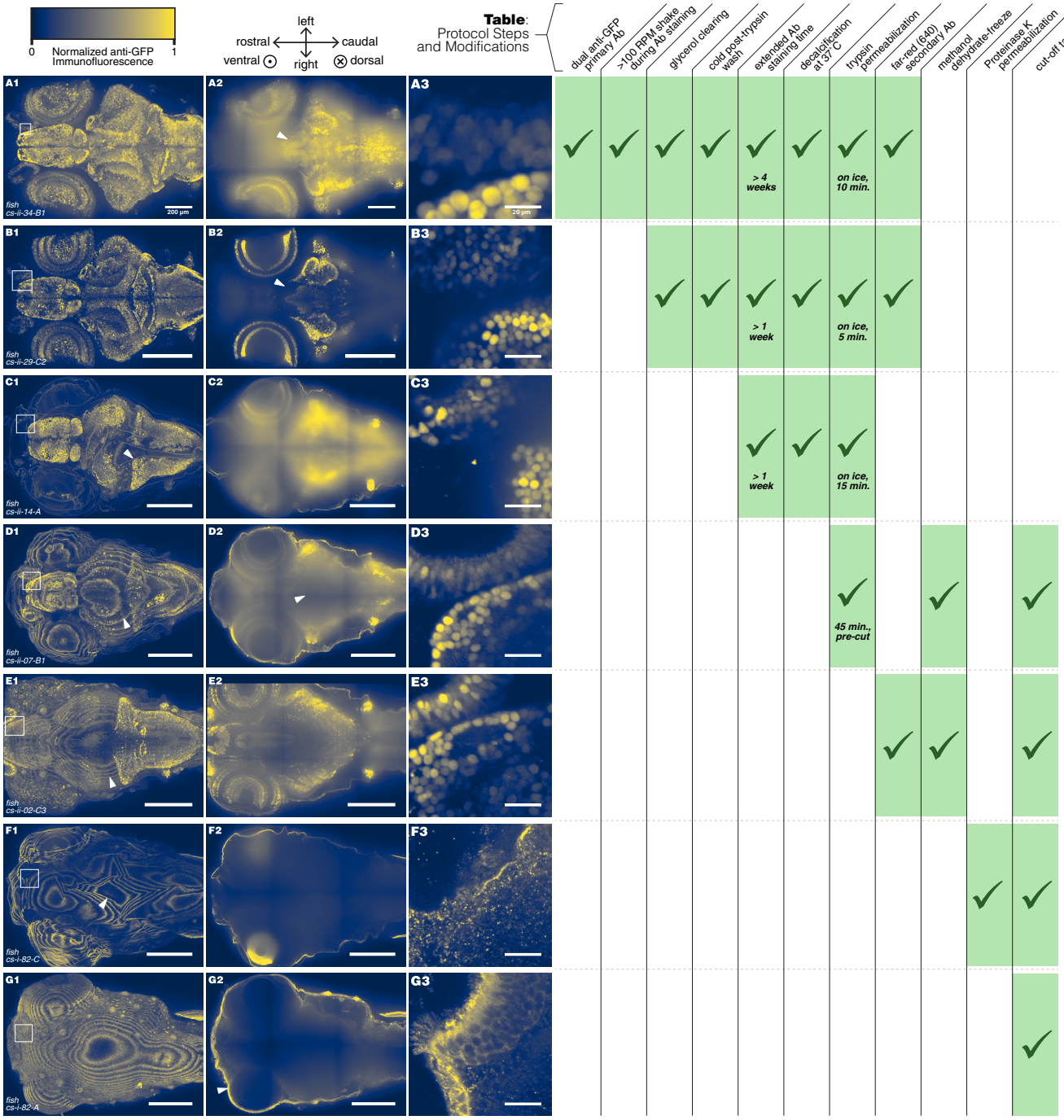
0
Normalized anti-GFP Immunofluorescence
1
left
rostral
caudal
ventral
right
dorsal
Table: Protocol Steps and Modifications
dual anti-GFP primary Ab
>100 RPM shake during Ab staining
glycerol clearing
cold post-trypsin wash
extended Ab staining time
decalcification at 37 C
trypsin permeabilization
far-red (640) secondary Ab
methanol dehydrate-freeze
Proteinase K permeabilization
cut-off tail
A1
A2
A3
B1
B2
B3
C1
C2
C3
D1
D2
D3
E1
E2
E3
F1
F2
F3
G1
G2
G3
fish cs-li-34-B1
fish cs-li-29-C2
fish cs-li-14-A
fish cs-li-07-B1
fish cs-li-02-C3
fish cs-i-82-C
fish cs-i-82-A
200 µm
20 µm
> 4 weeks
on ice, 10 min.
> 1 week
on ice, 5 min.
> 1 week
on ice, 15 min.
45 min., pre-cut

[17, 18]. However this did not improve our imaging results. We also tested utilizing far-red dyes (640 nm) laser line) to improve the imaging of deep regions.

4.11D Protocol was improved by performing trypsin permeabilization of the tissue *prior* to cutting the tail.

4.11C Protocol improved by extending Ab staining time from a few days to > 1 week. We found that performing decalcification at 37 °C increase tissue permeabilization. We made further improvements to limit over-digestion by shortening trypsinization time and performing that step ≈ 0 °C (i.e. on ice) rather than at 4 °C (i.e. in refrigerator).

4.11B Protocol improved by performing clearing of tissue in glycerol (70%) and glycerol-saturated agarose immediately prior to imaging, by performing a washes after trypsinization at 4 °C to limit over-digestion, and by utilizing secondaries for the far-red 640 nm laser line.

4.11A Protocol improved by utilizing a cocktail of two anti-GFP primary antibodies (Abs, and two corresponding secondary Abs with identical fluorophores), by utilizing vigorous 200 RPM shaking for Ab staining incubations, and by incubating samples in Abs for more than 4 weeks.

4.4.4.1 Further Tissue Processing Optimization

As noted in §4.3 and shown in Figure 4.8 we struggled to demonstrate high-quality structural staining for some targets, including Oxytocin receptor, vesicular GABA transporter, and serotonin. It is possible at a step in our tissue processing protocol is masking or deteriorating these antigens and preventing successful staining. We can further test protocol modification to determine how to improve staining across antigens. As a starting point we can determine if our bleaching step (see §4.5.7.3) is leading to the loss of some of these antigens by performing the staining procedure with and without bleaching. The authors of the Z Brain Atlas remark: "bleaching can…destroy antigens and worsen staining" [19] citing Li *et al.* who notice that immunostaining signal in bleached embryos was "much weaker" compared to phenylthiourea (a melanin inhibitor applied to developing embryos and larvae in the water) treatment [20]. We believe further experiments and literature review could enable us to improve the protocol to produce consistent staining results across a wide array of antigens.

4.5 Methods

4.5.1 Transgenic Line Development

The majority of our technology demonstrations and experiments were performed using *nacre*w^2/w^2 zebrafish expressing a fusion protein of calcium indicator jGCaMP8s [3] and

an nuclear localization peptide human histone H2B [21] under the HuC promoter for pan-neuronal expression at the 7 dpf stage [22]. This transgenic line is referred to as *Tg*(HuC:H2B-GCaMP8s) throughout the text.

Plasmids for genetic insertion of this fusion protein were designed using standard methods for Tol2-mediated transgenesis [23]. Plasmids were manufactured by commercial vendors and injected (at 50 ng µL^{-1}) into *nacre*w^2/w^2 1-cell embryos with transposase mRNA (50 ng µL^{-1}, made with mMessage mMachine SP6 kit by Ambion). Injected fish were raised up to sexual maturity and candidate founders were outcrossed and their progeny screened for readily visible green fluorescence in the brain at 2 – 3 dpf. One founder (of 9 tested) had about 15% of F1 progeny inherit an expressing transgene.

4.5.2 Zebrafish Husbandry and Embryo Care

Adult zebrafish were housed in a core facility (Koch Institute Zebrafish Core Facility) in tanks in groups of 3 – 15, fed regularly, and kept on a 14/10 h light/dark cycle. "Fish facility water" was prepared as diluted saline (InstantOcean Sea Salt, InstantOcean SS15-10) mixed to a conductance of 460 µS cm^{-1} and adjusted to a pH of 6.9 to 7.0 by the addition of sodium bicarbonate; this water was circulated through all tanks and continuously monitored, filtered, and pH-corrected.

Adult zebrafish were mated by combining male and female fish in wire-bottomed embryo collection tanks overnight. Embryos (if produced) were collected from the tank floor by pouring tank water and tank rinsate through a fine mesh sieve (tea strainer). Embryos were washed and transferred into fresh fish facility water in 50 – 150 mm dishes and stored at 28 °C on a 14/10 h light/dark cycle. Embryos were washed and cleared of debris and malformed embryos daily for the first 3 days post-fertilization, then every other day through day 7. After day 5, embryos were fed with a suspension of paramecia daily.

All procedures involving animals at the Massachusetts Institute of Technology (MIT) were conducted in accordance with the US National Institutes of Health Guide for the Care and Use of Laboratory Animals and approved by the MIT Committee on Animal Care.

4.5.3 Larvae Mounting and Sample Preparation

To prepare for imaging, larvae were first screened for GCaMP expression. Individual larvae were transferred into wells of a 24-well plate, then examined on an epifluorescence scope and manually scored for expression level and health (e.g. typical swim frequency, heart beat, etc). The highest scoring healthy larvae were set aside to be mounted and imaged for experiments.

Selected zebrafish larvae aged 6 – 7 dpf were then mounted for live imaging. First, an aliquot (e.g. 1.5 mL) of low-gelling-temperature agarose (1.5% in fish facility water) was liquefied, vortexed, and held at 45 °C. Then the zebrafish larva was transferred into a 50 mm glass-bottomed dish (with a 35 mm window) in a small drop of fish facility water. The remaining water around the larva was carefully withdrawn to a minimal volume (≈ 25 µL) then, quickly, a drop (≈ 100 µL) of the warm agarose was applied on top of the larva form-

ing a mound ≈ 10 mm in diameter and 2 mm tall. Very quickly and carefully, the larva was positioned upright near the top of the agarose mound in a straightened body position with the use of fine forceps (Fine Science Tools Dumont #55 Forceps, 11295-51). The agarose embedding the larva was allowed to partially harden by waiting 2 minutes, then agarose was applied around the central mount up to the rim of the 35 mm-diameter window and allowed to harden fully by waiting 5 min.

The nose and tail of the larva were gently freed from the agarose by dissection. To prepare for agarose removal, the agarose was cut with a microknife (Fine Science Tools Dissecting Knife, 10056-12) in a 90° "V" from the larva's nose and in a square "U" from the base of the tail to the rim of the dish window extending ≈ 5 mm to the left and right of tail. The areas of agarose to be removed were then cut in two, one section proximal to the larva and one distal. The distal blocks of agarose were remove first. Then, the dish was filled with fish water above the agarose mound (≈ 10 mL) and the proximal blocks of agarose were gently torn away from the larva's nose (for the rostral block) and off of the larva's tail (for the caudal block). Any blocks agarose now suspended in the dish were removed with a micro-spatula (Fine Science Tools 10092-12 and 10090-17) and suction from wide-tipped pipettes.

After mounting, the larva was maintained at 28 °C until imaging. The protocol for aligning the olfactory stimulation needles to the larva's nose are described in §3.5.6 while the protocols for performing whole brain imaging and tail-imaging is described in the following sections, §§ 4.5.5 and 4.5.6 respectively.

4.5.4 Larvae Imaging Alignment

Dish-mounted larvae would need to be aligned to multiple subsystems before performing imaging experiments: to the sample stage (centered in *xy* on the brain), the behavioral camera (centered in *xy* on the tail), the brain imaging camera (centered in *xy* on the brain), and the olfactory stimulation needles (directed to the nose). The process for stimulation needle alignment is described in §3.5.6 and is performed last, the other alignment procedures are described here.

Before loading the larvae on to the stage and beginning the alignment process, we removed the objective from the nosepiece of the 2P system.

First, we aligned the dish-mounted larvae to the sample stage. The alignment dovetail was inserted into the dish-holding platform, §4.2.2.1 (see also clear plastic bar in Figure 3.8). We then roughly aligned the crosshair of the alignment dovetail to the center of the field of view of the behavioral camera by moving the stage in *xy*. Then we rotated the larvae and dish so that the rostral-caudal axis roughly pointed along the stage's *x* direction and the nose pointed toward the stimulators. After this rough alignment, we placed the dish onto the platform and gently lowered the clamping fork over the rim of the dish by tightening the fork clamping screw. At this point the clamping fork and dish could still translate freely in *x* and *y*. Then using a live feed from the behavioral camera, we aligned the larvae directly over the crosshair of the alignment dovetail. With this, the larvae was

aligned to the stage and we tightened down the dish clamping fork fully to lock the dish and larvae to the stage.

Second, we aligned the larvae's tail to the behavioral camera. We removed the alignment dovetail and illuminated the fish by appropriately positioning the infrared LED assemblies so that we would have a clear view of the fish. Using the x and y sample translation stages, we positioned the larvae's tail in the center of the field of view of the behavioral camera. We would then adjust the zoom of the behavioral camera's lens such that the field-of-view is ≈ 4 tail-lengths in height. Prior to focusing the behavioral camera onto the fish, we would adjust the z-position of the larva to ensure it was roughly aligned to the stimulation direction of the middle stimulator; this was accomplished by extending the middle stimulator toward the fish, then carefully adjusting the z-position of the larvae and the stimulation subsystem such that both would be in the middle of their z-adjustment ranges and the stimulation needle is roughly aligned to the nose of the fish. Finally, the behavioral camera would be focused onto the larva's tail using the z-positioner and the lens's focusing ring. With this, the behavioral camera is aligned onto the larva's tail.

Third, we aligned the 2P imaging objective to the larvae's brain. We raised the nosepiece of the scope to the top of it's adjustment range, then carefully attached our imaging objective (typically the Nikon 16× for whole-brain imaging) to the nosepiece. Then, we put the 2P system in brightfield mode and carefully brought the larva into focus and into field of view by slowly lowering the objective and roughly aligning the illumination light coming out of the objective to the larva's location by eye. Once roughly aligned we use a live feed of the brightfield camera to bring the brain into view and focus. For this alignment we utilize the 2P x- and y scanhead translation servo motors and the 2P z objective translation servo motor. We then switched the imaging to two-photon imaging mode and used a live, low-power, galvo-resonant scan to check the location and orientation of the larvae. Using the live scan preview, we adjusted the z-rotation of the larvae using the stage rotation mount to perfectly align the rostral-caudal axis with the imaging x-axis. Then, using the x-axis rotation stage and y-axis goniometer, we rotated the dorsal-ventral axis of the larva in line with the imaging z-axis and the lateral axis of the larvae with the imaging y-axis. Once this alignment is complete we centered the objective z-piezo (e.g. to $z$piezo = 200 µm for a 400 µm piezo) and move the focal plane to the center of the fish brain using the 2P z servo motor. Then we defined the z-scan range for the z-piezo to cover the brain along its dorso-ventral extent.

Fourth, as previously mentioned, the stimulator needles were aligned to the larva's nose, beginning with the middle needle, then the left and right. During this alignment process sample stage, behavioral camera, and 2P objective positions are not adjusted. See §3.5.6 for the full procedure. With the alignment complete, we moved to perform live imaging.

4.5.5 Two-Photon Whole-Brain Calcium Imaging

4.5.5.1 System Calibration

In a typical 2P imaging session, the first step is to warm-up and calibrate the imaging system (by PrairieView now Bruker). The Ti:Sapphire laser (Spectra Physics MaiTai) is turned on, tuned to 800 nm and allowed to warm up for > 30 min. Then, a fluorescent alignment target is placed at the objective nosepiece and the pitch- and yaw- angles of the alignment mirror coupling the laser into the 2P scan-head are adjusted to center the beam on the target with all galvos centered. For even finer alignment, we can utilize a position power meter (Thorlabs S440C) to quantitatively center the beam.

To calibrate the output power, we first choose a target objective output power which is typical during the imaging session (e.g. Ptarget = 75 mW). We tune the laser to our imaging wavelength 950 nm, and mount the imaging objective (Nikon 16×, CFI75LWD16XW or Olympus 20×, XLUMPLFLN20XW) to the nosepiece of the system and measure the power output from the objective with the scanning galvos centered. We adjust the "pockels" setting in the 2P control software to achieve a reading of Pobj,i, then we record the power reading from the scan-head pick-off window Ppo. We use the ratio

$$A_i = \frac{P_{\text{obj},i}}{P_{\text{po}}} \tag{4.1}$$

to compute an attenuation value Ai for objective i. We utilize this attenuation value to convert pick-off window power readings during imaging to objective power values. Assuming no changes to the light path alignment, these attenuation values can remain accurate over multiple imaging sessions. Typical attenuation values for our system would be 7.49 for the 20× objective and 9.23 for the 16× objective.

After system calibration and prior to imaging we perform the system alignment procedure described in §4.5.4.

4.5.5.2 2P Whole-brain Calcium Imaging

To perform whole-brain calcium imaging we typically imaged in galvo-resonant scan mode at a scan resolution of 512 × 360 voxels in xy respectively, limiting the field of view in y to the the maximum lateral extent of the brain with a small margin. We imaged with a laser wavelength of 950 nm and an approximate continuous power of 73 mW at the objective output. We utilized a GaAsP photodetector adjusted to about 90% of the maximum sensitivity.

z-acquisition would be defined to capture 20 – 50 z-planes depending on the z-resolution and volumetric acquisition rate desired. The z-acquisition was defined to utilize the objective piezo and a "maximum-speed" acquisition mode that calibrates synchronization of the piezo movements and the planar scan. Once set, we define the number of scans to repeat based on the duration of the acquisition, typically 5 – 25 min which is equivalent to 400 – 2000 acquired volumes.

4.5.5.3 Functional Calcium Imaging Analysis

4.5.5.3.1 Calcium Imaging Data Pre-processing Imaging data acquired from our 2P imaging system is output as a directory of image files (`.tiff`) and metadata files (`.xml`). The image files are split arbitrarily, so before further processing, these files must be compiled into a coherent and annotated multi-dimensional dataset. We utilized a custom python library to convert the output from the 2P imaging system into a `numpy.ndarray` wrapped into a custom `ImagingDataset` object with parsed and computed metadata. The library and conversion scheme can be reference in the dissertation repository Appendix A; in short, the main purpose of this conversion was to get the imaging data into a format that could be quickly loaded, was annotated, and could be easily passed to downstream processing steps.

After conversion, the first frame in time was dropped from the dataset because the acquisition rhythm was not yet in a steady-state for the first frame and therefore the imaged z-locations were out of alignment with the rest of the data set. Also, the first two z-planes were dropped from datasets with unidirectional scanning, since these planes would show a "flyback" artifact due to the rapid return of the objective to the top of the scan at the beginning of each volumetric acquisition.

4.5.5.3.2 Extraction of Regional Calcium Activity Timecourses To perform analysis of calcium activity in different anatomical regions, Figure 4.10B, we first aligned the data to a reference anatomical database. We utilized the "Z Brain Atlas"—originally produced by the Engert and Schier Labs at Harvard University in 2015—as our reference ([13] and hosted online at `https://zebrafishexplorer.zib.de`). The Z Brain Atlas contains aligned volumetric imaging data from an array of different stained antigens and various transgenic larvae with specific promoters driving expression of fluorescent proteins as well as aligned volumetric binary masks of ≈ 300 named anatomical brain regions. All Z Brain Atlas data is taken from larvae aged 6 dpf.

We performed non-rigid alignment using the Computational Morphometry Toolkit (CMTK) Python package between a maximum intensity projection (MIP) through time of each of our calcium imaging dataset and the *Tg*(elavl3:H2B-RFP) transgenic Z Brain Atlas dataset since the expression patterns are expected to be similar to our transgenic fish,[2] a typical registration result is shown in Figure 4.7. We then utilized this alignment transform to computationally register all of the binary region masks into the "live" image space. Then, for each region i we took the average of all region voxels at each timepoint to produce the raw fluorescent timecourses $F_{\text{raw},i}(t)$. We computed a baseline $F_{\text{baseline},i}(t)$ by taking a ≈ 4 min, right-aligned (i.e. only consider past values for the rolling computation), rolling,

[2] *elavl3* and *HuC* are different names for the same promoter, see §4.5.1 and [22, 24] for context of the different namings.

1% quantile of $F_{\text{raw},i}(t)$ and backfilling the from $F_{\text{baseline},i}(t = 250\,\text{s})$ to all prior timepoints[3].

$$F_{\text{baseline},i}(t = t_n) = \texttt{quantile}_{0.01}\left[F_i(t = t_{n-W}), \ldots, F_i(t = t_n)\right] \tag{4.2}$$

Finally the relative fluorescent intensity $(\Delta F/F)_i(t)$ was computed as

$$\left(\frac{\Delta F}{F}\right)_i(t) = \max\left\{0, \frac{F_{\text{raw},i}(t) - F_{\text{baseline},i}(t)}{F_{\text{baseline},i}(t)}\right\}. \tag{4.3}$$

This scheme is annotated in Figure 4.10B–C.

4.5.6 Behavioral Recording

Once the behavioral camera is aligned to image the tail and the other imaging and stimulation components are positioned as described in §4.5.4, we performed a final adjustment of the inferred LED illumination assemblies. Because the objective and stimulation needles can cause undesired reflections and block the illumination light, it was important to ensure the LEDs were put in the best position to minimize these issues. We also adjusted the iris on the output of the LEDs to maximize illumination intensity on the tail and minimize ghosting and flare from excess light and reflections. With these illumination adjustments made, we then moved to define our imaging parameters.

We utilized a the Pixelink Capture OEM software[4] for image acquisition. Typically, 2 × 2 pixel binning was turned on, a square region of interest (ROI) was defined around the the fish with the tail centered, the frame rate was set to 250 fps, and the sensor gain adjusted near it's maximum setting. The duration of the recording was usually set to be 10 – 20 s longer than the synchronized 2P acquisition, and a hardware trigger was primed such that acquisition began with a TTL signal to the camera. A full discussion of the synchronization and triggering of the imaging and stimulation systems is provided in §5.4.1. Images were recorded into a software-specific raw binary `.pds` (i.e. Pixelink data stream) file.

4.5.6.1 Video Conversion and Pre-Processing

After acquisition, the raw `.pds` file was converted to a standard video format (we utilized `.avi`) and the time stamp of each frame was extracted. This conversion was performed using a custom C++ script utilizing the Pixelink API to read each frame's image data and metadata from the `.pds` file. The extracted data was used to produce a `.avi` video file using the OpenCV API and a `.csv` file containing a table of each frame's integer index and timestamp in nanoseconds. For a further discussion of this conversion software and relevant code samples, see Appendix A.

[3] e.g. with the code `df.rolling(window=(250*frame_rate)).quantile(0.01).bfill()`, see https://pandas.pydata.org/docs/reference/api/pandas.DataFrame.rolling.html

[4] which is part of the Pixelink software development kit; it can be found at https://pixelink.com/products/software/sdk/

4.5.6.2 Tail Movement Quantification

Following the conversion of the files, we utilized the ZebraZoom python software to analyze the `.avi` file and extract tail angle and tail position at each video frame. ZebraZoom provides a graphical user interface (GUI) for performing the video analysis and setting the tail tracking parameters, typical parameters utilized for analysis are shown in . After defining the analysis parameters by referencing a few example frames, we used the ZebraZoom GUI to analyze the entire video producing an `.h5` file with the analysis results. The analysis results `.h5` file contained data arrays for the measured tail angle and the tracked tail *xy*-positions at 9 points from the tail base to the tail tip for every frame of the video. These data were compiled into a data table (i.e. a `pandas.DataFrame` in python) for the entire video.

4.5.6.2.1 Handling Video Issues Before moving to other processing steps, we needed to deal with two issues: 1) noise in the tracking results and 2) dropped frames in the original recording.

There were multiple types of noise in the tracking output due to issues with the tracking and noise in the original video. We primarily addressed "glitches" in the tracking results marked by a value in a vector drastically different from the preceding and following values. We suppressed these glitch values issue by taking a three-sample, right-aligned rolling median for every data vector in the data table. This median-filtered data table was then ready for further processing.

Because of the nature of the high speed recording, there were occasionally frames scheduled to be captured, but that were ultimately not written to the `.pds` file. Therefore the time t_n of frame n could not be assumed to be given by

$$t_n = n \times F_o \tag{4.4}$$

where F_o is the original frame rate in Hz. Rather we had to use the `.csv` file record of each frame's time to "look up" the time of each frame. As a result, the temporal pitch from frame to frame was not consistent. To make the data table of tail parameters homogeneously spaced in time, we resampled the raw table to $\gtrsim$ twice[5] the original frame rate, $F_{rs} = 500\,\text{Hz}$, linearly interpolating between samples. We then applied a Gaussian filter to the data with a standard deviation $\sigma = 3/F_o\,\text{s}$ to smooth any artefacts produced from the oversampling step.

After these two data-cleaning steps we had a new data table with reduced noise and homogeneous sampling in time.

4.5.6.2.2 Swim Bout Detection To detect when bouts of tail motion occurred within the recording, we utilized a scheme similar to Mirat *et al.* [26]. In short, we used the tail

[5] We *over*sample to a bit more than twice the original frame rate to minimize any information loss from the original data as informed by the Nyquist-Shannon sampling theorem [25].

angle time-series $\theta(t)$ and produced a baseline time-series $\theta_b(t)$ by taking a 30 ms rolling mean of $\theta(t)$. We then considered tail movement to "occur" when

$$|\theta(t) - \theta_b(t)| > 1.15° . \tag{4.5}$$

Regions of movement, by this definition, were merged into a single bout if they were less than 75 ms apart. Finally, bouts of movement that were otherwise detected, but had an angle range < 3° were not considered to be valid bouts of movement. This protocol essentially generated a one-dimensional binary mask having value `1` at time-points during a movement bout and value `0` for all other time-points when the tail is not flagged as moving. The results of this procedure are shown by the red-colored regions in Figure 4.9C.

4.5.6.2.3 Curvature Calculation With the resampled and filtered tail tracking data table, we could utilized the vector of tail x and y locations $\langle x(t,u),\ y(t,u)\rangle$ to compute the curvature $c(t,u)$ along the length of the tail where t is time and u is the distance along the tail. The curvature at along the tail over time is given by:

$$c(t,u) = \frac{\frac{\partial x(t,u)}{\partial u}\frac{\partial^2 y(t,u)}{\partial u^2} - \frac{\partial y(t,u)}{\partial u}\frac{d^2 x(t,u)}{\partial u^2}}{\left(x^2(t,u) + y^2(t,u)\right)^{(3/2)}} . \tag{4.6}$$

By this formulation positive curvature represents a right-handed bend and negative curvature represents a left-handed bend of the tail. We assume the spacing between tail points is uniform, so u can be considered the integer index of the tail position from $u = 0$ at the tail base to $u = 9$ at the tail tip.

4.5.7 Immunofluorescent Staining and Imaging

4.5.7.1 Tissue Processing with Mesh Baskets

Zebrafish larvae were treated using basket processing. For this method, solutions were pre-pipetted into the wells of a 6-, 12-, or 24-well plate and the larvae were transferred between these solutions in mesh baskets. This method does not require decanting solutions with a pipette, Well plate cell culture inserts were used as the baskets (with the largest pore size to allow for drainage). However, cell strainers can also function as baskets, though these typically will only fit into 6-well plates. Baskets can also be constructed manually (see Thisse Lab protocol, "Equipment Setup" section) from plastic tubes and mesh. To transfer the larvae between solutions, a working volume of the next solution was first pipetted into an empty well. Working volumes used were 5 mL, 2.5 mL, and 1.5 mL for 6-, 12-, and 24-well plates respectively. Then, using forceps the basket was quickly dabbed on a blotting surface (usually a clean Kimwipe over a bed of paper towels) to remove excess liquid. Where-after the basket would be carefully placed into the well containing the next solution. The basket was placed in at an angle to prevent trapping bubbles underneath the mesh bottom. It should be noted that when beginning a wash step, it may be advantageous to "rinse" the

larvae and basket first. This can be done by preparing two "rinsing" wells of washing solution, where the larvae are processed and transferred through these two rinsing wells (with no incubation time) before beginning the first wash.

PBS-Tween, our washing solution, was prepared as a solution of 0.1% w/v Tween-20 (polyoxyethylene (20) sorbitan monolaurate) in 1× phosphate buffered saline (PBS) in 18 MΩ water (ddH_2O). All washes were performed with PBS-Tween on an orbital shaker unless otherwise indicated.

4.5.7.2 Tissue Fixation

Zebrafish larvae aged 5 – 7 days post-fertilization (dpf) were fixed in a freshly prepared solution of buffered paraformaldehyde (4% w/v in 1× PBS) at 4 °C with shaking for 1 overnight (12 – 24 h). Following fixation, the larvae were washed at room temperature (RT) 6 times for 10 minutes per wash (6 × 10 min).

4.5.7.3 Tissue Preparation

The zebrafish larvae were bleached in bleaching buffer (0.75% w/v KOH, 0.8% w/v peroxide, 0.1% w/v Tween 20 in ddH_2O) in darkness at RT for 4 hours (or until the eyes lost all pigment). The larvae were then washed at RT 3 × 10 min. Next, the larvae were decalcified in bone decalcification buffer (50 mM Na_2 • EDTA, 0.75% w/v Triton X-100 in 1× PBS) at RT with shaking overnight, then washed at RT 3 × 10 min. Following this treatment, for the purposes of antigen retrieval the larvae were transferred into Tris-HCl (150 mM, pH 9.0) and incubated at RT for 5 minutes, then at 70 °C with shaking (200 revolutions per minute (RPM)) for 15 minutes, then washed at RT 3 × 10 min. The larvae were pre-incubated in PBS-Tween at 0 °C (i.e. on ice) for 5 min to ensure the tissue was chilled. Then, larvae were permeabilized with Trypsin-EDTA (0.05% Trypsin-EDTA in washing solution) and incubated at 0 °C with shaking for exactly 10 min. Permeabilization was halted with one wash at 4 °C for 5 min, followed by 3 × 10 min washes at RT.

4.5.7.4 Immunohistochemistry

The zebrafish larvae were incubated in blocking solution (2% v/v normal donkey[6] serum, 1% w/v bovine serum albumin, 1% v/v dimethyl sulfoxide in washing solution) at RT while shaking for at least 1 hour as a pre-blocking step. The larvae were then incubated with primary antibodies diluted in blocking solution at 4 °C for 1 – 4 weeks, shaking at 150 RPM minimum. The primary staining cocktail was replaced with an identical freshly prepared mixture about halfway through the staining run. Following this, the larvae were washed at RT 9 × 10 min, then washed once at 4 °C overnight. The larvae were then transferred into blocking solution and incubated at RT while shaking for at least 1 hour as a second pre-blocking step. Next, the larvae were incubated with secondary antibodies diluted 1:500 in blocking solution at 4 °C for 1 – 4 weeks with shaking at 150 RPM minimum. The secondary

[6] Donkey serum should be replaced with serum from the host in which the secondary antibodies were raised.

staining cocktail was replaced with an identical freshly prepared mixture halfway through the staining run. If performed, nuclei were stained with DAPI (1:500 dilution in blocking solution) for 2 overnights at the end of the staining process.

4.5.7.5 Glycerol Clearing

To prepare for imaging, the larvae were optically cleared (i.e. tissue rendered less scattering) through incubation in increasing concentrations of glycerol. After complete washing out of staining reagents, the larvae were incubated in 25% glycerol (25% glycerol in 1× PBS) at RT with shaking for 30 min, followed by 30 min incubations in 50% glycerol and, finally, 70% glycerol (both w/w in 1× PBS) [27].[7]

4.5.7.6 Mounting

Stained and cleared larvae were mounted in glycerol-saturated agaorse for imaging on an inverted microscope. An aliquot (≈ 1.5 mL) of glycerol-saturated agarose (60% w/w glycerol[8], 2% agarose in 1× PBS) was heated to 85 °C[9], held at 85 °C for 4 min to fully liquefy, vigorously vortexed for 60 s to homogenize, then held at 55 °C to maintain in the molten state. In a glass-bottomed dish (typically a Ø35 mm dish with a Ø5 mm glass window) a small drop of 70% glycerol (≈ 20 µL) was placed in the center of the dish. Then, very carefully, a single larva was transferred from the processing basket into the 70% glycerol drop using fine angled forceps (Fine Science Tools Dumont #5/45 Forceps, 11251-35) holding the larva by the end of its tail[10]. The warm glycerol-saturated agarose was then pipetted onto the larva, completely filling the windowed region of the dish (≈ 500 µL). Quickly, while the agarose was molten, the larva was straightened, pushed to the bottom of the dish, and oriented such that the dorsal brain is pointed down to the glass window (for imaging on our inverted confocal) with the use of fine forceps (Fine Science Tools Dumont #55 Forceps, 11295-51). The agarose was allowed to harden for ≈ 5 min then 70% glycerol (≈ 5 mL) was added to the dish to further saturate the agarose and tissue. The mounted larva was incubated at 4 °C with gentle shaking (30 – 60 RPM) for > 1 h to allow the agarose to completely set.

4.5.7.7 Confocal Imaging

To obtain images of the stained, cleared, and mounted larvae, we utilized a spinning disk confocal microscope (Nikon and Andor) and performed standard imaging techniques. Typical imaging parameters were 40×objective, 6 fields of view per z-planes, 10 z-planes at

[7] Thank you to Erin Song as well as the Kunes and Engert Laboratories at Harvard for showing me and helping me to implement this clearing step

[8] A 70% w/w glycerol, 2% agarose solution does not fully gel due to the high glycerol concentration and is not suitable for larvae mounting; based on our tests, reducing the glycerol concentration to 60% w/w ameliorates this issue while also not causing any "de-clearing" of the tissue.

[9] the temperature of the glycerol-saturate agarose should not be allow to increase above 90 °C since the dissolved glycerol will begin to quickly degrade and yellow above this temperature.

[10] the larvae are very sticky once in 70% glycerol, so using a pipette to transfer the tissue is not done at this point since the the tissue will often adhere to the walls of pipettes

20 µm spacing for low resolution test images (or 200 z-planes at 1 µm for high resolution datasets), imaged on 405 nm, 488 nm, 561 nm, and 633 nm standard imaging channels depending on the secondary antibodies utilized.

4.6 Conclusion

In this chapter we have first shown the design and successful implementation of a system for recording of larval tail motion. We have also demonstrated our ability to quantify those recordings into a timeline of detected bouts of tail motion. Second, We have shown the ability to perform whole-brain calcium imaging using galvo/resonant two-photon microscopy, register those recordings onto an anatomical atlas and then segment and normalize voxel values into calcium traces. Third, we have presented an optimized and expansion microscopy-compatible protocol for immunohistochemical staining against GCaMP (for registration) and other relevant epitopes. The development of the hardware, processing pipelines, and methods to achieve each of these readouts primes us to move toward integration, bringing together all of these modalities along with stimulation to enable rich, multi-modal experiment-driven datasets to push forward the goal of understanding sensory processing.

4.7 References

1. Yasuda, R. *et al.* Imaging calcium concentration dynamics in small neuronal compartments. *Science's STKE : signal transduction knowledge environment* **2004.** ISSN: 15258882. https://www.science.org/doi/10.1126/stke.2192004p15 (219 Feb. 2004).
2. Mank, M. & Griesbeck, O. Genetically encoded calcium indicators. *Chemical Reviews* **108,** 1550–1564. ISSN: 00092665. https://pubs.acs.org/doi/full/10.1021/cr078213v (5 May 2008).
3. Zhang, Y. *et al. jGCaMP8 Fast Genetically Encoded Calcium Indicators* (Nov. 2020). https://janelia.figshare.com/articles/online_resource/jGCaMP8_Fast_Genetically_Encoded_Calcium_Indicators/13148243.
4. Grienberger, C. & Konnerth, A. Imaging Calcium in Neurons. *Neuron* **73,** 862–885. ISSN: 0896-6273. http://www.cell.com/article/S0896627312001729/fulltext (5 Mar. 2012).
5. Weisenburger, S., Prevedel, R. & Vaziri, A. Quantitative evaluation of two-photon calcium imaging modalities for high-speed volumetric calcium imaging in scattering brain tissue. *bioRxiv,* 115659. https://www.biorxiv.org/content/10.1101/115659v1 (Mar. 2017).
6. Stosiek, C., Garaschuk, O., Holthoff, K. & Konnerth, A. In vivo two-photon calcium imaging of neuronal networks. *Proceedings of the National Academy of Sciences* **100,** 7319–7324. ISSN: 00278424. https://www.pnas.org/doi/abs/10.1073/pnas.1232232100 (12 June 2003).
7. Keiser, G. in *Biophotonics: Concepts to Applications* 147–196 (Springer Singapore, Singapore, 2016). ISBN: 978-981-10-0945-7. https://doi.org/10.1007/978-981-10-0945-7_6.
8. Shaw, P. A. *et al.* Two-Photon Absorption: An Open Door to the NIR-II Biological Window? *Frontiers in Chemistry* **10,** 921354. ISSN: 22962646 (June 2022).
9. De Vito, G. *et al.* Fast whole-brain imaging of seizures in zebrafish larvae by two-photon light-sheet microscopy. *Biomed. Opt. Express* **13,** 1516–1536. https://opg.optica.org/boe/abstract.cfm?URI=boe-13-3-1516 (Mar. 2022).
10. Lin, A. *et al.* Imaging whole-brain activity to understand behaviour. *Nature Reviews Physics 2022 4:5* **4,** 292–305. ISSN: 2522-5820. https://www.nature.com/articles/s42254-022-00430-w (5 Mar. 2022).
11. Wee, C. L. *et al.* Social isolation modulates appetite and avoidance behavior via a common oxytocinergic circuit in larval zebrafish. *Nature Communications 2022 13:1* **13,** 1–17. ISSN: 2041-1723. https://www.nature.com/articles/s41467-022-29765-9 (1 May 2022).

12. Hammond-Weinberger, D. R. & Zeruth, G. T. Whole mount immunohistochemistry in zebrafish embryos and larvae. *Journal of Visualized Experiments* **2020.** ISSN: 1940087X. https://app.jove.com/t/60575 (155 Jan. 2019).

13. Randlett, O. *et al.* Whole-brain activity mapping onto a zebrafish brain atlas. *Nature Methods* **12,** 1039–1046. ISSN: 1548-7091. http://www.nature.com/articles/nmeth.3581 (11 Nov. 2015).

14. Corradi, L., Zaupa, M., Sawamiphak, S. & Filosa, A. Using pERK immunostaining to quantify neuronal activity induced by stress in zebrafish larvae. *STAR Protocols* **3,** 101731. ISSN: 2666-1667 (4 Dec. 2022).

15. Rosen, L. B., Ginty, D. D., Weber, M. J. & Greenberg, M. E. Membrane Depolarization and Calcium Influx Stimulate MEK and MAP Kinase via Activation of Ras. *Neuron* **12,** 1207–1221. https://doi.org/10.1016/0896-6273(94)90438-3 (1994).

16. Freifeld, L. *et al.* Expansion microscopy of zebrafish for neuroscience and developmental biology studies. *Proceedings of the National Academy of Sciences of the United States of America* **114,** E10799–E10808. ISSN: 1091-6490. http://www.ncbi.nlm.nih.gov/pubmed/29162696 (50 Dec. 2017).

17. Zimmerman, S. G., Peters, N. C., Altaras, A. E. & Berg, C. A. Optimized RNA ISH, RNA FISH and protein-RNA double labeling (IF/FISH) in Drosophila ovaries. *Nature Protocols 2013 8:11* **8,** 2158–2179. ISSN: 1750-2799. https://www.nature.com/articles/nprot.2013.136 (11 Oct. 2013).

18. Schulte-Merker, S. in Westerfield, M. *The Zebrafish Book. A Guide for the Laboratory Use of Zebrafish (Danio rerio)* 4th ed. Chap. 9 Sec. 8 (University of Oregon Press, Eugene, OR, USA, 2000). https://zfin.org/zf_info/zfbook/chapt9/9.8.html.

19. *Frequently Asked Questions, Z Brain Atlas, Engert Lab* https://zebrafishexplorer.zib.de/faq.

20. Li, Z. *et al.* Phenylthiourea Specifically Reduces Zebrafish Eye Size. *PLOS ONE* **7,** e40132. ISSN: 1932-6203. https://journals.plos.org/plosone/article?id=10.1371/journal.pone.0040132 (6 June 2012).

21. Fetcho, J. R. & Liu, K. S. Histone–GFP fusion protein enables sensitive analysis of chromosome dynamics in living mammalian cells. *Current Biology* **8,** 377–385. ISSN: 0960-9822 (7 Mar. 1998).

22. Kim, C. H. *et al.* Zebrafish elav/HuC homologue as a very early neuronal marker. *Neuroscience Letters* **216,** 109–112. ISSN: 0304-3940. https://doi.org/10.1016/0304-3940(96)13021-4 (2 Sept. 1996).

23. Kwan, K. M. *et al.* The Tol2kit: A multisite gateway-based construction kit for Tol2 transposon transgenesis constructs. *Developmental Dynamics* **236,** 3088–3099. ISSN: 1097-0177. https://onlinelibrary.wiley.com/doi/full/10.1002/dvdy.21343 (11 Nov. 2007).

24. Good, P. J. A conserved family of elav-like genes in vertebrates. *Proceedings of the National Academy of Sciences* **92,** 4557–4561. ISSN: 00278424. https://www.pnas.org/doi/abs/10.1073/pnas.92.10.4557 (10 May 1995).

25. Shannon, C. E. Communication in the Presence of Noise. *Proceedings of the IEEE* **86,** 447–457. http://astro.if.ufrgs.br/med/imagens/shannon.pdf (2 Feb. 1998).

26. Mirat, O., Sternberg, J. R., Severi, K. E. & Wyart, C. ZebraZoom: An automated program for high-throughput behavioral analysis and categorization. *Frontiers in Neural Circuits* **7,** 48122. ISSN: 16625110 (June 2013).

27. Wee, C. L. *et al.* A bidirectional network for appetite control in larval zebrafish. *eLife* **8.** ISSN: 2050084X (Oct. 2019).

CHAPTER 5

Integration: Correlation of Data Across Modalities in a Single Zebrafish

5.1 Introduction

The ultimate goal of this thesis work is to integrate our knowledge of larval zebrafish behavior, the context of controlled olfactory stimulation, functional imaging of neural activity, behavioral imaging of tail movements, and structural maps of epitope markers of interest. This combination requires the validation of each of these techniques individually (as shown in Chapters 3 and 4), an experimental framework which is able to benefit form the various modalities, and the data processing and analysis pipeline to integrate and correlate the results across modalities.

Given the time required to develop the technology and hardware—including investment in design, assembly, iteration, integration, debugging, and application—necessary to do these correlative experiments, the results in this chapter will have a relatively narrow scope. We will focus primarily on a few pieces of pilot data which demonstrate the kinds of experiments that we have the capability of performing rather than attempting to showcase a robust series of hypothesis-driven experiments. Although we do discuss our plans for some such biologically interesting experiments in §5.3.5.

As mentioned in §3.1.1 there have been some previous exploration of the bi-lateral processing of olfactory inputs by Sy *et al.* [1]. For our pilot demonstration experiment, we chose to replicate an experiment from [1]. In their bilateral stimulation experiment Sy *et al.* present the larva with ≈ 30 s pulses with cadaverine to the left olfactory epithelium (OE) alone, right OE alone, or both OEs (see Figure 3.35C) to compare calcium responses for the different stimulus directions. Additionally, to leverage the capabilities of our system to stimulate with more than one odor, we extended on the protocol from Sy *et al.* and also performed stimulation of the left and right olfactory epithelia with different odors simul-

taneously. This experiment aimed to prob how activity changes and behavioral responses modulate when different odors are presented alone versus at the same time.

5.2 Results

Here we present results from three experiments integrating stimulation, olfactory presentation, and behavioral observation. The first experiment, shown in Figures 5.1 and 5.2, was a positive control run of the system where a tactile pulses of water (no odor) are applied to the fish's nose. We also combined the results from two proof-of-concept experiments in Figures 5.5 and 5.6 where we performed stimulation with cadaverine, amino acids, and a negative control (fish water) from both lateral directions. Finally, we present the results from preliminary trials to register structural and functional data.

5.2.1 Positive Control Tactile Pulse Trials

Two photon calcium imaging region-segmented and combined over multiple tactile pulse trials revealed an increase in calcium activity at stimulus onset for almost all neurons as well as a decrease in calcium activity at stimulus cessation (Figure 5.1). We also observed that some of the rostral-most brain regions show a decrease from baseline calcium activity during the course of the stimulus which then returned to baseline once the stimulus ended including the olfactory bulb and olfactory epithelium (Figure 5.2A1). There are also a collection of caudal brain regions (annotated "C1" in Figure 5.2C) which show show relatively strong calcium pulsations during the stimulus interval Table 5.1.

An analysis of statistical significance across stimulation trials between various time windows (pre-stimulation, early post-stimulation, etc.) reveals 39 regional comparisons having a $p < 0.01$ and an effect size $\Delta\,(\Delta F/F)$ of at least 10 % (Figure 5.2B). Among these we observed a subset of regions which show strong calcium activity that initiates after stimulus cessation including the Preoptic Otpb Cluster, the Vglut2 cluster 3, and the Caudal Hypothalamus, Figure 5.2A2. We also see these regions cluster (by a negative correlation distance metric) together in cluster annotated C2 in Figure 5.2C, Table 5.3. Furthermore, the activation of these regions corresponds to the observed timing of swim bouts; namely, we see a jump in the number of swim bouts at stimulus cessation (Figure 5.2D–E).

5.2.2 Bilateral Odor Stimulation Trials

Region-segmented calcium imaging data combined across trials of stimulation with odors pulses from both left and right show a stereotyped response (even to control odor application) in the rostral-most brain regions including the olfactory bulb and olfactory epithelia, see the tops of each heatmap in Figure 5.3. This response appears as the rise in calcium activity over the first ≈ 10 s of stimulation and a fall in the calcium activity after ≈ 20 s after stimulus cessation. The cadaverine stimulation appears to show a brief, brain-wide calcium pulse ≈ 10 s after stimulus onset, Figure 5.3A. The amino acid stimulation appears to show an extended, brain-wide increase in calcium signal for the duration of the stimulation

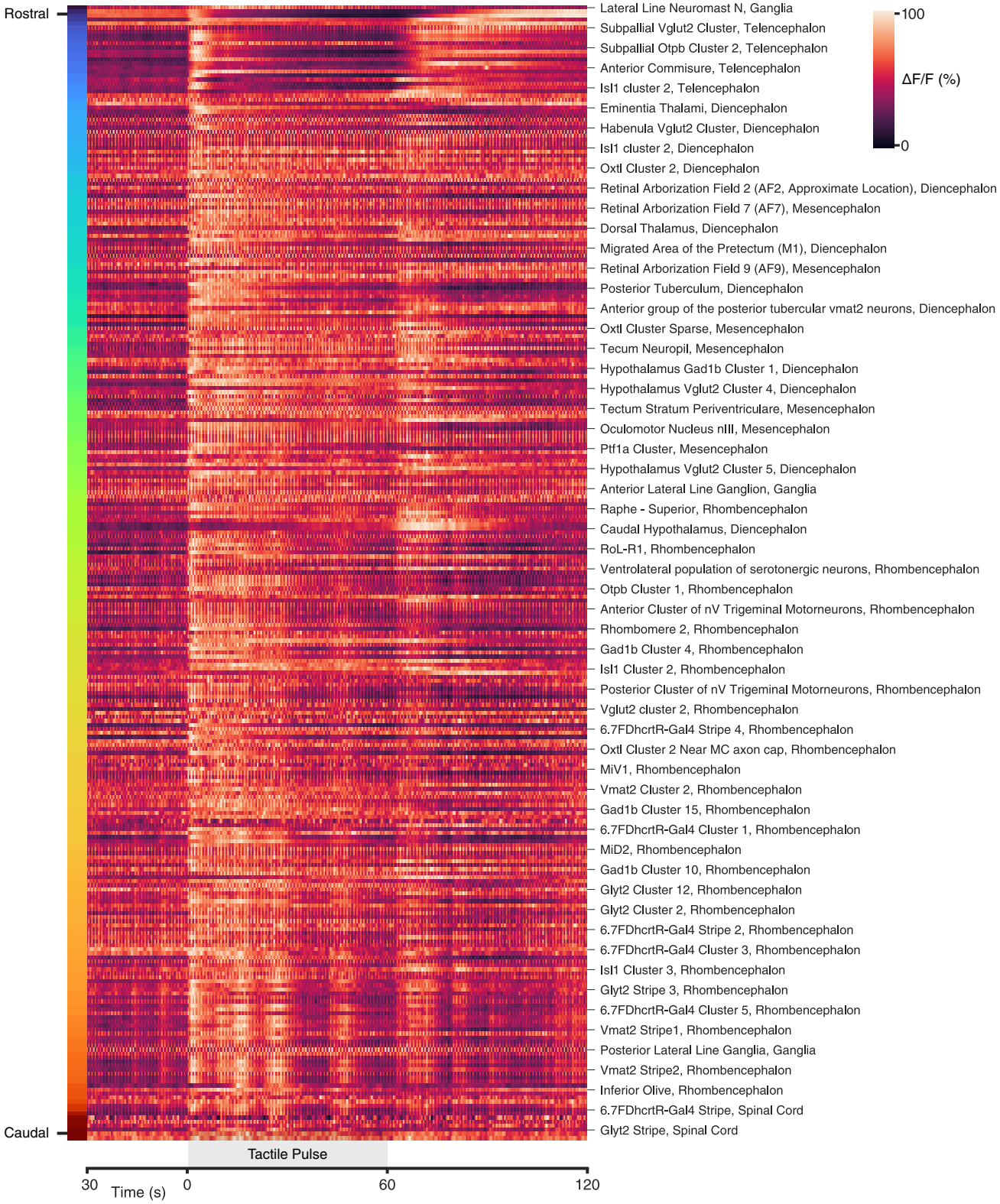

Figure 5.1: Whole-brain imaging reveals cross-regional calcium activity responses at tactile pulse onset and cessation. Heatmap of calcium activity responses across ≈ 300 brain regions averaged across ≈ 10 tactile pulse trials; the *x*-axis represents time with the tactile pulse applied from $t = 0 - 60$ s (gray shaded patch); regions are ordered and colored along the *y*-axis by the position* in the brain along the from caudal to rostral (colors correspond to left axis clustered heatmap in Figure 5.2B); brighter patches of the heatmap represent larger ΔF/F according to the colorbar in the top right.
*Note: *Region position is computed by taking the average x-position of all voxels in the brain region mask.*

and persisting for a few seconds after stimulus cessation, Figure 5.3B. The negative control stimulation does not appear to show a noticeable response in most of the central and more caudal brain regions, Figure 5.3.

We observe a strong increase calcium signal in the subpallial dopaminergic cluster immediately after amino acid stimulus cessation when the odor was delivered from the left side Figure 5.5B. This response pattern was not observed for the subpallial dopaminergic cluster for any other stimulation trials with different odors or tactile pulse. Stimulation with cadaverine (we were only able to obtain data for the trials with stimulation coming from both directions) shows an increase across a few brain regions in response to stimulus onset. Regions and time windows of calcium activity evaluated to be statistically different from baseline across trials are listed in Table 5.4.

Performing principal component analysis and dimensionality reduction on the region-segmented data in response to the different odor stimuli does not show strong clustering, Figure 5.4A–B; indicated that the evoked responses my be confounded or not very substantial. The analysis does reveal that trials across experimental runs appear to be distributed among one another (and not segregated) in low dimensional space, suggesting a level of robustness and consistency for our stimulation procedure and brain imaging protocol; see Figure 5.4C–D.

For none of the trials did we observe significant activation for stimulation from the right stimulator. For each of the odors we observed less than 15 significant activity comparisons.

Analysis of swim bout timing shows that there are some trials with a much higher fre-

Figure 5.2 ***(following page)*****: Six brain regions show significant differential activation in response to tactile pulses; tail movements suggest stimulus cessation is more behaviorally evocative than stimulus onset.** **A**: Line plots of of the mean calcium (Ca++) activity of six brain regions which showed significant responses to tactile pulse stimulation (grey shaded box) beginning at time t = 0 s. Plots for the 12 individual trials for each region are shown in thin faint lines. Top plot, **A1** shows regions that show a decrease in Ca++ activity over the course of the stimulation and bottom plot **A2** plots 3 regions that show an increase in Ca++ activity over the course of stimulation. Time windows utilized for the analysis in **B** are shown in dashed yellow boxes. **B**: Scatter "volcano" plot of statistical significance $-\log_{10}(p)$ vs. effect size $\Delta(\Delta F/F)$ for all recorded regions comparing mean Ca++ activity from a baseline time window (–30 to –1 s) to the mean Ca++ activity in the following five stimulus time windows: 1 – 10 s ("early stim"ulus), 10 – 30 s ("mid stim"ulus), 30 – 59 s ("late stim"ulus), 61 – 70 s ("early post"-stimulus), and 70 – 100 s ("late post"-stimulus). "Significant" comparisons were selected as those with $|\Delta(\Delta F/F)| > 10\%$ and $(-\log_{10}(p)) > 2$ (black points and dotted lines showing thresholds), with the remaining comparisons considered "insignificant" (grey circles). Significant comparisons corresponding to one of the six regions plotted in **A** are shown with a five-point star in corresponding colors with the region number and comparison time-window annotated. **C**: Heatmap of mean Ca++ activity vs. time for ≈ 300 brain regions during tactile pulse stimulation. Same as Figure 5.1); however, rows/regions are ordered based on hierarchical clustering (dendrogram tree along left side) where the correlation between region responses provides a distance metric between regions. The horizontal length of the line reflects the extent of correlation between regions (shorter = more correlated). Colored bar along the *y*-axis represents rostral to caudal position according to the colormap. **D**: Swarmplot of the timing (point's position along *x*-axis) and angle range (point's color) of swim bouts as they occurred relative to a tactile stimulus at $t = 0$ s pooled across ≈ 3–6 trials. Point's *y*-position is not important and only used to separate points which would otherwise overlap. Time windows utilized for the analysis in **E** are shown in dashed yellow boxes. **E**: Bar plot of the average number of swim bouts* counted during a tactile stimulus within three time-windows—with $t = 0$ s marking stimulus onset (dotted grey line)—pre-stimulus: –30 to –1 s, stimulus: 1 – 30 s, and post-stimulus: 61 – 90 s. Individual observations making up each mean are also shown (white points).
*Note: *Time windows in a trial where no swim bouts were detected were dropped from the analysis.*

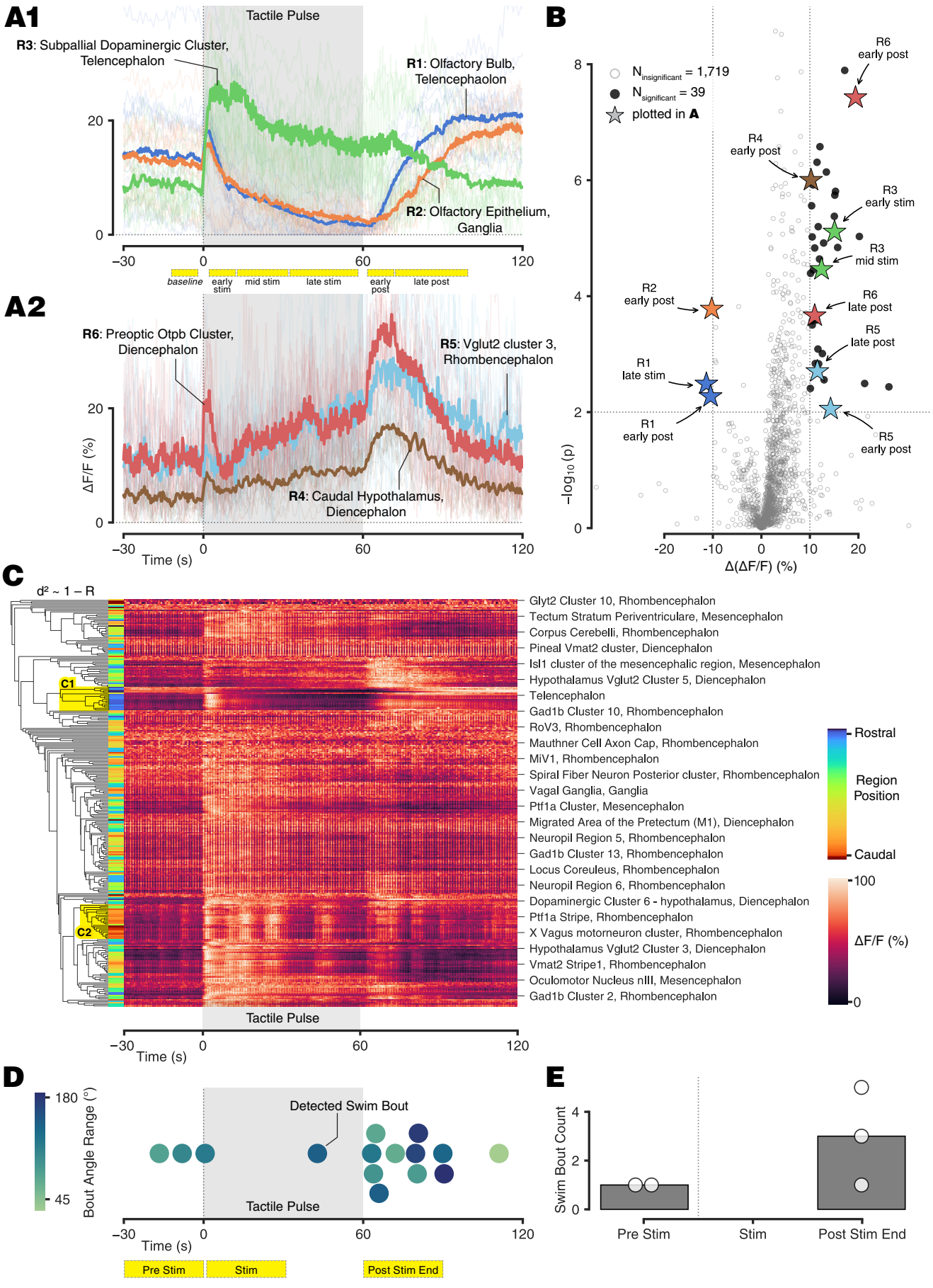
A1
Tactile Pulse
R3: Subpallial Dopaminergic Cluster, Telencephalon
R1: Olfactory Bulb, Telencephaolon
R2: Olfactory Epithelium, Ganglia
baseline
early stim
mid stim
late stim
early post
late post
A2
R6: Preoptic Otpb Cluster, Diencephalon
R5: Vglut2 cluster 3, Rhombencephalon
R4: Caudal Hypothalamus, Diencephalon
ΔF/F (%)
Time (s)
B
N insignificant = 1,719
N significant = 39
plotted in A
R6 early post
R4 early post
R3 early stim
R3 mid stim
R2 early post
R6 late post
R5 late post
R1 late stim
R1 early post
R5 early post
−log10 (p)
Δ(ΔF/F) (%)
C
d² ~ 1 − R
C1
C2
Glyt2 Cluster 10, Rhombencephalon
Tectum Stratum Periventriculare, Mesencephalon
Corpus Cerebelli, Rhombencephalon
Pineal Vmat2 cluster, Diencephalon
Isl1 cluster of the mesencephalic region, Mesencephalon
Hypothalamus Vglut2 Cluster 5, Diencephalon
Telencephalon
Gad1b Cluster 10, Rhombencephalon
RoV3, Rhombencephalon
Mauthner Cell Axon Cap, Rhombencephalon
MiV1, Rhombencephalon
Spiral Fiber Neuron Posterior cluster, Rhombencephalon
Vagal Ganglia, Ganglia
Ptf1a Cluster, Mesencephalon
Migrated Area of the Pretectum (M1), Diencephalon
Neuropil Region 5, Rhombencephalon
Gad1b Cluster 13, Rhombencephalon
Locus Coreuleus, Rhombencephalon
Neuropil Region 6, Rhombencephalon
Dopaminergic Cluster 6 - hypothalamus, Diencephalon
Ptf1a Stripe, Rhombencephalon
X Vagus motorneuron cluster, Rhombencephalon
Hypothalamus Vglut2 Cluster 3, Diencephalon
Vmat2 Stripe1, Rhombencephalon
Oculomotor Nucleus nIII, Mesencephalon
Gad1b Cluster 2, Rhombencephalon
Rostral
Region Position
Caudal
ΔF/F (%)
Tactile Pulse
Time (s)
D
Bout Angle Range (°)
Detected Swim Bout
Tactile Pulse
Time (s)
Pre Stim
Stim
Post Stim End
E
Swim Bout Count
Pre Stim
Stim
Post Stim End

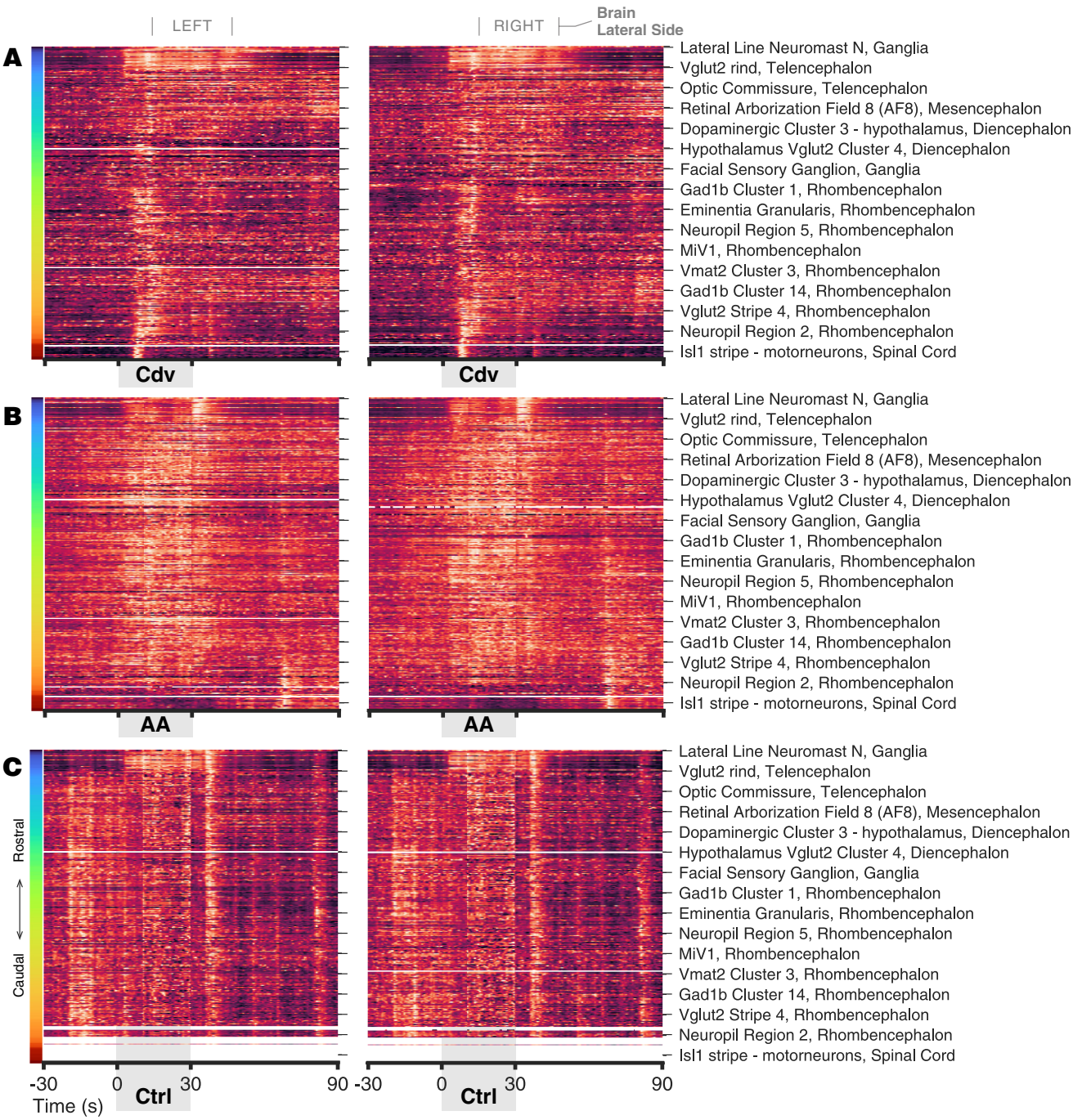

Figure 5.3: Calcium activity patterns show a consistent response to stimulation onset with different odors in rostral-most regions, distinct patterns in more caudal regions, and lateral similarity across time.. All plots show heatmaps of normalized calcium activity across time (*x*-axis) for ≈ 300 brain regions (*y*-axis) with regions sorted from rostral to caudal (left color bar). Heatmap values are averaged across multiple trials and each region/row is normalized to have the same max value. The activity from the left lateral side of each brain region is shown on the left heatmaps, and right brain regions are shown on the right. A subset of rows are labeled for reference. Each of the sub-panels differs in the odor used for stimulation from $t = 0$ s to $t = 30$ s (grey blocks below *x*-axes). The odor stimulation direction for all trials aggregated here is "both." **A**: Cadaverine ("Cdv", 2 mM). **B**: 12 amino acid cocktail ("AA", 12 mM). **C**: Negative control, fish water ("Ctrl").
Note: Figure 5.5 shows a subset of this data as line plots as well as tests for statistical significance. Some brain regions were not contained in the field of view for any imaging session; missing data is shown as empty/white lines in the heatmaps.

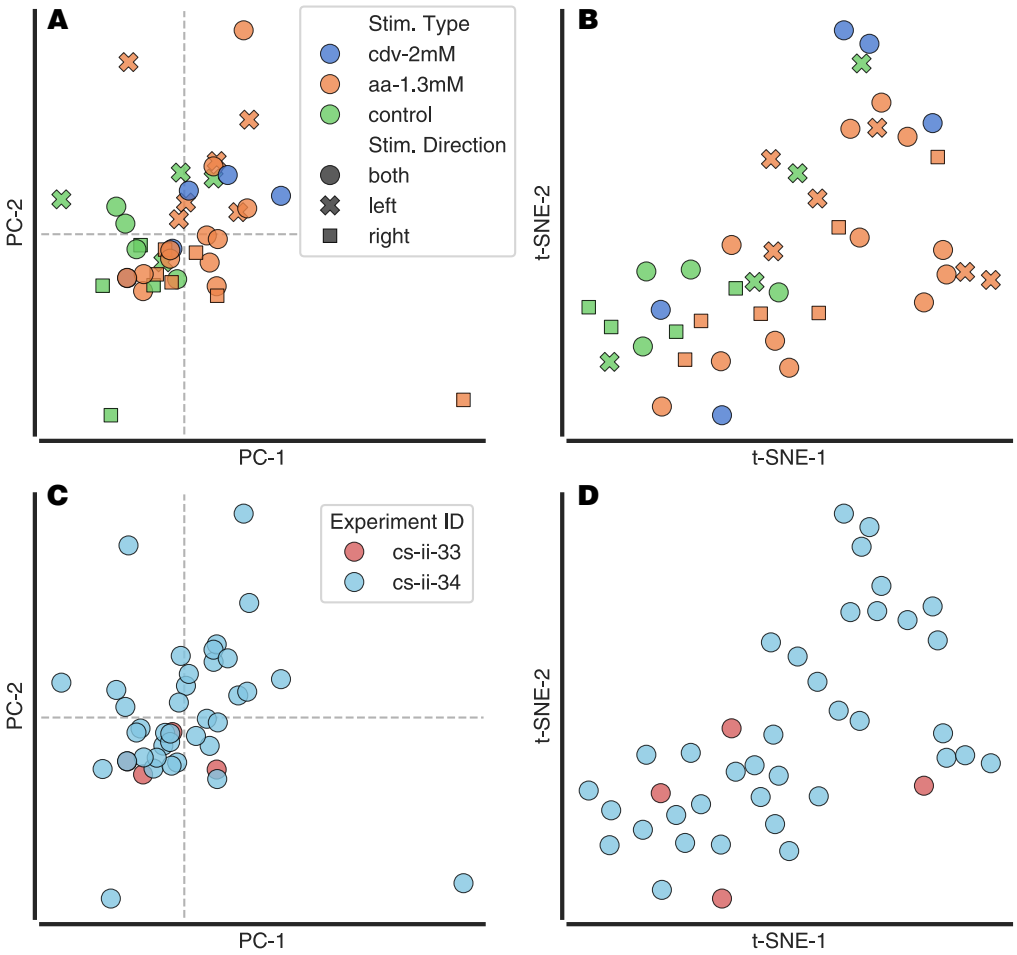

Figure 5.4: Multiple dimensionality reduction methods show difficulty in discriminating brain activity changes due stimulation with different odors across trials, but suggest experimental reproducibility. **A:** The difference in calcium activity $\Delta F/F$ between a 10 s time window pre-stimulus onset and a 10 s time window after stimulus onset was computed for ≈ 200 brain regions; giving a vector of $\Delta\left(\Delta F/F\right)$ values for each odor stimulation trial. Principal component analysis was preformed on this set of vectors and the trials were plotted along principal components 1 (x-axis) and 2 (y-axis). Points are colored by the odor (cadaverine: blue, amino acid: orange, negative control: green) and the marker shape indicates the stimulus direction (both: circle, left: 'x', right: square). Dashed lines indicate the origin of the axes. **B:** Similar to **A**; however the *t*-distributed stochastic neighbor embedding (*t*-SNE) dimensionality reduction method was applied to the trial change in activity vectors **C:** Identical plot to **A** except that the points are colored by the stimulation experiment ID which took place on different days and with different larva (cs-ii-33: red, cs-ii-34: light blue). **D:** Identical to **B** except the same experiment ID recoloring as **C**.

quency of swim bouts compared to others. Most swim bouts were measured to be ≈ 5 – 25°. Among the different trials we observed one comparison with $p < 0.05$; when the larva was stimulated with an amino acid cocktail from the right stimulus direction there was a "significant" increase in the number of swim bouts from pre-stimulus-start to post-stimulus-cessation.

It is important to note that we observed that individual larva can have notably different characteristic swim frequencies and angle ranges of swims Figure 5.7. For example, fish cs-ii-29B typically performed < 1 swim bout per minute, while fish cs-ii-33A typically performed more than 30 swim bouts per minute Figure 5.7A. Fish cs-ii-33A and cs-ii-34A show a large number of very low magnitude swims; while fish cs-ii-29B show a median bout tail angle range of ≈ 90°, Figure 5.7B. This individual variability helps explain some of the reason we see in Figure 5.6D–F such marked differences in the number of detected bouts under different stimulation conditions (as not all conditions were performed in equal number with all fish).

5.2.3 Towards Live-Fixed Registration

For multiple live imaging experiments, we took the same larva from stimulation and live imaging through a full immunostaining pipeline as described in §4.5.7. By eye, we see a correspondence between the 3D images which are shown in Figure 5.8; however, we have not yet attempted computational registration and alignment of the images.

5.3 Discussion

5.3.1 Achievement of Aims

These data demonstrate the achievement of a number of the goals for the project which we set out to achieve as described in Chapter 1. We have produced a number of pilot datasets which combine bilateral olfactory stimulation, whole-brain calcium imaging, and

Figure 5.5 *(following page)*: Some brain regions may show significant differential activation in response to bilateral pulses with different odors. A B C: Line plots of calcium (Ca++) activity vs. time for four brain regions averaged (bold lines) across bilateral odor pulse trials (stimulation window in light gray region); individual trial plots are also shown (thin, faint lines). Plots in the left column correspond to Ca++ activity from the left brain hemisphere and the right column corresponds to the right brain. Each row is labeled with the direction from which the stimulus originated (see Figure 3.35C–D)*. The odors delivered were for each group of traces are annotated: **A**: cadaverine (2 mM), **B**: 12 amino acid cocktail (1.3 mM), and **C**: negative control, fish water. **D E F:** Scatter "volcano" plots of statistical significance $-\log_{10}(p)$ vs. effect size $\Delta(\Delta F/F)$ all recorded regions comparing mean Ca++ activity from a baseline time window (–30 to –1 s) to the mean Ca++ activity in the following two stimulus time windows: 1 – 20 s (during "stim"ulus), 31 – 50 s (post-"stim"ulus). "Significant" comparisons were selected as those with $|\Delta(\Delta F/F)| > 15\%$ and $(-\log_{10}(p)) > 2$ (black points and dotted lines showing thresholds), with the remaining comparisons considered "insignificant" (grey circles). Significant comparisons corresponding to one of the four regions plotted in **A** – **C** are shown with a five-point star in corresponding colors with the region number, region hemisphere, stimulus direction, and comparison time-window annotated. Separate scatter plots shown for each stimulation odor: **D**: cadaverine, **E**: amino acid, **F**: negative control.
*Note: *Trials with single-sided cadaverine pulses were not successfully recorded due to hardware errors. Symbols: N_i : number of insignificant observations; N_s : number of significant observations.*

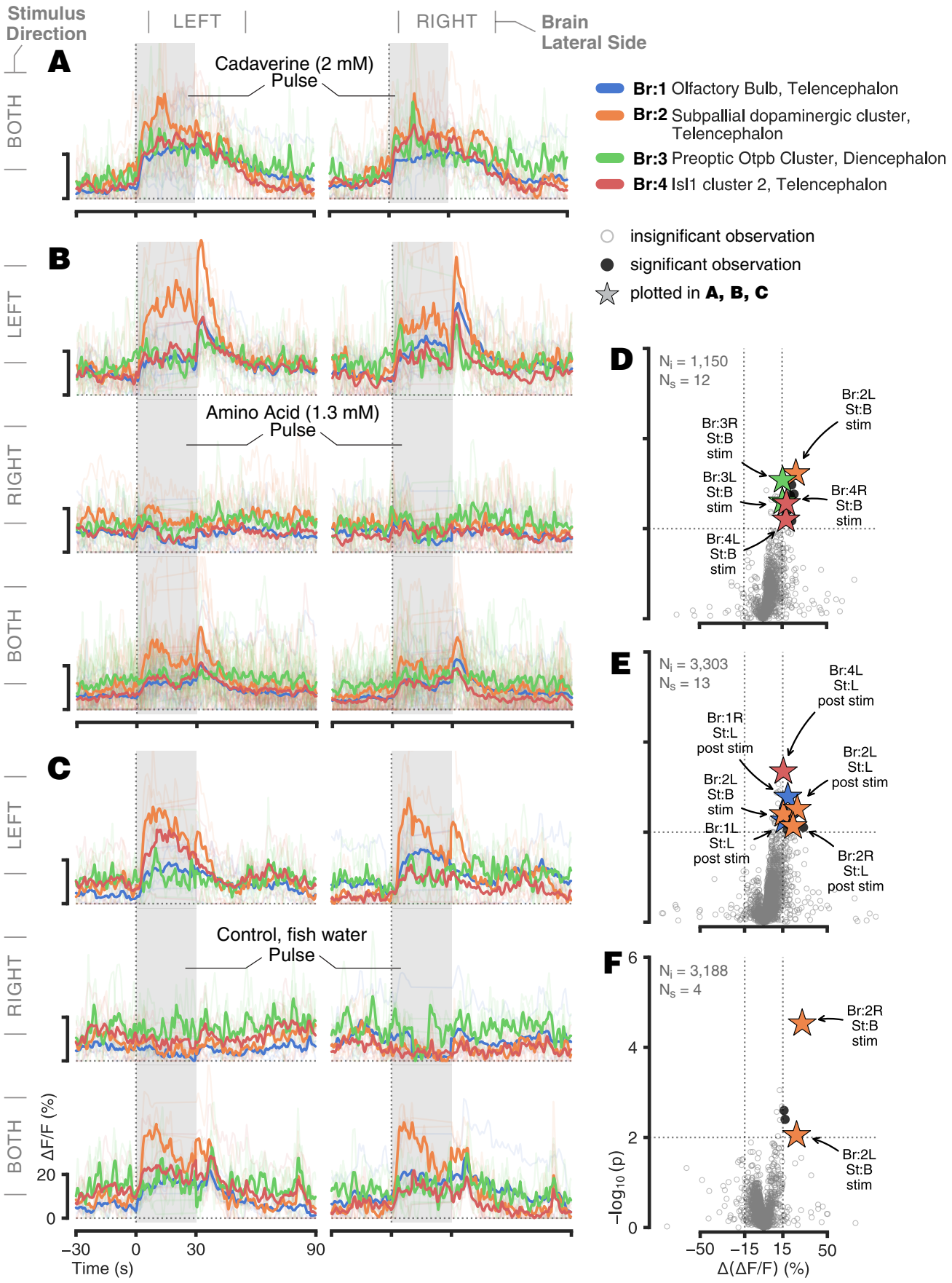
Stimulus Direction
LEFT
RIGHT
Brain Lateral Side
BOTH
A
Cadaverine (2 mM) Pulse
B
LEFT
RIGHT
Amino Acid (1.3 mM) Pulse
BOTH
C
LEFT
RIGHT
Control, fish water Pulse
BOTH
ΔF/F (%)
20
0
−30
0
30
90
Time (s)
Br:1 Olfactory Bulb, Telencephalon
Br:2 Subpallial dopaminergic cluster, Telencephalon
Br:3 Preoptic Otpb Cluster, Diencephalon
Br:4 Isl1 cluster 2, Telencephalon
insignificant observation
significant observation
plotted in A, B, C
D
Ni = 1,150
Ns = 12
Br:2L St:B stim
Br:3R St:B stim
Br:3L St:B stim
Br:4R St:B stim
Br:4L St:B stim
E
Ni = 3,303
Ns = 13
Br:4L St:L post stim
Br:1R St:L post stim
Br:2L St:L post stim
Br:2L St:B stim
Br:1L St:L post stim
Br:2R St:L post stim
F
Ni = 3,188
Ns = 4
Br:2R St:B stim
Br:2L St:B stim
6
4
2
0
−log10 (p)
−50
−15
15
50
Δ(ΔF/F) (%)

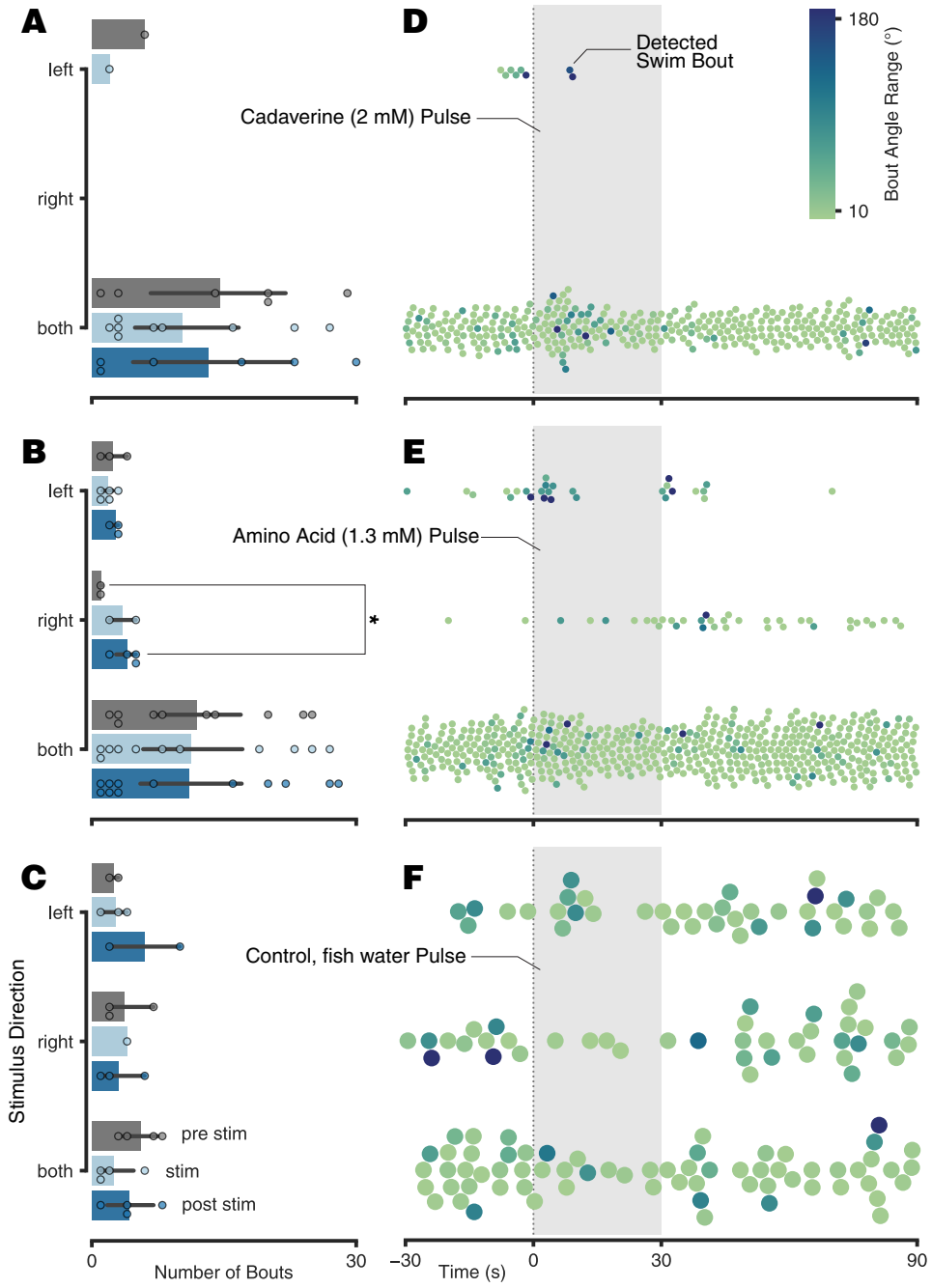

Figure 5.6: We compare swim bout frequency and magnitude in response to bilateral stimulation with various odors. **A B C**: Bar plots of the average number of swim bouts counted within three time-windows (colors) for different stimulus directions (*y*-axis). The time windows are as follows—with $t = 0$ s marking stimulus onset—pre-stimulus: −20 to −1 s (grey bar), stimulus: 1 – 20 s (light blue bar), and post-stimulus: 31 – 50 s (dark blue bar). 95% confidence intervals on the mean are shown (black lines) and individual observations making up each mean (points). Subplots correspond to odor delivered: **A**: cadaverine (2 µM), **B**: 12 amino acid cocktail (1.3 µM), and **C**: negative control, fish water. **D E F**: Swarmplots of the distribution of the time (point position along *x*-axis) and angle range (point color; darker ~ larger angle) of swim bouts as they occurred relative to an odor stimulation at $t = 0$ s for different stimulation directions (*y*-axis) pooled across . Point *y*-position or size within a condition group is not important and only used to separate points which would otherwise overlap. Subplots correspond to odor delivered: **C**: cadaverine, **D**: 12 amino acid cocktail , and **E**: negative control.
Note: For bar plots, only time-windows in a trial with at least one swim bout were included in the analysis.

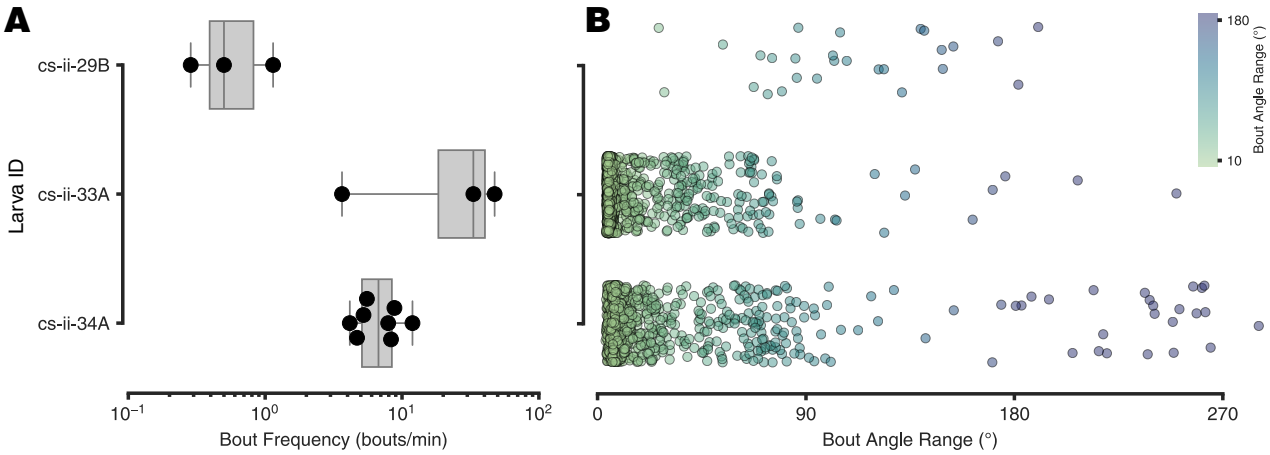

Figure 5.7: Individual larva show different characteristic swim bout frequencies and a broad range of bout tail angle magnitudes with most swims being low magnitude. **A**: Boxplots of the mean swim bout frequency for each behavioral recording taken of 3 different larvae. Each point represents a tail imaging recording and its position along the *x*-axis is the total number of bouts in a given recording divided by the duration of the recording in minutes. **B**: Strip plot of the tail angle range for each detected swim bout aggregated across all recordings for the same 3 larva. Each point represents a detected swim bout; color and *x*-position reflect the angle range of the bout. Points are randomly spread in *y* within each larva id category to aid in distinguishing bout points.
*Note: The x-scale in **A** is logarithmic.*

behavioral tail imaging. Though these datasets are not perfect, nor were they acquired towards the investigation and testing of a specific hypothesis, they represent the successful implementation of the stimulation and acquisition hardware as well as the development computational pipeline to parse, analyze, and correlate the readouts across modalities and stimulation trials.

5.3.2 Evaluation of Statistical Significance

When performing many tests for statistical significance, it is important to consider the expected false discovery rate and use that expectation to contextualize our observations. In our tactile pulse experiment region-segmented calcium trace analysis, we performed 1,758 comparisons to find statistically significant calcium activity differences from the baseline. With a p cutoff of 0.01, we would expect to find ≈ 18 "false positives" at random (i.e. comparisons where we reject the null hypothesis when we should not). In this experiment, we found 39 which suggests that about half of these observation are true significant results.[1] For our proof-of-concept experiments we are not performing evaluations of hypotheses or drawing scientific conclusions; however, it is still important to consider this context.

5.3.3 Issues with Stimulation Reliability

As noted in §5.2.2, we did not observe responses when delivering odors to the right olfactory epithelium by the right stimulation manifold. We believe this is due to an unexpected

[1] In reality, the analysis is complicated by the fact that our comparisons are not independent; however, we can still get a general sense for contextualizing our results.

clog in the right stimulation needle which prevented significant flow out of the manifold. An initial review of the flow sensor logs show that flow rates through the right manifold did not consistently reach the target 0.1 mL min^{-1} flow rate. This is a significant issue given the design goals of our stimulation system and it presents a roadblock in performing the bilateral analysis of activity and behavioral responses. We will discuss methods to mitigate the problem of poor stimulation reliability and consistency and allow for quicker intervention

5.3.3.1 Software Alerts and Automated Monitoring

A key issue with the simulation system virtual instrument related to reliability is that that software does not yet take advantage of the real-time flow sensor data and the known solenoid positions to evaluate if the measured flow matches the expected flow. Such a comparison, if implemented would make it possible for the software to alert the operator if there is a potential issue with a given solenoid or a given stimulation line in real time. Toward this end, we can implement this functionality by allowing the user to input the target output odor flow rate, then we can program the software to monitor the flow rate through which ever solenoids are currently open and report the flow as a percentage of the target; furthermore, if the flow drops below a threshold (i.e. 80%) the software would display a warning dialog or light, in real-time so that the operate can be aware of the issue and intervene as needed. We can also implement a "self-test" subroutine in which the system would open each solenoid for 15 s in sequence and the the average, minimum and maximum flow rate through the line would be reported; values which fall outside of a specified range would be flagged to the operator and the results would be saved to a log file.

These software modifications would enable issues in the stimulation to be discovered preemptively rather than during analysis, after and experimental setup is taken down.

5.3.3.2 Needle Handling Procedures

One of the most sensitive and fragile components of the stimulation system are the delivery needles §3.2.1.1. These needles have a microscopic, ≈ 50 µm bore which can easily become clogged from any dust or debris in the upstream fluid lines or which can be introduced while handling the needle during system setup; clogs can also be formed if solution containing dissolved solids is allowed to dry out inside of the needle. To more effectively manage the introduction of potentially clogging components to the needle or fluid system, we can develop a protocol which limits handling of the stimulation needles to bio-safety cabinets or other filtered air environments (e.g. clean-room). Furthermore, we can develop a pro-

Figure 5.8 *(following page)*: We show pre-registered 3D images of an individual larva's *in vivo* native fluorescence and *ex vivo* immunofluorescence.. **A**: Orthogonal maximum intensity projections of a 3D image of GCaMP expression in a larval zebrafish brain (fish ID cs-ii-34A) taken by stitching two fields of view from a high resolution scan on our two photon microscopy system immediately following live whole-brain imaging. This is the "bridge" dataset described in §4.4.2.2. **B**: Similar to **A**, except the 3D image shown is of immunofluorescence against GCaMP taken using 15 stitched fields of view on our spinning-disk confocal microscope of the same larva as **A**.
Note: Scale bars is 200 µm.

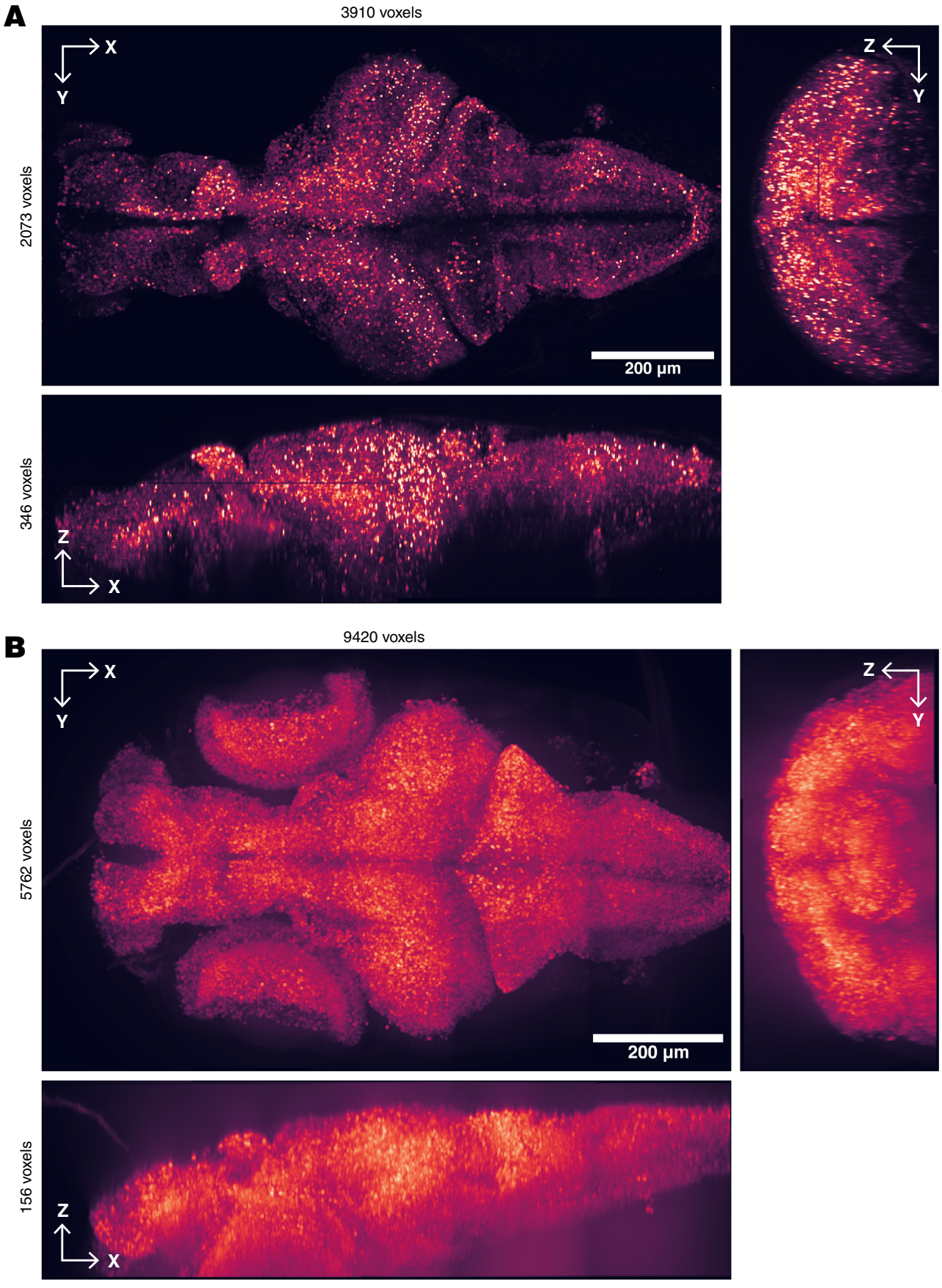
A
3910 voxels
X
Y
Z
Y
2073 voxels
200 µm
346 voxels
Z
X
B
9420 voxels
X
Y
Z
Y
5762 voxels
200 µm
156 voxels
Z
X

cess for clearing off the mating surfaces for all fluidic connections which are made during setup connecting to the stimulation manifold. Finally we can test and develop a protocol for stimulation needle cleaning and storage which removes and prevents buildup of dried solutes or other contaminants.

5.3.4 Extracting a Fingerprint of Tactile Stimulation

It may prove useful to be able to assess the presence of unintentional tactile stimulation due to flow rate changes in our olfactory stimulation trials. This is so that we can be more confident that the applied stimulation is purely olfactory and our downstream conclusions can rely on that assumption. We can do this by, computationally, creating a vector of the relative changes in activation for each brain region from pre-stimulus to stimulus and from stimulus to post-stimulus averaged across multiple tactile stimulation trials (using a set of time windows similar to the procedure outlined in §5.4.3.2). This vector would serve as our reference "fingerprint" of tactile stimulation. In other experiments, we could then perform the same vector extraction for single trials or groups of trials and evaluate the correlation to the reference tactile stimulation data for both the odor-ON transition and the odor-OFF transition. If an experimental trial correlated strongly with the tactile pulse reference, we might consider the run to potentially be causing tactile stimulation of the fish and we could make an intervention in the stimulation parameters or hardware setup reduce any tactile effects.

We could apply more advanced machine learning methods to quantify the amount of "tactile contamination" in a stimulation trial; however, currently we have very few datasets and replicates which would make getting robust results with such methods more difficult. For this reason it would be most tractable to utilize correlation or similar metrics for now.

Note: We believe that the observed lack of differential response was due to a clog in the right stimulation needle as discussed earlier. However, one might notice that our clustering analysis, Figure 5.4, does not show the right stimulation direction trials to be completely overlaid with the control trials. This can be explained in two ways: 1) the flow of odor was intermittent and thus led to some response but much less robust (which clustered differently). 2) If there was indeed a clog or intermittent flow, then when the odor line was switched on and the fish water line off, there would be a strong possibility for tactile stimulation which could illicit an undesired but differential (and deferentially clustering) response compared to the control.

5.3.5 Future Experimental Designs

5.3.5.1 Comparing Directional Diversity to Component Diversity

A relatively simple experiment we would like to perform is to compare a larva's response to a mixture of 2 – 3 odors (e.g cadaverine and amino acid) delivered in two different ways. First, when delivered as a pre-mixed combination of the cadaverine and amino acid solutions. And, second, when amino acid is delivered from the left and cadaverine is delivered from the right (and vice versa). This experiment could help use to understand and see if

there are any differences in neuronal processing or behavioral responses due to presentation with a bilateral mixture (different odors at each olfactory epithelia) and stimulation with a stoichiometric mixture (the same 50:50 mix at both olfactory epithelia).

5.3.5.2 Nature of Directional Encoding of Stimulation

We want to understand the extent to which stimulation with a given odor to the right olfactory epithelium is "experienced" differently from stimulation with the same odor to the left olfactory epithelium and if the location information is preserved at higher brain regions or is lost. To assess this, we can stimulate a larva with repeated pulses from the left or right individually.[2] Then we can average across the single-sided trials and evaluate what brain regions show different activation patterns for left vs. right. This initial investigation can serve as a building-off point for creating and testing focused hypotheses.

5.3.5.3 Olfactory Kin Recognition

Another set of stimulation experiments we can perform is aimed at developing a deeper understanding of the ways the larva respond to conspecific fish odor (see the following references for more on zebrafish olfactory kin recognition [2–6]). We can utilize correlated stimulation and imaging to develop a model of how the activation of the stress-related oxytocin (OXT) neurons in socially isolated fish is attenuated by conspecific fish odor [7]. While completely piecing apart the circuit involved in the pathway using a structural or connectomic approach is viable, we aim, through the following experimental approach, to test a hypothesis regarding how the components of the fish odor mixture are integrated to produce OXT suppression.

The hypothesis of this aim is that the individual chemical components of kin odor would not lead to significant OXT suppression; however, after combining a critical number of components contained in kin-odor there would be an ensemble response triggering significant OXT suppression (and potentially other attractive-like outputs). We have chosen this behavioral system because of the universality—across behaviors and species—of neural integration of sensation to produce (or not produce) a response; developing a model of this process in the very specific case of the cascade from olfactory neurons to OXT suppression may provide us with an opportunity to propose a generalizable hypotheses of how computations are performed on many sensory inputs.

Our correlated imaging and stimulation approach would enable us to develop this model informed by not only by patterns of neuronal activation and/or suppression under different conditions, but also by the cellular identities of deferentially activated neurons and the structural projections from neurons of interest.

5.3.5.3.1 Experimental Approach The general design of the experiments would follow this structure:

[2] We did acquire such data in the trials discussed in §5.2.2; however, due to a poor delivery of odors from the right stimulator (§5.3.3) we were not able to successfully perform this proposed experiment and analysis.

1. Fish larvae aged 6 – 8 dpf would be isolated for ≈ 2 h.
2. Live whole brain calcium imaging imaging would be performed to get a baseline recording; with specific focus on the olfactory bulb and the OXT neuron regions.
3. Odors would be presented 2 – 5 times with an inter stimulus interval of ≈ 5 min and the response recorded during each stimulus; odor order would be randomized.
4. Larvae would be fixed and the immunohistochemical staining performed.

We can apply this pipeline to three different "titrations" which each attempt to progressively pare down the components of fish odor so we can observe responses at points along that gradient.

5.3.5.3.1.1 Odor Diversity Titration In this set of trials, we would raise larvae at a concentration of 40 larvae per dish. Fish odor would be prepared at a concentration of 2 fish/mL from 1, 2, 3, 4, 5, 10, and 20 individual fish by incubating them in the appropriate volume of filtered facility water for 2 h. These "diversity" preparations would be applied as stimulants via the protocol outlined above.

5.3.5.3.1.2 Odor Concentration Titration We would raise larvae at a concentration of 40 larvae per dish. In this case fish odor would be prepared from 20 fish at concentrations ranging from 5 fish/mL to 0.001 fish/mL by incubating in the appropriate volume of filtered facility water for 2 h. These would be the "concentration" preparations.

5.3.5.3.1.3 Synthetic Component Titration In these trials, we can raise select larvae in chemical isolation from their kin, but still with visual stimuli from other larvae by placing them in glass beakers. From 4 – 7 dpf, larvae would be imprint-ed with a cocktail of ≈ 5 different synthetic MHC peptide ligands (as described by Hinz *et al.* in [5]) the total peptide concentration would be 6.25 nM. MHC peptide stimulants would be prepared from 1, 2, 3, and 4 individual peptides and the original mixture, each at a final total peptide concentration of 6.25 nM. These would be the "synthetic component" preparations.

5.3.5.3.1.4 Model Construction Using data collected from the three trials, we would produce curves of regional olfactory bulb activation and OXT neuron suppression vs odor diversity, odor concentration, and peptide component number. If our hypothesis is correct, we would see a linear response for the olfactory bulb activations and a step- or 'S'-shaped response for OXT suppression. Using segmented activity from live imaging we would identify intermediate neurons which correlate with odor at all levels, but have a response that is uncorrelated with

OXT suppression at low odor levels and correlated with OXT suppression at high odor levels. If these "threshold" neurons are identified by activity, we would probe their projections and cellular identity in the *ex vivo* imaging. Using these insights, we would attempt to design a network model to explain the observed responses.

5.3.5.3.2 Expected Outcomes From this study we expect to evaluate the presented hypothesis. If the hypothesis is correct, we would expect results as outlined in the paragraph above; however, if the hypothesis is false or in-conclusive, we would expect to find, for example, that the titrations across the scale produce OXT suppression. This might imply that the system is highly sensitive and acts as "all-or-none" within the regime we test. Many other possibilities could also be observed, but we would ultimately obtain, at a minimum, a partial answer to our hypothesis. Additionally, we would have a model for the responses grounded in both the structure and activity of the system and potentially be able to apply the model to other behaviors or activation patterns.

5.3.5.3.3 Alternative Approaches To validate our results, we could attempt to correlate the level of OXT suppression and additional predictions of our model with relative times in an Atema choice flume. This would additionally incorporate a behavioral readout into to compare with our immobilized and modeled results.

Based on the first experiments for this aim, it may make more sense to utilize fish with selective expression of activity in OXT neurons to make the readouts more facile. This however would compromise our ability to look for intermediate components in the OXT suppression pathway.

It is important to keep in mind that the brains of 5 – 10 dpf larvae are early in development and many behaviors may not be as robust as they are in more mature individuals; results from a given larvae may, more often than otherwise, not accurately represent the generalized result. One way to address this would be to average results over more fish (i.e. increase n) to gain statistical power in the analysis. We could also attempt choice trials (in which we measure the relative residence times within two laminar streams containing different odors, the Atema two-channel choice flume) for each fish and only perform live imaging on fish that demonstrate the kin preference behavior consistently over some threshold. However, it could also be interesting to try to account for heterogeneity in the activity recordings or behavioral observations with the aspects of neural connectivity or the relative abundances of different neuron types in key regions.

A potentially exciting means for chemically separating natural fish odor (as an additional titration or if other titrations fail to resolve a response) would be to perform chromatographic fractionation of fish odor prepared in water. These fractions could be analyzed by mass spectroscopy (either directly by GCMS or indirectly by sampling each fraction) to optimize the chromatographic separation parameters (e.g. column type, additional solvents, etc.). Once optimized, the fractions could be applied to the fish like the proposed "synthetic component" titration.

5.4 Methods

5.4.1 Synchronizing Acquisition Modalities and Stimulation

Before synchronizing acquisition of two-photon imaging, behavioral imaging, and olfactory stimulation we needed to follow the procedures for aligning all of the systems to the fish as

Table 5.1: Correlated cluster of brain regions showing a synchronized pulsing calcium activity. Row indices correspond to the row within clustered heatmap of Figure 5.2C and annotated as "C2".

	Region
212	Glyt2 Stripe 3, Rhombencephalon
213	Hypothalamus Gad1b Cluster 3 Sparse, Diencephalon
214	Hypothalamus Vglut2 Cluster 6, Diencephalon
215	Isl1 Stripe 1, Rhombencephalon
216	VII' Facial Motor and octavolateralis efferent neurons, Rhombencephalon
217	Gad1b Stripe 3, Rhombencephalon
218	Vglut2 Stripe 4, Rhombencephalon
219	Vmat2 Stripe3, Rhombencephalon
220	Ptf1a Stripe, Rhombencephalon
221	Gad1b Stripe 1, Rhombencephalon
222	Vglut2 Stripe 3, Rhombencephalon
223	Vmat2 Stripe2, Rhombencephalon
224	Glyt2 Stripe 2, Rhombencephalon
225	Vglut2 Stripe 2, Rhombencephalon
226	Cerebellar Neuropil 1, Rhombencephalon
227	Glyt2 Stripe, Spinal Cord
228	Vmat2 Stripe1, Spinal Cord
229	Noradrendergic neurons of the Interfascicular and Vagal areas, Rhombencephalon
230	6.7FDhcrtR-Gal4 Stripe 1, Rhombencephalon
231	X Vagus motorneuron cluster, Rhombencephalon
232	6.7FDhcrtR-Gal4 Stripe, Spinal Cord
233	Otpb Cluster 6, Rhombencephalon
234	Gad1b Stripe 2, Rhombencephalon
235	Rhombomere 7, Rhombencephalon

described in §3.5.6 and §4.5.4. Then we would ensure that the stimulator cart umbilical BNC connection to the two photon system trigger is connected as well as the BNC connection to the camera trigger (located on at the stimulation platform) is connected. These two connections provide the ability to simultaneously begin all procedures and acquisitions.

With these connections made, we prepare the imaging parameters both for the two-photon volumetric acquisition and for the high-speed behavioral imaging camera. Based on the total duration of the stimulation sequence (displayed in the stimulation system virtual instrument), we would set the both of the imaging acquisition durations to be 10 – 30 s longer than the total stimulation duration. Then each imaging system is primed in software to begin imaging upon receiving a hardware TTL trigger. With both systems primed we then used "START" button with the stimulation system virtual instrument to begin logging the experiment timeline, send pulses to both imaging systems, and begin the configured stimulation sequence at the same moment.

5.4.2 Resampling Imaging Data to the Stimulation Time-course

Once two photon imaging data was segmented and aggregated for each imaging run as described in §4.5.5.3.2 and the behavioral imaging data was quantified and sifted for bouts as described in §4.5.6.2.2, we essentially had data tables where each entry, among other

Table 5.2: Brain regions and time windows with significant* responses to tactile stimulation relative to a pre-stimulus baseline. Entries are sorted from smallest p value to largest. These 39 observations correspond to the solid points and stars in the volcano plot Figure 5.2B. *Observation were considered significant if $p < 0.01$ and $\Delta\left(\Delta F/F\right) > 10\%$.

	Region	Time Bin	$\Delta\left(\Delta F/F\right)$	$-log_{10}\left(p\right)$
1	Dopaminergic Cluster 6 - hypothalamus, Diencephalon	Early Stim	+17.2%	7.9
2	Preoptic Otpb Cluster, Diencephalon	Early Post	+19.4%	7.4
3	Vmat2 Cluster 1, Rhombencephalon	Early Stim	+12.1%	6.6
4	Dopaminergic Cluster 6 - hypothalamus, Diencephalon	Mid Stim	+11.5%	6.3
5	Hypothalamus - Caudal Hypothalamus Neural Cluster, Diencephalon	Early Post	+13.4%	6.1
6	Caudal Hypothalamus, Diencephalon	Early Post	+10.2%	6.0
7	Ptf1a Cluster 1, Rhombencephalon	Early Stim	+10.6%	5.9
8	Hypothalamus Vglut2 Cluster 4, Diencephalon	Late Post	+15.3%	5.8
9	Preoptic area Vglut2 cluster, Diencephalon	Early Post	+15.1%	5.7
10	Subpallial Otpb Cluster 2, Telencephalon	Early Stim	+10.4%	5.6
11	Telencephalic Migrated Area 4 (M4), Telencephalon	Late Post	+15.0%	5.4
12	Otpb Cluster 4, Rhombencephalon	Early Post	+11.7%	5.2
13	Subpallial dopaminergic cluster, Telencephalon	Early Stim	+15.1%	5.1
14	Hypothalamus Vglut2 Cluster 4, Diencephalon	Early Post	+20.2%	5.0
15	Hypothalamus - Caudal Hypothalamus Neural Cluster, Diencephalon	Late Post	+10.5%	5.0
16	Hypothalamus - Intermediate Hypothalamus Neural Cluster, Diencephalon	Early Post	+12.8%	4.9
17	Vmat2 cluster, Telencephalon	Early Stim	+15.7%	4.8
18	Ptf1a Cluster, Mesencephalon	Early Stim	+11.0%	4.8
19	Gad1b Cluster 18, Rhombencephalon	Early Stim	+12.0%	4.6
20	Subpallial dopaminergic cluster, Telencephalon	Mid Stim	+12.4%	4.5
21	Vmat2 cluster, Telencephalon	Mid Stim	+10.7%	4.5
22	Otpb Cluster 4, Rhombencephalon	Mid Stim	+10.1%	4.4
23	Olfactory Epithelium, Ganglia	Early Post	−10.2%	3.8
24	Preoptic Otpb Cluster, Diencephalon	Late Post	+11.0%	3.7
25	Anterior preoptic dopaminergic cluster, Diencephalon	Early Post	+11.4%	3.6
26	Hypothalamus Olig2 cluster 2, Diencephalon	Early Stim	+10.5%	3.6
27	Gad1b Cluster 18, Rhombencephalon	Mid Stim	+10.5%	3.5
28	Hypothalamus - Intermediate Hypothalamus Neural Cluster, Diencephalon	Late Post	+11.7%	3.1
29	Dopaminergic Cluster 7 - Caudal Hypothalamus, Diencephalon	Early Post	+12.6%	3.0
30	Glyt2 Cluster 5, Rhombencephalon	Early Stim	+11.1%	2.8
31	Olfactory bulb dopaminergic neuron areas, Telencephalon	Early Stim	+11.8%	2.8
32	Vglut2 cluster 3, Rhombencephalon	Late Post	+11.5%	2.7
33	Olfactory bulb dopaminergic neuron areas, Telencephalon	Late Post	+12.9%	2.6
34	RoM1, Rhombencephalon	Early Stim	+21.3%	2.5
35	Olfactory Bulb, Telencephalon	Late Stim	−11.3%	2.5
36	Lateral Line Neuromast N, Ganglia	Mid Stim	+26.3%	2.4
37	Olfactory bulb dopaminergic neuron areas, Telencephalon	Mid Stim	+10.1%	2.4
38	Olfactory Bulb, Telencephalon	Early Post	−10.5%	2.3
39	Vglut2 cluster 3, Rhombencephalon	Early Post	+14.3%	2.1

attributes, contained a relative timestamp of "seconds since trigger" t_{trig} Additionally we referenced the stimulation log produced by the stimulation virtual instrument (see §3.2.7.3 and repository linked in Appendix A), which was a data table where each entry referenced the beginning of a given step in the stimulation sequence along with the $t_{\text{trig},i}$ of the ith step.

Before resampling we determined the duration pre-stimulus T_{pre} and post-stimulus-end T_{post} to include (for example, in Figure 5.1 we used durations of $T_{\text{pre}} = 30\,\text{s}$ and $T_{\text{post}} = 60\,\text{s}$). Then, for each relevant stimulation step we computed the trigger-based start time for the stimulation step $t_{\text{trig,start}} = t_{\text{trig},i} - T_{\text{pre}}$ and the trigger based end time for the step $t_{\text{trig,start}} = t_{\text{trig},i} + T_{\text{post}} + T_{\text{stim}}$ for the step (where T_{stim} is the stimulus duration). Using $t_{\text{trig,start}}$ and $t_{\text{trig,end}}$ we filtered the entries of each data table to include only those with t_{trig} within that range, we offset the trigger-based time to the stimulus-based time by subtracting $t_{\text{trig},i}$. For the two-photon imaging data, we would then resample the data table to a set of consistent stimulus-based time points on the range $[-1 \times T_{\text{pre}}, T_{\text{post}} + T_{\text{stim}}]$ s.

Table 5.3: Correlated cluster of brain regions showing a marked increase in calcium activity at both stimulus onset and stimulus cessation. Row indices correspond to the row within clustered heatmap of Figure 5.2C and annotated as "C1".

	Region
61	Olig2 Cluster, Telencephalon
62	Subpallial Otpb strip, Telencephalon
63	Olfactory Bulb, Telencephalon
64	Olfactory Epithelium, Ganglia
65	Lobus caudalis cerebelli, Rhombencephalon
66	Telencephalon
67	Pallium, Telencephalon
68	Vglut2 rind, Telencephalon
69	Subpallial Otpb Cluster 2, Telencephalon
70	Subpallial Gad1b cluster, Telencephalon
71	Subpallium, Telencephalon
72	Isl1 cluster 1, Telencephalon
73	Isl1 cluster 2, Telencephalon
74	S1181t Cluster, Telencephalon
75	Anterior Commisure, Telencephalon
76	Telencephalic Migrated Area 4 (M4), Telencephalon

Table 5.4: Brain regions and time windows with significant* responses to bilateral stimulation with cadaverine, amino acid, or control stimuli. Entries are sorted by stimulation odor, then sorted from smallest p value to largest. These 31 observations correspond to the solid points and stars in the volcano plots in Figure 5.5D–F. *Observation were considered significant if $p < 0.01$ and $|\Delta(\Delta F/F)| > 15\%$.

Stim. Odor		Stim. Dir.	Region Side	Region name	Time Bin	$\Delta(\Delta F/F)$	$-log_{10}(p)$
Cadaverine	1	both	left	Subpallial dopaminergic cluster, Telencephalon	Stim.	+25.8%	3.2
	2	both	right	Preoptic Otpb Cluster, Diencephalon	Stim.	+15.4%	3.1
	3	both	left	S1181t Cluster, Telencephalon	Stim.	+22.5%	3.0
	4	both	left	Subpallial Otpb Cluster 2, Telencephalon	Stim.	+24.4%	2.8
	5	both	left	Vmat2 cluster, Telencephalon	Stim.	+21.4%	2.7
	6	both	right	Anterior Commisure, Telencephalon	Stim.	+15.9%	2.6
	7	both	left	Preoptic area Vglut2 cluster, Diencephalon	Stim.	+16.2%	2.6
	8	both	left	Preoptic Otpb Cluster, Diencephalon	Stim.	+15.2%	2.6
	9	both	right	Isl1 cluster 2, Telencephalon	Stim.	+18.4%	2.6
	10	both	left	Preoptic area Vglut2 cluster, Diencephalon	Post-Stim.	+19.5%	2.5
	11	both	right	Anterior preoptic dopaminergic cluster, Diencephalon	Stim.	+17.9%	2.4
	12	both	left	Isl1 cluster 2, Telencephalon	Stim.	+18.0%	2.2
	13	both	left	Anterior Commisure, Telencephalon	Stim.	+18.1%	2.2
	14	both	right	Preoptic area Vglut2 cluster, Diencephalon	Stim.	+22.6%	2.2
Amino Acid	1	left	left	Isl1 cluster 2, Telencephalon	Post-Stim.	+15.5%	3.3
	2	left	right	Olfactory Bulb, Telencephalon	Post-Stim.	+19.0%	2.8
	3	left	left	Otpb Cluster 1, Diencephalon	Post-Stim.	+15.8%	2.5
	4	left	left	Subpallial dopaminergic cluster, Telencephalon	Post-Stim.	+26.4%	2.5
	5	both	left	Subpallial dopaminergic cluster, Telencephalon	Stim.	+15.5%	2.4
	6	left	right	Olfactory bulb dopaminergic neuron areas, Telencephalon	Stim.	+19.0%	2.4
	7	left	left	Vmat2 cluster, Telencephalon	Post-Stim.	+18.2%	2.3
	8	left	left	Olfactory Bulb, Telencephalon	Post-Stim.	+16.4%	2.3
	9	left	right	Olfactory bulb dopaminergic neuron areas, Telencephalon	Post-Stim.	+18.5%	2.2
	10	left	left	S1181t Cluster, Telencephalon	Post-Stim.	+23.6%	2.2
	11	left	right	Subpallial dopaminergic cluster, Telencephalon	Post-Stim.	+23.1%	2.1
	12	both	right	RoM1, Rhombencephalon	Post-Stim.	+31.3%	2.1
	13	left	left	Olfactory Epithelium, Ganglia	Post-Stim.	+18.6%	2.0
Control	1	both	right	Subpallial dopaminergic cluster, Telencephalon	Stim.	+30.2%	4.5
	2	both	right	Olfactory bulb dopaminergic neuron areas, Telencephalon	Stim.	+15.9%	2.6
	3	right	right	Torus Lateralis, Diencephalon	Post-Stim.	+16.8%	2.4
	4	both	left	Subpallial dopaminergic cluster, Telencephalon	Stim.	+25.8%	2.1

To the filtered and time-adjusted data table we added a column representing the stimulation type (e.g. `cadaverine-left`) and the trial ID (e.g. `cs-ii-29_run-334_trial-2`). With these additional tags, we could concatenate all of the different trials tables into a single data table to perform aggregation, statistical analysis, and visualization.

5.4.3 Analysis of Region-Segmented, Stimulation-Correlated Calcium Imaging Data

5.4.3.1 Hierarchical Clustering of Calcium Traces

After resampling and aligning regional calcium traces accross multiple stimulation trials, we aggregated the results for each region by taking their average. The pairwise correlation coefficient R between traces for each possible pair of regions was computed and then converted to a distance metric proportional to $1 - R$. This distance metric was then used to hierarchically cluster the regions from "closest" (i.e. most tightly correlated) to "farthest" (i.e. least correlated) in agglomerative groups[3]. This was accomplished via the `seaborn.dendrogram(...)` Python function with keyword argument `metric='correlation'`.

5.4.3.2 Statistical Testing of Region-Segmented Calcium Data Correlated to Stimulation

To perform statistical comparisons of calcium activity from multiple experiments, we first determined a set of time windows representing different phases over the stimulation sequence. For example, for the analysis presented in Figure 5.2B we utilized the following intervals (in stimulus-based time):

- Pre-stimulus (reference): $t \in [-30\,\text{s}, -1\,\text{s}]$
- Early Stimulus: $t \in [1\,\text{s}, 10\,\text{s}]$
- Mid Stimulus: $t \in [10\,\text{s}, 30\,\text{s}]$
- Late Stimulus: $t \in [30\,\text{s}, 59\,\text{s}]$
- Early Post-stimulus: $t \in [61\,\text{s}, 70\,\text{s}]$
- Late Post-stimulus: $t \in [70\,\text{s}, 100\,\text{s}]$

Then, for each brain region, for each trial, for each stimulation interval, we aggregated all the values within the stimulation interval by taking the mean. The set of means across multiple trials for a given brain region could be compared to the pre-stimulus/reference set of means across trials to compute an effect size (difference between the mean of the means) and a p-value by performing a Student's t-test. With these metrics, a given brain region's response was statistically compared and evaluated for each of the specified time windows.

[3] See documentation for Python function `scipy.cluster.hierarchy.linkage`

5.4.4 Quantification of Swim Bout Counts Correlated to Stimulation

Once we adjusted the time points of swim bout data to be stimulation-based rather than trigger/imaging-based and concatenated trials together as described in §5.4.2 we used binning to quantify the number of bouts which occurred within different time windows for each trial, yielding bout "count" values. Similar to the statistical comparison of means in §5.4.3.2 we can visualize and statistically compare the bout counts between time windows by creating sets across trials for the various conditions. For these analyses we ensured all time windows had the same duration so that the magnitude of the counts could be compared (alternatively we can also divide count values by the window length to produce a window size-agnostic bout frequency).

5.5 Conclusion

In this culminating chapter, we demonstrate our ability to synchronize olfactory stimulation acquisition to two photon whole-brain calcium imaging, infrared behavioral recording, as well as move towards registration to *ex vivo* immunohistochemical maps in an individual larva. With these acquired datasets we observed significant responses in a number of brain regions to tactile stimulation and noticed a trend of increased tail movement after stimulus cessation. We also performed a series of trial experiments where we delivered different odors bilaterally and, by inspecting response heatmaps, saw what appear to be different patterns of for each odor. Interestingly; however, we did observe similar patterns regardless of odor in the rostral regions near the olfactory epithelia.

In this report we do not perform a hypothesis-driven set of experiments; however, this demonstration proves the type rich datasets we can now obtain and we outline a number of investigation we will move toward to study olfactory kin recognition and bilateral stimulus discrimination. This work represents an exciting application of newly developed platform and moves us toward building an understanding of the brain in a way that integrates stimulation, behavior, functional activity, and biomolecular structure.

5.6 References

1. Sy, S. K. H. *et al.* An optofluidic platform for interrogating chemosensory behavior and brainwide neural representation in larval zebrafish. *Nature Communications* **14.** https://doi.org/10.1038/s41467-023-35836-2 (227 2023).
2. Gerlach, G. & Lysiak, N. Kin recognition and inbreeding avoidance in zebrafish, Danio rerio, is based on phenotype matching. *Animal Behaviour.* ISSN: 00033472 (2006).
3. Gerlach, G. *et al.* Behavioural and neuronal basis of olfactory imprinting and kin recognition in larval fish. *Journal of Experimental Biology* **222.** ISSN: 00220949 (Feb. 2019).
4. Hinz, C. *et al.* Kin recognition in zebrafish, Danio rerio, is based on imprinting on olfactory and visual stimuli. *Animal Behaviour* **85,** 925–930. ISSN: 00033472 (5 May 2013).
5. Hinz, C. *et al.* Olfactory imprinting is triggered by MHC peptide ligands. *Scientific Reports* **3,** 2800. ISSN: 2045-2322. http://www.nature.com/articles/srep02800 (1 Dec. 2013).
6. Wee, C. L. *et al.* Zebrafish oxytocin neurons drive nocifensive behavior via brainstem premotor targets. *Nature Neuroscience* **22,** 1477–1492. ISSN: 1097-6256. http://www.nature.com/articles/s41593-019-0452-x (9 July 2019).
7. Wee, C. L. *et al.* Social isolation modulates appetite and avoidance behavior via a common oxytocinergic circuit in larval zebrafish. *Nature Communications 2022 13:1* **13,** 1–17. ISSN: 2041-1723. https://www.nature.com/articles/s41467-022-29765-9 (1 May 2022).

CHAPTER 6

Conclusion

Through this thesis work I have made several contributions to the fields of microscopy and zebrafish neuroscience. I have created, formalized, and implemented a suite of multi-view light field reconstruction algorithms that can improve resolution and reduce aliasing in reconstructed 3D images to enable high-frame-rate recordings of neural activity. I have designed, assembled, and utilized hardware and software to create a system, unlike any other reported, for multi-directional olfactory stimulation of the larval zebrafish with up to ten separate odor channels. I have optimized an expansion microscopy-compatible immunostaining protocol for whole-mount zebrafish which preserves registration epitopes to

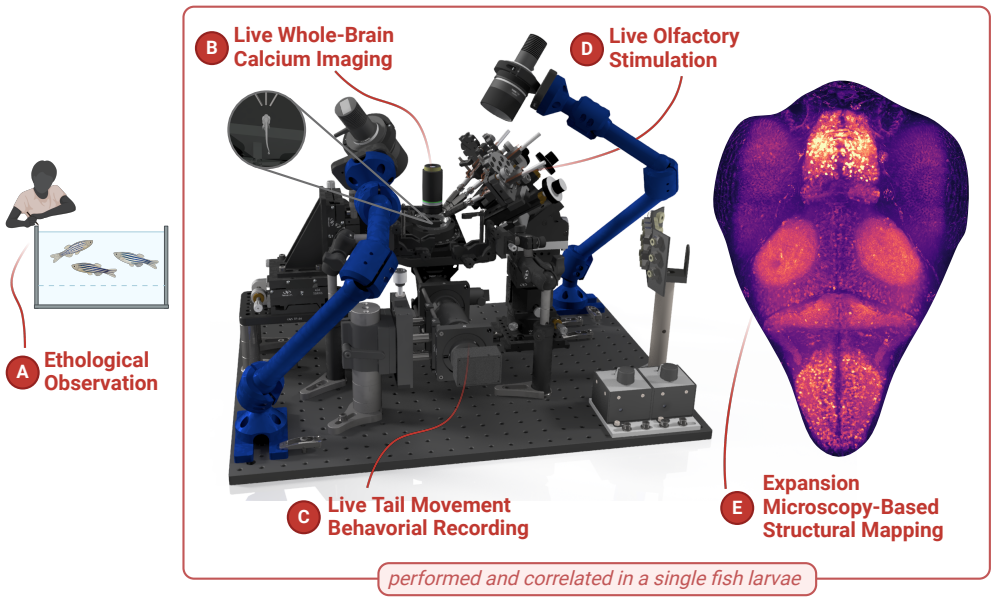

Figure 6.1: Our work shows that we have taken a leap forward toward the overall objective of this thesis research. The goal of this thesis work to enable a deeper and more complete understanding of the brain by combining (A) existing knowledge and observations zebrafish, (B) *in vivo* recording of neural activity, (C)) live observation of behavior, and (E) *ex vivo* structural and biochemical mapping of neuronal organization in the context of (D) sensory stimulation all in an individual organism.

move towards the neuron-level alignment of structural and functional data. I have performed a set of proof of concept experiments and analyses which demonstrate the ability to integrate olfactory stimulation, whole-brain calcium imaging, behavioral recording, and structural staining in individual larva, Figure 6.1. I am excited to present this work and provide thesis document to catalog this work and allow those listed initiatives to be improved and built upon.

APPENDIX A

Software, Firmware, and Data Repository

All code, virtual instruments, and Arduino firmware as well as instructions for accessing data are contained in the following GitHub repository: https://github.com/CorbanSwain/2024-Corban-Swain-MIT-BE-Doctoral-Dissertation-Public-Repository/tree/main. Any questions, comments, or issues regarding this work can be posted to the "Issues" or "Discussions" sections of the repository (as of September 2024).

This thesis was proofread and edited with the support of Ed Boyden, Maxine Jonas, Panagiotis Symvoulidis, Roderick Swain, and Denise Swain.

This thesis is set in the typeface Equity by Matthew Butterick and was compiled using XeLaTeX.